ulm university universität
uulm

An approach to parallel acquisition in STED microscopy

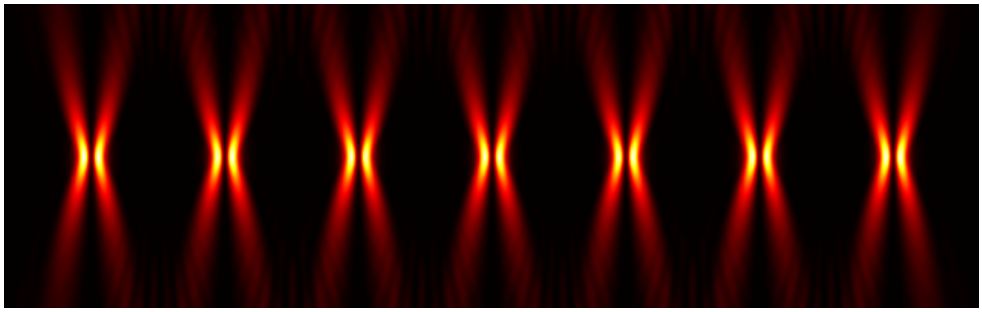

Dissertation zur Erlangung des Doktorgrades Dr.rer.nat.
der Fakultät für Naturwissenschaften
der Universität Ulm

vorgelegt von

Uwe Hermann Peter Jantzen
aus Karlsruhe

2021

Begutachter:
Prof. Dr. Jens Michaelis
Prof. Dr. Kay-Eberhard Gottschalk

Betreuer:
Prof. Dr. Jens Michaelis

Dekan:
Prof. Dr. Thorsten Bernhardt

Tag der Promotion:
09.02.2022

Contents

Introduction **ix**

Acknowledgments **xi**

1. Super-resolution optical microscopy **1**
1.1. Abbe limit . . . 1
1.1.1. Rayleigh criterion . . . 2
1.2. Fluorescence microscopy . . . 3
1.2.1. Fluorescence . . . 4
1.3. Microscope principle and confocal microscopy . . . 5
1.4. Super-resolution techniques . . . 7
1.5. Stimulated emission in STED microscopy . . . 9
1.6. Beam shaping in STED microscopy . . . 12
1.7. Resolution improvement in STED microscopy . . . 14
1.8. STED techniques . . . 18
1.8.1. Time gating . . . 18
1.8.2. Fast scanning . . . 18
1.8.3. Alternate illumination/STED beam shapes . . . 19
1.8.4. Variable pixel dwell time . . . 19
1.8.5. Power modulation . . . 20

2. Experimental overview **21**
2.1. Spatial Light Modulator . . . 22
2.2. Multi-Mirror scanning . . . 22
2.3. Hardware control through FPGA . . . 24
2.4. Software . . . 25
2.5. Parallel Imaging . . . 25
2.6. Laser timing . . . 26
2.7. Polarization . . . 28
2.8. Optical components . . . 28
2.8.1. Mode cleaning and ellipticity . . . 28

2.8.2. Lenses . . . 29
2.8.3. Filters . . . 29
2.8.4. Waveplates . . . 30
2.8.5. Polarizers . . . 31
2.8.6. Mirrors . . . 31
2.8.7. Mechanics . . . 32

3. Optical setup and alignment **33**
3.1. Setup . . . 33
3.2. Filters . . . 35
3.3. Optical tools and alignment methods . . . 38
3.3.1. Beam positioning and collimation . . . 39
3.3.2. Back reflections . . . 39
3.3.3. Beam profiling . . . 40
3.3.4. Component positioning . . . 44
3.3.5. Telescope alignment and cylindrical telescopes . . . 44
3.3.6. Transmission lines . . . 45
3.3.7. Infrared laser alignment . . . 45
3.3.8. Confocal alignment . . . 46
3.3.9. Polarization alignment . . . 47
3.3.10. Fluorescent samples . . . 48

4. Beam shaping **51**
4.1. Wave optics . . . 52
4.1.1. The plane wave . . . 53
4.1.2. Plane wave decomposition . . . 54
4.1.3. Free space propagation . . . 54
4.1.4. Transmission through thin media . . . 54
4.1.5. Optical Fourier transform . . . 55
4.2. Vector diffraction theory . . . 56
4.2.1. Construction of diffraction integral for high numerical apertures . . . 57
4.2.2. Fast focus field calculations . . . 59
4.2.3. Polarization influence and central minimum . . . 61
4.3. Spatial light modulator . . . 62
4.3.1. Diffraction efficiency . . . 63
Zero-order . . . 64
Cross-talk reduction . . . 64
4.3.2. Pitfalls . . . 68

4.3.3. Description of optical aberrations . . . 69
Zernike polynomials . . . 71
4.3.4. Beam optimization prior to imaging . . . 73
Razor blade measurement on SLM . . . 74
Manual correction routine and vortex placement . . . 75
4.3.5. Zernike analysis algorithms . . . 77
STED image metric . . . 77
Binary phase profiles . . . 78
Pinhole transmission . . . 79

5. Confocal multiplexing **81**
5.1. Fan-Out algorithm . . . 82
5.1.1. Algorithm . . . 82
5.1.2. Implementation for SLM . . . 85
Altered search function . . . 85
Performance and other search algorithms . . . 86
5.2. Gerchberg Saxton algorithm . . . 90
5.2.1. Algorithm . . . 90
5.3. Resulting field geometries . . . 91

6. Hardware devices and control **95**
6.1. Sample scanning . . . 95
6.1.1. Manual stages . . . 95
6.1.2. Piezo stage . . . 97
6.1.3. Scanning mirrors . . . 98
Ray tracing . . . 98
Geometric mirror model . . . 100
Spatial positioning and scanning angles . . . 101
Performance tests . . . 103
Mirror mounting . . . 104
6.1.4. Voltage control of scanning mirrors . . . 105
Resistor noise/Bit noise . . . 107
6.2. Laser timing . . . 107
Timing alignment procedure . . . 109
6.3. Parallel acquisition . . . 110

7. FPGA **113**
7.1. Model specifications . . . 114
7.1.1. Electrical connections . . . 114
DAC interface . . . 114
7.2. VHDL programming . . . 115
7.2.1. Simulations . . . 117
7.2.2. IP cores . . . 117
7.2.3. Floor planning - connecting to the outside world . . . 118
7.2.4. Timing constraints . . . 119
7.2.5. USB communication . . . 119
7.3. Program structure . . . 120
7.4. Scanning . . . 121
7.4.1. Scan controller . . . 121
7.4.2. DAC controller . . . 122
7.4.3. Parameter Handling . . . 123
7.4.4. Waveform transmission . . . 123
7.5. Image acquisition . . . 124
7.5.1. Finite State Machine . . . 124
7.5.2. Signal acquisition . . . 126
Time gating . . . 128
7.5.3. SDRAM . . . 128
Communication constraints . . . 129
7.5.4. Data formation module . . . 129
7.5.5. Address formation module . . . 130
7.5.6. Data sorting . . . 131
7.6. Debugging . . . 132

8. Software **135**
8.1. Python . . . 135
8.2. Microscopy suite . . . 137
8.2.1. Program structure . . . 137
8.2.2. User interaction . . . 139
Main GUI . . . 139
Fit GUI . . . 139
SLM GUI . . . 140
8.2.3. Parameter handling . . . 142
8.2.4. Timers . . . 143
8.2.5. Image acquisition . . . 144

8.2.6. Scripting 145
8.3. Software compendium 145

9. Measurements **147**
9.1. Spatial light modulator optimization 147
9.2. Multi-beam characteristics 149
9.2.1. Ghost orders 149
9.2.2. Diffraction efficiency 150
9.2.3. Point spread functions on gold beads 155
9.3. STED measurements 158
9.3.1. Nitrogen-Vacancy centers in nano-diamonds 158
9.3.2. Gattaquant STED-nanoruler 162

10. Summary and Outlook **165**

A. Appendix **169**
A.1. VHDL examples 169
A.2. Scripting in microscope suite 171
A.3. Sample preparation 172
A.3.1. Nanodiamond samples 172
A.3.2. Gold bead sample 173

Glossary **175**

List of Figures **179**

List of Tables **183**

Bibliography **185**

Curriculum Vitae **193**

Introduction

Observing the machinery that makes up the human body is the key to understanding who we are. When the first human looked through the lenses of a microscope some 400 years ago, the world that was suddenly visible to the eye changed our perception forever. Since then, we came a long way and our techniques and skills improved, our observations gained higher precision, (especially with the advent of electron microscopy,) but still many processes remain obscured. Fluorescence microscopy, paired with the biochemical means to target and label specific parts of our specimens, brought many of these processes within grasp. Super-resolution microscopy came as the culmination of this endeavor by delivering images in unprecedented clarity.

Many of the still open questions revolve around processes in living organisms and therefore in-vivo measurements, which have high requirements for spatial and temporal resolution. This is the area where the technique of stimulated emission depletion (STED) has a lot of potential and also possibly the edge over other super-resolution techniques. It is a scanning based confocal microscopy method, where a second laser (STED beam) creates sub-diffraction sized fluorescent volumes utilizing the process of stimulated emission.

The fluorescent probes in STED are molecules with limited chemical stability under continuous illumination. This poses a major constraint and limits the window of observation. Although advances are made in longevity and brightness, it is still imperative to find measurement methods that extract the most information out of these fluorescent emitters. It was shown by Schneider (2013) [1], Kilian et al. (2018) [2] and Wu et al. (2015) [3] that clever temporal patterns and fast scanning reduce optical bleaching and increase cell viability, but all of these scanning techniques are limited by a narrow field of view. In contrast, there is scanning of massive multi-focal patterns that allows for a large field of view[4] but that is prone to intense bleaching.

Here, I present a technique that combines the best of both worlds and the possibility to enable video-rate STED with a large field of view in the future. A spatial light modulator that splits the STED laser beam into an array of beamlets works in tandem with an field programmable gate array (FPGA) that can acquire data from a single-photon avalanche diode (SPAD) array. This enables simultaneous imaging at multiple confocal volumes. Although imaging is performed at multiple locations, their spatial separation is large enough,

so that their photo physical behavior can be viewed as independent and all benefits of fast scanning are still available. Next to numerical estimates, I explored this concept in experimental form by developing a new STED microscope in the Institute of Biophysics at Ulm University. Before delving into the developed method, the optical setup and the experiments, I will give an overview on the field of super-resolution microscopy.

Acknowledgments

As with any complex project, this thesis would not have been possible without the support of many different people. I want to take a moment to express my thanks and gratitude to these people and mention their invaluable contributions to this work. First, I want to thank Prof. Jens Michaelis for being my supervisor and entrusting me with this project. He always had an open door and took time for discussions that guided me and taught me how to structure myself and my work flow. Next, I want to mention Prof. Kay Gottschalk from the Institute of Experimental Physics, who took the time to act as second examiner and introduced me to the field of biophysics in a very enjoyable lecture. In a time of need Prof. Steffen Stenger from the Institute of Medical Microbiology and Hygiene helped in financing my employment and as part of a cooperation project between our institutes. For this I am very grateful. I also want to thank Prof. Frank Slomka from the Institute of Embedded Systems/Real Time Systems for allowing me to use their infrastructure during FPGA development and putting me in contact with students interested in contributing to this work. In this context I want to thank Simon Ardouin and Michael Volk. Simon joined for a three-month project and contributed to the development of the data acquisition module on the FPGA, while Michael dedicated his master thesis to the development of the mirror scanning module on the FPGA. Both of them helped me to get an entry point into the field of very high speed integrated circuit hardware description language (VHDL) programming. I also want to thank Nicolas Roeser and Florian Hock, two PhD students in this institute who helped with their feedback in many discussions. I want to further thank Prof. Gregor Thalhammer and Prof. Alexander Jesacher from the Institute of Biomedical Physics at the University of Innsbruck. Their field of research includes spatial light modulator (SLM) applications and they were very helpful in frequent discussions about this topic. Prof. Angelo Gulinatti, Prof. Ivan Rech and Francesco Ceccarelli from the SPADlab at the Politecnico Milano, Italy, were providing us with the SPAD detector array prototype that will be used for multiplexed imaging. I am very grateful that they wanted to join us in collaboration. Everyone in the Biophysics Institute was a constant source of feedback and help and I can not thank them enough for creating a working environment that was cooperative and enjoyable throughout the whole time I spent working there. Especially I have to thank Jakob Bühler, a master student who spent the time of his thesis improving many parts of the STED

microscope, rounding off many rough edges in the process and implementing quality of life changes intended for future researchers who will use the microscope. Also mentioned should be Bernhard Gruchmann, who designed several custom electronic devices that are integral part of the microscope. Further thanks go to Carlheinz Röcker, Thomas Vomhof, Michael Watola, Matthias Reisser, Tobias Eilert, Timo Weggler and Christian Ganslmayer for many helpful discussions about optics and programming. Also members of the Institute of Quantum Optics were very helpful and I want to thank them. Manfred Bürzele helped in the design of the digital-to-analogue converter (DAC) board, Richard Waltrich provided us with fluorescent nitrogen vacancy center (NV) nano-diamond samples and Nikolas Tomek helped with his expertise in FPGA discussions. The facilities at Ulm University include an electronics and a mechanical workshop and several people were doing excellent work for many years in their contributions to the project. From the mechanical workshop I want to thank Martin Feierabend, Wolfgang Rapp and Jürgen Mähnß. From the electronics workshop I want to thank Reinhard Liske, Dominik Gaeta and Roland Klopfer. Thanks also go to Stefan Jenisch from the Institute of Electronic Devices and Circuits, who supported us with custom coatings and coating-related discussions. Several people from different companies should also be mentioned for their support that went beyond our expectations. These people are Götz Zinner from B.Halle Nachfl. GmbH, Thorge Holm from NKT Photonics Technology GmbH and Eugenie Strasser from Laser 2000 GmbH. Last but not least I want to thank my partner, Farzaneh Vaghefikia for her support during this time. She helped me to focus and and keep a clear head in stressful times.

1. Super-resolution optical microscopy

For over a century, the general consensus was that light microscopy has a hard resolution limit, namely the Abbe-limit proposed by Ernst Abbe[5] in 1873. However, in 2014, Eric Betzig, Stefan W. Hell und William E. Moerner received the Nobel Price in Chemistry for their contributions that kick-started super-resolution microscopy, a field that surpasses this limit. Today, it is possible to resolve image objects on the nanometer-scale with light microscopy in the visible spectrum.

This chapter will elaborate on the resolution limit and the techniques required to circumvent it. Next to a general description of super-resolution, it will also introduce the reader to the field of stimulated emission depletion (STED) microscopy, the main topic of this thesis.
To understand STED, we first cover the topics of fluorescence, stimulated emission and confocal microscopy. Then, the technique of STED itself and the current state of the art is discussed to build a relevant context for this work.

1.1. Abbe limit

The resolution limit for discerning features in an object was discovered by Abbe while working with diffraction gratings[5]. Monochromatic light incident on the grating plane gets diffracted into several orders while the angular spacing of these orders depends on the grating spacing d. To resolve the grating structure, the imaging system has to collect at least the first diffraction orders next to the central zero-order. This guarantees that the information of the grating periodicity is collected. The detection cone of the imaging objective determines the smallest grating spacing d that can still be resolved. The Abbe diffraction limit is[5]:

$$d = \frac{\lambda}{2\,n\,sin(\alpha)} \tag{1.1}$$

Here, λ is the wavelength of light, n is the index of refraction and α is the half-angle of the detection cone. Often the definition of the numerical aperture (NA) is used. It is defined

as $NA = n \cdot sin(\alpha)$. The Abbe limit can only be reached if the light is focused onto the grating. Both the illumination and detection require the same NA.

1.1.1. Rayleigh criterion

In superresolution microscopy often single light-emitting molecules are imaged. In this context, another definition of the diffraction limit is useful, one that originates from the field of astronomy. Stars are commonly modeled as point sources in imaging, since their solid angle, the angular area of emission as seen from earth, is very small. Imaging such a point source with a telescope is analogous to imaging the light emission of a single molecule with a microscope. An image of such an emitter will display an intensity pattern of a disk with concentric rings called Airy disk. The diameter of this pattern depends on the aperture of the observing device. In his original publication[6], Rayleigh calculated the intensity pattern originating from a rectangular aperture leading to a intensity distribution following the square of a sinc function. When the central maximum of a second airy pattern coincides with the first minimum of a first airy pattern, the intensity on the midpoint between the respective maxima has a relative intensity of 0.8106. Rayleigh defined this as the limit of closeness where the two light sources can still be resolved.

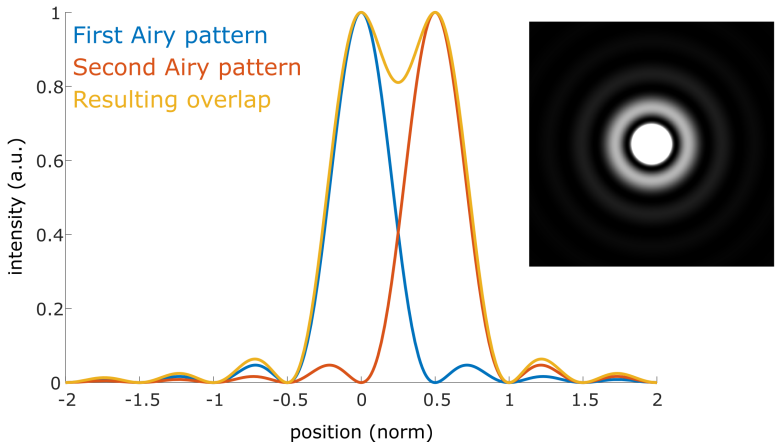

Figure 1.1.: A Matlab plot of the sinc functions for Airy patterns created by an ideal rectangular aperture in the imaging path. The function overlap signifies the shape that is still called resolvable with a minimum between the two main maxima at a value of 0.8106. The inset shows an Airy pattern created by a circular aperture. For clarity, the relative intensity in the inset has been oversaturated.

To compare this criterion in a context of microscopy, it is worth looking at the intensity pattern $I(\rho)$ of the Airy disk as expressed by the numerical aperture[7] and stemming from

a circular aperture. Here, ρ is the radial distance from the optical axis at the focal point of the optical system.

$$I(\rho) = [2\frac{J_1(k_{em}\, NA\, \rho)}{k_{em}\, NA\, \rho}]^2 \tag{1.2}$$

Here, J_1 is the first-order Bessel function of the first kind and $k_{em} = 2\,\pi/\lambda$ is the emission wave number. The Rayleigh criterion as expressed in terms of the numerical aperture and the distance between two emitters Δx is:

$$\Delta x = 0.61\,\frac{\lambda}{NA} = 0.61\,\frac{\lambda}{n\,sin(\alpha)} \tag{1.3}$$

This equation shows the direct relation to the Abbe limit. In real imaging systems, optical aberrations lead to changes in the image of a point emitter. A general term for the image intensity distribution created by a point emitter in an imaging system is called point spread function (PSF). This PSF can be seen as the optical analogue to a Green's function describing the delta response of a differential operator or the impulse response function (IRF) in signal processing.

1.2. Fluorescence microscopy

Historically, daylight was used as microscope light source. Using a broadband lamp as a replacement for the sun is still common today and we get to know this kind of microscopy as pupils in biology classes. Since the light spectrum of these broadband lamps typically covers a large spectral area in the visible range, this is called white light microscopy. When looking at biological tissue or cells with a white light microscope, there is not much contrast between different parts of the sample. Scattering and reflection depend mainly on changes in refractive index or particle size and much of the nano-machinery appears as an indiscernible mass. Specificity is key to getting a better picture.
In fluorescence microscopy, a sample is labeled with fluorescent markers, called fluorophores. The labeling can be targeted at specific substructures to allow for the display of parts of interest in different colors. In 1871, fluorescein[8] was discovered, a small dye molecule that emits blue light after appropriate excitation. It was used as one of the first fluorophores for staining of biological samples. It enabled the development of the first fluorescence microscope in 1911[9]. Over time, a plethora of different labeling techniques were developed, allowing for specific labeling in almost any case[10]. The study of the green

fluorescent protein (GFP) purified from jellyfish by Shimomura [11] in 1979, which was later rewarded with a shared Nobel prize, revolutionized the field by providing fluorescent labels that can be expressed by living cells.

1.2.1. Fluorescence

Fluorescence is an effect that directly stems from the electronic states of the fluorescent molecule. After absorbing a photon, the molecule transitions into an excited state. The absorbed energy can then be emitted through photons in radiative decay paths or dissipated into heat through non-radiative decay paths. The transition probabilities between the electronic states determine the optical properties of the fluorophore. To illustrate this behavior, a Jablonski diagram is drawn in Figure 1.2. It sketches the electronic states, their energy levels and possible transitions.

The diagram shows the lowest three electronic states S_0, S_1 and T_0 of a fluorophore. The dotted lines above the electronic states represent the vibrational levels of these states. The letters stand for the spin-multiplicity of the energy levels, namely S for singlet state and T for triplet state. After excitation with a high energy photon, the system relaxes into the vibrational ground state of the first excited electronic state. From there, the remaining energy can be emitted as a photon through fluorescence, dissipated through non-radiative decay paths, or the system can transition through a non-radiative decay path into the first triplet state. This triplet state is long-lived and the main reason for bleaching of the fluorophore. If the fluorophore is excited again before reaching its ground state through phosphorescence, it can reach higher energetic states. These can undergo chemical reactions leading to non-reversible changes in molecule structure and loss of fluorescent properties. Under standard laboratory conditions, the lifetime broadening of all states leads to a continuous absorption and emission spectrum for each fluorophore. Since part of the excitation energy is lost due to vibrational relaxation, the emission spectrum of the fluorophore is shifted to lower energy and therefore light with longer wavelength. An example is shown in Figure 1.3. This offset is named Stokes shift after Sir George Gabriel Stokes who discovered a behavior of fluorspar where ultra violet light is absorbed and the following emission is in the visible range[13]. He wrote a footnote with the intention of coining the new word "fluorescence" for this behavior, which was described in the text as dispersive reflection. Many fluorophores have a similar structure for the vibrational states in the ground and excited states, then the spectra for emission and absorption resemble mirror images of each other. However, this is not always the case as discussed in Ishikawa-Ankerhold, Ankerhold, and Drummen (2012) [14].

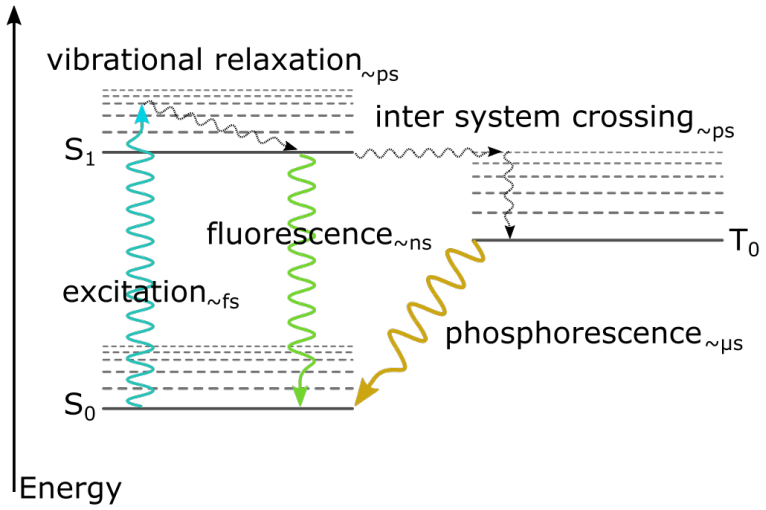

Figure 1.2.: The diagram shows the lowest three electronic states S_0, S_1 and T_0 of a fluorophore. The dotted lines over the electronic states represent the vibrational levels of these states. The solid arrows represent optical transitions, while the dotted arrows represent non-radiative transitions. By absorbing a high-energy photon, the system can be excited into the state S_1 from which it can emit fluorescence. The emitted photons will be red-shifted and contain less energy than the excitation light. In addition to the emission of fluorescence, the system has another radiative decay path. Through non-radiative relaxation it can transition from the S_1 state to a longer lived triplet state that itself can decay with the emission of phosphorescence or non-radiatively[12].

1.3. Microscope principle and confocal microscopy

The standard microscope we get to know as pupils consists of two lenses acting like a cascade of magnifying glasses. The samples are typically illuminated homogeneously from below with white light. While this is a very hands-on approach that gives the student an impression of microscopy, it comes with the disadvantage of bad optical sectioning for the researcher. During image acquisition, only a single plane in the sample is conjugate to the imaging plane of a camera or our retinas, but light from all other regions of the sample still contributes to a blurry background in the image.

There are multiple techniques that enable us to take a sharp and crisp image of a given sample plane by altering this basic microscope design. For example, in total internal reflection fluorescence (TIRF) microscopy the sample is illuminated by an evanescent light

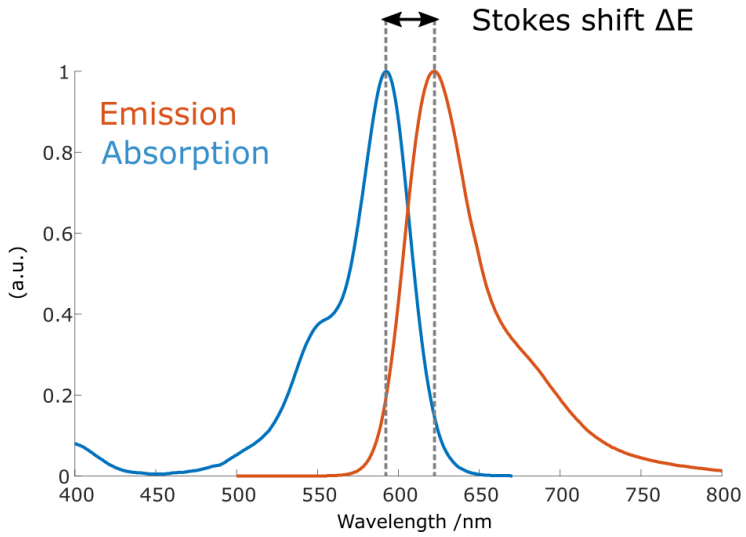

Figure 1.3.: Stokes shift: Part of the excitation energy is lost due to vibrational relaxation and the emission spectrum of the fluorophore is shifted to lower energy and longer-wavelength light (Matlab plot of Atto590 spectrum. Fluorescence data provided by ATTO-TEC GmbH, Siegen).

field originating from the total internal reflection of a laser at a substrate boundary. This light field decays exponentially over a few hundred nanometers into the sample, creating only a thin illuminated slice that then can be imaged. Other techniques create thin light sheets that act as similar illumination sources. In addition to restrictions in the illumination geometry, the detection geometry can also be altered. In a confocal microscope the wide-field image detection is replaced by point detection. A pinhole is placed in front of a photon detector and conjugate to a point in the focal plane of the microscope objective (Figure 1.4) coining the name confocal microscope. This detection scheme will detect a maximum of light from a light source placed at this focus, e.g. a fluorophore, while cutting away a large percentage of out-of-focus light. A region of interest in a sample can then be scanned point by point to create an image. In most confocal microscopes this detection is combined with focused illumination and the same objective is used for illumination and detection. The final resolution of the microscope then becomes the product of the illumination and detection PSFs[15]. Using the Rayleigh criterion as a basis and modeling the detection pinhole as an infinitesimal small point, the resolution limit becomes:

$$\Delta x \approx 0.37 \frac{\lambda}{NA} \tag{1.4}$$

In a real experiment, the resolution is ultimately limited by noise and optical aberrations. A

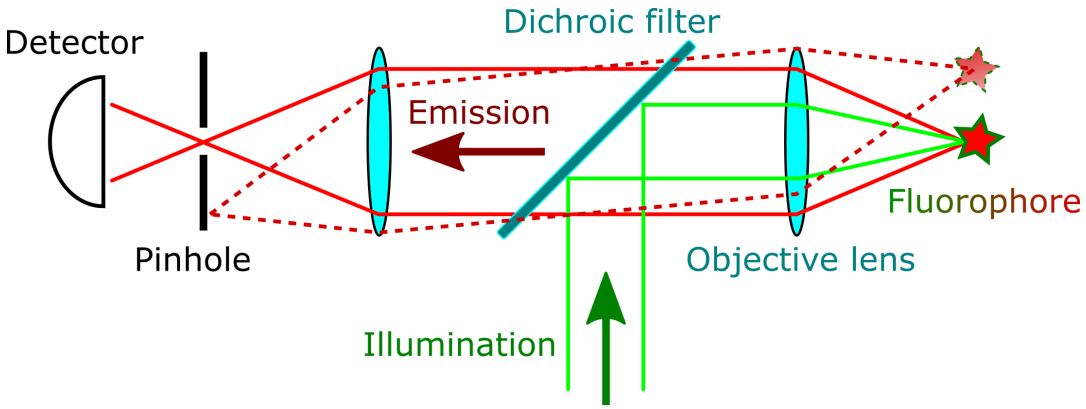

Figure 1.4.: The image shows the concept of a confocal fluorescence microscope. A flourophore at the focal point of the objective lens is excited by green light and the red-shifted emission is detected. The green excitation beam is coupled into the beam path by an interferometric dichroic filter that has high transmission for red light and high reflection for green light. The lens in front of the detector focuses the emitted light through the pinhole only if the fluorophore position coincides with the focal point of the objective lens.

large enough detection pinhole is needed to collect enough light for a good signal-to-noise ratio (SNR). However, this also increases the size of the detection PSF. In addition to this, the aperture of the objective is often not evenly illuminated, but a beam with Gaussian intensity profile is used. This will lead to an increase in the excitation PSF size and a further reduction in resolution.

1.4. Super-resolution techniques

Detectors used in microscopes always consist of some element that integrates the number of impinging photons over some time period. This number is then attributed to an image pixel corresponding to a position in the sample. As long as multiple emitters of the same wavelength are in close proximity and simultaneously active during this integration time, the resolution of the their image will always be diffraction-limited. In contrast, although the image of a single emitter will result in an Airy disk with a diffraction-limited size, its center position can be determined precisely. The variance of the mean position σ_x scales inversely with the square root of the number of collected photons N (Equation 1.5). This implies that the positional accuracy is conceptually only a technical limitation. It arises from the positional stability of the emitter during the integration time and the number of collected photons.

$$\sigma_x(N) = \mathcal{O}(1/\sqrt{N}) \tag{1.5}$$

For an image of multiple emitters, an increase in resolution with this scaling is possible if their emission can be separated in time. To achieve this temporal discrimination, there are multiple options. For stochastic optical reconstruction microscopy (STORM), the used fluorophores are tailored to have dark and bright states, with a mechanism to stochastically switch between the two states. By controlling the labeling density and the transition rates between the states, there is a subset of non-overlapping emissions at a given time. After acquiring enough images a composite image can be created, now containing all emitter positions with higher accuracy (Figure 1.5).

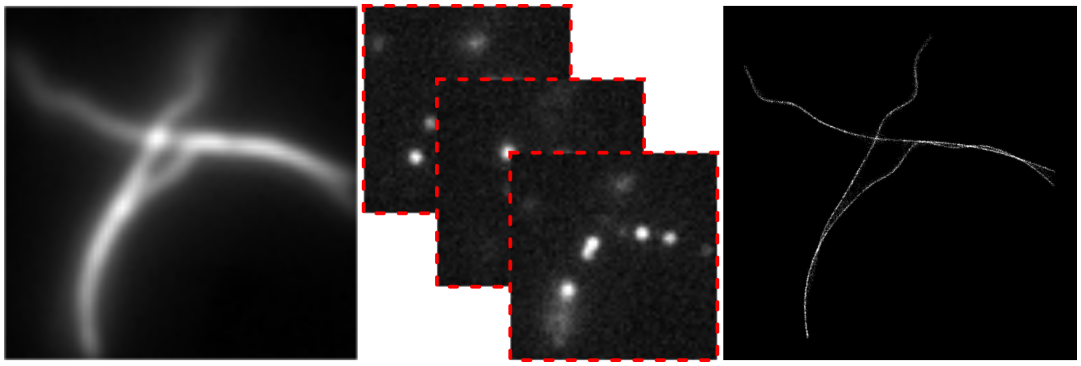

Figure 1.5.: The right image shows a conventional diffraction-limited widefield image. After acquiring a stack of images with sub-sets of active emitters (middle), a super-resolution image can be reconstructed (data from Sage et al. (2019) [16]). In this particular case, the reconstruction was performed from a stack of 500 images.

Another possibility to excite a smaller subset of emitters is by deterministic switching techniques like ground state depletion (GSD) or STED, the technique used in this thesis. For GSD, a laser is tuned to drive a transition from the ground state into a long-lived triplet state that cannot fluoresce. In STED, a laser is used to drive the process of stimulated emission, an optical transition from the first excited state that is competing with the spontaneous fluorescence decay. With higher laser power, the rate constant for stimulated emission increases and the probability for a spontaneous decay decreases. The power dependence of these processes can be exploited to create sub-diffraction fluorescent volumes with a low number of emitters. To achieve this, the laser beam profile can be tailored to contain small and isolated areas where the intensity is low enough to still permit fluorescence. The rest of the light field has a high intensity and prohibits fluorescence. Although the minimal excitation volume is diffraction-limited, these areas can have sizes well below the diffraction limit (Figure 1.6). The overlay of an excitation laser with this STED beam will then

result in fluorescence being emitted from areas smaller than the diffraction limit, effectively increasing image resolution.

The light field geometries involved in super-resolution techniques are especially susceptible to optical aberrations. In biological samples, additional aberrations can originate from local changes in refractive index or scattering. Therefore, the thickness of objects under study is typically limited to tens of µm. To alleviate this problem, various super-resolution experiments aim to decrease optical aberrations with the help of diffractive optical elements (DOEs), e.g. deformable mirrors or spatial light modulators (SLMs).

The next sections will provide an in-depth discussion of the theoretical background of STED microscopy. They will explain the behavior of stimulated emission in the context of pulsed lasers, how to tailor laser beams for STED and arrive at quantitative expressions for the resolution improvement.

1.5. Stimulated emission in STED microscopy

The process of stimulated emission is best visualized with a Jablonski diagram showing the relevant energy levels and transitions (Figure 1.7). Fluorescence is described as part of a radiative decay path from the first excited electronic state S_1 back to the groundstate S_0. When introducing a second laser beam, called STED beam, next to the excitation laser a further radiative decay path from S_1 back to the S_0 can be introduced into the system. If the STED beam is red-shifted in relation to the excitation laser, but has a wavelength that is still part of the emission spectrum of the fluorophore, there is a probabilty for stimulated emission. In stimulated emission the fluorophore transistions from the vibrational groundstate L_2 of the first excited electronic state S_1 into the vibrational state L_3 of the electronic groundstate L_0. The light emitted in this process has the same wavelength as the stimulating photon thereby red-shifting the fluorophore emission. If this wavelength shift is large enough, an optical filter can be used to separate the spontaneous fluorescence emission from stimulated emission.

The first STED paper by Hell and Wichmann (1994) [17] describes the rate equations of stimulated emission. The population probabilities n_{0-3} of the vibrational levels L_{0-3} can be described by a set of coupled differential equations. Here, σ_{01} is the cross section of excitation and σ_{23} is the cross section of stimulated emission ($\approx 10^{-16}\,\mathrm{cm}^2$), τ_{vibr} are the vibrational relaxation times ($\approx ps$), Q is the quenching rate ($\approx 10^8\,\mathrm{s}^{-1}$), τ_{fluor} is the fluorescence lifetime ($\approx 3\,\mathrm{ns}$). The functions $h_{exc}(x,t)$ and $h_{STED}(x,t)$ describe the photon density rate at a given time and location. Typical laser power densities for the STED laser

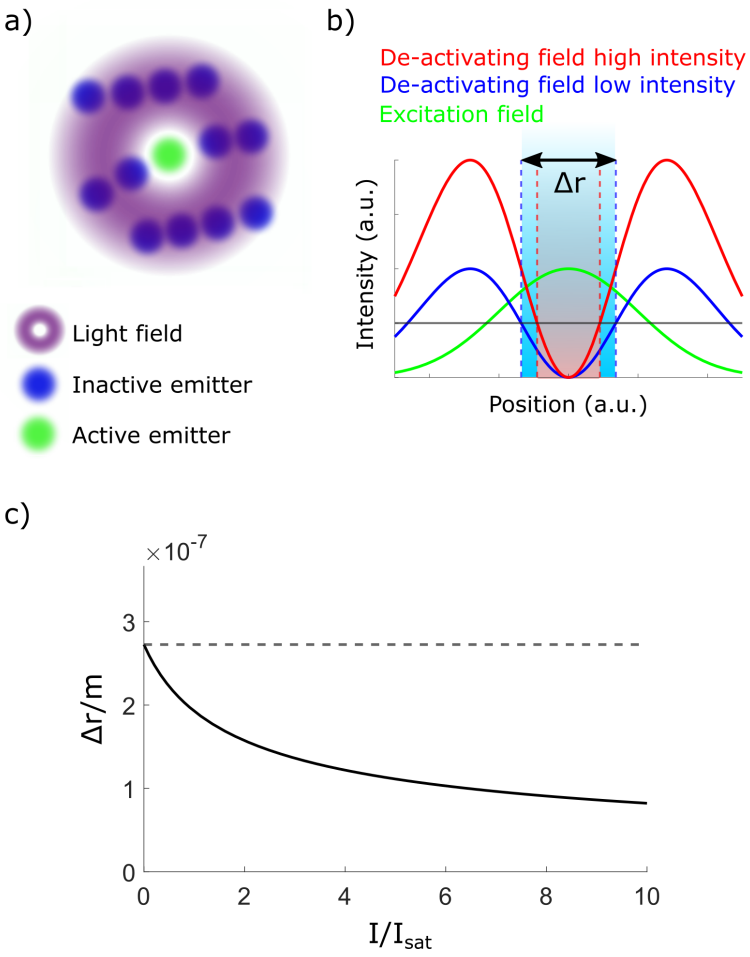

Figure 1.6.: a) A light field with intensity zero in the center is used to switch off emitters. Only emitters close to its center are able to fluoresce spontaneously. b) The horizontal solid line depicts a threshold in intensity for this light field, indicating an area in which emitters can fluoresce (blue area). Increasing the intensity will lead to a smaller area below this threshold (red area), effectively decreasing the volume of active emitters. With high enough intensity, the size of this volume can be pushed below the diffraction limit. c) Power dependence of Δr as exemplified by the resolution enhancement in STED (section 1.7). Here, Δr is plotted as function of the intensity ratio I/I_{sat} calculated in equation 9.1. The objective NA is 1.42 and the wavelength is $774\,\mathrm{nm}$.

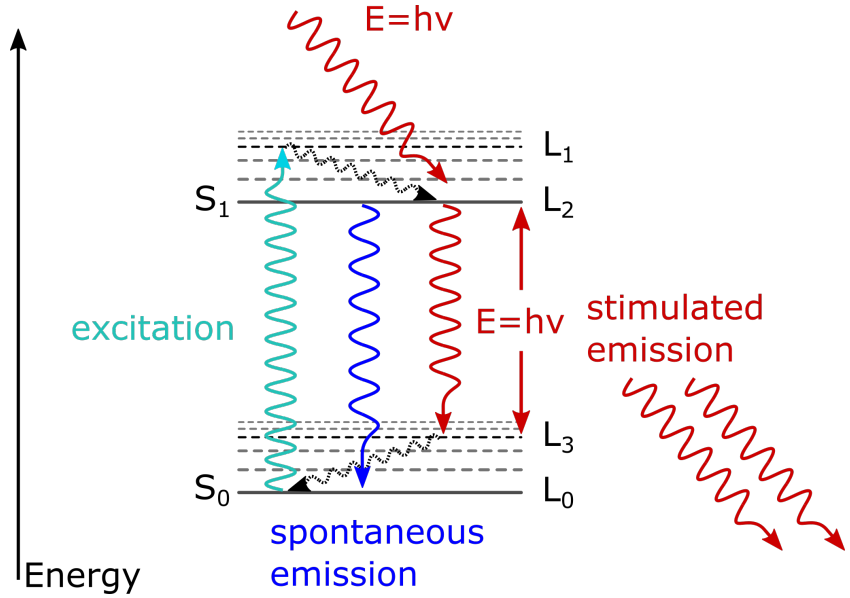

Figure 1.7.: Jablonski diagram of stimulated emission. Transistions between the vibrational levels L_{0-3} are shown. After excitation and vibrational relaxation, the lifetime of the state L_2 is on the order of nanoseconds. A laser with wavelength in the emission spectrum of the fluorophore can be used to force a radiative decay through stimulated emission into the state L_3. If the power of this laser is high enough the probability of spontaneous fluorescence vanishes, forcing the fluorophore to emit another photon at the same energy $E = h \cdot \nu$ as the laser driving the stimulated emission.

are in the range of MW cm^{-2}, while the excitation power is smaller by a factor of 10^{-3} to 10^{-4}.

$$\frac{dn_0}{dt} = h_{exc}\sigma_{01}(n_1 - n_0) + \frac{1}{\tau_{vibr}}n_3 \tag{1.6}$$

$$\frac{dn_1}{dt} = h_{exc}\sigma_{01}(n_0 - n_1) - \frac{1}{\tau_{vibr}}n_1 \tag{1.7}$$

$$\frac{dn_2}{dt} = h_{STED}\sigma_{23}(n_3 - n_2) - \left(\frac{1}{\tau_{fluor}} + Q\right)n_2 + \frac{1}{\tau_{vibr}}n_1 \tag{1.8}$$

$$\frac{dn_3}{dt} = h_{STED}\sigma_{23}(n_2 - n_3) + \left(\frac{1}{\tau_{fluor}} + Q\right)n_2 - \frac{1}{\tau_{vibr}}n_3 \tag{1.9}$$

To visualize the time development of the fluorophore state, the excitation laser h_{exc} and STED laser h_{STED} can be modeled as pulsed lasers with gaussian functions in time having a uniform and constant spatial extent. Figure 1.8 shows the solution of the rate equations following the interaction with the excitation and STED pulses. After excitation, the vibrational excited state population n_1 quickly decreases populating the state L_2. Fluorescence then slowly decreases the population probabilty n_2. As soon as the high power STED pulse arrives, the state L_2 starts to decay until it is completely depleted.

1.6. Beam shaping in STED microscopy

In the first concept of a STED microscope[17], the PSF of the excitation beam in a confocal microscope is sandwiched between the two PSFs of a split STED laser. This leads to an effective fluorescent volume that is flattened in one spatial direction dependent on the positioning of the STED PSFs. Since then, more options for advanced beam shaping are available. These enable the creation of field geometries that lead to isotropic fluorescent volumes in two[18] or three[19] dimensions or feature multiple minima[4] for the creation of STED microscopy with multiple foci. The most prominent way to create a STED beam with an intensity zero leading to isotropic sub-diffraction resolution in two dimensions is with the help of Gauss-Laguerre beams. The focus of a Gauss-Laguerre beam with the spatial mode TEM_{01} has the most narrow intensity minimum leading to the highest resolution increase in STED microscopy. It can be created by applying a phase term $\exp(i\phi)$ and left-handed circular polarization to a Gaussian laser beam. The STED beam can then be

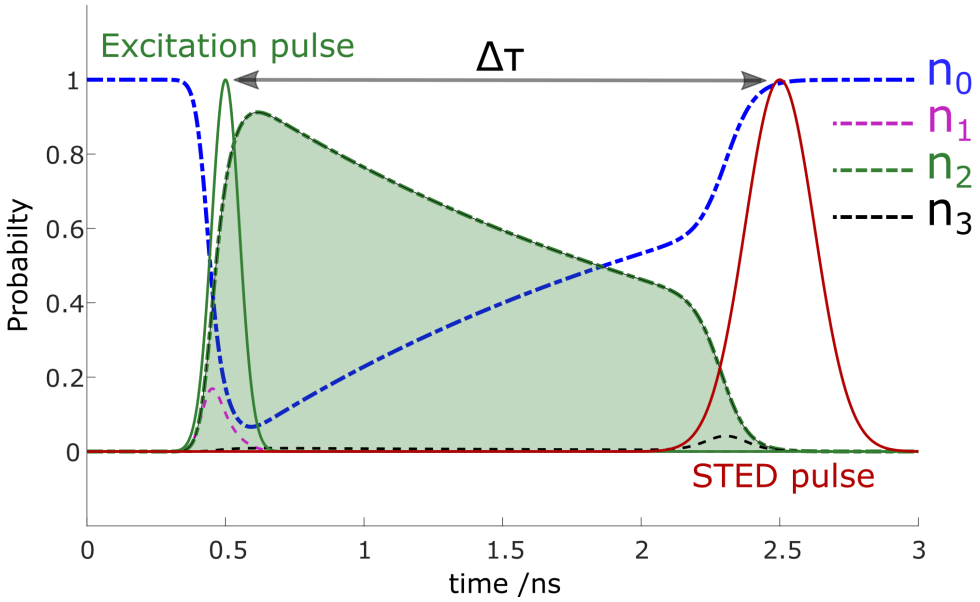

Figure 1.8.: Time evolution of the population probablities of the fluorophore energy levels in a typical time scale calculated in Matlab. After an excitation pulse, the population n_2 of the fluorophores excited state L_2 increases. The vibrational state population n_1 is shortlived and decays shortly after the excitation pulse ends. In the time before the STED pulse arrives, the n_2 population decreases through spontaneous fluorescence. When the STED pulse arrives, the n_2 population is fully depleted and the vibrational state L_3 is populated in the process. For clarification, the time difference between the excitation and STED pulse $\Delta\tau = 2\,\text{ns}$ as well as the vibrational relaxation times $\tau_{vibr} = 20\,\text{ps}$ have been increased in the calculations. The shape of the laser pulses corresponds to their normalized temporal intensity distributions. These are approximated by Gaussian profiles with $\sigma_{STED} = 125\,\text{ps}$ and $\sigma_{exc} = 50\,\text{ps}$ that correspond to the laser pulse durations used in the experiment.

written as a modified Gaussian beam. At the beam waist $z = 0$ the electric field $\vec{E}_0(r)$ of the beam is:

$$\vec{E}_0(r) = E_0 \, \vec{x} \, exp\left(\frac{-r^2}{w_0^2}\right) \, exp(i\phi) \tag{1.10}$$

Here, E_0 is the electric field amplitude, $\vec{x}$ is the polarization vector, w_0 is the waist radius of the beam and ϕ is the angle about the optical axis. The phase term $\exp(i\phi)$ together with circular polarization will lead to destructive interference of all beam contributions in the focal point. The PSF of a Gauss-Laguerre beam has to be calculated through vector diffraction since the high NA of a microscope objective prohibits the use of the scalar Fraunhofer diffraction equation. An analytical solution for the Debye-Wolf vector diffraction integral of ideal Gauss-Laguerre beams was derived by Török and Munro (2004) [18]. The solution is given in cylindrical coordinates in the vicinity of an objective focal point. Figure 1.9 shows the intensity contributions arising from the electric field components E_x, E_y and E_z in the focal plane of the microscope objective. It should be noted that the circular polarization direction has to be left-handed for an increasing phase-term $\exp(i\phi)$ and vice versa to guarantee a vanishing E_z component at $r = 0$. It is also crucial that the polarization of the STED beam and excitation beam is identical for the highest depletion effect[18].

1.7. Resolution improvement in STED microscopy

To get an estimation equation for the resolution improvement in STED microscopy, the time development of the rate equations (Figure 1.8) and the spatial profiles of the beams (Figure 1.9) can be approximated by simpler expressions[20]. We consider the approximation that the time profile of the STED pulse is a square pulse with sufficient intensity to keep the rate constant for the stimulated emission $k_{STED} \gg k_{fluor} = 1/\tau_{fluor}$. This means that the probability to fluoresce spontaneously $\eta(r)$ only depends on the intensity $I_{STED}(r)$ and duration τ of the STED pulse, since the fluorescence decay during the pulse itself becomes negligible. With $\sigma_{23} = \sigma$:

$$\eta(r) = n_2(r) = exp[-\sigma\tau I_{STED}(r)] \tag{1.11}$$

The spatial profile of a STED beam leading to the highest possible resolution increase in one dimension should feature two maxima centered around a point of zero intensity, with the smallest possible distance between the two maxima. A light field that fulfills this

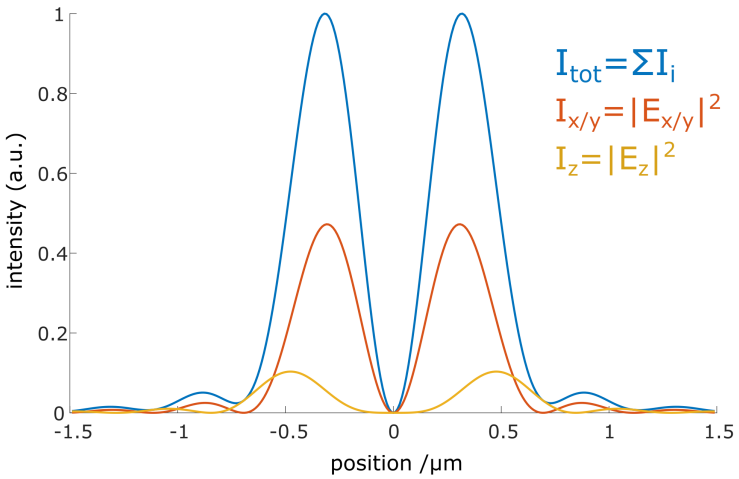

Figure 1.9.: Matlab plot of the electric field contributions to the total intensity of the STED PSF according to the formulas in Török and Munro (2004) [18]. The parameters for the calculations were an NA of 1.42 and a laser wavelength of $775\,\mathrm{nm}$, as used in our experiment. Contrary to the paraxial approximation, the electric field contributions along the optical axis E_z can not be neglected at a high NA. Only the use of circular polarization leads to a cancellation of the E_z components at $r = 0$.

requirement is a standing wave with a spatial period of one wavelength. Taking into account that an objective lens has an aperture angle α that limits the angle of incidence in the focal plane, the spatial profiles of the STED and excitation beams in the focal plane can be written as:

$$h_{exc}(r) = Ccos^2(\pi rnsin(\alpha)/\lambda_{exc}) \tag{1.12}$$

$$I_{STED}(r) = \zeta I_{sat} sin^2(\pi rnsin(\alpha)/\lambda_{STED}) \tag{1.13}$$

Here, $\zeta = I_{STED}^{max}/I_{sat}$ is the saturation factor, I_{STED}^{max} is the maximum intensity and $I_{sat} = 1/\sigma\tau$ is the saturation intensity where the fluorescence level has dropped to $1/e$. The spatial profile of the effective fluorescence spot then is:

$$h(r) = h_{exc}(r)\,\eta(r) \tag{1.14}$$

With $\lambda_{exc} \approx \lambda_{STED} = \lambda$ and $r < \lambda/(2n)$, the full-width at half-maximum (FWHM) of $h(r)$ can be approximated with a Taylor expansion up to second order to:

$$\Delta r = \frac{\sqrt{8}}{\pi\sqrt{1 + I_{STED}^{max}}} \frac{\lambda}{2\,n\,sin(\alpha)} \approx \frac{\lambda}{2\,n\,sin(\alpha)\,\sqrt{1+\zeta}} \tag{1.15}$$

The resolution increase is following a square root power dependence and has no theoretical lower boundary in this approximation. For $\zeta \to 0$, this resolution limit consistently resembles the Abbe limit. It should be noted that for real experiments this approximation has to be extended by including the possibility for direct excitation due to the finite lifetime of the vibrational states, as previously stated in Equation 1.8. Typical maximum values for the resolution in current microscopes, also influenced by the positional stability of the fluorescent markers, are in the range of $20\,\mathrm{nm}$. The dependence of η on pulse durations and laser power is studied by Leutenegger, Eggeling, and Hell (2010) [21] in an in-depth analysis of the rate equations and connected experiments. The case of continuous wave (CW) excitation and STED light as well as pulsed STED is explored.

At higher STED intensities, where $k_{STED} = I_{sted}\,\sigma \approx k_{vibr} = 1/\tau_{vibr}$, the vibrational excited groundstate L_3 has a non-zero probability for re-excitation to the excited state S_1. The rate equations initially stated have to be modified to include this transition. As a result, η will plateau at higher powers limiting the obtainable resolution in STED (Figure 1.10). The blue curves depict CW STED with increasingly lighter color for higher excitation intensities.

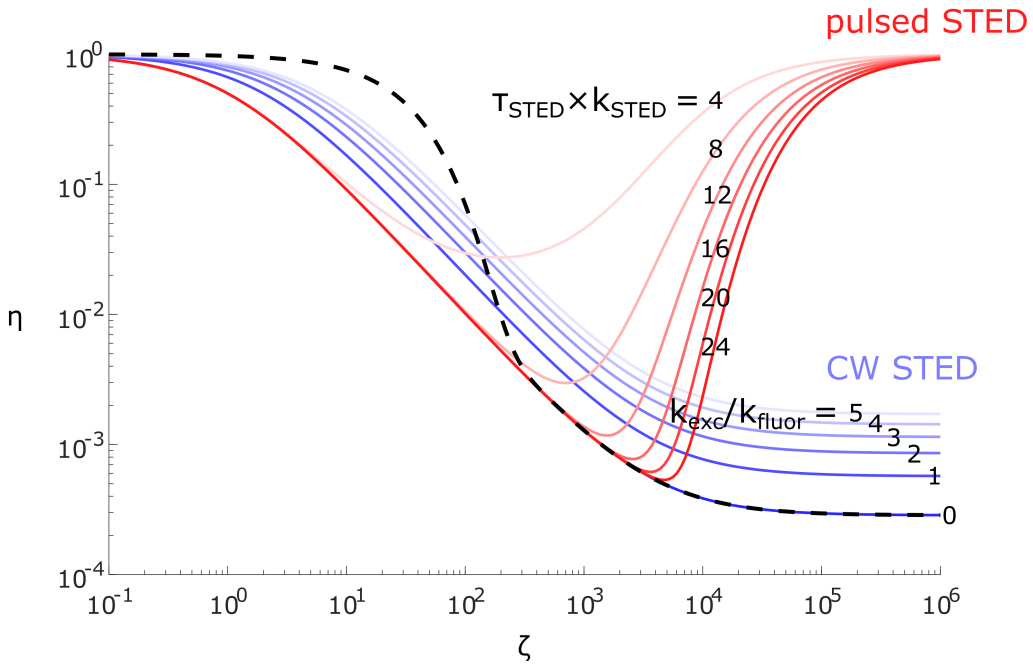

Figure 1.10.: Dependence of the fluorescence probability η as function of the STED laser intensity ratio ζ. The lower blue line is the limit for CW excitation and depletion with $k_{exc} = 0$. The increasingly lighter blue lines show the change to higher excitation rates $k_{exc} \approx k_{fluor}$, where the excitation from $S_0 \rightarrow S_1$ goes into saturation. The black dashed line shows that for pulsed STED the short pulse-width needs to be compensated with higher intensity. The red curves show lines of constant pulse energy, where τ_{STED} is decreased with increasing ζ. For higher intensities, pulsed STED outperforms CW STED (Matlab plot based on calculations in Leutenegger, Eggeling, and Hell (2010) [21]).

Since $\zeta \propto I_{STED}^{max}$, pulsed excitation and depletion is advantageous and lower values of η can be reached with the same average intensity. The red curves show pulsed STED with $\tau_{STED} k_{STED} = const.$. This corresponds to STED pulses of constant energy with increasingly darker color for higher energy. There is a clear optimum for η for each pulse energy. The calculated values for the corresponding pulse widths are in the range of ≈ 150 ps. Additional experimental factors like electronic jitter of the excitation laser or the power dependence of photo-bleaching were shown to have an influence not included in the model. This leads to larger optimal values for the pulse width and the value used in this experiment is ≈ 750 ps for the STED laser.

1.8. STED techniques

At the time of writing, STED is a field of research that already contains many variations in implementation. All of these variations aim to improve STED imaging in one way or another. A few of these approaches should be mentioned to illuminate, in which directions the field of STED has developed during the time of this thesis and act as examples for alternative approaches or future expansions of our microscope.

1.8.1. Time gating

With time gating, fluorescence photons that get emitted shortly after the excitation pulse are discarded in the detection, since they carry less spatial information[22]. The resolution increase depends on the fluorophore lifetime and the temporal pulse width of the STED laser. For our microscope, the expected resolution increase is between $5\,\%$ and $10\,\%$, and, since the gating can easily be implemented through additional hardware similar to our time-delay module (chapter 6.2), it is a likely candidate for a future extension of the microscope.

1.8.2. Fast scanning

STED imaging requires scanning of the confocal volume and is often limited by the inertia of mechanical scanners. Due to the photo physics of the fluorophore, a sufficiently fast scanning approach opens the possibility of illumination schemes that allow for triplet state relaxation. In this context, it was shown that resonant scanning with galvanometric scanning mirrors leads to a reduction in photo bleaching[3]. Here, the survival time of fluorophores was increased up to $80\,\%$ for a high illumination dose ($110\,\mathrm{mW}$ STED power at $80\,\mathrm{MHz}$ pulse repetition rate). However, even the fastest mechanical scanners ($16\,\mathrm{kHz}$) still have a comparatively slow speed. The fastest scanning approach today is with electro-optical deflectors (EODs). In the past, EOD were degrading the beam profile, but Schneider et al. (2015) [23] showed that current EODs can be used for STED imaging. They reported that fast scanning ($250\,\mathrm{kHz}$) with an interleaved illumination scheme lead to an increase of collected photons (3 times more) and a slower decay rate for bleaching. More information can be found in the dissertation of the author. However, this technique is difficult to implement from a technical point of view.

1.8.3. Alternate illumination/STED beam shapes

Instead of a Gauss-Laguerre beam, other beam shapes can be used for STED imaging. One approach, implemented in a microscope previously built in our institute (Osseforth (2014) [24]), uses a top hat phase mask in addition to a phase vortex to create a STED PSF that will lead to an almost isotropic three dimensional resolution increase. This is a useful technique for many cell and tissue samples and is commonly used to image three dimensional structures. This is also a planned future extension of this microscope. Another approach was examined by York, Ingaramo, and Cooper (2017) [25]. The core idea is to acquire a STED image that has a higher resolution increase in one spatial direction and then combine multiple STED images from different directions to calculate an image with isotropic resolution. This has the advantage that a one dimensional resolution increase can be achieved with lower STED intensity. A substantial decrease in net illumination dose is predicted. For the best effect, a beam is proposed that features two lines of high intensity with a central line of low intensity and that overlaps with the excitation beam. With this configuration, a wide-field acquisition with camera would record a complete line in the image with an objective perpendicular to the STED/excitation line. This line then will be scanned across the sample. This results in an image that features higher spatial resolution perpendicular to the line direction. By rotating the sample and the line with respect to each other, multiple images can be acquired, and their spatial information can be combined to again reach a composite image with almost uniform resolution increase. This theoretical idea is technically challenging and can most likely be realized with Bessel beams in an adapted lattice-light-sheet microscope setup as described in Chen et al. (2014) [26], but has not been attempted so far. A variation of this method can be implemented on our STED microscope, and I will discuss its feasibility at the end of this thesis.

1.8.4. Variable pixel dwell time

While scanning a STED image, typically the same time t_{acq} is spent at every distinct location that is later attributed to an image pixel. However, if at a given location either a very low signal or very high signal is present, the total amount of light collected can be predicted with good accuracy after a fraction of t_{acq}. This was analyzed by Staudt et al. (2011) [27] and coined "RESCue" STED. Recently this was utilized by Vinçon et al. (2020) [28], where an EOD in tandem with a acousto-optical modulator (AOM) and galvanometric mirror scanner moves the beam to the next position as soon as an accurate prediction can be made. This adaption of the technique leads not just to a light dose reduction, but also a scan time reduction of up to $85\,\%$. Of course, the improvement and the accuracy of the predictions

is dependent on the sample geometry. This technique offers one of the largest reductions in illumination dose, but comes with considerable technical difficulties, since it requires the synchronization and interplay of two different scanners and a hardware based estimation for the light collection. Another drawback in the implementation by Vinçon et al. (2020) [28] is that half of the fluorescence is lost in the detection path. In all beam scanning techniques the scan process has to be reversed to collect fluorescence in a stationary point detector and only one polarization direction of the fluorescent light can pass the EODs. Two EOD paths with orthogonal polarization direction could solve this issue. However, this would increase the complexity even further.

1.8.5. Power modulation

In fluorescence life time analysis, the temporal behavior of fluorophores can be used to distinguish different fluorophore types. A technique based on the same mathematical models can be used to improve STED resolution by up to a factor of two. This is a very impressive result, especially since it does not need any specialized hardware. Sarmento et al. (2018) [29] showed that the non-linearity of the STED process can be used to encode more spatial information about the fluorophore positions in STED images with the help of time dependent power modulations of the STED beam. In contrast to fluorescence life time analysis which needs specialized high speed detection hardware, here, the temporal variation can be on a slow time scale, e.g. accross multiple images with different power. This technique is very versatile and can be implemented on any STED microscope, including ours, and is compatible with all presented STED techniques. The only drawback is an increased effort in post-processing.

2. Experimental overview

To get accustomed to the experimental layout of the stimulated emission depletion (STED) microscope, it is helpful to look at the grand scheme of things before getting lost in details. In this chapter, I will focus on an experimental overview and introduce the reader to the individual parts and components. This will be followed up in the next chapter by the precise layout of the optical table. Figure 2.1 shows a box diagram of the microscope containing the sub-division into the major components. The optical table contains lasers for fluorophore excitation and a laser for STED. The laser beam paths are combined, and the sample under study is scanned by a piezo stage or scanning mirrors. During the scanning process, the fluorescence emission is collected and processed in a field programmable gate array (FPGA), a programmable chip. It acts as a multiple purpose device and handles image processing as well as the hardware control of scanning mirrors. After acquisition, a complete image is transferred to a PC.

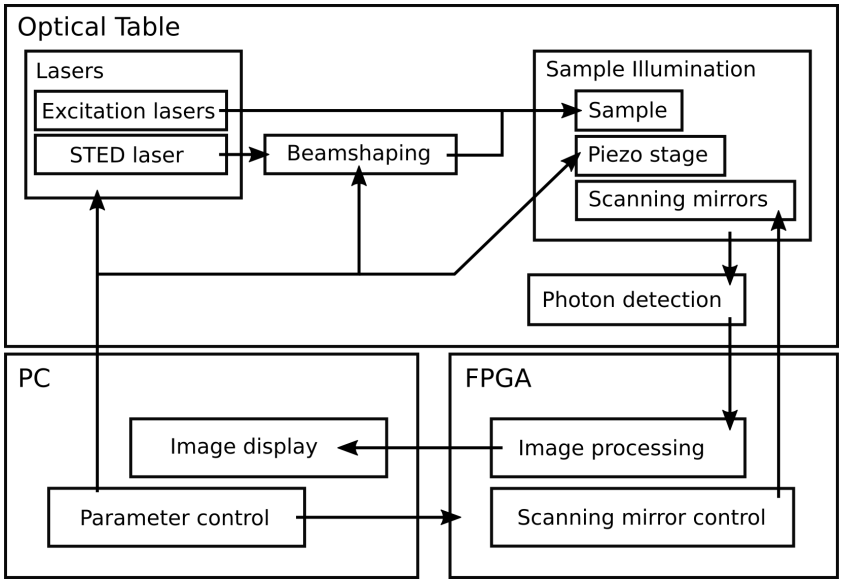

Figure 2.1.: Box diagram showing the interplay of microscope components. The sub-division into three major parts is based on the three major aspects of this work: optical design, software development, and hardware control.

2.1. Spatial Light Modulator

One of the core elements in the experiment is a spatial light modulator (SLM). It is used to create the STED beam, to correct optical aberrations, and for beam multiplexing. An SLM is a device, able to apply a defined phase modulation to the wavefront of a laser. The type of SLM used in this experiment is an electronic chip device (Figure 2.2). At its core, a layer of birefringent crystals is placed between two grids of electrodes. The electrodes are arranged in a rectangular grid of pixels with a surface area of $\approx 1\,\mathrm{cm}^2$. By controlling the electrode voltage, the crystals will orient in the electric field and create a variable optical path length for linearly polarized light of a defined direction. The voltage at every pixel is controlled independently and the device can be connected through standard display interfaces, e.g. DVI-D or VGA. The device concept exists in two configurations. In the first, the device will be placed in the beam path and the wavefront of the transmitted beam will acquire a pixel dependent phase shift. In the second, more popular version, a mirror is attached to the layer structure and the device is used in a reflective manner with a small angle of incidence (AOI). The beam then travels through the pixel layer, gets reflected and travels through the pixel layer a second time. In this way, the acquired optical path length is doubled. This double pass is a big advantage, since the crystal layer thickness is limited by the electric field geometry. The electric field needed for independent pixels has straight field lines between the opposing electrodes of each pixel. However, with increasing distance between these electrodes, the field structure will degrade through interaction with neighboring pixels.

The reflective back plane has an innate curvature due to imperfections in the manufacturing process. This will lead to wave front errors if left uncorrected. The shape of the curvature has to be determined by non-trivial interferometric measurements. It is therefore a big advantage if this phase correction is provided by the manufacturer.

2.2. Multi-Mirror scanning

In a confocal scanning microscope, the point of illumination has to move relative to the sample for imaging. For the physical construction of the microscope it is important to consider which of the two will be moved, since the inertia of moving components restricts the speed of image acquisition. Piezo-electric stages that move the sample can be operated at scanning speeds in the range of tens to hundreds of Hz, while galvanometic mirrors offer scanning speeds up to tens of kHz. This should make scanning mirrors an obvious choice. However, this comes at the cost of higher experimental complexity.

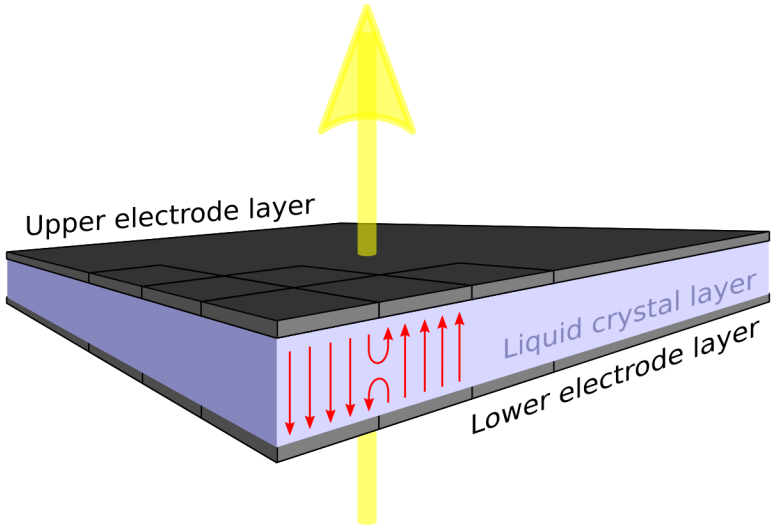

Figure 2.2.: Basic structure of an electronic SLM. The yellow arrow visualizes the transmission direction for a beam of light. The red arrows show the electric field lines when the voltage on electrodes of neighboring pixels is reversed. The stray fields at the pixel borders increase with the crystal layer thickness. This limits the maximal phase stroke possible with negligible pixel cross-talk.

For imaging with mirrors, the incident laser beam has to be moved accross the sample, maintaining a beam direction parallel to the optical axis. Therefore, the beam has to stay centered in the back-focal plane of the objective while changing its angle (Figure 2.3). There are two ways to achieve this. Firstly, a 4-f relay telescope can translate a mirror-plane into the back-focal plane of the objective. This requires a single mirror per scan direction. However, using a 4-f relay telescope will add additional length to the optical pathway and the lenses will add additional aberrations to the laser beam. The second way is a beam walk, where the beam angle in the back-focal plane is varied, while the position is kept constant. This requires two mirrors per scan direction. The second method reduces the optical path length and the total number of elements in the beam path. The drawback here is that it requires fine-tuning of mirror distances and precise synchronization of the mirrors, which comes with increased experimental complexity. Since STED microscopy is highly drift and stability-dependent and space on the optical table is limited, the latter option was chosen.

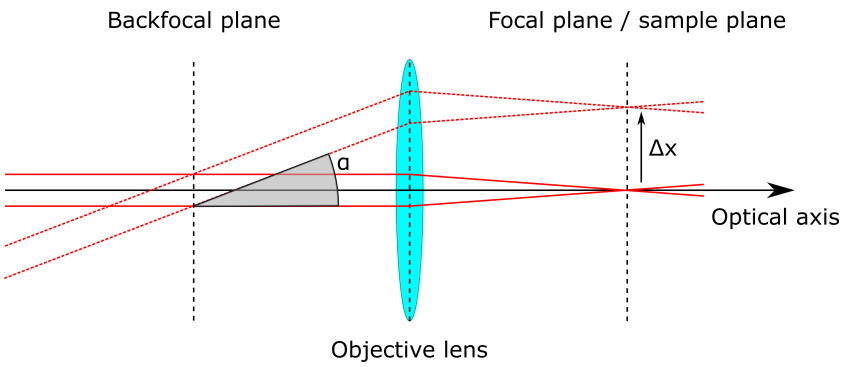

Figure 2.3.: An idealized objective lens transfers the angle of an incoming beam α into a focal point offset $\triangle x$.

2.3. Hardware control through FPGA

The experiment requires control, readout and interplay of lasers, shutters, detectors, cameras, galvanometric mirrors and piezo-electric stages. To ensure this wealth of different devices will function as a single easy-to-operate unit, a well-designed hardware interface is imperative. The current choice for this element is an FPGA evaluation module (EVM). An FPGA is an integrated circuit (IC) for which a programm can be written with the very high speed integrated circuit hardware description language (VHDL), and a compiled configuration file is then uploaded through an interface from a personal computer, e.g. USB. Usually, an FPGA is not the first choice for this kind of task since the learning curve of FPGA implementation is steep. However, several factors made a strong argument in favor of an FPGA. After working on confocal microscopes with hardware interface cards from National Instruments previously, they were a natural first choice for this experiment. However, after delving into the details, it became apparent that they were lacking the proper timing control needed for fast imaging and that options with enough entry points for parallel data-acquisition were not available. This also was the case for other common options like Arduino or Raspberry-PI devices. Custom-built solutions based on FPGAs were very expensive and could therefore not be taken into consideration. In contrast, advantages of an FPGA EVM are a large number of physical inputs and outputs, data-storage through on-board synchronous dynamic random access memory (SDRAM), highly parallel data-processing and a fast clock speed. This enables it to fulfill a large number of tasks. Here, it is used for data-acquisition, image processing, as a scan-controller, and as a time-gating module. As a bonus, FPGA EVMs are comparatively cheap.

2.4. Software

The microscope software acts as a hub, connecting all different devices and enabling their communication. The main goal is to start with a software that is easy to adapt and that can handle communication with a large number of devices. The programming language of the software should be easy to learn, while still being efficient and have a large user base. It is important to have enough debugging history from other users as an online knowledge base. This is immensely helpful in writing and debugging code. The choice for this experiment is the programming language python™. It comes with many open access software packages for data processing, image processing, graphical user interfaces (GUIs) and control for hardware devices of many manufacturers. In addition to the choice of programming language, it is a good idea to look for existing software that can be adapted. This can also save a lot of development time. In this context, a software suite called QuDi from Binder et al. (2017) [30] should be mentioned. It is a modular experimental control suite written in python™. This program has many useful core features, mainly the distinction into GUI, logic and hardware modules, and a connector system enabling the easy addition of new modules. It is built around the package PyQt (pronounced "pie cute"), an extensive GUI and multi-threading library. It is suited for the operation of experiments that require simultaneous and interconnected control of multiple hardware components. Detailed explanations to software development during this project can be found in chapter 8.

2.5. Parallel Imaging

A planned future extension of the setup is parallel imaging with an array of confocal volumes. This can be used to either increase the field of view of the microscope or to increase the acquisition speed at the same field of view. Using a higher number of lasers and photon detectors as separate devices in order to create more than just a few confocal volumes is not feasible. The scalabilty falters with cost, space and the complexity to combine a large number of beam paths that would be needed for a significant speedup. Other groups looked into creating a large number of confocal volumes by creating a lattice structure for the STED beam[4]. However, their method lead to intense photo-bleaching, again limiting the usefulness for live cell imaging. Since fluorophores have a probability to transition into a longer-lived triplet state, it is important that after a pass of the confocal volume there is a short time window for triplet state relaxation. It was shown that fast scanning with only short passes of the confocal volume over each dye molecule is able to prevent excessive photo bleaching[3]. Taking these considerations into account, there has to be an optimum

for the number of confocal volumes for a given field of view and scan speed.

In this context, we investigated if an SLM can facilitate beam multiplexing and split one beam into several orders. Since simple diffraction gratings are able to split an incoming beam into multiple orders, the idea of controlling the number, magnitude and position of these orders with the help of a flexible grating on the SLM seemed feasible. In the course of this investigation, we tested and modified two different approaches for phase profile calculation until we reached satisfactory results. I will discuss both methods and their suitability for the use in STED microscopy in chapter 5. The excitation beams can be split up in a similar manner by either another SLM or alternatively a diffractive optical element (DOE), which is basically a glass plate with a surface relief, where the height profile of the relief determines the optical path length.

For each created confocal volume that has its own STED and excitation beamlet, the emitted fluorescence has to be collected by its own single photon detector. From a point of data acquisition, this is analogous to the simultaneous acquisition at multiple confocal microscopes. Commercially available data acquisition modules are limited to a low number of input channels and come with limited options for configuration. In addition, the number of typical photon detectors in confocal microscopes can not be easily scaled. To achieve this imaging scheme, a custom solution was designed as part of this thesis. In a collaboration with Francesco Ceccarelli, Angelo Gulinatti and Ivan Rech from the SPADlab at Politecnico di Milano, a newly developed array detector[31] was integrated into the experiment. The largest and most complex VHDL submodule on the FPGA is dedicated to read out and process the incoming data stream from this array detector. The photon detector itself is built on chip as a rectangular 8 by 8 array of single-photon avalanche diodes (SPADs). Each SPAD has an active area with a diameter $D = 50\,\mu\text{m}$ and the active areas are spaced $250\,\mu\text{m}$ apart (Figure 2.4). Similar to other single photon detectors, a single impinging photon will create an avalanche of charge carriers at a biased diode. This will lead to a measureable current. A quenching circuit will then set the diode voltage bias to zero to reset the diode for the next activation. The dead-time between possible activations is on the order of $\approx 30\,\text{ns}$. This timing behavior is best used in the interplay with pulsed lasers and non-saturated excitation, where per excitation pulse only a small number of photons is expected in detection.

2.6. Laser timing

The pulses of the excitation lasers and the STED laser have to be synchronized. The pulse duration of the excitation laser is in the range of $300\,\text{ps}$, while the STED pulses have a

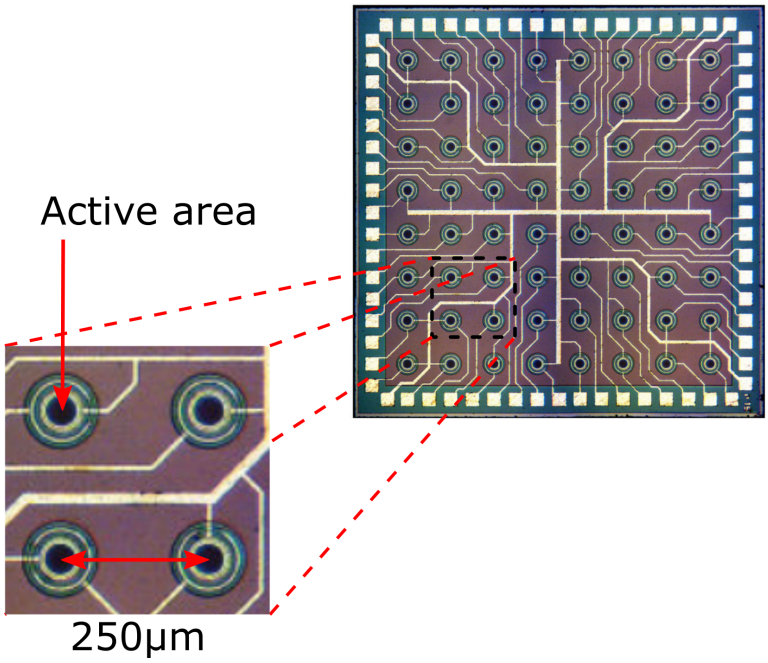

Figure 2.4.: The dark areas on the chip correspond to SPADs with a diameter of $50\,\mu m$ and a spacing of $250\,\mu m$. Each active area has its own quenching circuit and the chip design allows for independent read-out of all SPADs.

duration of $750\,ps$. As previously discussed, the STED pulses have to arrive shortly after the excitation pulses. To achieve the maximal depletion effect, the fine-tuning of the timing has to be determined experimentally in a calibration measurement. To adjust the timing of the pulses, several options can be combined. Fiber-coupling into fibers of different length can be used for coarse adjustment of the optical path length difference. The path difference in the range of meters and centimeters translates to a time difference in the nanosecond range ($1\,m \equiv 3.3\,ns$). Since the lasers have to be electronically triggered by a master oscillator, the length of the connecting cables can also be adjusted for timing alignment in a similar manner. In the experiment, cable lengths between one and five meters were used. For finer adjustment, linear stages with retro-reflectors can yield a range of $\approx 100\,ps$. In addition to these options, microchips are available that can be used to create electronic delays in a large range from ns to ps. Since the optical table of the experiment has limited space and optical fibers add additional complexity to the beam-path, purely electronic delay elements are a good option. These come with their own complexity in board design and implementation, but they offer greater flexibility and the on-site manufacturing facilities at the university of Ulm were capable to handle such a request. Chapter 6.2 discusses our experimental implementation of timing adjustments.

2.7. Polarization

Although already discussed in the previous chapter, it should again be emphasized that special care should be taken of the polarization state in the microscope. Perfect circular polarization is crucial to achieve good STED depletion. Furthermore, as stated by Török and Munro (2004) [18], for the highest STED depletion, the polarization of the excitation lasers has to match the STED beam polarization.

2.8. Optical components

The actions, typically performed on a beam of light, can be categorized into a couple of different types of manipulation: changes in position and direction, changes in shape and size, spectral changes as well as changes in polarization. In theory, all these manipulations are performed by separate elements placed in the beam path. In reality, most optical components influence all beam parameters to a certain extent and have various imperfections. Further complexity is introduced by the physical properties of the mechanical mounts housing the optics on the optical table.

2.8.1. Mode cleaning and ellipticity

The spatial profile of most laser beams does not correspond to a perfect Gaussian beam with transverse electromagnetic (TEM) mode TEM_{00}. Especially diode lasers have highly elliptical radiation patterns that possibly contain higher order modes. For mode cleaning, the laser can be coupled into a single mode fiber or focused on a small round pinhole. This dampens undesired beam contributions and results in a beam that can be used in the experiment. When using a sufficiently small pinhole, the interference pattern of a point source is created and an aperture can be placed to isolate its main lobe. It can be collimated through a lens and the resulting beam is then almost Gaussian. Unfortunately, the pinhole has to be small compared to the beam size to act as point source. This will not only dampen the undesired beam contributions, but also the Gaussian mode, resulting in a high loss of laser power. Fibers are the better option and have multiple advantages. Firstly the emitted beam is Gaussian, secondly the light can be guided to a desired location on the optical table, and finally the Gaussian mode contribution can be transmitted with only minor losses. The magnitude of dampening of other modes in the fiber depends on its length, therefore a minimal length of $\approx 1\,\mathrm{m}$ is needed. If the beam does not contain

higher transverse electromagnetic (TEM) modes it is possible to correct ellipticity with telescopes with cylindrical lenses. This has the advantage that only a minor power loss is introduced through absorption and surface reflections of the lenses. However, to align such a telescope, the beam parameters have to be measured in a precise and fast manner. This is discussed in chapter 3.3.3.

2.8.2. Lenses

An ideal lens features a parabolic thickness profile. When applying a parabolic phase change to a Gaussian beam wave front, its parameters will change, while its spatial mode will be completely preserved. Placing a convex version of this lens at the waist of a Gaussian beam will focus the beam and create a new waist at the focal point of the lens. Most standard lenses are manufactured with spherical surfaces that can be created by cutting away material with a rotating arm. This deviation from a parabolic surface leads to spherical aberrations. Whenever necessary, specialized aspherical lenses should be considered. Since the index of refraction is a function of wavelength, a lens made from a single material will have a wavelength-dependent focal point position. Achromatic lenses can be created with a composite lens design consisting of multiple lens parts with different refractive indices. This allows for a more constant focal point position over a range of wavelengths.

2.8.3. Filters

In a STED microscope, the excitation light needs to be coupled into the same beam path as the STED light, while the emission from the sample needs to be separated from the excitation beam path. These tasks are performed by interference filters that have wavelength-dependent reflection and transmission. For the use in fluorescence microscopy, there is a general distinction between dichroics, laser filters and emission filters. Dichroics are used at an angle of incidence (AOI) of $45°$ to combine two beam paths. The AOI of $45°$ limits the possible edge steepness and reflectivity of the filters. For filters currently sold, the smallest edge steepness is in the range of $20\,\mathrm{nm}$ while the best reflectivity is on the order of 99%. The coating process for dichroic filters results in a considerable amount of surface tension. To ensure that an incoming wave front is not distorted, substrate materials should at least have a thickness of $\geq 3\,\mathrm{mm}$. This is especially necessary for all filters involved in the STED beam path, due to the high requirements for wave front conservation. Laser filters are bandpass filters that only transmit a small band around the laser wavelength. They are used at an AOI of $0\,\mathrm{deg}$ and are intended to filter out residual

pump light or harmonic frequency contributions in the case of lasers using non-linear components. Emission filters are broadband filters that are intended to transmit as much light as possible in the emission spectrum of used fluorophores, while still having a high blocking ratio at the laser wavelengths used in the experiment. The blocking ratio is often specified with the optical density (OD), where the transmission is 10^{-OD}. Typical emission filters have a range from $\mathrm{OD}5$ to $\mathrm{OD}7$. When using typical values of $\approx 200\,\mathrm{mW}$ of STED laser light, an OD of ˜15 is needed to remove all laser light in the detection. This is only possible with cascading filters.

2.8.4. Waveplates

To change the polarization type or orientation, half-wave and quarter-wave plates are used. These are typically made from birefringent materials that have a fast and a slow optical axis which are perpendicular to each other. The axes differ in refractive index, and in light transmission, the electric field components along each axis will accumulate a different phase value. Linear polarization can be turned or transformed into elliptical or circular polarization by tuning this phase difference. Due to production inaccuracy, the thickness will vary and the exact phase value will differ from the theoretically desired values of π and $\pi/2$. It can not be stressed enough that for STED microscopy it is absolutely necessary to use polarizers with very high quality, since perfect circular polarization is needed to create a true central minimum in the STED point spread function (PSF). Even small deviations in polarization can lead to a large loss in signal-to-noise ratio (SNR) during imaging[32]. Waveplates are available in low-order or zero-order designs. For a low order design, the phase difference between polarization directions is π and $\pi/2$ with an addition of integer multiples of 2π. This allows for the manufacturing of single slab optics that are still just a few hundred microns thick. For a zero-order design the waveplate is constructed from two thicker birefringent crystal plates that are rotated in relation to each other to provide exactly π or $\pi/2$ phase difference. In general, waveplates are often used in a manner, where the plate is rotated frequently. In these cases, they should be examined for positional or angular deviations of the beam. Manufacturing errors can lead to wedge shapes or displacements of rotation axes of the housing and the optic itself. In our experiments, these errors lead to focal point offsets of $> 1\,\mu\mathrm{m}$, unacceptable for STED microscopy.

2.8.5. Polarizers

The experiment requires several polarization filters. The SLM requires linearly polarized light and also all laser powers are fine-tuned by rotating the laser polarization with respect to a linear polarization filter. Thin film polarization filters can not be used in the experiment, since even the best designs possess residual absorbency larger than $5\,\%$. This would lead to immediate destruction of the filters, since the lasing threshold of the diode lasers in the experiment is above $100\,\mathrm{mW}$ and they can not be operated at low power. Better choices are polarizing beam splitter (PBS) cubes, they offer extinction ratios better than 1:1000 and have low intrinsic absorption. Light of one polarization direction will be reflected off in a 90° angle and can be lead to a beam dump. It should be noted that PBS cubes are sensitive to angular deviations, where the angle of incident light deviates from 0°. This can happen through misalignment or when the PBS cube is used with convergent or divergent laser beams. This is especially problematic with small and divergent laser beams, since then the beam can acquire profile-dependent polarization or intensity variations. It is also problematic when a PBS cube in a rotation mount is used to determine the degree of circular polarization. Here, it is especially important that the rotation axis coincides perfectly with the laser beam axis. For small laser beams with a high divergence angle, a Glan-Thompson polarizer is a better option. It is less susceptible to changes in the AOI and also features higher extinction ratios of 1:10000 or better.

2.8.6. Mirrors

Mirrors define the beam path on the optical table. Ideally, a reflection on a mirror just alters the direction of the optical axis and keeps other beam parameters preserved. In reality, this is not the case. Mirrors are manufactured with polished metallic surfaces or dielectric multi-layer coatings on some optical substrate like glass. The reflection at mirrors therefore has a spectrum for amplitude and phase that depends on wavelength, beam incidence angle and polarization state.

Dielectric mirrors can be custom-designed by altering the layer structure and the used materials. This is usually needed for the reflectance of laser light with higher powers. Residual laser absorption inside the substrate material can damage the mirror and polarization-dependent reflection can violate the conservation of the polarization state. Metallic mirrors typically have a high reflectance over a broader wavelength range and are therefore used as multi-purpose solutions, if a very high reflectance or polarization conservation is not needed.

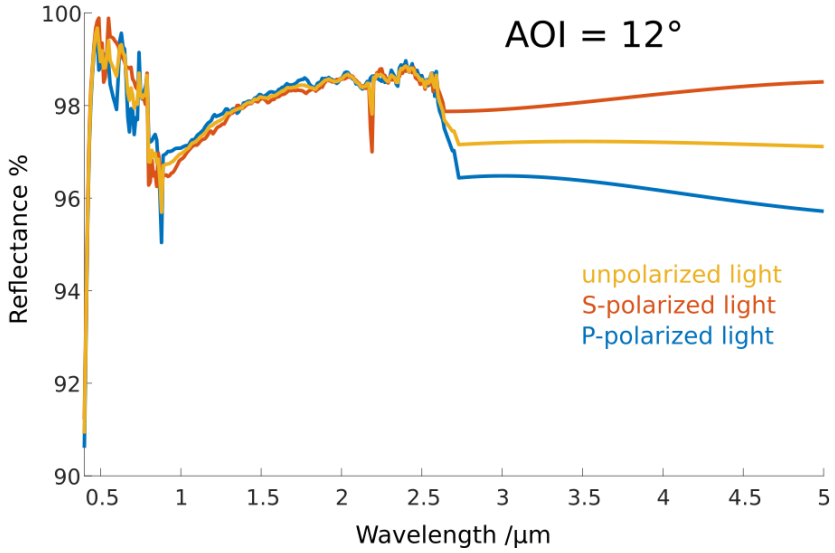

Figure 2.5.: The reflectance spectrum of a silver mirror at an angle of incidence of $12°$ (data from Thorlabs GmbH[33]). Metallic mirrors offer a high broadband reflectance, but there are still polarization and wavelength-dependent differences. Dielectric filters can be custom-designed to offer a higher and more uniform reflectance value over a small range of input parameters.

2.8.7. Mechanics

The selection of good mechanical mounts is imperative to assure the intended functionality of the experiment. Since the goal are super-resolution images with a resolution $\approx 25\,\mathrm{nm}$, any drift in beam position or angle is detrimental to the experiment. To reduce thermal drift, mechanical holders should only provide the minimum number of degrees of freedom needed for the mounted optical component. The smaller the number of moving components, the higher the stability. Special care should be taken that these degrees of freedom are independent. For many standard components on the market this is not the case, and when necessary premium components should be considered. For our application we chose the Polaris® line from the company Thorlabs GmbH. The optical path lengths between components should be kept short as a general rule. Every angular drift of the beam will lead to a position error that increases with travel distance.

3. Optical setup and alignment

In this chapter, the current state of the setup on the optical table will be presented. A detailed explanation of all beam paths in the first part of the chapter will be followed up by a discussion of spectral considerations and the implemented optical filter selection. The final section contains an alignment guide that describes a number of crucial alignment procedures.

3.1. Setup

Figure 3.1 shows a sketch of the beam paths and optical components on the optical table. All component abbreviations are listed in Table 3.1 with company names and article designations. Since all beam paths in a confocal microscope either end or start in the confocal volume, we will separate the discussion accordingly into stimulated emission depletion (STED), excitation and detection beam paths with end or start point in the confocal volume. The constant value for the beam height on the optical table was chosen as $80.1\,\mathrm{mm}$. For the STED beam path we start from the $774.51\,\mathrm{nm}$ laser head (L3). The cylindrical telescope (Z1) corrects ellipticity and astigmatism of the STED laser. It is followed by a clean-up filter (F1) that filters out residual green light of the STED pump laser. Afterwards, a combination of a half-wave plate (HWP1) in a rotation mount and Glan-Thompson-polarizer is used to manually fine-tune the laser power. The telescope (T1) collimates and magnifies the beam to fill the spatial light modulator (SLM) surface ($6\sigma \approx 12.5\,\mathrm{mm}$). The SLM imposes the phase vortex needed to create the STED beam and additionally introduces phase corrections. The beam passes through the dichroic (D1), which is a longpass with cutoff at $760\,\mathrm{nm}$. The telescope (T4) de-magnifies the beam to match the aperture size of the microscope objective. This telescope has two lenses with focal lengths $f_1 = 30\,\mathrm{cm}$ and $f_2 = 20\,\mathrm{cm}$ to decrease the beam size by a factor of 1.5 and increase the diffraction angles by a factor of 1.5 (in the small angle approximation). In this way, a larger surface dimension of the SLM ($15.9\,\mathrm{mm}$ by $12.8\,\mathrm{mm}$) can be utilized to create larger diffraction angles at the objective back-focal plane (radius of $9\,\mathrm{mm}$). Finally, the beam enters the sample tower which contains a quarter wave plate (QWP), scanning mirrors, piezo and manual stages

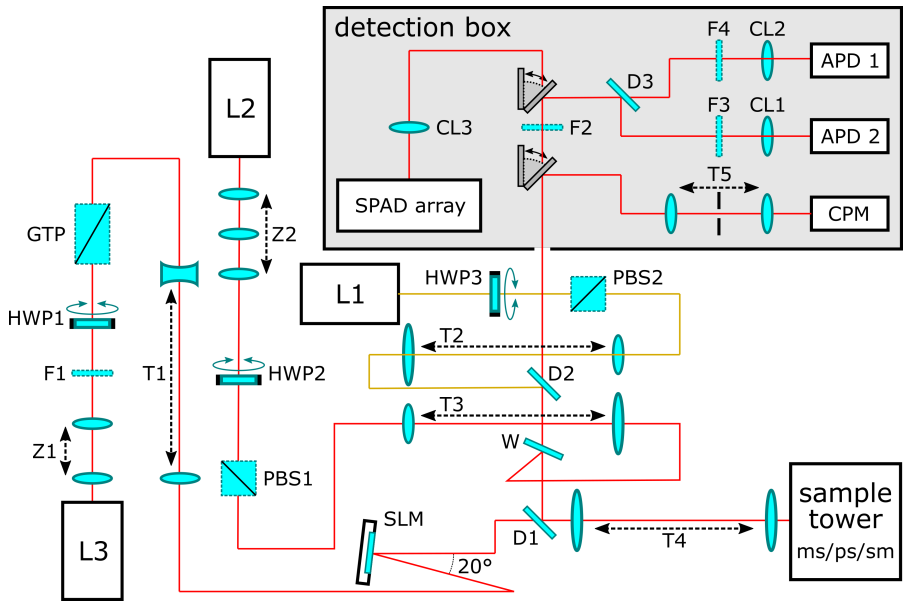

Figure 3.1.: Sketch of the layout on the optical table. Components are referenced to their corresponding declaration in Table 3.1. Here, all declarations are derived from their respective functions: "L"(lasers), "F"(filters), "T"(telescopes), "PBS"(polarizing beam splitter), "D"(dichroic), "HWP"(half-wave plate), "W"(wedge), "Z"(cylindrical telescopes), "APD"(avalanche photo diode), "CPM"(channel photo multiplier), "CL"(collimation lens), "SPAD"(single photon avalanche diode) and "SLM"(spatial light modulator).

as well as the microscope objective and sample. This sample tower is discussed in greater detail in chapter 6.1. The yellow excitation beam with $592\,\mathrm{nm}$ wavelength starts out at the laser head (L1). Again a half-wave plate (HWP3) and polarizing beam splitter (PBS2) is used for manual power setting. After magnification through the telescope (T2), the beam is reflected by the $595\,\mathrm{nm}$ long pass filter. It passes the wedge (W) and is reflected on the dichroic (D1), from here on it overlaps with the STED beam path. The red excitation beam path with $634\,\mathrm{nm}$ wavelength begins at the laser head (L2). It also has a cylindrical telescope (Z2) for ellipticity correction. Again the power is fine-tuned with HWP2 and PBS1, and the beam is magnified with the telescope (T3). On the the wedge (W), about $4\,\%$ of the laser power is reflected into the beam that travels towards D1. From D1 it is again reflected and overlaps with the STED beam path. The detection beam path starts from the sample tower, where the fluorescence is de-scanned by the scanning mirrors. It then passes T4 and is reflected of D1, from D1 it passes W and and D2 and reaches the detection box. In the detection box, two flip-mirrors can be used to steer the beam either into the channel photo multiplier (CPM) path, the avalanche photo detector (APD) path or the single-photon

avalanche diode (SPAD) array path. The CPM path features a telescope with $400\,\mu m$ pinhole as spatial filter. The CPM itself has an active area of about $2\,mm^2$ and a focusing lens (not depicted) attached to it. For the APD path, the beam passes the $634\,nm$ laser filter (F2) before the beam is split at the dichroic (D3) that separates the color channels. The color filters (F3 and F4) are band pass filters for the respective color channel, while the collimation lenses (CL1 and CL2) are focusing the fluorescence into multi-mode fibers that are connected to APD1 and APD2. The SPAD array is currently not actively used for imaging, but F3 or F4 can be moved in front of the SPAD array depending on which color channel should be used in multi-beam mode. As a later addition for multi-beam imaging, each excitation beam path will be supplemented with a diffractive optical element (DOE) that will transform each beam into a bundle of beams. This concludes the discussion of the spatial layout. In the next section, we will take a closer look at the fluorescence emission spectra to determine the ratio of fluorescence light that will reach each detector.

3.2. Filters

As discussed in the previous section and listed in Table 3.1, the setup contains a number of optical filters. These are intended to combine the beam paths, split the detection channels and filter laser light before it can reach the detectors. It is important to maximize the amount of fluorescence for each color channel, while simultaneously guaranteeing a high blocking ratio for the laser lines. All filters have been bought from AHF Analysentechnik AG (Tübingen). The company provides detailed transmission spectra for a variable angle of incidence (AOI). A Matlab routine was written, based on the fluorophores that are currently used for STED, namely Atto590 and Atto647n (ATTO-TEC GmbH, Siegen), and the filter spectra. It estimates the total transmitted fluorescence F_t, the cross-talk CT and the optical density (OD) at the three laser lines ($592\,nm$,$634\,nm$ and $775\,nm$) for each color channel. Here, $F_t = S_r/S_f$ is calculated by the ratio of the integrated residual spectrum S_r that is left after passing all filters in the respective color channel and the integrated fluorophore emission spectrum S_f. The optical density (OD) at the laser lines is calculated by multiplying the attenuation factors of each filter at the respective wavelength. The cross talk CT is calculated from the expected cross excitation per channel. Since both color channels are temporally separated, the only source of cross-talk is direct excitation of the other fluorophore for each channel respectively. Here, we estimate with non-saturated excitation and normalize the excitation with the intended color to 1, while we estimate the cross-excitation for the other fluorophore color according to the absorption spectrum with a factor σ_a. For excitation of Atto647n by $592\,nm$ light $\sigma_a = 0.25$, while for excitation of

Table 3.1.: Table containing essential optical components.

Acronym	Description	Company	Article designation
HWP1	$\lambda/2$ plate 592nm	B.Halle	RLQ 2.10.0589
HWP2	$\lambda/2$ plate 634nm	Thorlabs	WPMH05M-532
HWP3	$\lambda/2$ plate 775nm	B.Halle	RLQ 2.15.0780
QWP	$\lambda/4$ plate 775nm	B.Halle	RZQ 4.15.0775
GTP	Glan-Thompson polarizer	B.Halle	PGT 2.08.05 AR780
PBS1	polarizing beam splitter	Thorlabs	PTW 0.15
PBS2	polarizing beam splitter	Thorlabs	PTW 0.10
SLM	spatial light modulator	Hamamatsu Photonics	X13138-02
L1	laser 592nm	NKT Photonics/One Five	Katana - 06 HP
L2	laser 634nm	NKT Photonics/One Five	Katana - 06 HP
L3	laser 775nm	NKT Photonics/One Five	Katana - 08 HP
APD1	avalanche photo-diode	Excelitas Technologies	SPCM-780-24-FC
APD2	avalanche photo-diode	Excelitas Technologies	SPCM-780-24-FC
SPAD array	SPAD Array detector	Politecnico Milano 1863, SPADlab	prototype
Fib1	multimode fiber	Thorlabs	M42L01
Fib2	multimode fiber	Thorlabs	M42L01
MS	manual XY-stage	Physik Instrumente	M-545.2MO
PS	piezo XYZ-stage	Physik Instrumente	P-545.3C8S
SM	scanning mirrors	SCANLAB	dynAXIS-S
D1	dichroic LP760	AHF	F48-760S thickness 3mm
D2	dichroic LP594	AHF	F38-594S thickness 3mm
D3	dichroic LP635	AHF	F48-636
W	Wedge	Thorlabs	F48-636
F1	laser clean-up filter 774nm	AHF	F39-780
F2	laser blocking filter 634nm	AHF	F40-641
F3	emission filter 592nm path	AHF	F39-622
F4	emission filter 634nm path	AHF	F37-698
T1	magnification telescope	B.Halle	custom aspheric lenses
T2	magnification telescope	Edmund Optics	doublets VIS-NIR coating
T3	magnification telescope	Edmund Optics	doublets VIS-NIR coating
T4	magnification telescope	Thorlabs	AC254-050-A-ML
MS	manual translation stage	Physik Instrumente (PI)	M-545.2MO
PS	piezo scanning stage	Physik Instrumente (PI)	P-545.3R8S
SM	scanning mirrors	SCANLAB GmbH	dynAXIS-S

Atto590 by $634\,\mathrm{nm}$ light $\sigma_a = 0.034$. The resulting spectrum is then passed through all filters to calculate the integrated residual spectrum $S_{r,CT}$ and then the cross-talk as the ratio $CT = S_{r,CT}/S_f$. Figure 3.2 shows the residual spectra for the two color channels in comparison to the fluorophore spectra, as well as the laser lines and the cross-talk. For the yellow color channel, with $592\,\mathrm{nm}$ excitation, we have $F_T = 27.7\,\%$, $CT = 0.2\,\%$ and $OD_{592} = 5.6 \times 10^{-10}$, $OD_{634} = 1.9 \times 10^{-8}$ as well as $OD_{775} = 5.6 \times 10^{-12}$. For the red color channel, with $634\,\mathrm{nm}$ excitation, we have $F_T = 62.5\,\%$, $CT = 1.5\,\%$ and $OD_{592} = 1.2 \times 10^{-11}$, $OD_{634} = 4.2 \times 10^{-14}$ as well as $OD_{775} = 7.8 \times 10^{-10}$. Filtering the $592\,\mathrm{nm}$ and $775\,\mathrm{nm}$ laser in both color channels is straight forward, since they do not overlap significantly with the fluorophore emission spectra. However, this is not the case for the $634\,\mathrm{nm}$ laser. To filter this laser, the best option are notch filters with a bandwidth of about $20\,\mathrm{nm}$. Instead of a notch filter that is centered around $634\,\mathrm{nm}$ and that would cut out most of the Atto590 emission spectrum, we use a notch filter centered at $641\,\mathrm{nm}$. By tilting this filter with $7°$ in respect to the optical axis, we shift the blocking band to lower wavelengths. According to the data provided by the manufacturer, this increases the blocking ratio at $634\,\mathrm{nm}$ from $\mathrm{OD5}$ to $\mathrm{OD7}$. The same method is also used for both emission filters (F3,F4) and they are tilted by $15°$ to optimize their spectral position.

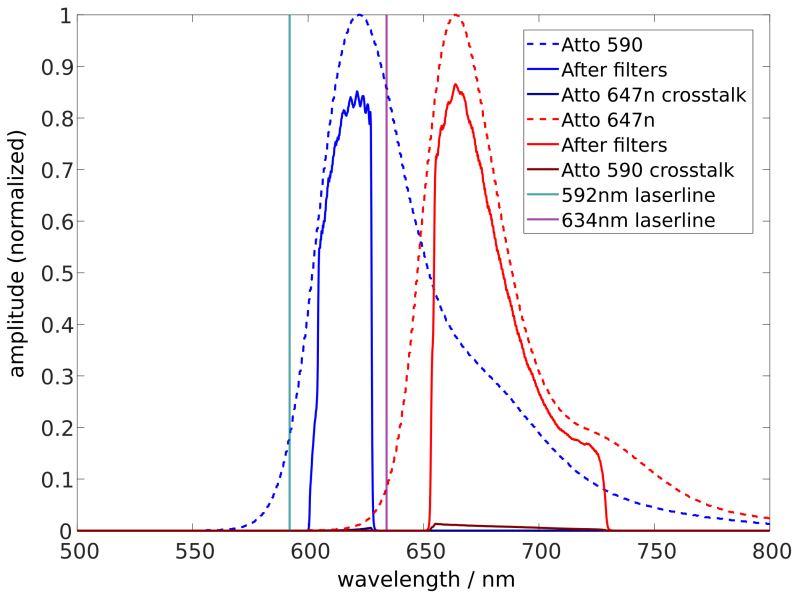

Figure 3.2.: Matlab plot of the spectra of the fluorophores Atto590 (blue) and Atto647n (red) (Attotec GmbH). The dotted lines show the fluorescence emission spectra, while the solid lines indicate the residual spectra, after passing all filters for the respective color channel. The vertical solid lines indicate the spectral position of both excitation lasers.

While combining the beam paths, again the $634\,\mathrm{nm}$ laser is problematic. Dichroics that are typically used to combine beam paths, have wider spectral edges and a band-pass dichroic would clip most of the fluorescence spectrum. Therefore, we use a glass wedge (W) to couple the $634\,\mathrm{nm}$ laser into the beam path. This glass wedge has a transmission of about $96\,\%$ and through its angled surfaces two diverging reflections. This makes it possible to spatially separate the stronger reflex and use it as excitation beam. Since the laser power in the red excitation channel is not a limiting factor, this option is possible. In total we therefore only lose $4\,\%$ fluorescence at the wedge.

The calculations in this section, based on company data sheets, were the basis for the filter selection in the microscope. Since no compatible laser was available at exactly $647\,\mathrm{nm}$, the approach with a wedge instead of a dichroic promised to lead to the largest total amount of collected fluorescence. A long pass filter with longer cutoff wavelength could be used as color separation to attribute more light to the yellow color channel. However, this will only slightly improve the collection efficiency in the yellow channel, while significantly reducing the collection efficiency in the red color channel. However, this remains a viable option, if it should become necessary to even out the light collection in both channels. Although STED imaging works with the current filter selection, the optical density at $774\,\mathrm{nm}$ could be improved by a factor of $OD = 10^{-3}$ in the future to reduce laser background. Here, the loss in fluorescence signal through an additional filter should be weighed against the background reduction.

3.3. Optical tools and alignment methods

In an optical setup, light has to run along a predefined path. This automatically defines a chain of dependencies, where each single optical component along the path needs to be aligned precisely. During construction, it is often possible to place components in succession, while using an optical read-out to determine when the alignment is correct. The highly coupled nature of the components in this alignment process makes it necessary to section this task into several sub-steps and divide the beam path into multiple regions. This section contains a set of tools and methods that will help the experimenter in this regard.

3.3.1. Beam positioning and collimation

For coarse positioning of a collimated laser beam, circular apertures can be placed on the desired optical axis. Aligning a laser beam to pass through two consecutive apertures will define its position and angle. The precision of this alignment process depends on three factors. Firstly, the distance between the apertures, secondly, the determination of the laser beam position in relation to the center of the apertures and finally the positioning accuracy of the apertures themselves. A power meter can be used to monitor the transmission of the beam through the apertures. If the aperture diameter is smaller than the beam diameter, it is possible to optimize the angle and position by optimizing on maximum transmission. The gaussian beam shape suggests that this procedure will be most sensitive if the aperture diameter is roughly equal to the full-width at half-maximum (FWHM) of the laser beam. With perfect alignment, the aperture stop will then coincide with the flanc of the gaussian profile, and small deviations from the optimum will lead to large changes in power. To assure constant reference positions, custom-build references were machine built (Figure 3.3). These "collimation obelisks" consist of a rectangular basis that can be placed against predefined hard stops along the optical path. The manufacturing precision is on the range of $\approx 1\,\mu m$ and the effective position accuracy is then limited by the placement of the obelisks against the reference stops. This positioning procedure is capable of aligning two laser-beams with enough accuracy to reach a single digit micrometer deviation in the location of their focal spots in the sample plane of the microscope.

Similar obelisks (left side of Figure 3.3) can be used for coarse alignment of beam collimation. This is visualized in Figure 3.4. Placing an obelisk with two pinholes in the beam path will split the gaussian beam into two beamlets. The diffraction pattern of these beamlets can be monitored on a second obelisk that has the same pinhole arrangement. If the beam was collimated and aligned, the main lobes of the beamlets will again pass through the second set of pinholes. Collimated in this regard means that the gaussian beam waist coincides with the position of the first set of pinholes and the wavefront at this position is flat. This corresponds to a beam with the smallest possible divergence angle.

3.3.2. Back reflections

As light propagates through optical elements, it encounters interfaces between areas of different refractive index that lead to reflections. Even at boundaries with anti-reflection coatings there is usually residual reflectance in the lower percent range. This can be very helpful to align lenses and other elements to the optical axis of a laser beam. To align a lens to the axis of a laser beam, a screen with a clearance hole is placed on the laser

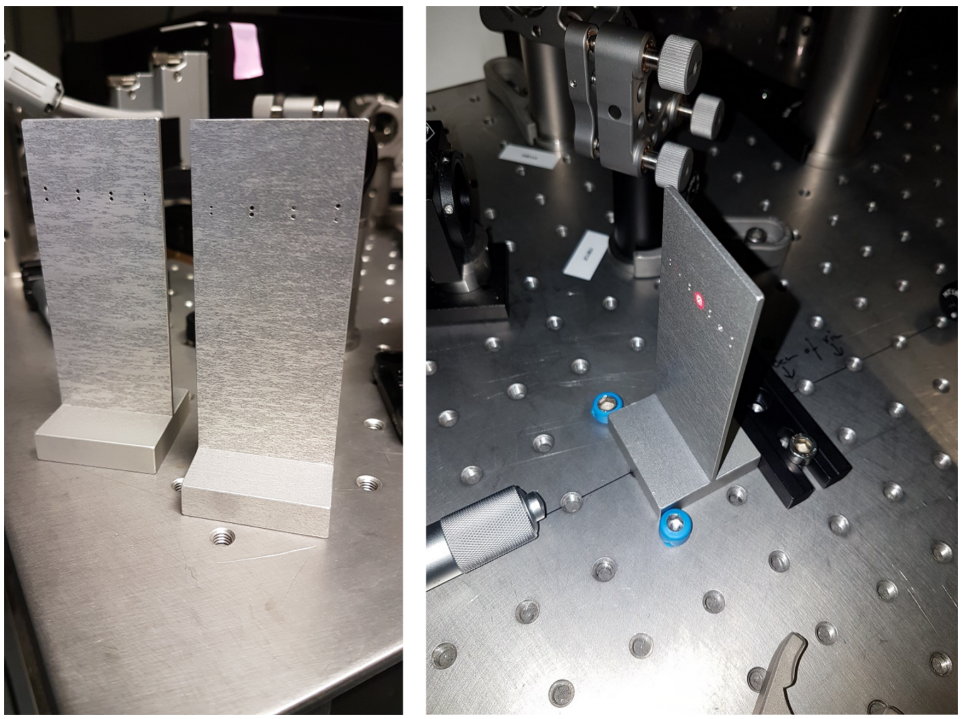

Figure 3.3.: Image of obelisks with different pinholes for collimation (left) and alignment (right).

beam before the lens. The screen normal as well as the clearance hole should be aligned to the beam axis. The laser beam then leads to divergent or convergent reflections that can be seen as disks on the screen. For fine tuning, the lens axis is readjusted until the reflections are concentric around the clearance hole.

3.3.3. Beam profiling

For every microscope, exact knowledge of the beam sizes and shapes is imperative. A size mismatch will lead to a smaller effective numerical aperture (NA) or clipping in the microscope objective, degradation of coupling efficiency in the detection and loss of diffraction efficiency and/or clipping at the SLM. A deviation from Gaussian beam shapes will lead to astigmatism and other optical aberrations in the focal field and further degrade coupling efficiency. Usually the beam size is calculated as $w(z)$, the radius of the beam, where the beam intensity has fallen to $I(w) = I_0/e^2$. Here, z is the coordinate along the optical axis. To get a precise measure of the beam size multiple options exist. In the first method the laser beam is clipped by the edge of a razor blade and the residual intensity is measured (Figure 3.6). The residual transmitted power $P(x)$ as function of the razor blade position x

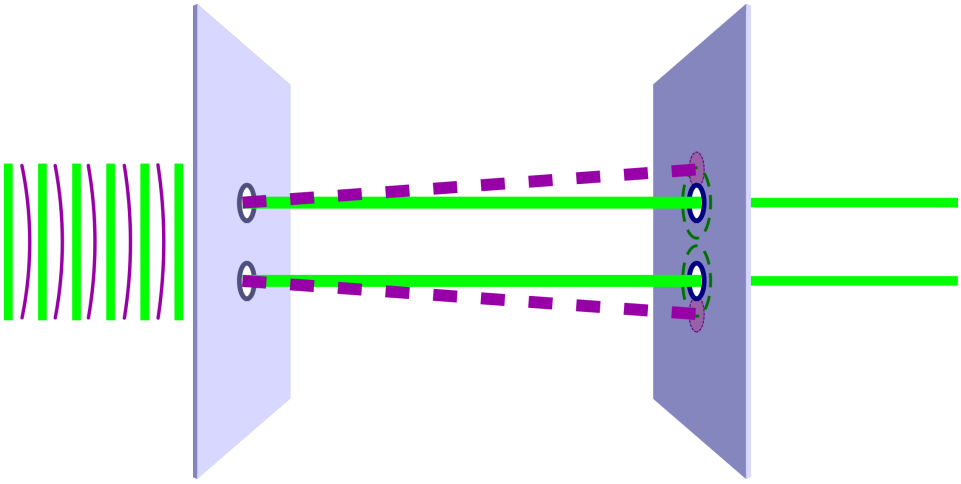

Figure 3.4.: A beam with flat wavefront (green) and a beam with wavefront curvature (purple) fall onto a screen with two pinholes. The bent wavefront leads to divergence of the beamlets.

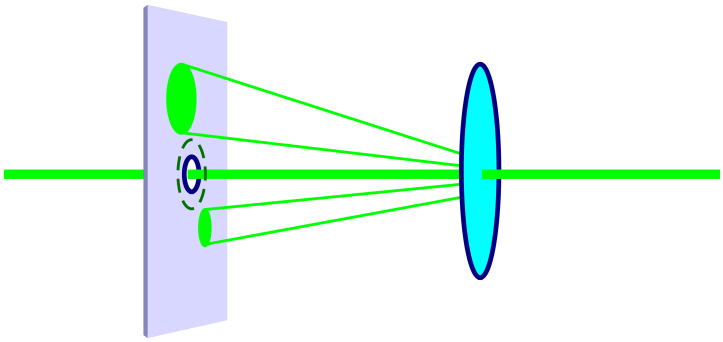

Figure 3.5.: Back reflections can be used for optical alignment. At perfect alignment all back reflections will be concentric.

can be written as a difference of the total power and the blocked power[34]:

$$P(x) = \frac{2P_0}{\pi w(z)^2} \int_{-\infty}^{+\infty} \int_{x}^{+\infty} exp\left[\frac{-2x'^2 + y^2}{w(z)^2} dx'dy\right] \tag{3.1}$$

This can be re-written with the help of the complementary error function 1-erf(x):

$$1 - \mathrm{erf}(x) = \frac{2}{\sqrt{\pi}} \int_{x}^{+\infty} e^{-t^2} dt \tag{3.2}$$

Leading to a more compact formula:

$$P(x) = \frac{P_0}{2}(1 - \mathrm{erf}\left(\frac{\sqrt{2}x}{w(z)}\right)) \tag{3.3}$$

The error function has no analytic solution, but data analysis software often has a numerical implementation. In our experiment, the residual power is measured with a power meter and Origin (analysis software from OriginLab Corporation) is used to fit Equation 3.3 to the measured data. Due to the manual positioning of the razor blade, this method is very time consuming and can take up to 5 minutes per measurement and spatial direction. Furthermore, it is prone to errors if the beam has an elliptical profile, since only one spatial direction is measured at a given time. The number of directions and positions along the beam that have to be measured to reliably identify the parameters of an elliptical beam makes the time consumption unfeasible for a manual measurement. Therefore, it should only be used with beams that possess circular symmetry around the beam axis. For these beams it is a practical tool to get a fast beam size estimation, e.g. when trying to optimize telescopes.

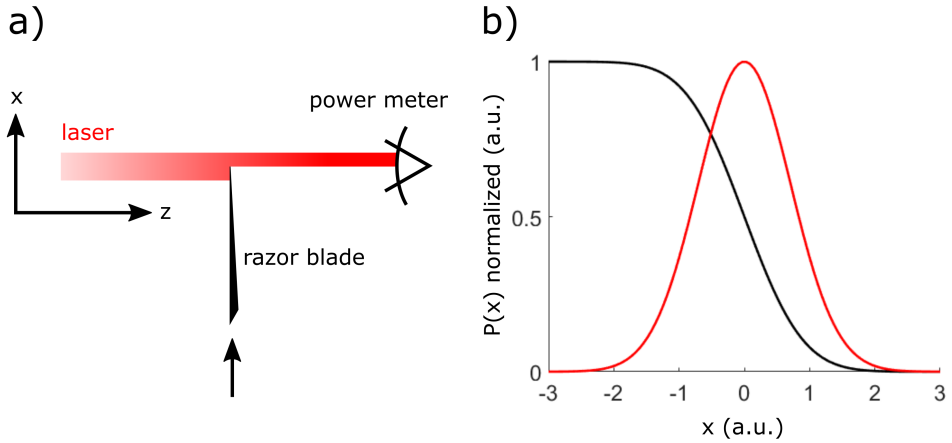

Figure 3.6.: Sketch of a beam width measurement with the help of a razor blade. a) shows the experiment, while b) shows a Matlab plot of the residual intensity, when the razor blade is moved along the x-axis.

As a second method the laser beam can be measured with a camera on the beam axis. This has the advantage that a complete two-dimensional slice of the beam is measured and the principal axes of any ellipticity in the beam can be calculated from the image. It should be noted that any interference effect in the beam can lead to intensity fluctuations that introduce errors to the measurement. This poses an experimental obstacle, since interference effects can originate from neutral density (ND) filters needed to attenuate the laser beam or the camera chip itself that often has a protective dielectric layer. In the

experiments, we used a custom beam-profiler camera (type DAT-WinCamD-LCM, Laser 2000 GmbH) with a motorized stage (type DAT-M2DU-200-WCD, Laser 2000 GmbH). The camera features a bare chip and additional ND filter wedges that have reduced interference, due to angled surfaces. The camera can be moved along the optical axis on the motorized stage and a measurement can produce a series of up to 60 slices with the beam profiler software (Laser 2000 GmbH) in a time of 30 seconds (Figure 3.7). This beam-profiler was very helpful to measure and correct the ellipicity of the lasers used in the experiment.

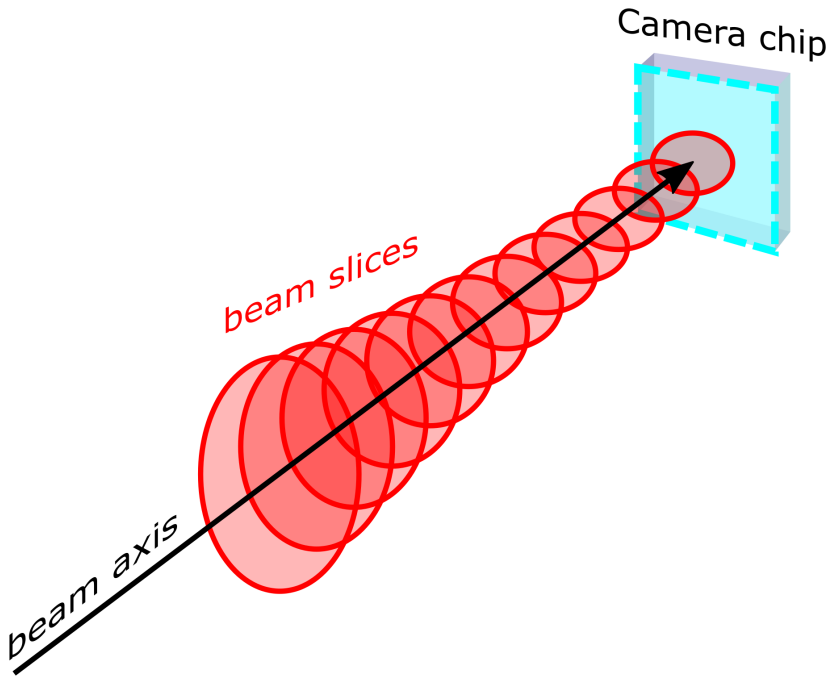

Figure 3.7.: Sketch of a measurement with the beam profiler. An elliptical beam can be analyzed by imaging a series of slices along the beam axis. In the experiment, the camera chip is moved along the beam axis with the help of a motorized stage. The stage and also the surface normal of the camera chip have to be positioned parallel to the optical axis for an accurate measurement. At correct stage alignment, the beam center should stay fixed on the camera during stage movement. At correct chip alignment, the projection of the beam onto the chip leads to the minimum in spatial extent for the major and minor ellipse axes.

3.3.4. Component positioning

Most components have a limited number of degrees of freedom with limited adjustable range. The coarse alignment of the setup has to be precise enough so that the intended final alignment can be reached within these limits. Precise placement of optical components can be achieved with the help of linear stages. These can be temporarily placed as hard stops, and the position of the component can be adjusted with the stage micrometer screws while monitoring changes to beam position and angle.

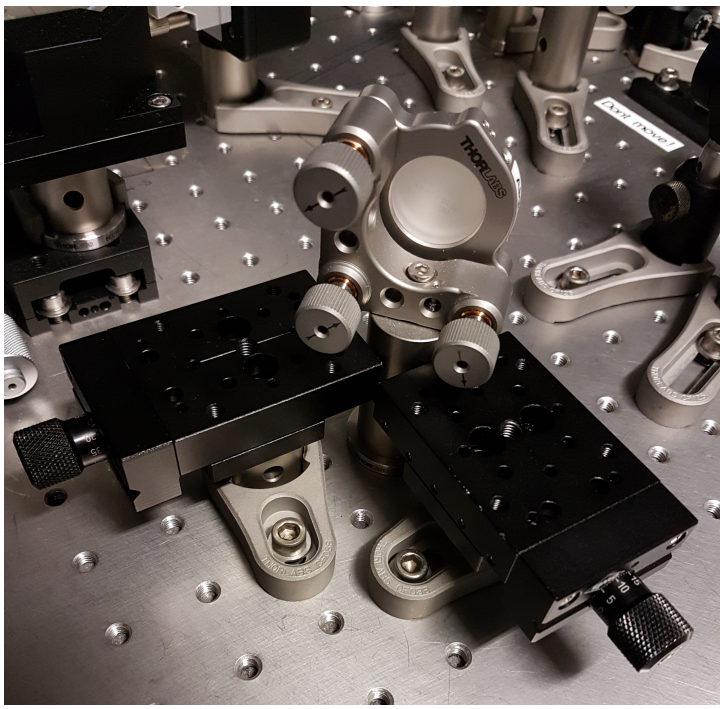

Figure 3.8.: Linear stages can be used to precisely place optical components. After locking down the optic mount, the stages can be removed again.

The setup should also contain enough defined hard stops and free space that can be used to place obelisks or irises. This is important to monitor the local beam path and it is especially important before and after telescopes to ensure that they can be realigned.

3.3.5. Telescope alignment and cylindrical telescopes

Telescopes have to be aligned in an iterative manner with the help of back reflections, obelisks and beam profiling. Since the initial diameter of our laser beams is small (about $300\,\mu\text{m}$), their divergence angles are large. This means that the translation of a telescope

along the beam axis will lead to significant changes in beam size. On the one hand this is a disadvantage, since then the beam size needs to be measured multiple times until the right position can be found. On the other hand it is an advantage, since the beam size can be fine tuned very precisely with a given set of lenses. This is especially useful, because most off-the-shelf lenses have a limited variety in focal lengths. As a first step the collimation obelisks should be used in tandem with razor blade measurements to find the desired telescope location along the beam axis. Then back reflections and the alignment obelisks should be used to center both lenses on the optical axis. Here, at least one of these lenses should be placed on a manual translation stage for the axial direction. Finally, the collimation is fine tuned again. For telescopes with cyclindrical lenses that are intended to correct beam ellipticity, the procedure is similar. Where for magnification telescopes a single razor-blade measurement is enough to determine the beam size, here a beam profiler has to be used to determine more beam parameters and monitor them continuously. First, the major and minor ellipse axes have to be measured and the cylindrical lenses have to be placed in rotation mounts and turned until they have the correct orientation. The lens positions are then fine-tuned, until a minimum in astigmatism is found, while simultaneously matching the divergence angles for both ellipticity axes.

3.3.6. Transmission lines

Optical components in the detection path of the experiment have to be isolated from room light in an opaque cardboard box. However, many alignment steps involve active image acquisition and a closed box limits the access to alignment screws of the involved components. Mechanical transmission lines can be built from flexible shafts commonly used for small electric motors. These can be connected to any component inside an isolated box, permitting access to designated alignment screws (Figure 3.9).

3.3.7. Infrared laser alignment

The wavelength of the STED beam is very close to the infrared spectrum and barely visible to the naked eye. Collimation obelisks with a power meter as read-out can help in defining the optical axis. However, it is impossible to use back-reflections in lens alignment without the purchase of expensive infrared viewers. A good way to deal with this dilemma is the use of a second laser beam in the visible range as a guide. For example, in the alignment of a telescope the infrared beam can be aligned on two obelisks. A visible beam can then be coupled into the beam path and co-aligned to the same obelisks. Dependent on the

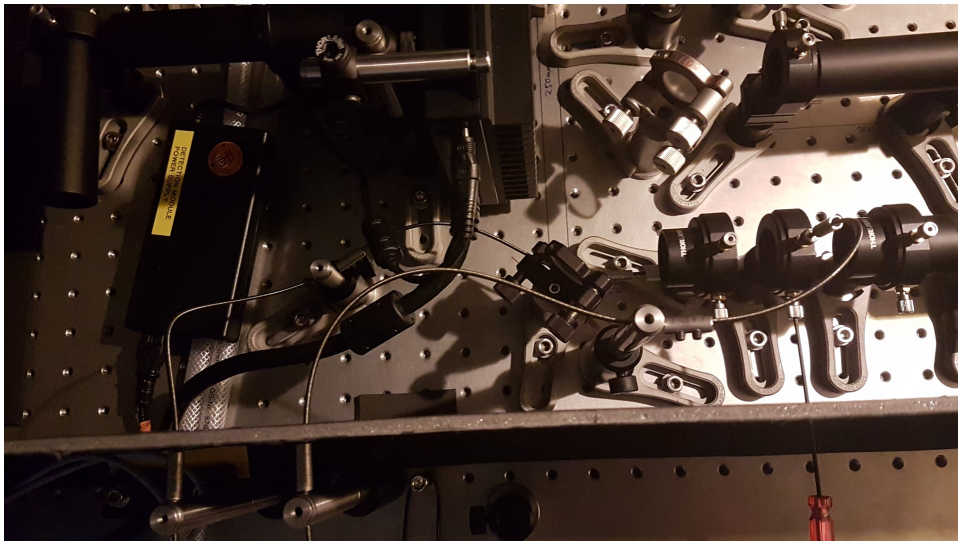

Figure 3.9.: A mechanical transmission line is connected to the adjustment screws of a pinhole mount. The pinhole transmission can now be tuned during active photon counting.

spatial configuration, it might be advantageous to use a backwards traveling visible beam. Following this, the lenses can be aligned with the help of the visible beam. Finally, the visible beam can be removed from the beam path.

3.3.8. Confocal alignment

To acquire super-resolution images with good signal-to-noise ratio (SNR), the co-alignment of all laser beams in the microscope should be precise enough that their focal positions overlap within an accuracy of about $20\,\mathrm{nm}$. After coarse manual alignment of all beam paths with obelisks (subsection 3.3.1), ideally the microscope should be able to acquire confocal images with either the CPM or APD. Here, it is important to find a good placement for the obelisks, since this alignment will get more precise the larger the distance between the alignment pinholes are and is mainly limited by the space on the optical table. The current option is in the last telescope ("T4" in Figure 3.1), where a distance of about $45\,\mathrm{cm}$ is possible. For this method all detection paths are equipped with alignment lasers that can replace the respective detector and travel in reverse direction through each detection path. In this way the detection paths can be aligned in the same fashion as the STED and excitation beams. However, since the distance between the obelisks is not large enough the focal spot positions of the excitation beams, the STED beam or the detection paths might still deviate by a few microns after this coarse alignment. To improve upon this

alignment a common practice in STED microscopy is the use of nanoscopic gold beads as confocal alignment sample. If the beads are much smaller than the point spread function (PSF) of the beams, the back scattered light will not only reveal the position of a beam, but also its shape. In this experiment, the main alignment sample consists of $80\,\mathrm{nm}$ gold beads (appendix A.3.2). At first, one beam should be chosen as reference and a single gold bead moved into its focus. With the bead in focus the detection paths can now be fine tuned until a maximum of the SNR is found. Then the other lasers can be aligned until they overlap with the reference. The microscope software has a specialized graphical user interface (GUI) to help in this matter (chapter 8.2.2) and enables a overlay precision on the order of $< 10\,\mathrm{nm}$. It should be noted that it is important to find single gold beads in a given sample in order to analyze the PSF. Figure 3.10 shows difference in brightness across spots in a gold bead sample. This can be due to bead size or aggregation. It is therefore prudent to look for "weaker" spots. They are more likely to be single gold beads of small size.
To manipulate the beam positions during confocal alignment three different options are available mentioned in order of increasing accuracy. All paths have manual fine adjustment mirror mounts. The excitation and STED paths additionally have piezo-controlled fine adjustment mirror mounts. The STED beam path also includes the SLM, where blazed gratings can be used for an angular change of the beam direction. In this regard the Zernike modes "tip" and "tilt" can be used at the SLM (chapter 4.3).

3.3.9. Polarization alignment

To adjust the polarization of the STED beam, a quarter wave plate (QWP) (Table 3.1) is situated directly below the microscope objective. The polarization direction after the SLM is linear and the correct orientation of the quarter wave plate (QWP) will transform this linear polarization into circular polarization. To align the QWP a polarizing beam splitter (PBS), a rotation mount and a power meter are needed. First, the top of the sample tower (section 6.1) and the microscope objective have to be removed to enable access to the beam. The polarizing beam splitter (PBS) in the rotation mount is then placed in the beam path instead of the objective and the power meter is used to monitor the transmitted power. With linear beam polarization, a continuous PBS rotation will lead to a periodic power variation. The QWP is now adjusted until this power variation becomes minimal. From the values of maximal and minimal power transmission (P_{max}, P_{min}) in this oscillation, we define the degree of ellipticity as $E = P_{min}/P_{max}$. For perfect circular polarization the periodic power variation should vanish. However, in the experiment the best values were $E = 96.5\,\%$. It should be noted that the surface normal of the PBS, the beam axis and the axis of the rotation mount have to be co-aligned precisely. Otherwise an asymmetry

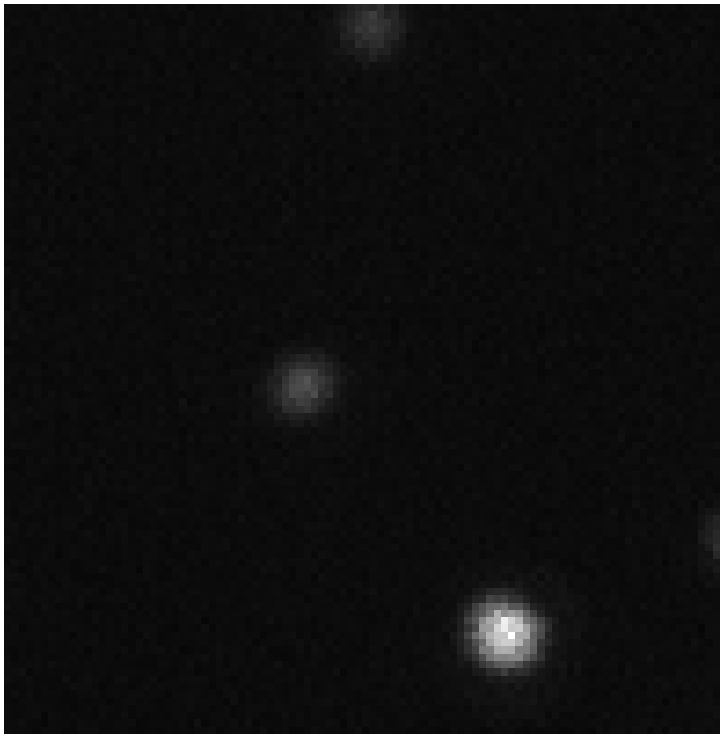

Figure 3.10.: $5\,\mu m$ by $5\,\mu m$ confocal x-y scan (perpendicular to the optical axis) of $80\,nm$ gold beads. Although the median of the gold bead diameters is $80\,nm$, there are size variations leading to differing brightness. Also, they can aggregate and form brighter clumps. Single beads typically are less bright.

will be present in the power variation leading to a difference in power for a $180°$ turn. This behavior can mask the underlying polarization and prevent and accurate polarization state readout. As control of the alignment, a $180°$ turn of the PBS should lead to the same power value.

3.3.10. Fluorescent samples

To characterize or improve the performance of the STED microscope, special fluorescent samples are needed. It is important to quantify the resolution increase before starting to image biological samples. For the purpose of characterization we use a STED-nanoruler from GATTAquant GmbH (Gräfelfing, Germany). A single nanoruler is a DNA origami structure labeled with two Atto647n (red) molecules and one Atto590 (yellow) molecule. They are arranged in a linear configuration (red-yellow-red) with Atto590 sitting in the middle. The distances between the outer molecules is $140\,nm$. The sample contains a

large number of these origami molecules on a standard microscope slide. It can be used to establish a quantitive measure of the microscope resolution and the co-alignment of multiple color channels. It consists of a DNA origami structure that places fluorophores of different color in defined distances in a sub-diffraction sized area. Imaging a nanoruler will provide a direct readout of the microscope performance (chapter 9.3). We also used nitrogen vacancy centers (NVs) in nano-diamonds[35] as non-bleaching fluorescent probes (appendix A.3.1). The NV is a crystal defect in diamond, widely used in the field of quantum optics[36]. It can be exited with our $592\,\mathrm{nm}$ laser and its fluorescence can be detected in the red color channel of the microscope. In the experiment, the NVs proved to be stable under constant STED illumination for multiple days, without losing their fluorescence property. This makes them an ideal probe, not just to verify the STED resolution, but also for timing alignment or to employ adaptive optics (AO) algorithms on the SLM that are based on the STED image quality.

4. Beam shaping

The most crucial part in stimulated emission depletion (STED) microscopy is the point spread function (PSF) quality of the depletion laser as well as its polarization. Since its shape is reminiscent of a donut, featuring a hole in the middle surrounded by a high intensity crest, the STED beam is often referred to as donut-beam. The intensity ratio between the crest and the center of the PSF has to be on the order of $\approx 10^3$ to reach a good signal to noise ratio while imaging. Already $\approx 1\%$ residual intensity in the center of the PSF reduces the signal-to-noise ratio (SNR) of STED images by a factor of two[32]. The intensity zero is highly susceptible to wave front errors and will quickly degrade with imperfect alignment, imperfections in optical components and sample aberrations. Although the impact of optical aberrations on the STED PSF has been discussed before[37], a tool for precise calculations of the expected PSF is necessary. The influence of many experimental factors, like polarization or surface curvatures of optical elements, is specific to each individual experiment, and a precise estimate of these factors is needed. For the chosen experimental implementation of wave front corrections, a spatial light modulator (SLM) is part of the experiment. It is used to correct wave front errors through adaptive optics (AO) algorithms. The spatial light modulator (SLM) is also used to create, depending on the experiment, either a single or an array of depletion beams that can be used for high resolution STED imaging or simultaneous STED imaging at multiple focal spots, respectively. However, the implementation of multiplexing algorithms warrants its own chapter.

This chapter will start with a short introduction to wave optics[38], thus providing a necessary basis for any discussion about SLMs. It then follows up with vector diffraction and its numerical implementation, providing a diagnostic tool set for PSF engineering in systems with high numerical aperture (NA). Finally, it will discuss the device properties of the SLM in the experiment and finish with a discussion of adaptive optics (AO) algorithms.

4.1. Wave optics

Light propagation inside a microscope is conveniently described by free space travel interrupted by optical components performing beam manipulations. Instead of calculating the wave function of the light field $U(x, y, z)$ at every position along its path, it is often better to describe the propagation in a small number of consecutive steps. Each part of the beam path is then modeled as an operation that connects the function $f(x, y) = U(x, y, 0)$ at an entry plane with the function $g(x', y') = U(x, y, d)$ at an exit plane[38] (Figure 4.1).

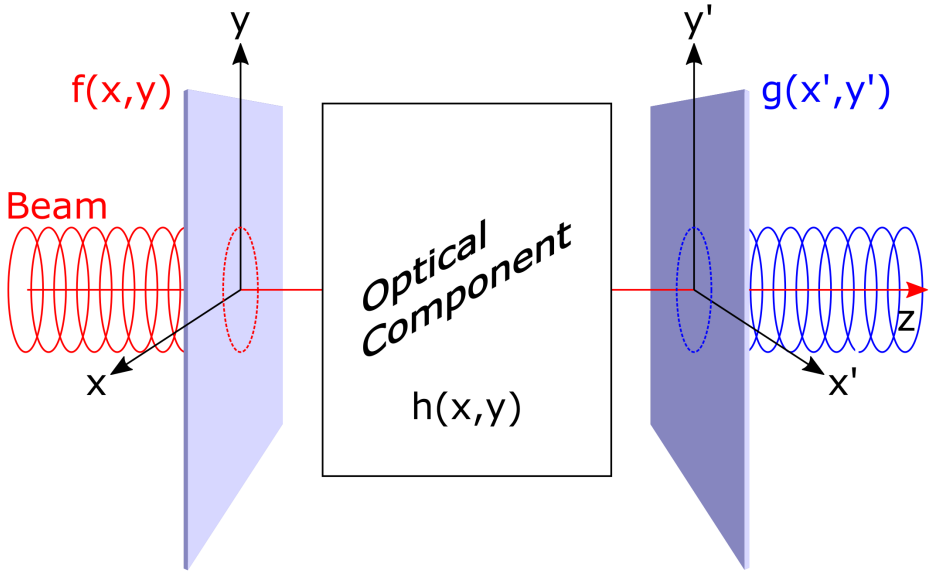

Figure 4.1.: A linear optical system connects the function $f(x, y) = U(x, y, 0)$ at an entry plane with the function $g(x', y') = U(x, y, d)$ at an exit plane[38]. This is facilitated through the convolution of the impulse response function $h(x, y)$ with the function $f(x, y)$.

This constitutes a linear system with the optical component described by an impulse response function $h(x, y)$, analogous to linear systems in data processing. The Fourier transform $H(\nu_x, \nu_y)$ of $h(x, y)$ is called transfer function and the function $g(x', y')$ can be calculated by a convolution.

$$g(x', y') = \int_{-\infty}^{\infty} \int_{-\infty}^{\infty} h(x' - x, y' - y) f(x, y) dx dy \tag{4.1}$$

This convolution can alternatively be written as multiplication in Fourier space of the transfer function $H(\nu_x, \nu_y)$ with $F(\nu_x, \nu_y)$, the Fourier transform of $f(x, y)$:

$$g(x', y') = \mathcal{F}^{-1}(H(\nu_x, \nu_y)F(\nu_x, \nu_y)) \tag{4.2}$$

To determine the mathematical form of a transfer function, it is helpful to view $f(x, y)$ as superposition of basis functions. The action of an optical component on this set of basis functions is often easier to understand. The typical set of functions used to construct light fields are either plane waves, spherical waves or even paraboloidal waves, depending on which approach is more convenient in the given case. The convolution, written as multiplication in Fourier space, already hints at a Fourier decomposition of $f(x, y)$ into a set of harmonic functions, and we will see that this corresponds to a decomposition into plane waves.

4.1.1. The plane wave

The monochromatic plane wave $U(x, y, z) = A \cdot \exp(-i(\vec{k}\vec{x}))$ is a basic solution of the time-independent Helmholtz equation. The wave vector $\vec{k}$ determines the travel direction of the wave and has a length of $|k| = 2\pi/\lambda$, where λ is the wavelength of light. The argument in the exponent is called the phase of the wave and constant on planes perpendicular to the travel direction, hence the name plane wave. In the plane $z = 0$ the plane wave gives rise to a harmonic function $f(x, y) = U(x, y, 0)$:

$$f(x, y) = A \cdot \exp(-i2\pi(\nu_x x + \nu_y y)) \tag{4.3}$$

With the definition of the spatial frequencies $\nu_x = k_x/(2\pi)$ and $\nu_y = k_y/(2\pi)$, the angles relative to the optical axis (z-axis) are defined by $\sin(\theta_x) \cdot |k| = k_x$ and $\sin(\theta_y) \cdot |k| = k_y$. These angles are related to the spatial frequencies by:

$$\theta_x = \arcsin(\nu_x \cdot \lambda) \tag{4.4}$$

For small angles relative to the optical axis this simplifies to:

$$\theta_x \approx \nu_x \cdot \lambda \tag{4.5}$$

This is called the paraxial approximation, and it means that spatial frequencies have a direct linear relation to the angles relative to the optical axis.

4.1.2. Plane wave decomposition

Any function on the plane $z = 0$ can be written as a Fourier decomposition from a complete set of harmonic functions:

$$f(x, y) = \int_{-\infty}^{\infty} \int_{-\infty}^{\infty} F(\nu_x, \nu_y) e^{-i2\pi(\nu_x x + \nu_y y)} \, d\nu_x \, d\nu_y \tag{4.6}$$

If we compare this integral with the harmonic function we get from a single plane wave at $z = 0$, we can interpret the Fourier transform $F(\nu_x, \nu_y)$ as complex amplitude in a plane wave spectrum of $f(x, y)$.

4.1.3. Free space propagation

From the plane wave decomposition we can immediately infer that the transmitted wave then has the form:

$$U(x, y, z) = \int_{-\infty}^{\infty} \int_{-\infty}^{\infty} F(\nu_x, \nu_y) e^{-i2\pi(\nu_x x + \nu_y y)} e^{-ik_z z} \, d\nu_x \, d\nu_y \tag{4.7}$$

Here, we reconstruct every plane wave by multiplication with the factor $e^{-ik_z z}$ where k_z is calculated by $k_z = \sqrt{k^2 - k_x^2 - k_y^2} = 2\pi\sqrt{\lambda^{-2} - \nu_x^2 - \nu_y^2}$. If we compare this with Equation 4.2 we can identify the transfer function of free space propagation with distance d as[38]:

$$H(\nu_x, \nu_y) = \exp\left(-2\pi i d \sqrt{\lambda^{-2} - \nu_x^2 - \nu_y^2}\right) \tag{4.8}$$

4.1.4. Transmission through thin media

Next to the propagation in free space, we need to understand how the light wave will be influenced when traveling through boundaries and propagating through media with

a refractive index $n > 1$. If a light wave travels through an optical component, the ratio $t(x, y) = U(x, y, d)/U(x, y, 0)$ between the incoming wave and the outgoing wave is called complex amplitude transmittance[38]. Usually the function $t(x, y, U_{in})$ depends on the direction of the incoming light field U_{in}. However, under a small angle approximation $t(x, y)$ becomes angle independent for thin optical elements[38]. This is the case if the incoming light wave only contains wave vectors with small angles θ to the optical axis and $\sin(\theta) \approx \theta$.

This has a very practical application for our experiment, since the small angle approximation is valid for collimated Gaussian and STED beams. This means that the interaction of our phase-only SLM can be written as simple multiplication:

$$U(x, y, d) = U(x, y, 0) \exp(i\Phi(x, y)) \tag{4.9}$$

Here, $\Phi(x, y)$ is the pixel dependent phase value of the SLM. For example, if we use the SLM to provide a phase modulation of $\Phi(x, y, z = 0) = k_\alpha x$ with $k_\alpha = |k| \cdot \sin(\alpha)$, we can change the propagation direction of an incoming plane wave $U(x, y, 0) = A \cdot \exp(ik_x x))$. Let the incoming plane wave travel at angle β with $k_x = k_\beta = |k| \cdot \sin(\beta)$. Then

$$U(x, y, d) = Ae^{i(k_\alpha + k_\beta)x} \tag{4.10}$$

This implies that the diffracted plane wave travels at the angle $\gamma = \mathrm{arcsin}(\sin(\alpha)+\sin(\beta))$. If we consider the case that $\alpha, \beta << 1$ then $\sin(\alpha) \approx \alpha$ and $\gamma = \alpha + \beta$. This has far-reaching implications for our experiment. As we have seen, every beam can be decomposed into a plane-wave spectrum. So, if we can deflect each component with the same angle, the beam properties are conserved, as long as the small angle approximation is valid.

4.1.5. Optical Fourier transform

Since the function values of the Fourier transform $F(\nu_x, \nu_y)$ are the amplitudes of plane waves traveling at different angles, we can calculate the Fourier transform of any function $f(x, y)$ through optical methods by creating a diffractive optical element (DOE) with transmittance $f(x, y)$. If we illuminate this diffractive optical element (DOE) with a plane wave, we create a wave function with the plane wave spectrum $F(\nu_x, \nu_y)$. Then we measure the amplitudes of the transmitted plane waves in dependence of the diffraction angle to reconstruct $F(\nu_x, \nu_y)$. Since plane waves have infinite spatial extent, it is necessary to find a way to spatially separate the plane waves of different k vectors. There are two ways to achieve

this. Either, the transfer function of free space can be examined for larger distances, or the transfer function of a lens can be used in the Fresnel approximation.

For large distances d, only a single plane wave contributes to the integral at the coordinates x' and y'. This means that the function $g(x, y)$ simplifies to[38]:

$$g(x,y) = \frac{i}{\lambda d} e^{-ikd} F(\frac{x}{\lambda d}, \frac{y}{\lambda d}) \tag{4.11}$$

This formula is valid in the Fraunhofer approximation, where $f(x, y)$ and $g(x, y)$ are confined to circles with radius r and r' in the input and output plane, with $r, r' \ll \sqrt{\lambda d}$. A similar observation is made for a lens with a parabolic transmittance profile $t(x, y)$. If the focal length of said lens is f, the relationship between the function $f(x, y)$ in its back focal plane and $g(x, y)$ in its focal plane becomes[38]:

$$g(x,y) = \frac{i}{\lambda f} e^{-i2kf} F(\frac{x}{\lambda f}, \frac{y}{\lambda f}) \tag{4.12}$$

This Fourier transform property of a lens is valid in the Fresnel approximation $\frac{\Theta^4 f}{4\lambda} \ll 1$, where Θ is the largest angle of a k vector with the optical axis. Again, the interpretation of this analysis is that in the focal plane of the lens the contributions to a point $g(x, y)$ can be attributed to only two spatial frequencies $\frac{x}{\lambda f}$ and $\frac{y}{\lambda f}$ and therefore a single plane wave.

It should be mentioned that the Fresnel approximation limits the application of the Fourier transform to lenses with low numerical aperture (NA) and therefore low angles Θ with the optical axis. As we will see, the field calculations for microscope objectives are more involved. Nevertheless, the Fourier transform property of a lens will come in handy when examining multi-beam expansion with the SLM, where comparatively small diffraction angles are employed.

4.2. Vector diffraction theory

In systems with high NA, the Fresnel approximation becomes invalid. Upon refraction in a microscope objective, the wave-vector distribution in the focused beam contains large angles with respect to the optical axis. The resulting non-negligible electric field components along the optical axis have to be included in the integration. In the following sections, I will highlight the key points that lead to a numerically solvable integral[39,40,41] used to calculate the focal fields in high NA systems. These calculations were employed to get estimates for

the ideal PSFs in our experiment, estimate influences of imperfect polarization and analyze beam conservation during multi-beam creation.

4.2.1. Construction of diffraction integral for high numerical apertures

To arrive at an integral describing diffraction at a microscope objective, the starting point is a model of the objective as an aplanatic imaging system obeying the sine-condition. The sine-condition states that spatial frequencies in the object and image space have a linear relation with a constant magnification factor. This implies that the imaging system produces distortion-free images and flat wave fronts will be translated into perfect spherical wave fronts. This is a reliable assumption for the diffraction theory of aplanatic microscope objectives, since it is also the premise of any microscope objective manufacturer and is kept true for imaging in distances from the optical axis typical in microscopy.

With this model as a basis, the electric field can be written as an integral decomposition of two plane wave spectra $\vec{U}$ and $\vec{V}$[39]. This integral is a general solution to the Helmholtz equation and consists of an integration over all wave vectors $\vec{k} = k\vec{s}$ attributed to plane waves traveling towards the image point P from the exit aperture plane of the imaging system. Here, $\vec{s}$ is the unit vector determining the direction of the wave vector $\vec{k}$, while k is its magnitude.

$$\vec{E}(P) = \int_{-\infty}^{\infty}\int_{-\infty}^{\infty} e^{ik(s_x x + s_y y)}[\vec{U}(s_x, s_y)e^{iks_z z} + \vec{V}(s_x, s_y)e^{-iks_z z}]ds_x ds_y \tag{4.13}$$

To find a solution to this integral, the argument is divided into three parts. Ray tracing is used to track parallel rays through the system to calculate the strength of the electric field in the exit aperture $\vec{E}(P')$ (the connection between ray and waveoptics can be found in Saleh and Teich (2007) [38], page 49). Then, the integral is re-written to find the correspondence between the field in the exit aperture $\vec{E}(P')$ and the plane wave spectra $\vec{U}$ and $\vec{V}$. Finally, the integral over $\vec{U}$ and $\vec{V}$ is re-written as integral over the field in the exit aperture $\vec{E}(P')$. This integral can be solved numerically.

In the case of confocal microscopy, the objective illumination can be considered as a point source in infinity, leading to flat wavefronts incident on the back-focal plane of the objective. This stays true for the use of Gaussian beams, since their amplitude can be modelled as an amplitude modulation of a plane wave wavefront as long as the Gaussian waist coincides with the back-focal plane. In this confocal case, the sine-condition takes the form[42]:

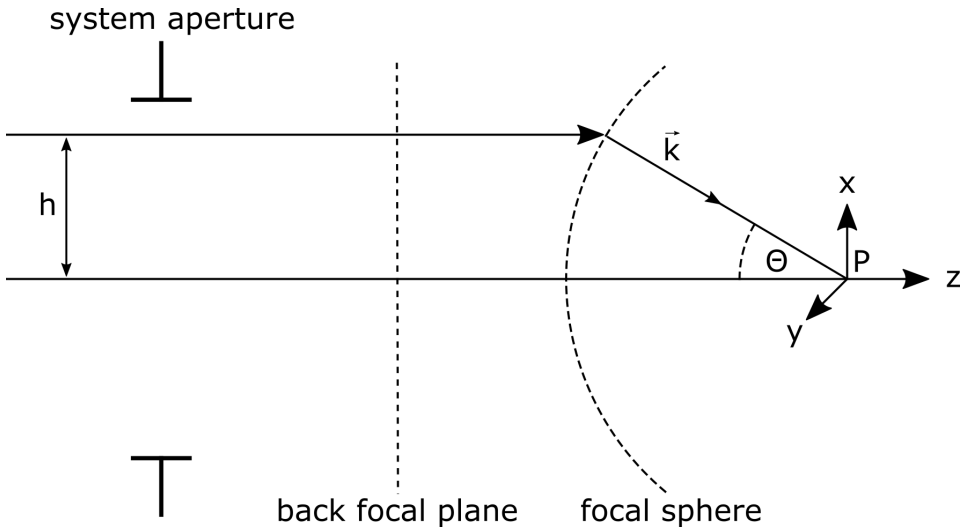

Figure 4.2.: Sketch of the aplanatic system obeying the sine-condition. An incoming parallel ray is refracted at the focal sphere with radius f. Integration of plane wave contributions over all possible $\vec{k}$ permitted by the system aperture enables the calculation of the focal field.

$$h = sin(\Theta) \cdot f \tag{4.14}$$

Here, h_0 is the height of an incoming parallel ray, f is the focal length of the objective and Θ is the angle between the conjugate ray and the optical axis. The intersection points P' of the parallel rays and their conjugate rays lie on a sphere with radius f around the image point P (Figure 4.2). This sphere will be considered as the exit aperture of the system used in the integration to determine the electric field in the vicinity of the objective focal point, also called the focal field. The complex amplitude of the electric field after refraction can be calculated considering ray optics, the surface elements of the entrance and exit aperture and conservation of energy[40]. This calculation leads to an angle dependent attenuation term:

$$|E_{ref}| = |E_{in}|\sqrt{cos(\Theta)} \tag{4.15}$$

Furthermore the electric field direction has to stay perpendicular to its corresponding ray. The electric field components have to be attributed to new unit vectors determined by the new travel direction of the wavevector $\vec{k} = k\vec{s}$ pointing towards the focal point. To calculate this attribution, the field $\vec{E}_{in}(P')$ of the incoming parallel ray is written in circular coordinates around the optical axis. The electric field is written as:

$$\vec{E}_{in}(P') = E_p\vec{e}_r + E_s\vec{e}_a \tag{4.16}$$

Here, $\vec{e}_a$ is the azimuthal unit vector and $\vec{e}_r$ is the radial unit vector and E_p and E_s are the field components parallel and perpendicular to the plane of refraction, respectively. The field component perpendicular to the plane of refraction keeps its field direction $\vec{e}_a$ after refraction. However, the radial field component vector is bent and has to be perpendicular to the azimuthal unit vector as well as the wavevector. This is expressed with a new unit vector $\vec{e}_{ka} = \vec{e}_k \times \vec{e}_a$. The unattenuated refracted field on the focal sphere $\vec{E'}_{ref}(P')$ can now be expressed as:

$$\vec{E'}_{ref}(P') = E_p\vec{e}_{ka} + E_s\vec{e}_a \tag{4.17}$$

The expression of $\vec{U}$ and $\vec{V}$ as functions of $\vec{E}_{ref}(P')$ as well as the derivation of the final integral are lengthy and omitted in this discussion. For a detailed derivation please turn to Wolf and Gabor (1959) [39] and Richards, Wolf, and Gabor (1959) [40]. It is, however, important to keep track of assumptions and approximations that went into this derivation. For the integration, Kirchhoffs boundary conditions are used, these state that the field components and their first derivations are zero on the screen outside the exit aperture. This is true if the exit aperture is large compared to the wavelength of light. For typical microscope objectives this is true. Furthermore it is required that $k_z z >> 1$ to guarantee a vanishing integral part. Since $k_z \approx |\vec{k}| = 2\pi/\lambda \approx 10^7 1/m$ and $z \approx f$, with typical sizes of the focal length f of $2 \cdot 10^{-3} m$ this condition is fulfilled. The final integral has the form:

$$\vec{E}(x,y,z) = -\frac{ik_0 f}{2\pi}\int\int_{\Omega}\frac{E'_{ref}(s_x,s_y)}{s_z}e^{ik(s_x x + s_y y + s_z z)}ds_z ds_y \tag{4.18}$$

Here, $k_0 = 2\pi/\lambda_0$ with λ_0 the vacuum wavelength, f is the focal length, s is the unit vector of the wave vector direction, Ω is the maximum solid angle of integration given by the NA of the objective and x, y, z are the positions in relation to the focal point of the objective, where the z direction is along the optical axis.

4.2.2. Fast focus field calculations

Numerical integration can be quite time-consuming and, after looking for a faster numerical implementation, Leutenegger et al. (2006) [41] realized that this diffraction integral resembles a Fourier transform. Since $s_z = cos(\Theta)$ and $k_x = -ks_x$ and $k_y = -ks_y$ (following their

definition of the azimuthal angle ϕ) it also follows that $ds_x = -dk_x/k$, $ds_y = -dk_y/k$ and the integral takes the form:

$$\vec{E}(x,y,z) = -\frac{if}{\lambda_0 k^2}\int\int_{\Omega}\frac{E'_{ref}(s_x,s_y)e^{ik_z z}}{cos(\Theta)}e^{-i(k_x x+k_y y)}dk_x dk_y \tag{4.19}$$

This corresponds to

$$\vec{E}(x,y,z) = -\frac{if}{\lambda_0 k^2}\mathcal{F}\left(\frac{E'_{ref}(k_x,k_y)e^{ik_z z}}{cos(\Theta)}\right) \tag{4.20}$$

with $\mathcal{F}$ presenting the Fourier transform. This integral can be solved numerically, using a discrete Fourier transform (DFT) with an implementation through the fast Fourier transform (FFT). It requires that each sampling grid dimension is a positive integer power of two. Furthermore, the factor $e^{ik_z z}$ is usually the fastest oscillating part of the integrand. For accurate results, the Nyquist criterion should be fulfilled and sufficient sampling of this phase factor leads to a minimum number M of sampling points per dimension[41].

$$M > \frac{2NA^2}{\sqrt{n^2 - NA^2}\frac{|z|}{\lambda_0}} \tag{4.21}$$

Matlab code from Leutenegger et al. (2006) [41] was adapted and used for focus field calculations in this thesis. Since the integration over the solid angle Θ in terms of k_x and k_y with equidistant sampling corresponds to an integration with equidistant sampling of the spatial dimensions x and y of the entrance aperture, the calculation could readily be extended for the use with additional phase profiles $\Phi(x,y)$ of a SLM. Since the SLM is used with a 4-f relay telescope, the field function $E'_{ref}(s_x(x), s_y(y))$ has to be multiplied with the phase profiles $\Phi(x,y)$ to calculate the effect of the SLM phase manipulation on the focal field geometry.

Images Figure 4.3 and Figure 4.4 show the PSFs of a Gaussian beam and a STED beam calculated with this algorithm. The profiles correspond to slices through the focal point along or perpendicular to the optical axis. It can be seen that the extension of the Gaussian PSFs along the optical axis exceeds the extension in a perpendicular plane. This elongation is responsible for a lower axial resolution in confocal microscopy.

For the calculation of the STED PSF, the field function E_{in} of the Gaussian beam was multiplied with the action of a quarter-wave plate as well as a phase vortex.

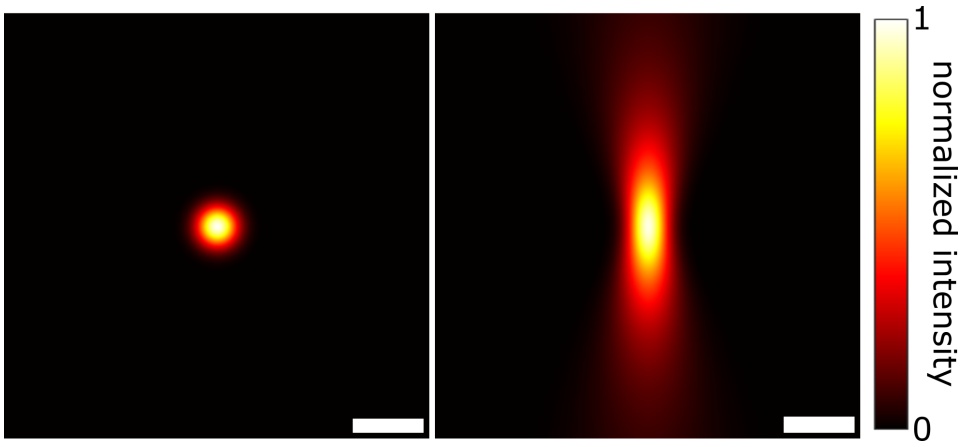

Figure 4.3.: FFC calculation in Matlab for slices through the focal field of a Gaussian laser beam in a high NA objective (scalebar $1\,\mu\text{m}$). The left image shows a slice perpendicular to the optical axis, while the right image shows a slice along the optical axis. The plot is based on an NA 1.42 objective and a wavelength of $\lambda = 774.51\,\text{nm}$.

4.2.3. Polarization influence and central minimum

The FFC algorithm can be used to calculate the effect of polarization on the quality of the central minimum in the STED PSF. Figure 4.5 shows a calculation, where the input polarization is altered and the residual center intensity I_{res} is calculated. Here, I_{res} is normalized to the donut crest and the polarization is defined as ratio of the STED beam intensity along the principal axes of the polarization ellipse. A value of zero polarization refers to linearly polarized light. The handedness of the polarization has to correspond to the handedness of the phase vortex to reach the lowest values for I_{res}. As mentioned, Galiani et al. (2012) [32] showed significant reductions in SNR for values of $I_{res} > 1 \times 10^{-3}$. Therefore, a value of above $95\,\%$ polarization as shown in Figure 4.5 should be aimed for in the experiment. A detailed analysis of further polarization effects on the STED beam can be found in Hao et al. (2010) [43]. An absolutely crucial remark to take from this paper is that for the highest STED depletion, the polarization of the excitation lasers has to match the STED beam polarization. To create the plot in Figure 4.5, the FFC algorithm can not be used directly. This is due to the fact that the FFT used in the FFC is not perfectly symmetric around a central point. The true minimum position of the STED beam will not coincide with one of the sampling points, and since the beam features steep edges in the center this will lead to large deviations for the smallest calculated value in the center from the true center value. In principle, the FFT could be padded with zeros to a higher power of 2 to decrease the sampling step size. However, this will exhaust Matlab capabilities before

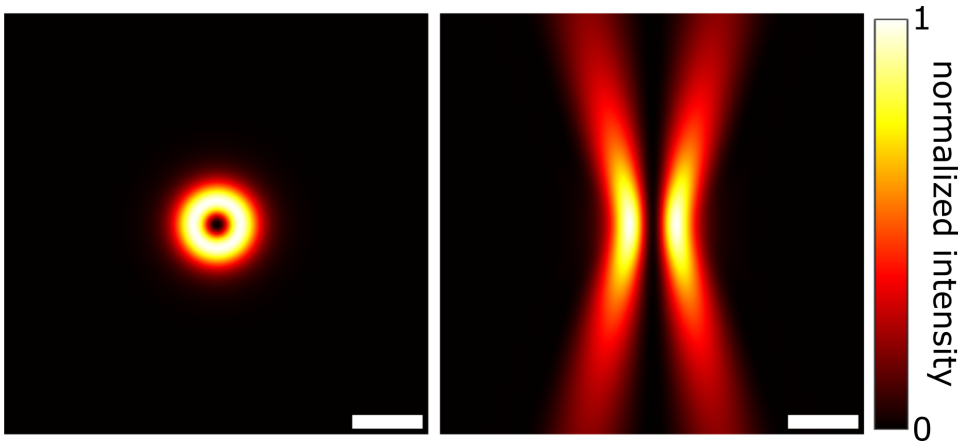

Figure 4.4.: FFC calculation in Matlab for slices through the focal field of a $774\,\mathrm{nm}$ STED beam in a 1.42 NA objective (scalebar $1\,\mu\mathrm{m}$). Since the shape is reminiscent of a donut, the STED beam is commonly referred to as donut beam. Again, the left image shows a slice perpendicular to the optical axis, while the right image shows a slice along the optical axis.

reaching satisfactory results. The better idea was to have a fast calculation of only a central FFT point with help of the Goertzel DFT and then introduce a series of linear phase shifts to the beam profile. These phase shifts correspond to a movement of the central minimum in the focal plane. Since the phase shifts can be made arbitrarily small, the central minimum can be moved arbitrarily close to the sampling point. This was done in an iterative manner until the minimum value kept the same order of magnitude for a couple of iterations, this was then taken as minimum. The same procedure is later used to analyze multi-beam profiles.

4.3. Spatial light modulator

The SLM type used in the experiments is a model X13138-02 of the company Hamamatsu. It is a reflective liquid crystal on silicon (LCOS) SLM capable of phase-only modulation. It features 1272x1024 pixels on an effective area of $15.9\,\mathrm{mm}$ by $12.8\,\mathrm{mm}$. The distance between neighboring pixels is $12.5\,\mu\mathrm{m}$. The main selling points of the device are a high fill-factor of $96\,\%$, a highly reflective di-electric coating with over $98\,\%$ reflectivity needed for the use with the high power STED laser, the comparatively high number of pixels and a surface correction profile that will be shipped with the module. The device is connected to a controller, which in turn is connected to the graphics adapter of a PC with a DVI-D cable. It is a plug-and-play device and recognized by common operating systems as a computer

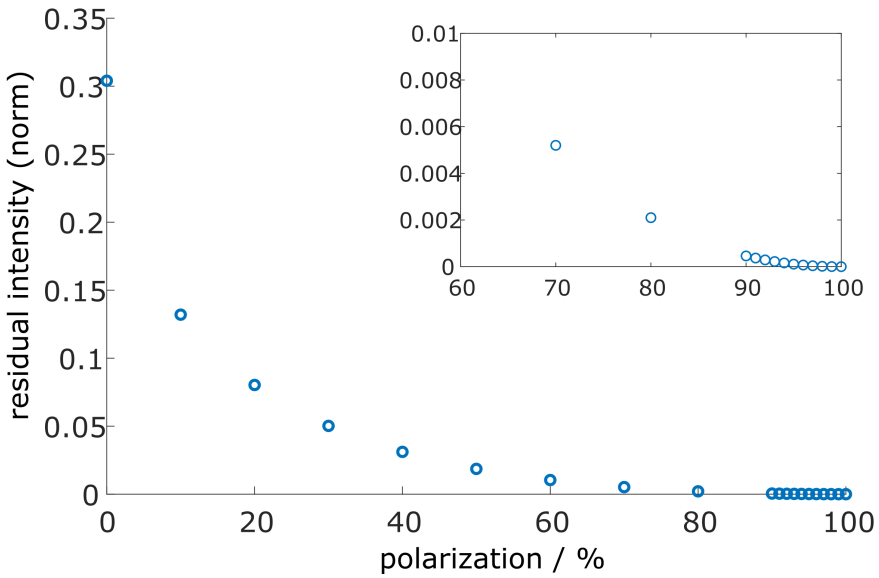

Figure 4.5.: Matlab graph of intensity values of the STED central minimum calculated with the FFC. The polarization is defined as the intensity ratio of the principal axes of the polarization ellipse, while the residual intensity I_{res} is calculated as ratio of the beams crest intensity to its center intensity. The inset shows a zoom into the range that is relevant for STED. At $I_{res} = 1\,\%$ already half of the fluorescence will be lost.

monitor. To control the phase of all pixels, an image is displayed on this monitor by any software capable of displaying full screen images. The color values of this image are translated by the controller into pixel control voltages that determine the phase value at each pixel. In the standard configuration, 8-bit grey-scale images are taken to control the voltage in 256 different steps corresponding to phase values limited from 0 to 2π. The thickness of the crystal layer varies accross the SLM surface and leads to local phase deviations. These are corrected with a correction image added modulo 256 to the desired phase profile image. By design, only linearly polarized light of a defined direction is diffracted at the SLM.

4.3.1. Diffraction efficiency

A common performance measure of an SLM is its diffraction efficiency η_D. This measure is generally used to describe the performance in deflecting light by comparing the light intensity incident on a DOE with the intensity diffracted into desired directions. Its exact definition therefore depends on the intended action of a given phase profile on the SLM. For a blazed grating, this action is to change the travel direction of an incoming beam, with

only one desired outgoing direction. Phase profiles intended for multi-beam imaging split a beam into a bunch of beams ordered in a grid of angles, and the diffraction efficiency is calculated by the intensity sum of all outgoing beams compared to the incident light intensity. Not all light can be diffracted by the SLM, and residual light from different sources will be found in a central so-called zero-order or higher orders.

Zero-order

It is important to keep track of all zero-order contributions in order to optimize the SLM performance and to understand the technical limits imposed on a given experimental design. Part of the light falls in between pixels and will get scattered or reflected at the back-plane. This can only be compensated for by buying a device with a high fill factor and good reflectivity. Any light polarized in the wrong direction will not acquire a pixel-dependent phase shift and will be reflected into the zero-order. Good polarization characteristics of the used light are therefore important. Since the device is pixelated, only a quantized version of a desired smooth phase profile can be displayed. As with all quantized functions, the quality of the approximation depends on the number of sampling steps and quantization levels. The wave front errors induced by quantization can not be fully contributed to the zero-order, dependent on the type of error they can also lead to higher unwanted orders with large diffraction angles.

Cross-talk reduction

As discussed previously in chapter 2.1, the interaction of the electric fields of neighboring pixels limits the display of sharp phase jumps. This leads to wavefront deformations and a loss of diffraction efficiency, which becomes very problematic for phase profiles intended for large diffraction angles, like the ones used in beam-multiplexing. This is best explained with the example of a blazed grating shown in Figure 4.6 a).

In Figure 4.6, incoming flat wavefronts perpendicular to the optical axis undergo a phase change, and the resulting wavefronts correspond to an outgoing beam traveling at an angle. Each incoming wavefront is separated into sections with a phase offset between sections of 2π. The outgoing flat wavefronts then are the superposition of interfering sections of consecutive incoming wavefronts. Taking a closer look on the wavefront profile in Figure 4.6 b) shows that the phase response of the SLM pixels to a triangular voltage profile features rounded edges. The phase output of the SLM to a triangular control profile can be compared to a low-pass filtered triangular signal. However, this effect can be partly

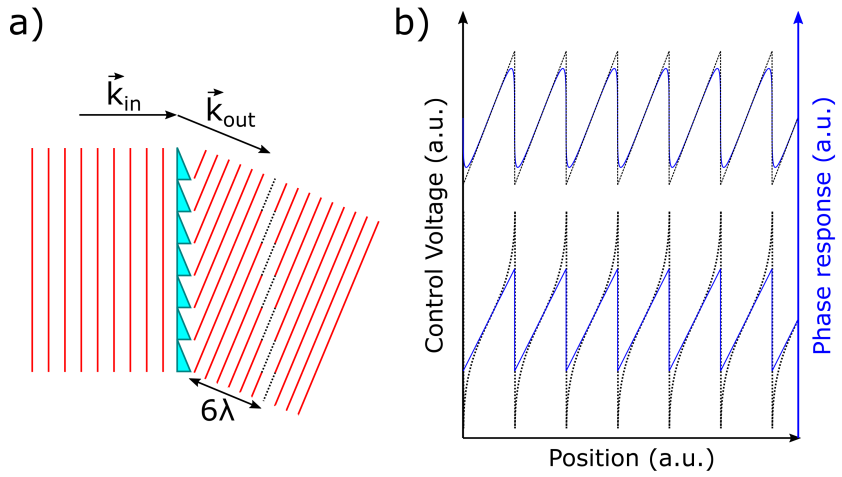

Figure 4.6.: a) shows plane waves undergoing a phase change at a blazed grating. The dotted sections indicate how in this example an incoming wavefront is distributed over seven consecutive outgoing wavefronts with a path length difference of 6λ. b) shows a sketch of pixel control voltages (black, dotted) and their corresponding phase responses (purple) on an SLM. To reach a phase response approximating the triangular shape of a blazed grating, it is necessary to increase the control voltages in the vicinity of phase jumps.

compensated by increasing the control voltages at the edges. The 8-bit mode of the SLM controller is locked to control values between 0 and 2π. This mode is simpler to use and can be sufficient for applications that have lower requirements for the diffraction efficiency or that need higher SLM update rates. However, in 8-bit mode, the control voltages can not be adjusted to perform an edge enhancement of the phase profile. Before purchasing the SLM, we made sure that the controller can also be configured for 12-bit operation, allowing a wider range of control voltages with finer steps exploiting the full range of phase shift per pixel. This makes it possible to implement the discussed edge enhancement. For this, instead of transmitting a 8-bit gray-scale image, a 24-bit three color image is transmitted, containing the desired 12-bit control signal as 8 bits of the red color channel and the least significant 4 bits of the green color channel. The remaining bits of the 24-bit image remain

unused. Figure 4.7 shows the 12-bit SLM calibration curve. A maximum phase shift of $\approx 2.81\pi$ can be reached in 12-bit mode. The curve plateaus for higher control voltages, when the crystals are aligned to the highest possible degree with the electric field lines.

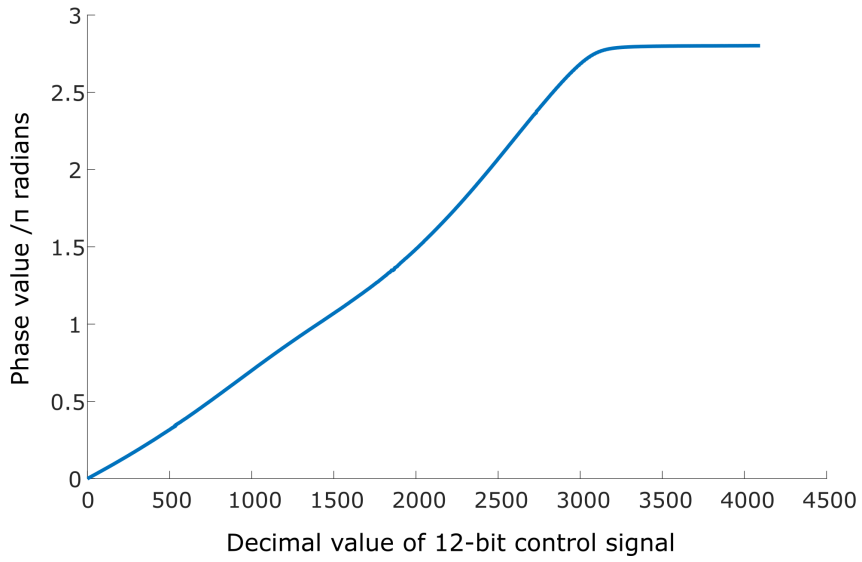

Figure 4.7.: The calibration curve, provided by Hamamatsu, shows the phase response of the SLM to the 12-bit control signal. Due to the birefringent nature of the liquid crystals, the maximum phase shift is limited with best field alignment and the curve plateaus at $\approx 2.8\pi$.

Since the phase profile on the SLM is just an image, common image sharpening techniques can be used. The edge enhancement of images is typically performed by a deconvolution with a Gaussian kernel. Since only neighboring pixels are expected to have non-negligible cross-talk, the kernel size can be chosen as small as a 3 by 3 matrix with zero entries on the corners. Since a deconvolution corresponds to a division in Fourier space, this operation is performed by first transforming the image as well as the kernel into Fourier space, performing the division and transforming back to get a deconvolved phase profile $phase_{decon}$. The transforms are implemented through a fast Fourier transform (FFT) and an inverse fast Fourier transform (iFFT).

$$phase_{decon} = iFFT\left(\frac{FFT(phase)}{FFT(kernel)}\right) \tag{4.22}$$

Here $phase$ is the matrix containing the phase profile values and the kernel has the form:

$$\begin{pmatrix} 0 & A & 0 \\ B & C & D \\ 0 & E & 0 \end{pmatrix} \tag{4.23}$$

For the SLM model used, the crystal orientation is influenced by the geometrical shape of electrode groves on the chip. This leads to asymmetric phase steps, and the kernel was chosen asymmetric to reflect this behavior. To derive a normalization condition for this kernel, we need to take a closer look on the intended action of the edge enhancement. As mentioned, the SLM acts as a kind of low pass filter. We want to reverse this filtering. The low frequency components of the spatial voltage profile should stay constant, since they will produce the desired phase response at the SLM. However, the high spatial frequencies, present at edges, will get dampened, and they should be compensated with an increase in amplitude (see Figure 4.6). This will lead to an overall shape of the phase response that is closer to the desired shape. In the deconvolution (Equation 4.22), we can see the kernel in the denominator. The Fourier transform of the phase profile $FFT(phase)$ contains the amplitude information of all spatial frequencies contributing to the phase profile. The division by the Fourier transform of the kernel $FFT(kernel)$ can then be understood as an amplitude modulation of the spatial frequency spectrum. The Fourier transform of a Gaussian kernel is again of Gaussian form. Normalizing this Gaussian in Fourier space to an amplitude $A = 1$ corresponds to a division by ≈ 1 for low spatial frequencies and by a factor smaller < 1 for increasing frequencies. Therefore, low spatial frequencies stay unchanged and higher frequencies get an amplitude increase. This performs the intended edge enhancement. The two-dimensional discrete Fourier transform (DFT) $y[k, l]$, which is the basis of the FFT is written as:

$$y[k,l] = \sum_{m=0}^{M-1} \sum_{n=0}^{N-1} e^{-2\pi i \frac{km}{M}} e^{-2\pi i \frac{ln}{N}} x[m,n] \tag{4.24}$$

Here, $x[m, n]$ is the kernel entry at the indices (m, n), where m and n are the integer pixel coordinates of the corresponding phase profile $phase[m, n]$. The spatial frequency coordinates k and l are integer multiples of the spatial frequency spacing Δf determined by $\Delta f = 1/(DFT\, points \cdot pixel\, spacing)$. The normalization condition for the kernel entries now derives from the normalization of the Gaussian with $y[0, 0] = 1$ as a sum over all kernel entries:

$$y[0,0] = 1 = \sum_{m=0}^{M-1} \sum_{n=0}^{N-1} x[m,n] \tag{4.25}$$

The matrix coefficients of the kernel have to be determined through an experimental performance evaluation while meeting this normalization condition. The results of this experimental evaluation are discussed in chapter 9.1.

4.3.2. Pitfalls

One thing to keep in mind with Hamamatsu SLMs is the dynamic color range of the used graphics adapter. The premature assumption that 24-bit images get send as 24-bit control signals to a connected monitor had to be verified and was false for some standard graphics adapters (NVidia). For the display of multi-media, often the "limited RGB" format is used, with decimal values ranging from 16 to 235 per color channel. Many TVs only interpret "limited RGB" data, where every value below 16 is translated to black, while every value above 235 is translated to white. Since all "full RGB" displays can work with "limited RGB" data, some graphics adapters only use "limited RGB" in order to be compatible to a wider variety of displays. However, for the display of phase-profiles this is problematic. For absolute proof of correct data transmission, a DVI-D receiver, capable of logging any incoming transmission, would be needed to decrypt the serial data protocol. The signal is transmitted in an encoded format, with a complicated data and clock transmission, therefore simple voltage analysis of the DVI-D connection will not suffice. However, the acquisition of such a device was not feasible with the given constraints. It is hard to design an optical experiment to test this behavior, since slight restrictions in the dynamic range of the SLM will lead to ambiguous changes in measured beam profiles. To at least get an indication of correct SLM display behavior, an experiment was thought up. As shown in Figure 4.7, the 12-bit operation of the SLM allows to define phase values up to 2.81π. This leaves room for an additional global phase shift of up to 0.81π of a blazed grating, with values ranging from 0 to 2π. If the data transmission is correct, the addition of a global offset of more than 0.81π should lead to clipping of the phase profile and an accompanying decrease in diffraction efficiency, while the addition of a global offset of less than 0.81π should not change the diffraction efficiency. To test this hypothesis in an experiment, the diffraction efficiency of a laser beam at a blazed grating was monitored. The measurement was performed two times to compare graphics cards from the manufacturers Intel and Nvidia and its result is shown in Figure 4.8.

The measurement shows that both graphics cards have a slight increase in diffraction efficiency when adding a global offset. This was not expected, since for correct calibration a global offset should not change the diffraction efficiency. Also, the expected drop in diffraction efficiency at a global offset of 0.81π has a weird shape that could not be explained. The slow increase in diffraction efficiency is probably connected to better alignment of the

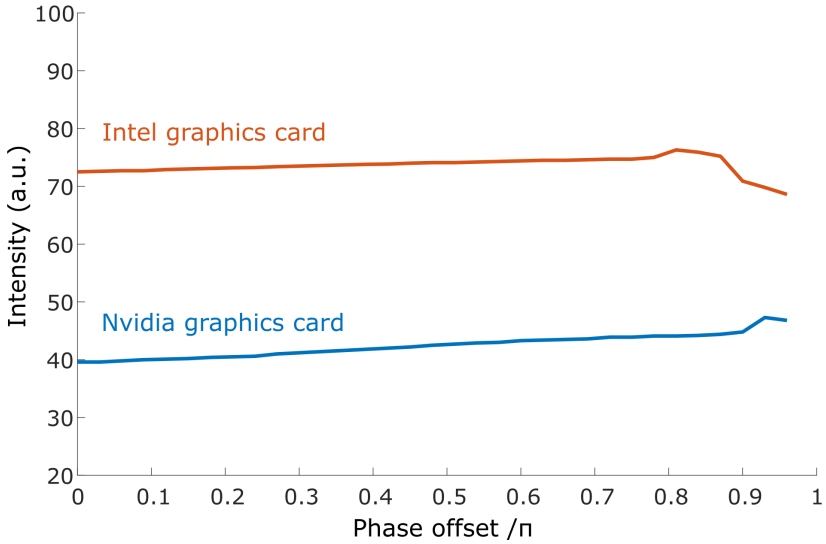

Figure 4.8.: Intensity of the STED laser diffracted at a blazed grating. Two different graphics card manufacturers were tested (Matlab plot of power meter values).

birefringent crystals at higher electric field strengths. However, no experiment could be conducted that would prove this hypothesis. After the offset measurement, an Intel Radeon RX 570 card was chosen for use in all further experiments, since it deviated less from the expected behavior. In any case, all further experiments were run at a constant phase-offset of $\Delta\phi = 0.4$ to place the phase profiles in the middle of the accessible range. This allows for the highest amplitude modulation of the edge enhancement.

4.3.3. Description of optical aberrations

A Gaussian imaging system is defined as an ideal optical system that translates spherical waves emerging from an object point P_0 to spherical waves converging on an image point P'[42]. This ideal image point P' is also called Gaussian image point. Figure 4.9 sketches how to describe aberrations from this ideal Gaussian imaging system. The Gaussian reference sphere is defined as the ideal wave front that is centered around P' and coincides with the origin of the exit aperture. Real optical systems have various imperfections that lead to an aberration of the wave front (depicted in blue). This leads to aberrations of the PSF. To describe this aberration, the difference in optical path length Φ between the ideal and the aberrated wavefront can be written as the function of the coordinates of the exit aperture (x, y) and the object point (x_0, y_0)[42]. Since only relative rotations between the two coordinate axes will have an effect on the function of Φ, it can be written in terms of $x_0^2 + y_0^2$,

Table 4.1.: Table containing the primary Seidel aberrations[44].

Seidel aberration	Functional form
Spherical aberration	ρ^4
Coma	$x_0\rho^3 cos(\Theta)$
Astigmatism	$x_0^2\rho^2 cos(\Theta)^2$
Field curvature	$x_0^2\rho^2$
Distortion	$x_0^3\rho cos(\Theta)$

$x^2 + y^2$ and $x_0x + y_0y$[42]. Φ can then be expanded into a power series with even powers in its coordinates k^{2n}. The terms of lowest power k^2 do not constitute optical aberrations but describe tip, tilt and defocus that correspond to a translation of the image point along the axes x,y and z. The terms of power k^4 are called primary Seidel aberrations. Table 4.1 lists the functional form of these aberrations, where $x = \rho cos(\Theta)$ and $y = \rho sin(\Theta)$, with Θ, the angle about the optical axis and ρ, the distance from the optical axis.

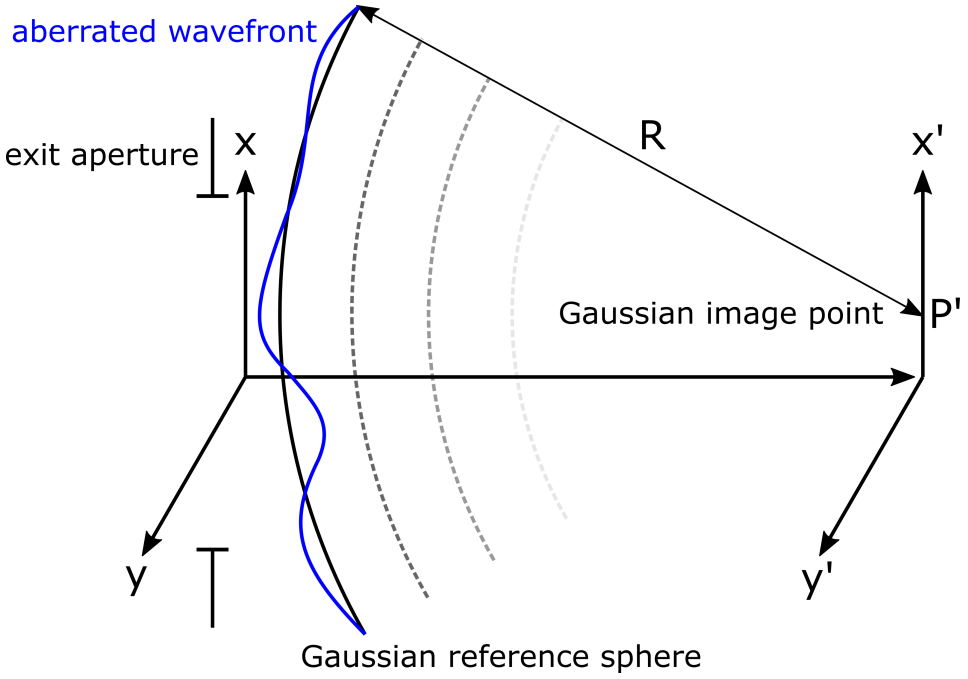

Figure 4.9.: Sketch of optical aberration as described as deviation from the Gaussian reference sphere. The entry aperture and the object point P_0 are omitted in the sketch.

For STED microscopy, it was shown that especially spherical aberration, coma and astigmatism degrade the STED PSF[37,19]. This can readily be understood by looking at each of

the three aberrations in an example beam path. Figure 4.10 shows how spherical aberration leads to an elongated PSF, where the beam power is distributed along the optical axis. Although spherical aberration does not contribute intensity to the central minimum of a STED beam, it will alter its width and crest height, therefore degrading the maximum possible resolution. Figure 4.11 shows how astigmatism stretches out the PSF into elliptical shapes the are displaced along the optical axis. Astigmatism has a strong influence on the central minimum of the STED PSF. It breaks the circular symmetry of the beam, and therefore reduces the destructive interference in its middle. Figure 4.12 shows how coma leads to a tail in the PSF. Again, this is problematic, since, for destructive interference in the center of the STED PSF, the beam should have a circular symmetry. It should be noted that the effect of coma on the STED PSF is similar to a displacement of the phase vortex that is used to create the STED beam in the first place. In both cases, the central minimum will move away from the optical axis. A measurement method that will discern both effects is crucial for the experiment. For this, a blazed grating can be used to perform a razor blade measurement on the SLM (chapter 4.3.4). This will enable beam positioning prior to aberration correction. However, it should be noted that this measurement is not able to reach a perfect distinction, and the shape of the PSF should additionally be analyzed. Coma will lead to a very distinct shape change that is better visible on a Gaussian PSF rather than on the STED PSF (Figure 4.14). Figure 4.11 shows how astigmatism can be caused by a lens with two surface radii R_1 and R_2. This will lead to a focal point shift in both spatial dimensions. In the STED PSF this will lead to an increase in center intensity. In our experiment, the main source of astigmatism is the ellipticity of the diode lasers. Higher order aberrations will also contribute to a PSF degradation, but usually these three aberrations have the largest coefficients in the expansion.

Zernike polynomials

Although all aberrations are a function of the object point coordinates, there is a more practical way to describe Φ for the use in confocal microscopy with the help of a stationary object point P_0. To consider why this is valid, one should visualize the confocal beam path. All beam paths in the microscope can be described as originating from point sources. All laser beams originate from a fiber output, while all detection paths end in a pinhole. All these endpoints are fixed in space. The only moving part is the beam scanning directly before the objective. However, microscope objectives can be approximated as ideal Gaussian imaging systems, as long as they are used for imaging close to the optical axis. Therefore, the complete beam path can be viewed as a cascade of an aberrated imaging system followed by the ideal imaging system of the objective. The relevant contributions to the

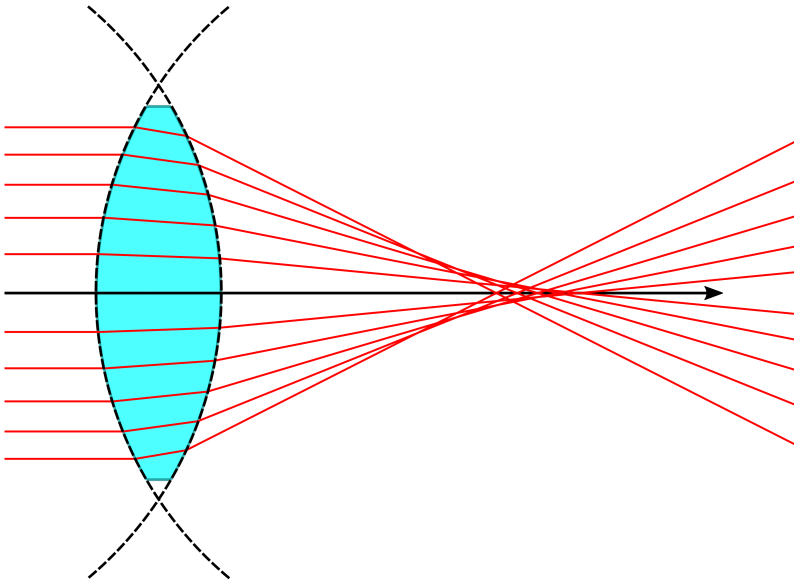

Figure 4.10.: Sketch of spherical aberration. Typically lenses are cut with spherical surfaces and rays further from the optical axis will focus earlier. This leads to a smeared out focal area, rather than a focal point.

wave front aberration in the experiment will accumulate before the objective, through imperfections of lasers, lenses, filters, polarizers, mirrors and further optical components. For the mathematical description of aberrations, the use of a stationary object point P_0 makes it possible to describe Φ solely as a function of the exit aperture coordinates[42] and expand Φ with the help of Zernike polynomials that constitute a complete basis set on the unit circle[42]. These Zernike polynomials can be displayed on an SLM that is in a conjugate plane to the objective back-focal plane. In this way, they can be used to compensate aberrations in the beam path before reaching the scanning mirrors and objective. The necessary expansion coefficients can be experimentally determined with the help of AO correction algorithms. The Zernike polynomials are defined by:

$$Z_m^n(\rho,\phi) = R_m^n(\rho)cos(m\phi) \tag{4.26}$$

With the radial functions $R_m^n(\rho)$:

$$R_m^n(\rho) = \sum_{k=0}^{\frac{n-m}{2}} \frac{(1-)^k(n-k)!}{k!(\frac{n+m}{2}-k)!(\frac{n-m}{2}-k)!}\rho^{n-2k} \tag{4.27}$$

Often the polynomials are ordered in series by the single number Noll index j, where j is

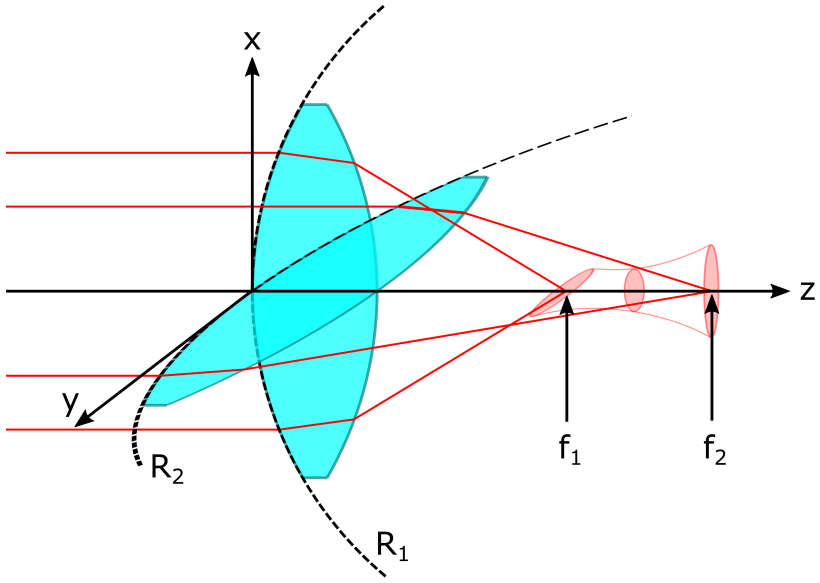

Figure 4.11.: When a lens has different curvature radii R_1 and R_2 along its axes, the respective focal points f_1 and f_2 for each spatial direction are displaced. The resulting field geometry is sketched in light red. The intensity profile will change along the optical axis from an ellipsoid in the y direction to a circle to an ellipsoid in the z direction.

a function of m and n. Table 4.2 shows how the Zernike polynomials are connected to the Seidel aberrations. The first zernike polynomial corresponding to a piston is just a global phase offset that will not influence the PSF shape. For correction algorithms it is important to see that most Zernike modes correspond to a combination of tip, tilt and defocus in combination with the Seidel aberrations.

4.3.4. Beam optimization prior to imaging

The STED PSF requires a well-defined beam position on the SLM as well as proper correction of optical aberrations to have zero laser intensity in its center. This section contains all alignment steps that are necessary to arrive at a beam good enough for STED imaging. It also lists two AO algorithms that can be used for an automated correction. However, currently the confocal volume still suffers from positional jitter, due to noise of the piezo stage and possibly instability of optics mounts. This makes the manual correction method still the most reliable alignment method, since the measures of beam-quality in the automated scripts are too unstable to converge to a well-corrected beam.

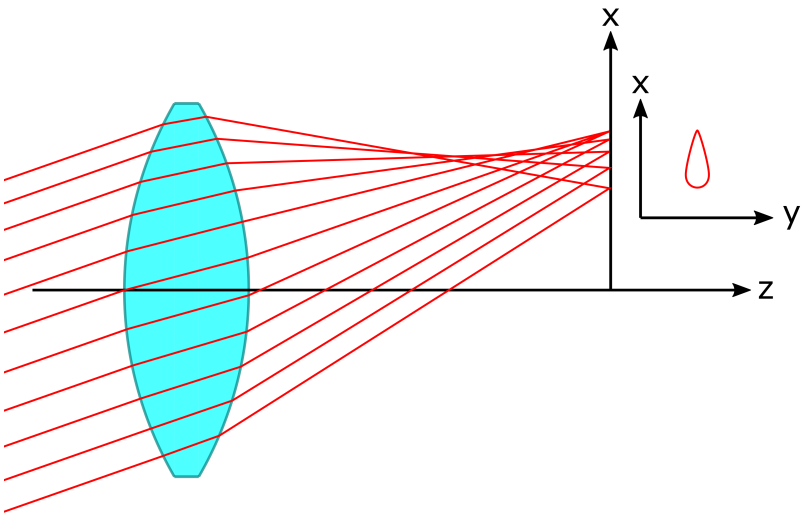

Figure 4.12.: When rays enter a lens with an angle relative to the optical axis, they will experience a focal point shift towards the optical axis. The effect increases for rays further from the optical axis, leading to an increase in the focal point size, as sketched in the small axis diagram. This effect is called coma, since the PSF features a tail and is reminiscent of a comet.

Razor blade measurement on SLM

As a first step, the razor blade measurement introduced in chapter 3.3.3 can also be implemented on the SLM. Instead of clipping the beam with a razor blade it can be clipped with a blazed grating. Instead of filling the whole SLM with a blazed grating, the grating can be displayed on only a part of the SLM surface. Now the border of the grating can be moved accross the whole SLM and the power in the diffracted order can be monitored. Figure 4.13 shows a sketch of the measurement and the measured data together with the fit of Equation 3.3. To center a laser beam on the SLM, the power of the complete grating P_{max} should be measured as well as the minimal back-ground power P_{min}, when no grating is displayed. Now the grating border can be placed exactly at the center of the SLM and the beam can be moved until the power is exactly $(P_{max} - P_{min})/2$. For this, it is helpful to isolate the diffracted order from the zero-order and higher orders with the help of a lens and an iris. It should be noted that if the beam position is far off, this procedure has to be performed multiple times and the position of the iris has to be adjusted repeatedly. The data shown in Figure 4.13 is the result of a razor blade measurement, after the beam was centered with the described procedure. The fit values of the beam position are 638.2

Table 4.2.: Table shows the connection between the first eight Zernike polynomials and primary Seidel aberrations[44]. The Noll index j is a single index, calculated from the indices m and n.

Noll index j	Seidel aberration
0	piston
1	tip
2	tilt
3	defocus
4	astigmatism and defocus
5	astigmatism rotated by 45° and defocus
6	coma and tip
7	coma rotated by 90° and tilt
8	spherical aberration and defocus

pixels for the horizontal direction and 508.9 pixels for the vertical direction. This is quite close to the center position (636, 512) of the SLM chip.

Manual correction routine and vortex placement

As a second step in manual alignment, the vortex position and Zernike polynomials have to be adjusted while monitoring the STED beam PSF on gold beads with the channel photo multiplier (CPM). For this, the STED beam power should be on the order of $10\,\mu W$. As a first step, the phase vortex should be disabled, and coma and spherical aberration should be corrected at the Gaussian PSF. Figure 4.14 shows line traces across the PSF, where one axis of the piezo stage is moved relative to the STED beam, while the count rate on the CPM is monitored. a) shows the effect of coma on the beam shape prior to correction, while c) shows the effect of spherical aberration. With the functions "coma horizontal", "coma vertical", "primary spherical", "secondary spherical" and "tertiary spherical", the beam can be manually corrected and b) and d) show the resulting PSF shape.

For the second step, the phase vortex is enabled and images of the STED PSF are acquired. With the help of these images, the vortex position can be fine-tuned and the functions "astigmatism oblique" and "astigmatism vertical" can be used to correct the astigmatism in the beam. The goal in this step is to change the PSF shape until it is circular symmetric and it has a zero center. First, the vortex should be adjusted until the minimum is roughly in

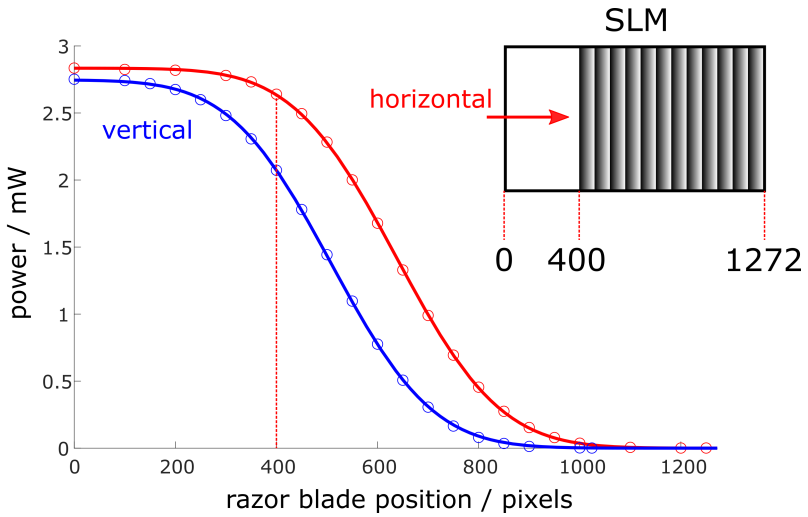

Figure 4.13.: Matlab plot of a razor blade measurement at the SLM. This measurement can be used to confirm a beam position in relation to the SLM surface. The sketch shows how the border of a blazed grating is moved over the SLM surface. The curves show data that was measured after the beam was centered on the SLM. The corresponding fit of Equation 3.3 lead to beam center coordinates of (638.2, 508.9). This is close to the center of the SLM (636, 512).

the center of mass of the beam. Then, to better visualize deviations from circular symmetry, the dynamic range of the image display should be adjusted until only the donut crest is visible (Figure 4.15). Now, the astigmatism modes can be changed until the best symmetry is reached. In this alignment step it pays off to revisit the vortex position after astigmatism alignment. The final measure of the beam quality should be a direct comparison of the beam center and the image background on the rim of the image. Here, it should be kept in mind that the STED PSF has a radial extent of about $3\,\mu m$. Typically an image size as small as $1.5\,\mu m$ by $1.5\,\mu m$ can be used for alignment. However, then the center intensity has to be below the "background" level. Currently, this measurement is difficult, since the confocal volume is not perfectly stable. A script was written to fit a two dimensional parabola to the image for an automatic readout. However it also proved to be affected by the positional jitter. Alternatively, the gold bead can be moved around trying to hit the beam center with the piezo stage, while monitoring the CPM count rate. In this way, the minimal count rate can be found after a bit of manual search.

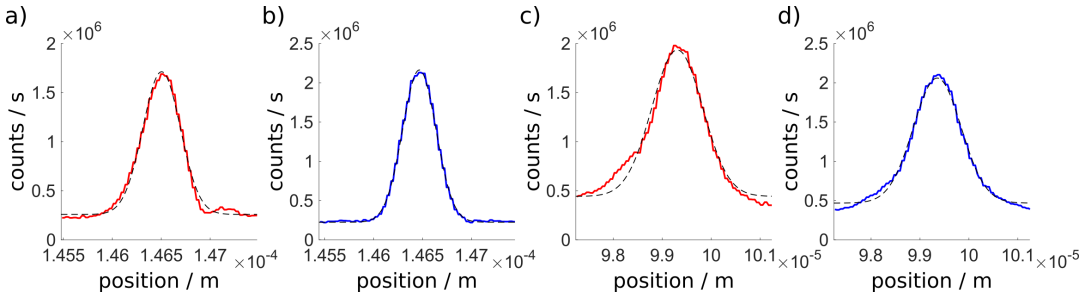

Figure 4.14.: Line traces and Gaussian fits (black dotted lines) across the Gaussian PSF of the STED beam with deactivated phase vortex. a) Shows how coma influences the beam shape in the y-direction, while b) is the corresponding trace, when coma has been manually corrected on the SLM. Similarly, c) shows how spherical aberrations influence the beam shape in the axial direction, while d) shows the beam after manual correction with the Zernike polynomials corresponding to primary, secondary and tertiary spherical aberration.

4.3.5. Zernike analysis algorithms

Several algorithms, published in the field of adaptive optics (AO), can be used to analyze the STED beam shape. For every algorithm, a script has been written that can be run in the microscope software. All of these algorithms aim to analyze the beam aberrations and calculate the individual contributions of each Zernike mode. However, as mentioned before, the microscope still suffers from positional instability and the experimental implementations of these algorithms reflected this instability. Although the algorithms showed promise in correction of low order Zernike modes (astigmatism and coma), they currently do not outperform the manual correction routine in terms of speed and fail for higher Zernike modes. However, as soon as the microscope stability will be improved in the future, these algorithms should be revisited, since they can potentially be used for a completely automated aberration correction. I will shortly explain the general idea behind each publication and explain the advantages and drawbacks that were becoming apparent in the experimental implementation.

STED image metric

In the paper from Gould et al. (2012) [19], a method is presented, where the quality of the STED image is quantified through a brightness and sharpness metric. The brightness metric simply is the total image brightness, while the sharpness metric is calculated from the frequency content of the Fourier transform of the image. The value of a combined

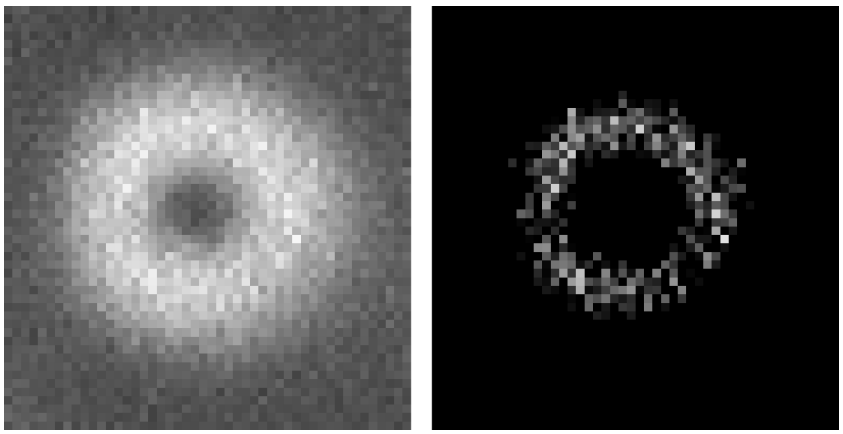

Figure 4.15.: Confocal image of STED PSF on a single gold bead. Image size is $1.5\,\mu m$ by $1.5\,\mu m$ and the pixel size is $30\,nm$. On the left, the full grey scale range is used, while on the right only a certain brightness range is selected to visually enhance the display of the donut crest. This can be done on the fly in the GUI and helps to visualize the beams symmetry.

metric of sharpness and brightness will follow the form of a parabola, when the amplitude of individual Zernike modes is altered. Monitoring the metric, while changing the bias amplitude on the SLM will reveal the center of this parabola, which represents the amount of aberration that is currently present in the beam. The advantage of this method is that it works directly on a STED sample. This means that sample specific aberrations can be corrected. The disadvantage is that STED images are fairly slow to acquire, in comparison with confocal images or the time trace of the detector readout that can be used by other approaches. Currently, the STED images are still too jittery and the metric is unstable. As a result, to estimate just one of the low order Zernike modes with good accuracy, more than 50 individual STED images have to be acquired. This leads to an extremely long time frame for the correction and is not feasible on any STED sample, but nitrogen vacancy centers (NVs) in nanodiamonds.

Binary phase profiles

Another approach was presented by Klauss, Conrad, and Hille (2017) [45]. Here, a binary phase mask can be created for each Zernike mode. Each Zernike mode is defined by a symmetric phase range, with zero phase in the middle of the range. To create the binary phase profile, a new function is created, where all values < 0 are set to 0, while all values > 0 are set to π. If this phase profile is displayed on the SLM and rotated, the center intensity of the PSF will undergo a periodic amplitude change if the corresponding Zernike

mode is currently contributing to the beam aberration. By the phase of this periodic change, the angle of the Zernike mode can be calculated. After the angle has been calculated, the amplitude of the Zernike mode can be changed until the amplitude modulation vanishes. For this method, the amplitude in the center of the PSF at the photon counter was too noisy to use as a direct readout. Instead, confocal images with small field of view were used, and a small radius of pixels in the middle of the PSF was used as readout. With this method astigmatism can be corrected, but already for coma the readout was again too noisy to give reliable values. This method could potentially be useful, but several things would have to be improved in the software to make it possible. The speed of the update function for the SLM has to be increased drastically, and a feedback has to be programmed that will synchronize the SLM update with photon counter. Then, a larger number of cycles in combination with a Fourier transform of the photon counter signal should be able to provide a more stable readout. For this approach it would be best to measure the noise spectrum at the photon counter and choose a rotation frequency of the binary phase profile that lies in a spectral area of low noise.

Pinhole transmission

Neil, Booth, and Wilson (2000) [46] propose a new modal wave front sensor, where an incoming beam is split and a negative and positive bias aberration of one Zernike mode is applied to each beamlet. The beams are then focused onto two pinholes, and the transmitted intensities I_1 and I_2 are measured. The sensor output $S = I_1 - I_2$ is then defined as the difference of these intensities. The paper calculates that this sensor is mainly responsive to aberrations in the beam that correspond to the same mode as the bias aberrations. For example, if I chose astigmatism as bias aberration, the coma contribution in the beam will lead to a contribution of $S = 0$. In this way in an iterative manner all modes can be readout. However, the orthogonality of the modes in respect to the sensitivity of the sensor is influenced by bias magnitude and pinhole size and shape. This approach might be feasible to adapt for a confocal microscope with SLM. Instead of two bias plates, the SLM can be used in an alternating fashion, where first the negative bias is applied and I_1 is measured and then the procedure is repeated for positive bias. Instead of a pinhole, reflective gold beads or a sample with reflective gold disks can be used. Although working in reflection, an equivalent for the action of a pinhole should be able to be found. A script has been written based on this paper, but more work will be needed to fully test this approach. So far, preliminary experiments on gold beads have shown that the sensor seems to be responsive to astigmatism.

5. Confocal multiplexing

As mentioned in the introduction, stimulated emission depletion (STED) microscopy differs from other super-resolution methods in that the switching processes between dark and bright states are deterministic with fast switching times. Furthermore, image acquisition is performed by a confocal volume scanning approach. Next to the movement speed of the confocal volume, the image acquisition speed is mainly limited by the repetition frequency of the excitation lasers, since it limits the number of collected photons in a given time frame and leads to a minimal pixel dwell time for STED images with good signal-to-noise ratio (SNR). In a previously built STED microscope at the Biophysics Institute, the pulsed lasers had repetition frequencies of $\approx 1\,\mathrm{MHz}$, leading to a pixel dwell time of $\approx 400\,\mu\mathrm{s}$ in the setup[47]. For a typical field of view of $30\,\mu\mathrm{m}$ by $30\,\mu\mathrm{m}$ and a typical pixel size of $12.5\,\mathrm{nm}$, this leads to an image acquisition time of 38.4 minutes. This makes it obvious that live cell imaging in this context is out of reach.
In contrast, for this experiment, one of the goals was to explore possible changes to the typical STED microscope design that would lead to faster image acquisition and live cell imaging capability. Of course, laser development progressed, and lasers available today have faster repetition rates. The lasers used in this experiment are operated at a repetition frequency of $30\,\mathrm{MHz}$, cutting the image acquisition speed by a factor of 30. However, to truly gain an edge over the existing STED design[47] in respect to speed, another idea was pursued. If we can divide the field of view into several sections and scan each section with their own confocal volume, then we can divide the image acquisition time by a further factor. We will see that in the chosen approach the minimum distance between confocal volumes is limited by the spatial separation of neighboring STED point spread functions (PSFs). This allows for distances between confocal volumes on the order of $4\,\mu\mathrm{m}$. The example field of view of $30\,\mu\mathrm{m}$ by $30\,\mu\mathrm{m}$ can now be divided into a quadratic grid of up to 49 confocal volumes. This will divide image acquisition time by another factor of 49 and push the time needed for a single image down to $\approx 1\,\mathrm{s}$, well within the range that becomes interesting for live cell imaging. To create multiple confocal volumes, the STED beam and excitation beams have to be divided into multiple beamlets that are intended to focus in a grid of spatially separated focal spots in the focal plane of the microscope objective. The next sections discuss two methods that calculate phase profiles for a diffractive optical element

(DOE) that can perform such a beam separation. The discussion of the data acquisition from multiple confocal volumes with the help of the field programmable gate array (FPGA) can be found in chapter 7.5.

5.1. Fan-Out algorithm

Two publications from the field of optical communication by Herzig, Prongué, and Dändliker (1990) [48] and Prongué et al. (1992) [49] describe a method to combine multiple coherent laser beams with the help of a diffractive optical element (DOE). They calculate a smooth transfer function $t(x, y)$ and laser beam-writing is used to implement this function as a surface relief on a transparent medium. This method leads to a close-to-perfect diffraction efficiency and uniformity and it is possible to adapt the core idea to the use with an spatial light modulator (SLM). Instead of combining multiple beams, here we follow the reversed beam path and create multiple beamlets out of a single STED beam. We will call this approach fan-out algorithm (FOA), inspired by the term used by Herzig, Prongué, and Dändliker (1990) [48].

5.1.1. Algorithm

We start the discussion with a number of point sources in the back-focal plane of a lens (Figure 5.1) that performs an optical Fourier transform (chapter 4.1.5). These are equally spaced along an axis perpendicular to the optical axis. This can be expressed as a series of delta functions, since we do not look at diffraction limited PSFs, but rather point sources[49]:

$$U(x, y) = \sum_{m=1}^{N} A_m exp(i\phi_m)\delta(x - x_m, y) \tag{5.1}$$

Here, A_m is the complex amplitude of each point source and ϕ_m is the corresponding local phase. We want to use the Fourier transform property of the lens valid in Fresnel approximation. The spatial dimensions of the lens and the point source spacing are therefore chosen accordingly. After the Fourier transform, the field in the focal plane takes the form[49]:

$$\hat{U}(\nu_x, \nu_y) = \sum_{m=1}^{N} A_m exp(i\phi_m) exp(2\pi i x_m \nu_x) \tag{5.2}$$

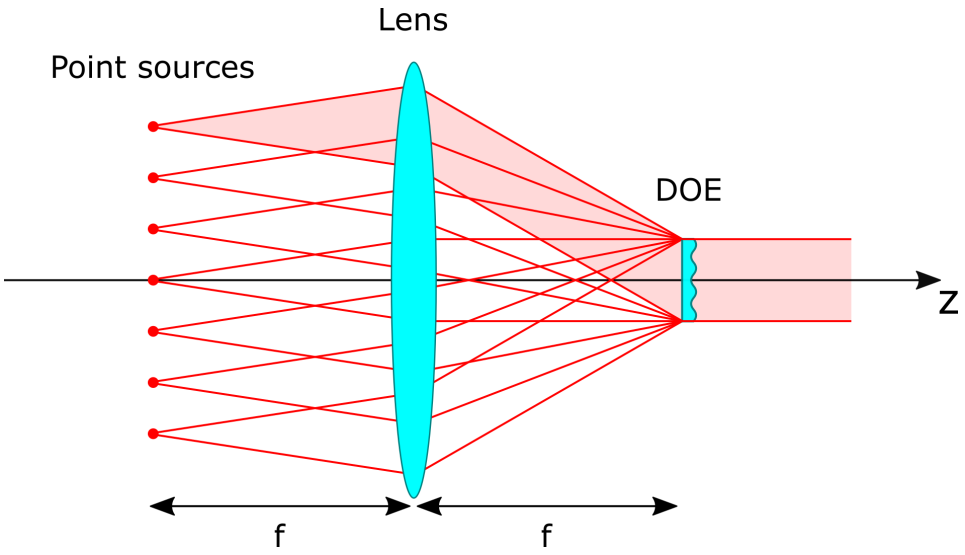

Figure 5.1.: The basic working principle for the FOA[49]: the light from multiple coherent point sources will interfere and lead to a complex field function in the focal plane of a lens. If this field function can be modeled as the complex transmittance $t(x, y)$ of a DOE, the wave front of each beamlet will be diffracted into the same travel direction along the optical axis, effectively combining all beamlets into a single beam.

For the optical Fourier transform, we have to evaluate at the spatial frequencies $\nu_x = \frac{x}{\lambda f}$ and $\nu_y = \frac{y}{\lambda f}$. If we compare $\hat{U}(\frac{x}{\lambda f}, \frac{y}{\lambda f})$ with the definition of a plane wave we can see that this Fourier transform corresponds to a sum of plane waves traveling at different angles, where the angles depend on the distances x_m to the optical axis. It follows that in a reverse direction, a plane wave, modulated by a complex transmittance $t(x, y) = \hat{U}(\frac{x}{\lambda f}, \frac{y}{\lambda f})$, splits up into several traveling directions.

We learned that for thin optical elements (SLM or DOE) we can multiply any incoming beam $f(x, y)$ with a complex transmittance $t(x, y) = \hat{U}(\frac{x}{\lambda f}, \frac{y}{\lambda f})$ to arrive at a transformed beam $f'(x, y)$. Since we can write $f(x, y)$ as Fourier decomposition (Equation 4.6), we arrive at:

$$f'(x,y) = \left(\sum_{m=1}^{N} A_m exp(i\phi_m) exp(2\pi i x_m \frac{x}{\lambda f}) \right) \cdot \int_{-\infty}^{\infty} \int_{-\infty}^{\infty} F(\nu_x, \nu_y) e^{-i2\pi(\nu_x x + \nu_y y)} \, d\nu_x \, d\nu_y \tag{5.3}$$

Pulling the integration into each term of the sum and adding the exponents, we arrive at:

$$f'(x,y) = \sum_{m=1}^{N} A_m exp(i\phi_m) \int_{-\infty}^{\infty}\int_{-\infty}^{\infty} F(\nu_x,\nu_y) e^{-i2\pi((\nu_x - \frac{x_m}{\lambda f})x + \nu_y y)}\, d\nu_x\, d\nu_y \tag{5.4}$$

After a coordinate transform $\nu'_x = \nu_x - \frac{x_m}{\lambda f}$ and renaming $\nu'_x = \nu_x$ we arrive at:

$$f'(x,y) = \sum_{m=1}^{N} A_m exp(i\phi_m) \int_{-\infty}^{\infty}\int_{-\infty}^{\infty} F(\nu_x + \frac{x_m}{\lambda f},\nu_y) e^{-i2\pi(\nu_x x + \nu_y y)}\, d\nu_x\, d\nu_y \tag{5.5}$$

We can see that this corresponds to a series of beams where the original wave vector spectrum is shifted by the spatial frequency $\nu_{shift} = \frac{x_m}{\lambda f}$. Since for small shifts the spectral frequency is proportional to the diffraction angle, the beamlets travel at angles $\theta_m \approx \nu_{shift}\lambda = \frac{x_m}{f}$. In the small angle approximation, the overall shape of the spectrum for each beamlet is not altered. This is at the core of the algorithm and very important for the use in STED microscopy. It implies that with the FOA a beam is split up into several travel directions, but the beam quality and shape is preserved. Given our desired field parameters, the small angle approximation can easily be fulfilled in the experiments.

The modulation of a beam $f'(x,y) = f(x,y) \cdot t(x,y)$ is physically only possible with amplitude and phase modulation. Since attenuation of a beam leads to unwanted losses and amplification of a beam at a DOE is not usually possible, the function $\hat{U}(\nu_x,\nu_y)$ needs to be optimized to contain no amplitude modulations. For this, we separate the phase and amplitude contributions of $\hat{U}(\nu_x,\nu_y)$ in the following way[49]:

$$\hat{U}(\nu_x,\nu_y) = |\hat{U}(\nu_x,\nu_y)| exp(i\Psi(\nu_x,\nu_y)) \tag{5.6}$$

We then look at the light intensity $I = |\hat{U}|^2$ and collect the terms that only depend on the emitter amplitudes A_m, in a separate sum[49]:

$$I(\nu_x,\nu_y) = \sum_{m=1}^{N} A_m^2 + 2\sum_{m<n}^{N} A_m A_n cos(2\pi\nu_x(x_m - x_n) + \phi_m - \phi_n) \tag{5.7}$$

Here, we can see that the second term represents a sum of intensity modulations. The phases $\phi_{m,n}$ are only a global phase offset for each beamlet and do not influence its field geometry. A search algorithm can therefore be used to find a set of $\phi_{m,n}$ that will minimize these intensity modulations. If we minimize the intensity modulations, the approximation of the function $\hat{U}(\nu_x,\nu_y)$ with constant amplitude $I = |\hat{U}|^2 = const = 1$ can be implemented

on a phase-only DOE, like an SLM or a surface profile with varying thickness on a transparent medium. Here, the magnitude of residual intensity modulations after the minimization is dependent on the number of beamlets and the beam angles. Next, we need to discuss which search algorithm can be used for minimizing the intensity modulations.

5.1.2. Implementation for SLM

The proposed minimization procedure[48] consists of two steps. First, a downhill simplex search algorithm optimizes the phases ϕ_m, then the amplitudes A_m are altered slightly to improve the uniformity in amplitude across beamlets. This procedure is intended for the production of smooth surface profiles and the performance has been described previously[48]. As a first try, the performance of a quantized version of this method, corresponding to the display on a pixelated SLM, was evaluated.

In our implementation, the difference to the original approach was the sampling of the phase function on a grid of points according to the SLM resolution, limiting the smoothness of the phase profile. The Matlab function "fminsearch", based on the Nelder-Mead algorithm (NMA)[50], was applied to minimize the interference terms by changing ϕ_m. This first step resulted in standard deviations for the intensity of up to $30\,\%$ for 5 beamlets (Figure 5.2). Choosing random starting points for the phases ϕ_m did not lead to different results. The following optimization of the starting amplitudes A_m, proposed as a second step, did not converge to better solutions. Compared to the results in the original publication[48] of close to $100\,\%$ uniformity, this was unsatisfactory. For the use with pixelated phase profiles, the search function had to be altered and multiple different search algorithms were analyzed for their performance.

Altered search function

The minimization function f_{min}, so far only consisting of the intensity modulation terms $\sum_k B_k^2$ as mentioned in Herzig, Prongué, and Dändliker (1990) [48], was extended with further terms to improve the expected uniformity. This time, the amplitudes A_m were also included in the variables of the optimization. On the one hand, this extends the search space and makes a search more difficult, on the other hand it enables the access to all degrees of freedom in a single optimization step. The minimization function f_{min} was chosen as:

$$f_{min} = w_M \cdot M_{r,norm} + w_A \cdot std_A + w_P \cdot std_P \tag{5.8}$$

Here $M_{r,norm} = M_r/M_{r,max}$ stands for the residual intensity modulation. The term M_r is expressed with $\sum_k B_k^2$ according to Herzig, Prongué, and Dändliker (1990) [48]:

$$\sum_k B_k^2 = \sum_k^{N-1} \left[\left(\sum_{m=1}^{N-k} A_m A_{m+k} cos(\phi_m - \phi_{m+k}) \right)^2 + \left(\sum_{m=1}^{N-k} A_m A_{m+k} sin(\phi_m - \phi_{m+k}) \right)^2 \right] \tag{5.9}$$

The term $M_{r,max}$ is defined by a similar definition as $\sum_k B_k^2$, but all the values of the periodic functions have been replaced by one:

$$M_{r,max} = \sum_k^{N-1} \left[\left(\sum_{m=1}^{N-k} A_m A_{m+k} \right)^2 + \left(\sum_{m=1}^{N-k} A_m A_{m+k} \right)^2 \right] \tag{5.10}$$

This was a straightforward way to introduce a normalization to the modulation terms. Without the normalization, the minimization will result in $A_m \to 0$, since this will minimize all terms. The terms std_A and std_P are calculated from the Fourier spectrum of the phase profile. While std_A is the standard deviation of the integrated intensity across the target orders, std_P is the peak intensity in each order. The weighting factors w_M, w_A and w_P are used to fine-tune the outcome of the minimization, giving more or less emphasis to each term. This is a standard practice for minimization processes with multiple contributions.

The introduction of these new terms was based on an educated guess for their physical implications. The peak intensity measures the focusing ability of the beam in the focal plane which is a measure of beam quality, while the integrated intensity is a measure for the power distribution among the orders. This approach was successful, and the resulting Fourier spectra indeed featured a much higher uniformity in average and peak power.

Performance and other search algorithms

Figure 5.2 shows the initial approach as comparison, when only using the minimization of the modulation terms and the NMA. The intended example target is the creation of five beamlets with a spacing between beams $\Delta x = |x_i - x_{i+1}| = 4\,\mu m$ in the focal plane of the microscope ($x_0 = -8\,\mu m$ to $x_4 = 8\,\mu m$). The algorithm is terminating in this case with values of $M_{r,norm} \approx 3.3\,\%$, $std_P \approx 30\,\%$, $std_A \approx 30\,\%$ and a diffraction efficiency of $\eta_D \approx 98\,\%$.

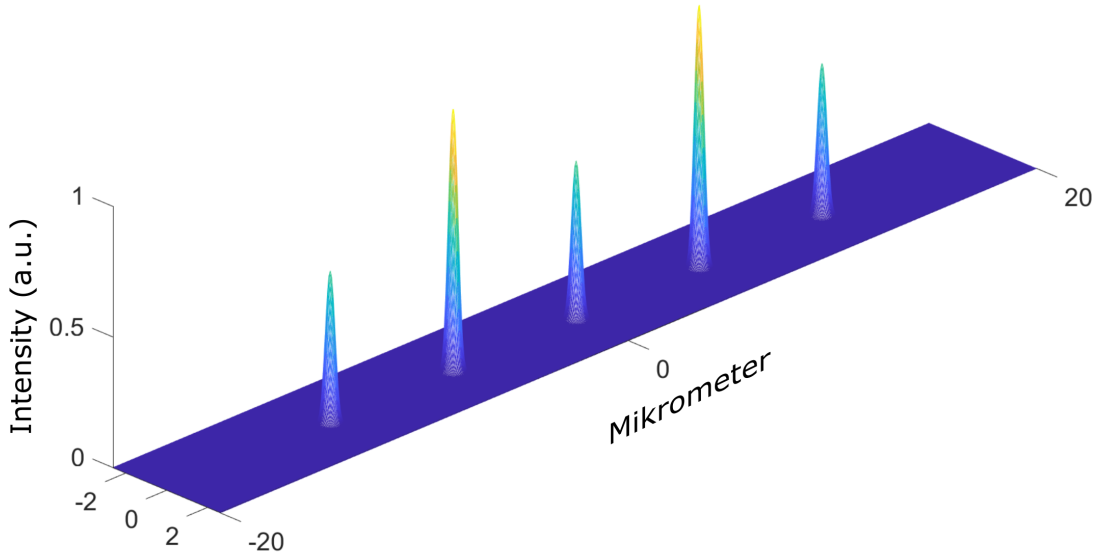

Figure 5.2.: The fast focus calculation result for the NMA, when only minimizing $M_{r,norm}$. Although the efficiency is close to $100\,\%$, the amplitude deviation between beams is large.

After adding the uniformity terms discussed in the previous section to f_{min}, the search with the NMA over the variables ϕ_m and A_m resulted in drastically improved uniformity (Figure 5.3). Again $\Delta x = |x_i - x_{i+1}| = 4\,\mu\text{m}$ was chosen as an example target. The algorithm was configured with random starting values for the phases ϕ_i between 0 and 2π and constant starting values for the amplitudes $A_m = 1$. No boundaries had to be set for either parameter, since the phase values are cyclic with 2π and the amplitudes kept converging to values in the vicinity of one. As weighting factors $w_M = 4$, $w_A = 1$ and $w_P = 1$ were used. The algorithm was not limited in function evaluations, but only through the default parameters that define, what constitutes a minimum. This time the search algorithm would lead to better values in uniformity with $std_P < 1\,\%$, $std_A < 1\,\%$, but also lower diffraction efficiency $\approx 88\,\%$. It lead to a spread of results, depending on the random starting point of the variables.

Since the NMA is a downhill procedure, it is prone to get stuck in local minima. Other

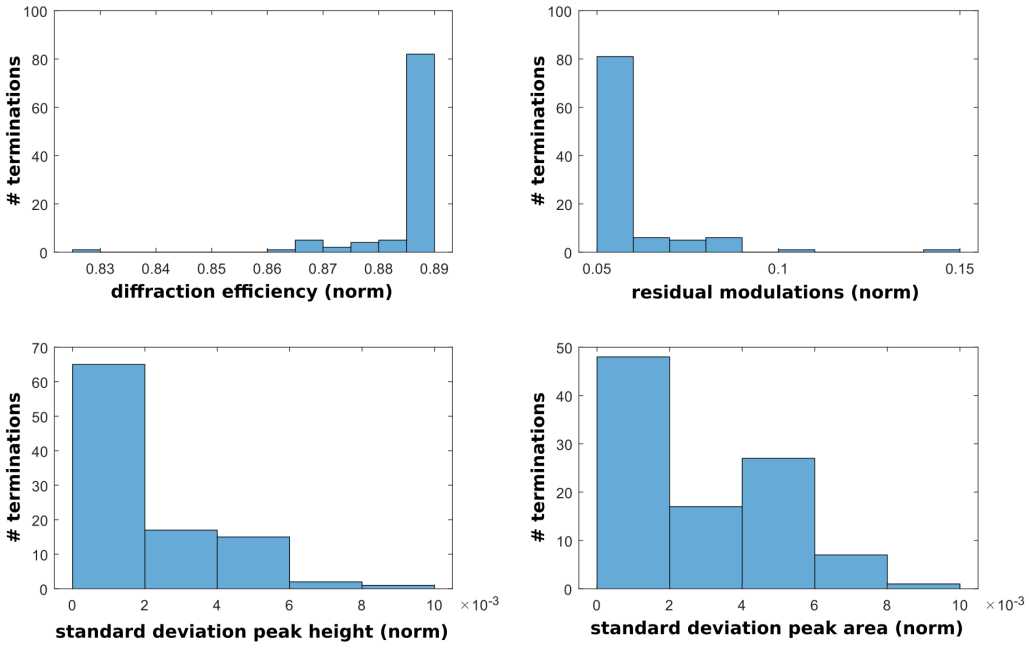

Figure 5.3.: With the new target function, the NMA leads to good uniformity. The algorithm terminates in a spectrum of values with $7\,\%$ spread in diffraction efficiency, dependent on the random starting parameters.

search algorithms are better suited to find global extrema in a given search space. This might increase the diffraction efficiency further and lead to more consistent results. For this idea, a combination of a genetic algorithm (GA) and pattern search algorithm, also standard options in Matlab, were used. The genetic algorithm takes a population of vectors $\vec{x_i} = (\phi_{m,i}, A_{m,i})$ as starting points in the search space. Again, the random starting values for the phases ϕ_i were between 0 and 2π and the starting values for the amplitudes were $A_m = 1$. In each generation, the performance of all $\vec{x_i}$ is evaluated by looking at the value $f_{min}(\vec{x_i})$. Then, a set of heredity operators combines the population $\vec{x_i}$ dependent on their performance into a new generation $\vec{x_i}'$, while always transitioning the best performing vectors unaltered to the new generation. These hereditary operators can include averaging of two $\vec{x_i}$, random mutations of any $\phi_{m,i}, A_{m,i}$ and other operations. This procedure is likely to explore a much larger area of the search space before going into a local minimum. As second step, the pattern search algorithm is again a downhill search algorithm, comparable to the NMA. It was not chosen due to better expected performance, but because Matlab offered a practical application of both search algorithms in succession.

The performance of the GA is shown in Figure 5.4. The parameters for the genetic algo-

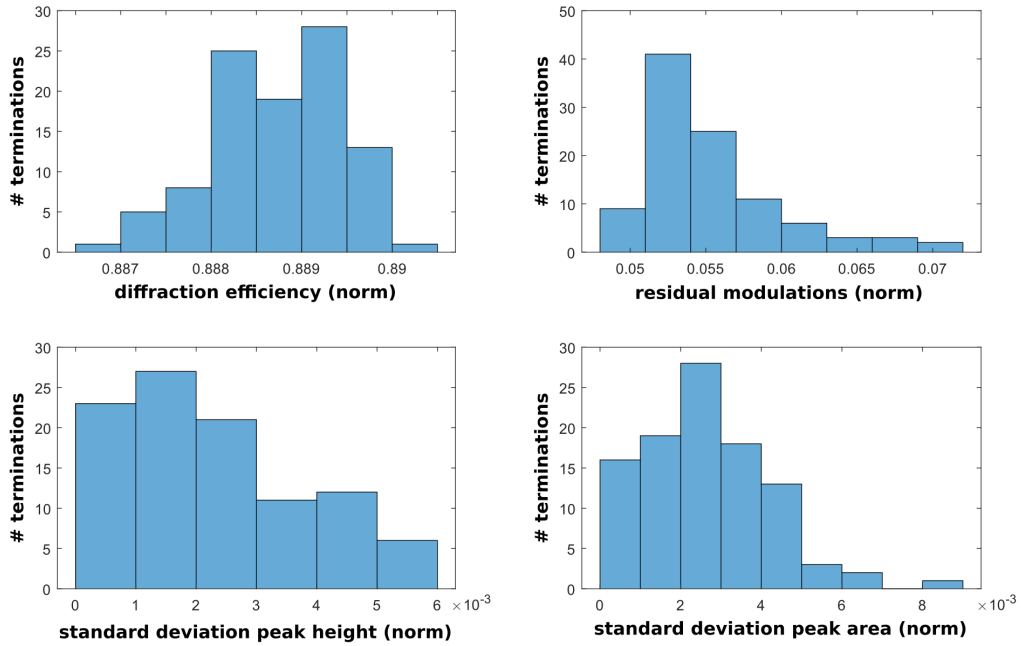

Figure 5.4.: The genetic algorithm, combined with the pattern search algorithm, shows similar results to the NMA. A population size of 2000 random starting parameter sets $\vec{x_i}$ was combined with 30 iterations for both algorithms, since this number of iterations was high enough to terminate in local minima of f_{min}. However, in contrast to the NMA, all terminations are consistently tighter grouped around the maxima in the spectra of the NMA.

rithm were a population size of 2000 individuals and 30 generations. The pattern search was allowed to run for an additional 30 iterations. The spread in η_D reduced, while the spread in uniformity kept similar ranges. The residual modulations decreased further, with a narrower distribution around $M_{r,norm} \approx 5.3\,\%$. It seems like the algorithm converges more consistently to the maxima in the spectra produced by the NMA. As a general note, comparing the diffraction efficiency η_D with the residual interference showed that there is a strong correlation, but not a direct linear relationship. This strengthens the argument that the residual modulations also lead to beam aberrations.

5.2. Gerchberg Saxton algorithm

The second algorithm for beam-multiplexing was found in the field of optical tweezers. There, researchers have an interest to create and control the position and strength of multiple optical traps. A widespread algorithm is the Gerchberg-Saxton algorithm (GSA) and an implementation according to Di Leonardo, Ianni, and Ruocco (2007) [51] was recommended by researchers with considerable amount of experience in the field of optical trapping (Prof. Alexander Jesacher and Prof. Gregor Thalhammer, Institut für Biomedizinische Physik, Innsbruck).

5.2.1. Algorithm

The main goal of the algorithm is finding a set of phase values for the SLM pixels ϕ_j that maximizes a set of energy fluxes I_m belonging to a grid of points x_m in the focal plane (Figure 5.5). For this, it is assumed that the SLM has uniform illumination by a plane wave. The Fourier transform property of a lens, written as discrete Fourier transform (DFT), is used to derive the energy flux $I_m = |V_m|^2$ through an area of size $f^2\lambda^2/(Nd)$ in the focal plane. Here, N is the number of SLM pixels, d is the pixel side length, f is the focal length of the lens and λ is the wavelength of light.

Instead of just maximizing $\sum |V_m|$, a weighted sum $\sum w_m|V_m|$ is maximized[51]. The sum is differentiated with regard to ϕ_j to arrive at an expression that connects the values of V_m to a set of ϕ_j.

$$\phi_j = arg\left[\sum_m e^{i\Delta_m^j}\frac{w_m V_m}{|V_m|}\right] \tag{5.11}$$

Here, $e^{i\Delta_m^j}$ is a phase factor calculated from the locations of the pixels x_j, y_j and the target locations x_m. Then, an iterative procedure starts with a set of ϕ_j creating a first set of V_m. This set can be chosen at random or by other methods. Then, the weights are adapted in each iteration in order to reduce the distance of $|V_m|$ from the average $< |V_m| >$[51]. This procedure was implemented and converged to phase profiles with typically $\eta_D = 93\,\%$ and almost perfect uniformity. To explain why these phase profiles also lead to a conservation of beam parameters, a reasoning analogous to the previous section can be followed. Maximizing the energy flux in a small number of points approximates a Dirac comb. Multiplication with a Dirac comb is equivalent to a convolution in frequency space. This in turn is equivalent to creating copies of the original beam spectrum centered around the spatial

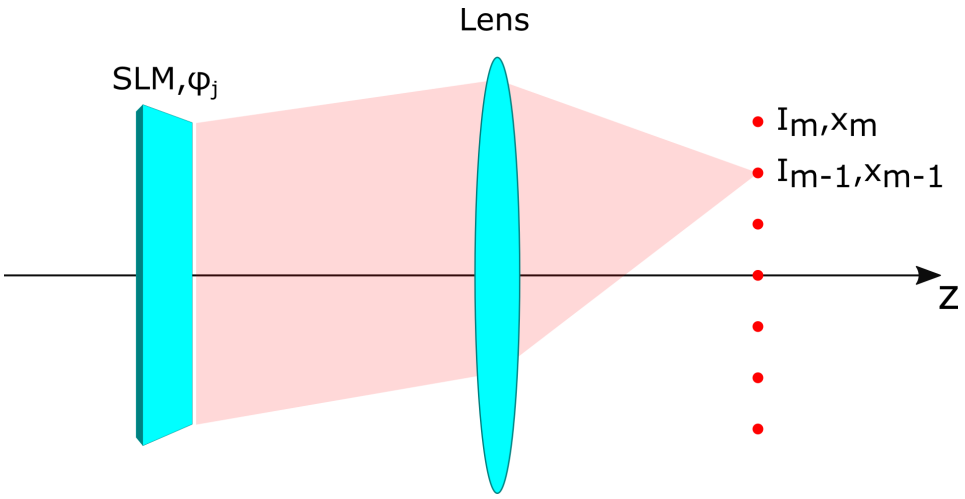

Figure 5.5.: An SLM is used to maximize the energy fluxes I_m through the areas around a set of points x_m in the focal plane of a lens. Di Leonardo, Ianni, and Ruocco (2007) [51] compared multiple methods of finding an optimum set of ϕ_j, showing that their version of the GSA, the weighted Gerchberg-Saxton algorithm (GSW), is able to reach high values of diffraction efficiency η_D and a low standard deviation between individual I_m.

frequencies $\nu_{x,n} = \frac{x_n}{\lambda f}$ and $\nu_{y,m} = \frac{y_m}{\lambda f}$. In the small angle approximation, this again is a series of beams traveling at different angles with conserved spectral shape, analogous to the fan-out algorithm (FOA). Now, we can compare both the weighted Gerchberg-Saxton algorithm (GSW) and FOA and analyze their suitability for STED microscopy. Here, we will look at theoretical predictions with the help of the fast focus calculation (FFC). In chapter 9.2 we will follow up by inspecting the behavior in an actual experiment.

5.3. Resulting field geometries

To get a performance estimate of the FOA and the GSW, the focal fields of arrays of STED beams were calculated with the FFC. The values for the diffraction efficiency η_D, the uniformity std_A and the normalized residual center intensities $I_{res,norm}$ can be extracted from these calculations. For a direct comparison, a five-by-five beam array with $6\,\mu m$ spacing in the sample plane was calculated with the GSW and FOA. Figure 5.6 shows a Matlab plot of the pattern. However, since the optical impression is identical, only one of the patterns is shown. The values for the uniformity are good for both approaches with $std_{A,GSW} = 3.2 \times 10^{-3}$ and $std_{A,FOA} = 2.8 \times 10^{-4}$. However, the diffraction efficiency differs by a significant amount with $\eta_{D,GSW} = 90.16\,\%$ and $\eta_{D,FOA} = 76.47\,\%$. Figure 5.7

shows that each beamlet calculated by the GSW has $\approx 15\,\%$ more intensity. However, there is a slight difference in the residual center intensities $I_{res,FOA} = 2.78 \times 10^{-6}$ and $I_{res,GSW} = 4.57 \times 10^{-6}$. As discussed in chapter 4.2.3, Galiani et al. (2012) [32] showed significant reductions in SNR only for values of $I_{res} > 1 \times 10^{-3}$. For all intents and purposes, the beam quality is therefore sufficiently good for both methods.

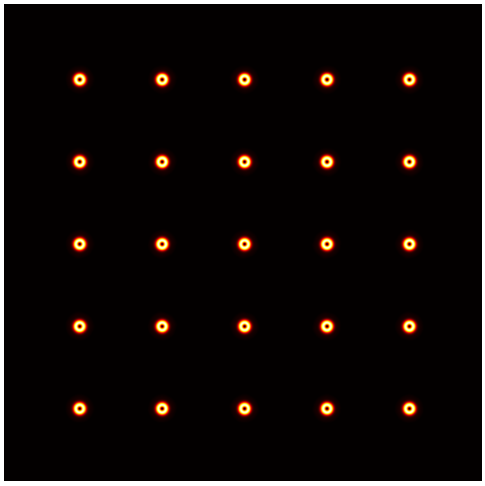

Figure 5.6.: Focal plane intensity as calculated through FFC for a five by five beam array with $6\,\mu$m spacing. The uniformity across the main beamlets is better $> 99.6\,\%$. The optical impression of the image is equivalent for both FOA or GSW calculations, therefore only one plot is depicted.

If the spacing Δx between the beams is decreased, at some point the PSFs of the beamlets will start to overlap. This will degrade the quality of the central minimum and poses a limit on the number of beams in a given area. Figure 5.8 a) shows, how $I_{res,norm}$ increases with decreasing distance at a five-by-five GSW pattern. The residual center intensity $I_{res,norm}$ is again calculated in relation to the maximum crest height of the respective order. We can see that the orders show an overlap when the distance Δx is below $5\,\mu$m. The beams can be brought closer together, with a $I_{res,norm}$ still acceptable, but Figure 5.8 b) highlights, how for small distances Δx (here $1.5\,\mu$m) the beams become increasingly asymmetric and the uniformity across the array decreases. The FFC also revealed that in general a combination of beam imperfections from different sources, like beam shape, polarization and overlap with neighboring orders, has a non-linear influence on the central minimum. It is therefore prudent to keep all different contributions as low as possible.

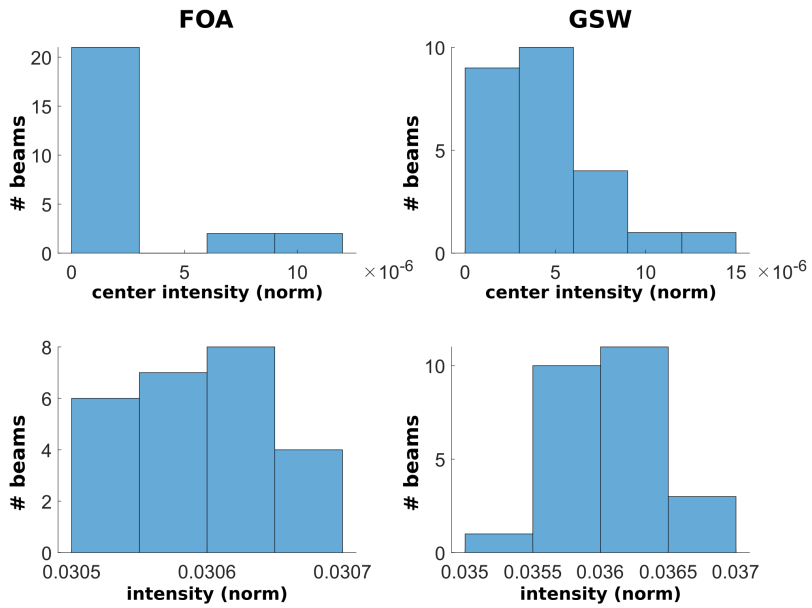

Figure 5.7.: Performance difference between phase profiles calculated with the FOA and GSW algorithms. The plot is based on a five by five beam pattern with a spacing of $6\,\mu m$ in the focal plane. The upper panels show the residual center intensities across the 25 STED beamlets, while the lower panels show the percentage of laser intensity.

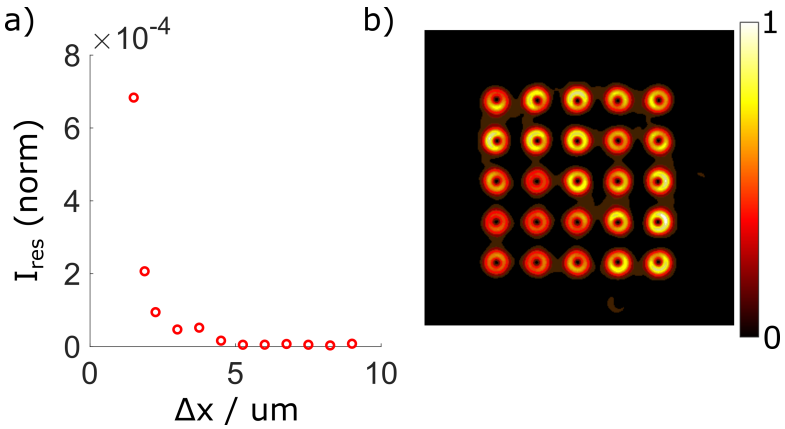

Figure 5.8.: a) shows a Matlab plot of the mean center value of a five-by-five beam array as created with the GSW and calculated with the FFC. The distance between the orders Δx is decreased until they start to overlap. In b) we can see, how for small Δx (here $1.5\,\mu m$) also the uniformity and beam symmetry decreases. A minimum of about $\Delta x = 5\,\mu m$ still guarantees a negligible influence.

6. Hardware devices and control

After delving into optical considerations centered around the spatial light modulator (SLM), the focus will now shift towards other key components of hardware in the microscope. The chapter discusses all confocal scanning hardware, laser synchronization as well as detector modules. Excluded from the discussion for now is the field programmable gate array (FPGA), since the scope of its VHDL module warrants a separate chapter.

6.1. Sample scanning

A sample is mounted in the microscope on a three-level tower. It consists of a ground level containing scanning mirrors, a second level containing two manual stages as well as a top level containing a piezo electric scanning stage (Figure 6.1).

6.1.1. Manual stages

The lateral stage (model number M-545.2MO, Physik Instrumente (PI)) allows for coarse sample positioning in a plane perpendicular to the optical axis. It features two manual micrometer actuators with a range of $25\,\mathrm{mm}$ for each spatial direction. For tilt and displacement control along the optical axis, a second manual stage was designed in Autodesk Inventor and manufactured by the mechanical workshop of the university. It has three adjustment screws, with steel ball tips and direction parallel to the optical axis, placed in a big equilateral triangle (as indicated in Figure 6.1). Each steel ball tip is in contact with the supporting platform in a notch, a rail and a plate, respectively. This configuration was designed to allow for quick removal of the upper two tower levels for alignment and cleaning purposes, with good positional repeat-ability and thermal stability. Any thermal expansion will lead to an increased distance between the three alignment screws. Since one of the steel ball tips can move along a rail, where the rail direction is along the center of the triangle, and another steel ball tip can move freely across a plate, the stage has a well-defined position for any given temperature. In contrast, a support with three notches could

not compensate for relative thermal drift and after thermal expansion it could not provide a stable position of the screw tips in these notches. As an application note, it should be mentioned that the manual stages and the scanning stage are quite heavy. For secure manual removal of the positioning stages, first the tilt stage should be lifted at the steel plate, then the rail and finally the notch. The same procedure should be run in reverse, when again placing the stages to guarantee a controlled descent.

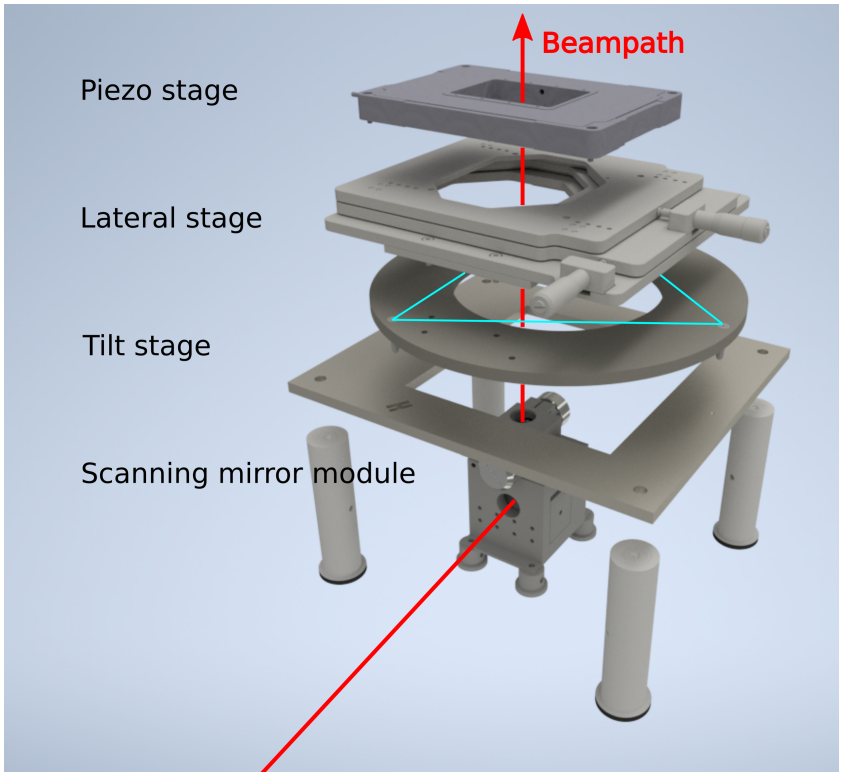

Figure 6.1.: The sample tower in an exploded view, where different parts have been vertically displaced for better overview. The sample is mounted in the opening of the piezo stage. Two manual stages are used for coarse adjustment of the sample tilt and position in relation to the optical axis. On the tilt stage, an equilateral triangle indicates the alignment screws on which the stage rests. Four scanning mirrors are mounted in the lowest module, enabling fast confocal scanning. (CAD models of the piezo and lateral translation stages from Physik Instrumente Karlsruhe, CAD models of the optical posts from www.thorlabs.com, illustrated with help of Autodesk Inventor).

6.1.2. Piezo stage

The scanning stage was also bought from Physik Instrumente (PI) in Karlsruhe (model number P-545.3R8S). It features piezo electric motors that can move a sample in a cubic volume of $200\,\mu m$ x $200\,\mu m$ x $200\,\mu m$. Since typical cell diameters are on the order of $10\,\mu m$, this allows to explore a large sample volume possibly containing many specimens. The position can be controlled in a closed-loop with the help of internal piezo-resistive sensors with an accuracy of $1\,nm$, according to the data sheet of Physik Instrumente (PI). However, measurements show that unfortunately the attached controller (model number E-727.3RDA, PI) cannot deliver this maximum accuracy. The position of the stage has a peak-to-peak value for the positional noise of $10\,nm$ in the x and y directions and $20\,nm$ in the z direction. Compared to the scanning mirrors with scan frequencies exceeding $300\,Hz$, the piezo stage has a large inertia, leading to maximum scan frequencies of $\approx 10\,Hz$ for small scanning volumes. This leads to image acquisition times for stimulated emission depletion (STED) images in the range of minutes. The position readout of the stage is used to calibrate image acquisition ranges with the scanning mirrors. Since the stage features a large scanning volume, it can be used to move the sample between consecutive mirror scans enabling fully automatic volume scans with decent speed. The controller is connected to the PC via USB 3.0 interface. A library of Python functions is available for this controller and enables embedding the stage control in the microscope software. Simple movement commands can be sent as direct USB commands, while the stage movement during image acquisition has to be controlled through internal wave tables containing the position information for each scan. An internal oscillator iterates through the wave table content during the scan and sends out the corresponding control voltages to the stage. The wave table contents can be created through embedded functions of the provided Python library or controlled directly by transferring wave forms created as tables in Python. The latter option allows for more control of the scan movement, since the embedded functions are somewhat limited. During the scan, the position sensors are used to create trigger signals as voltage outputs. These are connected to physical inputs of the FPGA to synchronize the stage movement with the data acquisition module on the FPGA, which writes the pixel information for each image. Here, the synchronization scheme is per pixel and for each pixel that should be written a single square voltage pulse is emitted. However, during measurements it became apparent that the position sensor readout arrives with a significant time delay in the detection module. This leads to a shift between image lines, since the position sensitive trigger signal activates too late and the stage has already moved past its intended position for any given pixel. After this became apparent, the calculation of the stage wave forms was re-written in terms of scanning speed v_{scan} in the linear part of the waveform. It was suspected that the readout time of the sensors and the processing speed inside the controller should not depend on

the stage scanning speed and lead to a constant time lag τ_{lag} of the trigger signals. The spatial offset Δx_{offset} between the lines then would have a relation ship:

$$\Delta x_{offset} = v_{scan}\tau_{lag} \tag{6.1}$$

A sample of gold beads was used as reference to determine experimentally whether this assessment is correct, but this relationship could not be verified. Discussions with the manufacturer (Physik Instrumente, Karlsruhe) were not able to determine the source of this behavior. Although the reason for this discrepancy still is unknown, a work-around exists. For a given parameter set, the lag can be determined by splitting an point spread function (PSF) image, as reflected by a single gold bead, into even and odd image lines and fitting a Gaussian intensity profile to each line set. The distance between the peak positions is then twice the lag distance. Since it is common to only use a small number of parameter sets for illumination time, pixel size and scan area, this method is feasible and can be used until the source of this problem is found.

6.1.3. Scanning mirrors

The scanning mirrors devices were bought from SCANLAB GmbH München (2x model dynAXIS S Type 1&2). The devices, depicted in silver in Figure 6.7, consist of an electric motor that has an octagonal mirror glued into a crevice at the end of its axis. Each motor is connected with a cable to its own amplifier board (SCANLAB GmbH München, model SSV30). The outer dimensions of the mirror type 1 are $18.4\,\mathrm{mm}$ by $10.7\,\mathrm{mm}$, while the dimensions of type 2 are $15.9\,\mathrm{mm}$ by $21.7\,\mathrm{mm}$. Here, the first number is the width perpendicular to the rotation axis and the second number the length along the axis. The choice for this set of mirrors was a combination of price, maximum scan speed, surface size and surface quality. The maximum controller scan range is $\pm 23.4°$ for a control voltage of $\pm 4.8\,\mathrm{V}$, while the maximum mirror scan range is limited to $\pm 12°$.

Ray tracing

As described previously (Figure 2.3), the movement during beam scanning corresponds to a tilt of the beam in the back-focal plane of the microscope objective. Two of the mirrors are responsible for beam movements in the xz and yz planes, corresponding to movements of the confocal volume in the directions x and y in the focal plane, respectively. To calculate the mirror positions and their movement during scanning, ray tracing was used. With the

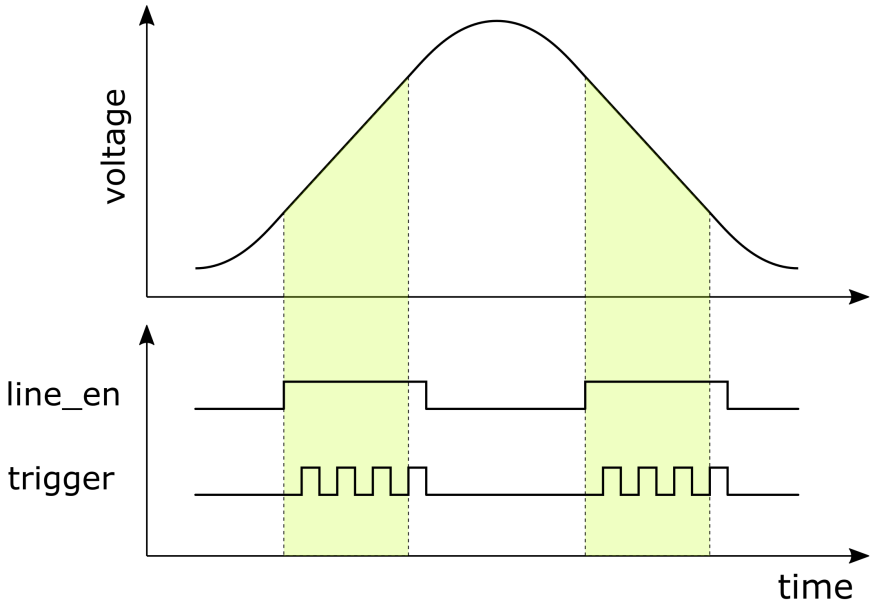

Figure 6.2.: Wave function for stage scanning. The upper panel shows the voltage profile for the fast scan axis during a stage scan. This corresponds to the scan of two lines in the image. The lower panel shows the synchronization signals connected to the data acquisition module in the FPGA. As soon as the stage moves in the linear part of the wave form, the signal **line_en** goes high and enables counting of photons. At each rising flanc of the **trigger**, the number of counted photons is stored in a pixel. After each line the photon counter resets.

help of the matrices from Mansell (2006) [52], the beam position and angle was determined on all mirrors and the back focal plane. This was part of the master thesis of Michael Volk[53]. Since only mirrors with flat surfaces are used in the calculations, the formulas are straightforward. The laser beam is defined through a starting position P_0 and travel direction $\mathbf{e}_0$ in Cartesian coordinates. Similarly, all mirrors and the back-focal plane are defined by a center point C_i and a surface normal $\mathbf{n}_i$. Then, the laser beam path is determined in an iterative manner with following formulas:

$$P_{i+1} = P_i + \left(-\frac{\mathbf{n}_{i+1} \cdot (P_i - C_{i+1})}{\mathbf{n}_{i+1} \cdot \mathbf{e}_i} \right) \cdot \mathbf{e}_i \tag{6.2}$$

$$\mathbf{e}_{i+1} = \mathbf{e}_i - 2(\mathbf{e}_i \cdot \mathbf{n}_{i+1})\mathbf{n}_{i+1} \tag{6.3}$$

$$bw_i = \sqrt{(P_i - C_i)^2} \tag{6.4}$$

The last equation defines the beam-walk bw_i as absolute distance of a ray intersection point from a mirror center. These formulas arise from geometric considerations depicted in Figure 6.3. It should be noted that Mansell (2006) [52] contains an error in the formula for the reflection of the direction. A matrix can be used to project global coordinate points onto the local coordinate system on each mirror surface. To construct this matrix, the axes of the local coordinate system $\mathbf{e}_{x/y/z,loc}$ are defined relative to the global coordinate axes $\mathbf{e}_{x/y/z,glo}$ and the surface normal of the mirror $\mathbf{n}$.

$$\mathbf{e}_{x,loc} = \mathbf{n},\ \mathbf{e}_{y,loc} = \mathbf{n} \times \mathbf{e}_{z,glo},\ \mathbf{e}_{z,loc} = \mathbf{e}_{x,loc} \times \mathbf{e}_{y,loc} \tag{6.5}$$

From this the transformation matrix M_T can be written as:

$$M_T = (\mathbf{e}_{x,loc}, \mathbf{e}_{y,loc}, \mathbf{e}_{z,loc}) \tag{6.6}$$

Only contributions along $\mathbf{e}_{y,loc}$ and $\mathbf{e}_{z,loc}$ are needed to describe offsets of beam contact points, therefore the matrix can be deprecated by removing its first row.

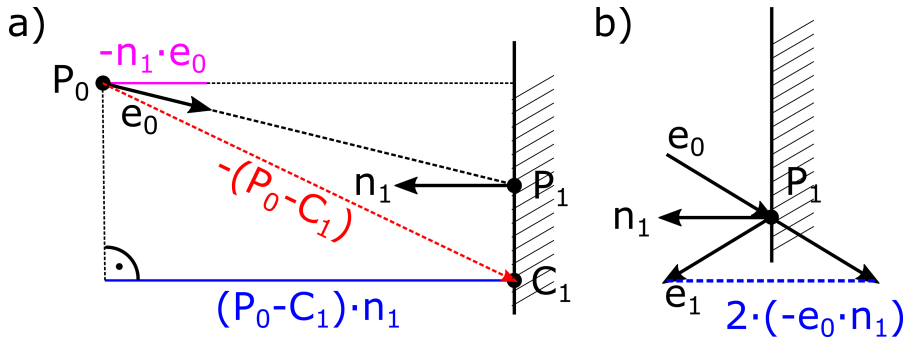

Figure 6.3.: The sketch indicates how to calculate the new position (a) and direction (b) of the beam, when it is reflected at a mirror surface.

Geometric mirror model

The formulas listed in the last section were used to define a function that propagates a beam of light through all 4 scanning mirrors into the back-focal plane in an iterative

procedure (Figure 6.4). The parameter input to the function are the five parameter sets C_i, $\mathbf{n}_i$ of the mirrors and the back-focal plane. Since two mirrors each have parallel scan axes that are perpendicular to the other two mirrors, and the direction of the scan axes are given by one of the global axes, the surface normal of each mirror can simply be defined by an angle α_i. Starting from $\mathbf{e}_{x,glo}$ the angles $\alpha_{1/2}$ are clockwise around the y-axis, while $\alpha_{3/4}$ are clockwise around the z-axis. When a ray of light starts along the axis defined by $\mathbf{e}_{x,glo}$, it should encounter all four mirrors at an $45°$ angle to reach the middle of the back-focal plane. This is used as reference and all α_i are defined by the scan angles δ_i of the mirrors, which are deviations from this reference.

$$\alpha_1 = 135° + \delta_1,\ \alpha_2 = 315° + \delta_2,\ \alpha_3 = 135° + \delta_3,\ \alpha_4 = 315° + \delta_4 \tag{6.7}$$

Each mirror is $\approx 2\,\text{mm}$ thick with a rotation axis parallel to the surfaces through the center. Therefore, each surface has a distance of $\approx 1\,\text{mm}$ from its rotation axis. This has to be included in the calculations, since each mirror midpoint then is dependent on the current scanning angle. To arrive at a set of scanning angles that belong to a desired focal point position, a minimization routine was used. Since the focal length of the objective is $3\,\text{mm}$, a desired position can be translated into an angle α_{bf} in the back-focal plane by:

$$\alpha_{bf,y,target} = \arctan(y/3\,\text{mm}),\ \alpha_{bf,z,target} = \arctan(z/3\,\text{mm}) \tag{6.8}$$

Now, the target set δ_{1-4} minimizes the beam-walk bw_5 on the back-focal plane, and it also minimizes the deviation of the ray angles at the back-focal plane $\alpha_{bf,y}$ and $\alpha_{bf,z}$ to their target values. At the start, the goal was to specify a y-value and z-value range and attain a set of δ_i for each value. However, it turned out later that the scanning angles show a strictly linear relation in the desired angle range and the calculation could be simplified by using the calculated linear coefficients.

Spatial positioning and scanning angles

After constructing the underlying geometry, it was important to find a spatial positioning of the mirrors that should be used in the experiment. For this, multiple requirements should be mentioned. Firstly, the distance to the back-focal plane of all scanning mirrors should be kept small. Long distances will lead to larger beam-walks on the mirrors and at some

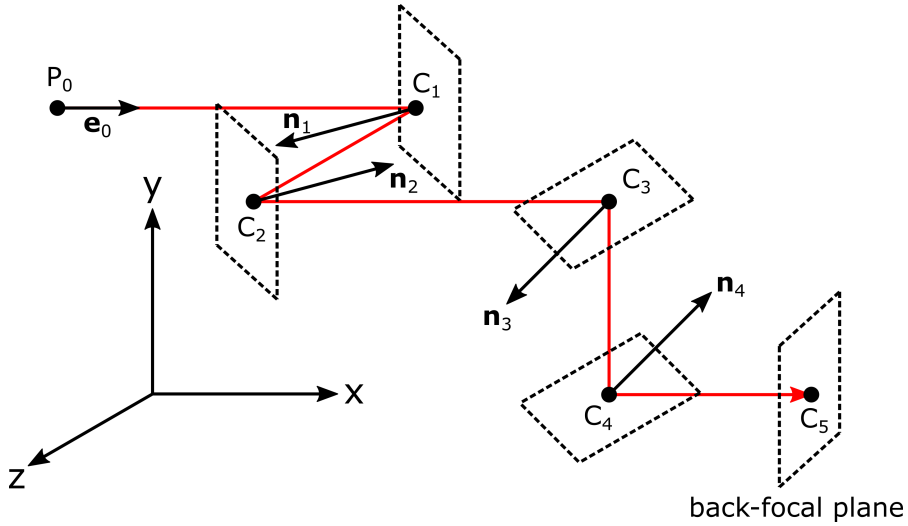

Figure 6.4.: The image shows a sketch of ray propagation through the mirror module when all mirrors are in their center position. At each mirror, an intersection point is calculated and the surface normal is used to determine the new propagation direction.

point to beam-clipping. Secondly, for multi-beam scanning the bundle of beams will be converging, and it needs to fit on the mirrors. Lastly, there is a minimal distance given by the geometry of the mirrors and mirror motors. While being moved in the accessible scan range, they should not touch each other. Keeping these boundaries in consideration, the final chosen spacing of the distances became $d_{P_0,C_1} = 100\,\text{mm}$, $d_{C_1,C_2} = 13\,\text{mm}$, $d_{C_2,C_3} = 15\,\text{mm}$, $d_{C_3,C_4} = 13\,\text{mm}$ and $d_{C_4,C_5} = 59\,\text{mm}$. In total, they add up to the length of $20\,\text{cm}$, which is the focal length of the last 4-f telescope lens (chapter 3.1, chapter 9.2) placed at P_0. These values were chosen as close as possible to the aforementioned requirements with a wiggle room of $1\,\text{mm}$ for the beam walk of the laser bundle on the first mirror and $1\,\text{mm}$ space between the mirror edges in the configuration. This was a personal choice intended to provide a sufficient safety margin during manual assembly of the module. To better visualize the Gaussian beams on the mirror surfaces, they were plotted in relation to the mirror dimensions using 3σ radius (Figure 6.5). The figure shows all beam projections calculated for maximum scan angles in single and multi-beam imaging. For single beam applications, the maximum target scan range per spatial direction was desired to be $60\,\mu\text{m}$. When displacing the confocal volume by $30\,\mu\text{m}$ in both spatial directions, the maximum scan angles will be reached. The maximum scan angles, as calculated by the described minimization routine, are then $\delta_{1,max} = 1.92°$, $\delta_{2,max} = 2.20°$, $\delta_{3,max} = 1.30°$ and $\delta_{4,max} = 1.58°$. For multi-beam imaging a smaller angle range is used, since for large beam angles the diffraction efficiency falls and the beam quality degrades. A distance of $21\,\mu\text{m}$ from the

optical axis for the outer beams of a 7 by 7 beam array was used as a maximum estimate for each spatial direction (chapter 9.2, chapter 9.1). The total scan range per beamlet and direction then is $7\,\mu m$, filling the whole scan area spanned by the beam bundle.

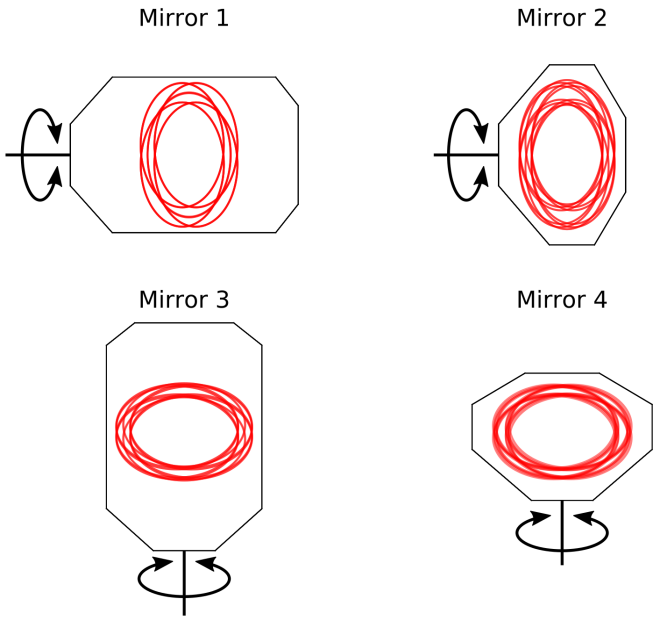

Figure 6.5.: Calculation of laser beam projected onto the four octagonal scanning mirrors. Each ellipse corresponds to the circle of intensity that encloses 99% laser power (3σ radius). The ellipses correspond to the overlap of all maximum and minimum scanning angles for single and multi-beam scanning.

Performance tests

The amplifier boards contain electrical test points that provide a position signal as analog output. Conveniently, they feature a one-to-one correspondence with the control voltages. To test the performance of the mirror motors, a standard laboratory power supply was used as power source and a function generator was connected to the signal input. An oscilloscope was used to compare the control voltage signal with the position voltage signal. As expected for a dampened oscillator, the position signal had a frequency-dependent phase shift. Since the inertia of the mirror acts as a mechanical low pass filter, the position signal showed reduced amplitude for higher frequencies, when getting closer to the specified maximum frequency of $1\,kHz$. Since the module is not shipped with a cooling unit, the tests had to be confined to a few quick measurements preventing overheating. Later custom

water cooling was added, as described in the next section. The conclusion of these tests and following discussions with the manufacturer were that prolonged usage without active cooling should be limited to frequencies < 100 Hz and that for scanning frequencies above 300 Hz the amplitude modulation has to be considered for scanning operation and possibly compensated. Since the mirrors swing in frequencies in the audible range, saw-tooth and rectangular control voltages lead to noises. This behavior later proved useful as control mechanism to debug control signal shapes that had unintended voltage jumps.

Mirror mounting

In a first iteration, a mount for the mirrors was designed and manufactured from a single piece of black anodized aluminum. This version included a chamber with anti-reflection-coated windows, an internal Nitrogen atmosphere and water cooling channels. The design was intended to keep the mirrors dust-free and the mirror motors cooled. However, there were several drawbacks with this design that became apparent when used. Firstly, the chamber windows were not considered harmful for fluorescent measurements, since any back-reflection of the lasers at this additional surface would get filtered out in the detection. However, in the experiment they lead to a significant background in reflective measurements of gold beads that were needed for alignment (chapter 3.3.8). Here, the detection filters could not be present and the background was so high that fine alignment and PSF monitoring on single gold beads was not possible. Secondly, the motor mounting in this design consisted of a clamping block, pushing the motor against the inside of a cylindrical cutout. This limited the thermal contact surface to roughly half of the maximum contact surface. Although several contact materials from Panasonic were tried to increase the heat flow (Figure 6.6), this lead to sub-optimal cooling. Lastly, the cooling path was constructed with several drill holes, which had to be sealed later. Even after using recommended sealing products, these drill holes proved to be prone to leakage.

In a second iteration, the water cooling was simplified to a single drill hole on each side (Figure 6.7). This creates closed coolant paths connected to a water supply with sealing ring connectors (RIEGLER & Co. KG, P/N 122.006-6M). Instead of creating a Nitrogen atmosphere to keep the mirrors clean, the chamber now can be opened without changing any alignment, allowing for easy cleaning access. The clamps were redesigned to encircle each motor, leading to better thermal contact. The earlier test of thermal contact materials from Panasonic were used as basis to choose a contact sheet material that is taped on the motors before mounting in said clamps (Panasonic Graphite Sheet PGS, thickness $50\,\mu$m, $30\,\mu$m polymer adhesive, article number EYG-A091205A). According to SCANLAB specifications, the mirror motors need to be electrically insulated when mounted. This

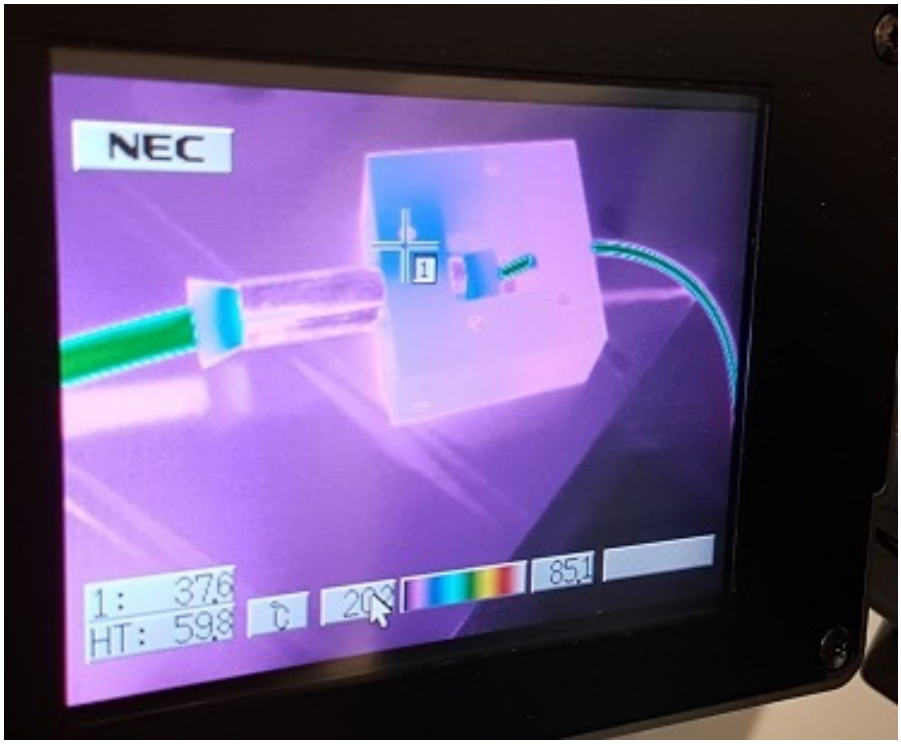

Figure 6.6.: Heat flow as measured in the rectangular mirror mounting block: boiling water is running through a pipe with the mirror motor dimensions (left to right). The heat flow is measured with a thermal camera and shows the asymmetric heat flow originating from the first mounting design where only one side of the motor had good thermal contact with the module.

composite material features good thermal conductivity and is an electrical insulator (conduction direction normal to the sheet). Below the mounting block of the motorized mirrors is a slider with a 45° mirror. This slider can either be removed to allow the laser beam to pass the module entirely or be replaced by a slider containing mounts for alignment optics. Four precision cut brass rails guide these sliders, leading to a good positional repeatability during exchanges. In this way the microscope objective can stay in place when re-aligning laser beams onto the module.

6.1.4. Voltage control of scanning mirrors

Analogous to stage scanning (Figure 6.2), each mirror gets controlled by a voltage waveform. To translate the digital waveform stored in the FPGA into a voltage signal, a digital-to-analogue converter (DAC) is used. The control voltage inputs of each amplifier board

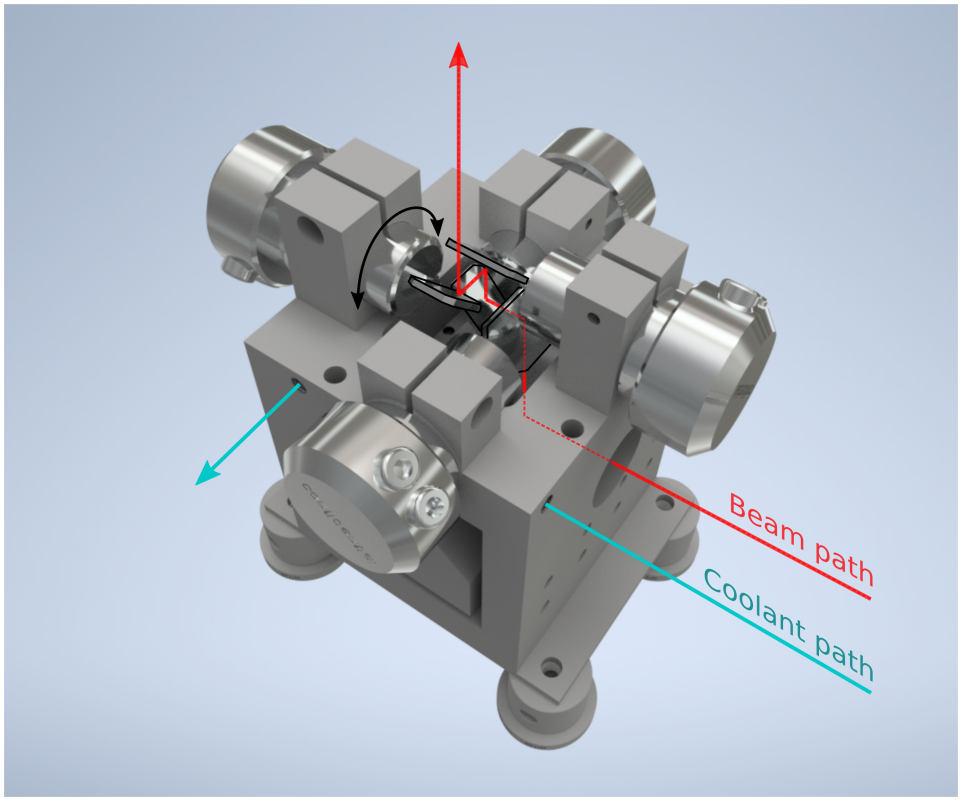

Figure 6.7.: Open view on the improved mirror module. For clarification the cap with the objective mount has been removed. After passing through the mirror block, the beam path will reach the microscope objective.

are connected to a DAC (Type: 7654, Texas Instruments Incorporated). The DAC itself is an integrated circuit (IC) that sits on the evaluation module (EVM) (Type: 7654 EVM, Texas Instruments Incorporated). It features four voltage output channels configured for an output of $-2.5\,\mathrm{V}$ to $2.5\,\mathrm{V}$ with 16-bit accuracy. The EVM is placed on a bigger circuit board. There, each output gets transformed by an IC (Type: LT6350, Analog Devices Inc.) to provide a differential output signal. Configurable voltage dividers, intended for scaling, are added. To achieve a clean and noise-free control signal, the board was connected to a high quality power supply (Type: A5TN110-230, Acopian Technical Company). The total resistance of the voltage dividers is $10\,\mathrm{k\Omega}$, leading to roughly $2\,\mathrm{k\Omega}$ output resistance. A high output resistance is important in order to limit the current flow at the output and maintain voltage stability.

Resistor noise/Bit noise

The resistor at the output is leading to an additional thermal noise N_{therm}. The root mean square (RMS) value of the noise $N_{therm,rms}$ can be calculated from:

$$N_{therm,rms} = \sqrt{4k_bTR \triangle f} \tag{6.9}$$

Here, k_b is the Boltzmann constant, T is the temperature, R is the output resistance of the device and $\triangle f$ is the frequency bandwidth of the transmitted signal. For the resistor noise we can calculate with $2\,\mathrm{k\Omega}$ output resistance, while for the bandwidth we can assume the mirrors to act as mechanical low-pass filters, effectively limiting the bandwidth. The amplitude breakdown is already starting at a frequency of $300\,\mathrm{Hz}$, and the performance tests with a frequency generator showed a significant amplitude reduction of $\approx 50\,\%$ at $1\,\mathrm{kHz}$. Although the exact form of the amplitude spectrum is not known, we use an educated guess, based on the behavior of a Butterworth low-pass filter. Since the $1\,\mathrm{kHz}$ point is already past the $-3\,dB$ point, a value of $3\,\mathrm{kHz}$ should have at least $-40\,dB$ attenuation. From this, we estimated that $3\,\mathrm{kHz}$ can surely be used as a maximum bandwidth. This leads to:

$$N_{therm,rms} = \sqrt{4 \cdot 1.3 \cdot 10^{-23}\,\mathrm{V\,A\,s\,K^{-1}} \cdot 300\,\mathrm{K} \cdot 2000\,\mathrm{V\,A^{-1}} \cdot 3000\,\mathrm{Hz}} \approx 300\,\mathrm{nV} \tag{6.10}$$

The bit noise of the DAC depends on the used maximum voltage V_{max} at the output:

$$V_{max,scan} = \frac{\delta_{max,scan}}{\delta_{max,DAC}} V_{max,DAC} = \frac{2.2^\circ}{23.4^\circ} 4.8\,\mathrm{V} \approx 0.45\,\mathrm{V} \tag{6.11}$$

Therefore, the bit noise of the 16-bit DAC is $N_{bit.} = 0.45\,\mathrm{V}/2^{16} \approx 7uV$. The resistor noise at the DAC output is therefore negligible in comparison to the bit noise. The bit noise translates to a position noise of the confocal volume of $d_{noise,bit} = 1.76\,\mathrm{nm}$.

6.2. Laser timing

The excitation and STED pulses have to arrive in short succession at the sample. For the strongest depletion, this has to be fine-tuned with a precision on the order of $\approx 10\,\mathrm{ps}$. As a reminder, the pulse width of the $774.51\,\mathrm{nm}$ STED laser is $750\,\mathrm{ps}$, while the pulse width

of both excitation lasers is 350 ps. In addition, both excitation lasers should be used in an alternating pattern. Since the fluorophore spectra of both color channels (red, yellow) are overlapping, there is residual cross talk when using both excitation lasers simultaneously. Since all three lasers feature an internal oscillator and external trigger entries, a digital solution for the timing synchronization was planned. Figure 6.8 shows the electrical interfaces of the lasers and the intended action of a delay and divider circuit board.

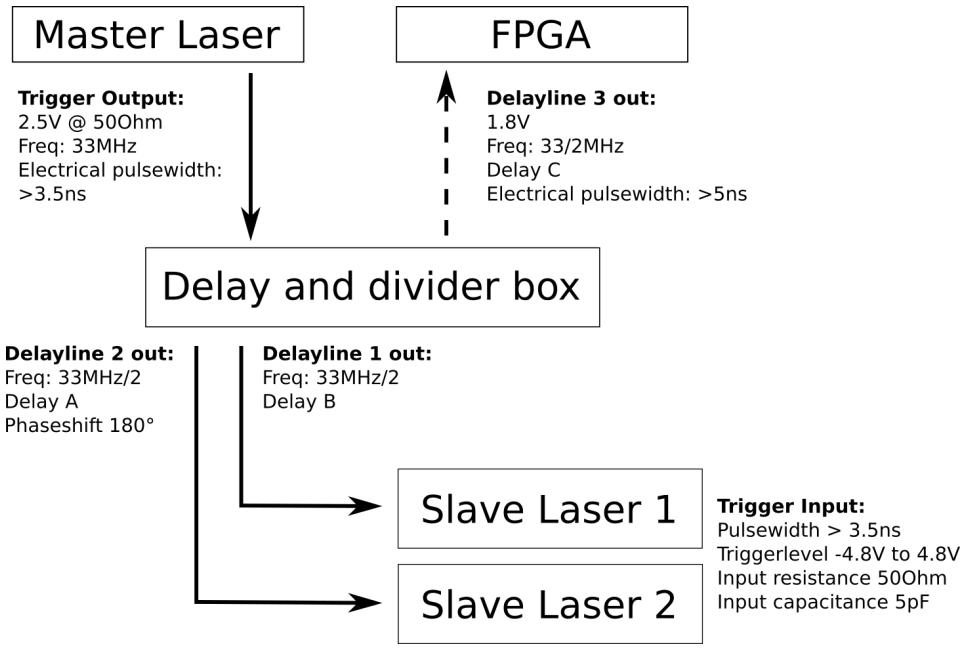

Figure 6.8.: Sketch of all input and output points for synchronization of all three lasers and the detection module in the FPGA.

The initial 30 MHz clock of the STED laser has to be divided for multi-color imaging by a factor of two, and each of the excitation lasers needs its own digital delay. In addition, a third synchronization line has to connect to the FPGA, responsible for opening the photon counters for both color channels at the right time. The main components on the board are an Arduino (Type: "Sparkfun Pro micro") and four ICs, a clock divider with three output lines (Type: LTC6954, Linear Technology Corporation) as well as three digital delay modules (Type: SY100EP195V, Microchip Technology Inc.). The Arduino is used to control the clock divider settings over a USB connection, while the digital delay is manually set by a series of mechanical switches (Figure 6.9). The electronic delay in each line can be fine-tuned between 2.1 ns and 10.8 ns with 10 ps accuracy. Since the clock frequency of the STED laser is at 30 MHz pulses have a spacing of $\delta t = 33.3$ ns. This still leaves up to a ≈ 20 ns range that cannot be covered by the digital delay module alone and has to be coarse-adjusted with the length of the connecting cables (6.2).

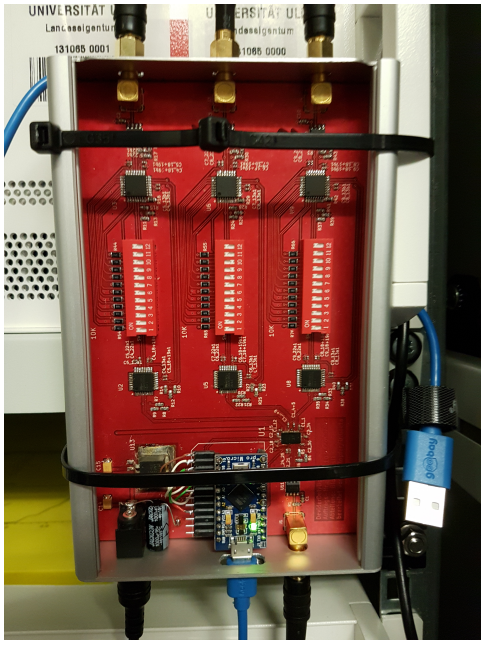

Figure 6.9.: Open view on the circuit board of the delay module. In the middle, three sets of twelve mechanical switches can be used to fine-tune each electronic delay line between 2.1 ns and 10.8 ns with 10 ps accuracy.

Timing alignment procedure

In a first step, the arrival time of the lasers is compared close to the sample, where all beams are overlapping. For this, a normal oscilloscope can be used together with a fast photo diode. The third delay line intended for the FPGA can be used as a fixed reference, in this way all lasers can be measured separately. It is sufficient to measure the flank position of the arriving laser pulses with an accuracy of ≈ 4 ns, since, as discussed previously, the delay module has a range of 8.7 ns for fine adjustment. To shift the laser pulses into this accessible range, the length of the connecting cables can be changed. A shift of 30 ns, corresponding to a cable length of 9 m, together with the shift of the delay module is enough to cover the total timing range between laser pulses. This is a cable length that will not result in any significant signal loss for this case. After this adjustment, the timing fine tuning can be performed on a fluorophore solution for either color channel. The phase vortex of the STED beam should be disabled for maximum effect and gold beads should be used before to overlap both Gaussian beams. The amount of depletion can then be measured, while changing the manual timing switches on the delay module, until a maximum is found. For precise results, it is useful to use a sufficiently high concentration of fluorophores, with enough diffusion of fresh fluorophores into the confocal volume, to prevent signal loss due

to bleaching.

6.3. Parallel acquisition

For simultaneous acquisition of multiple fluorescent volumes, a single photon array detector is needed. Arrays of single-photon avalanche diodes (SPADs) are still an active field of research, and most commercial solutions were not suitable for our experiment. Either they featured a low number of SPADs, time averaged readout, non-quadratic grid geometries or high dead-times, not usable with the 30 MHz pulse frequency of our lasers. In cooperation with Angelo Gulinatti from the SPADlab research group at the technical university Politecnico di Milano (Milano, Italy), we received a prototype SPAD array detector (section 2.5). The device was published by Ceccarelli et al. (2016) [31]. To operate the device, the chamber hosting the SPADs has to be flushed with clean Nitrogen to remove any residual moisture. This is explained in more detail in a provided manual that should be studied carefully before use. The device is connected over USB to the lab PC, and a custom software was provided that is able to read-out moisture levels and time averaged count rates on all 64 individual SPADs. After the image acquisition on the FPGA (chapter 7.5) was implemented, the device was tested in tandem with the FPGA and a typical stage scanning movement. In the first test, shown on the left in Figure 6.10, an image was acquired without light source inside a dark optical shielding box. The first channel of the data acquisition, in the top left corner, was connected to an internal oscillator as light source. All other channels are connected to their respective SPAD outputs. As can be seen, one of the middle SPADs features a higher noise. In a second test, shown on the right in Figure 6.10, an attenuated laser was guided onto the SPAD chip inside the optical box, in order to confirm that the light acquisition was working. A video was recorded during movement of the laser across the array, showing how different channels lit up. The maximum stable video rate of the detection module of the FPGA was experimentally determined to be between 20 Hz and 25 Hz. At higher imaging frequencies, the images would start to show artifacts.

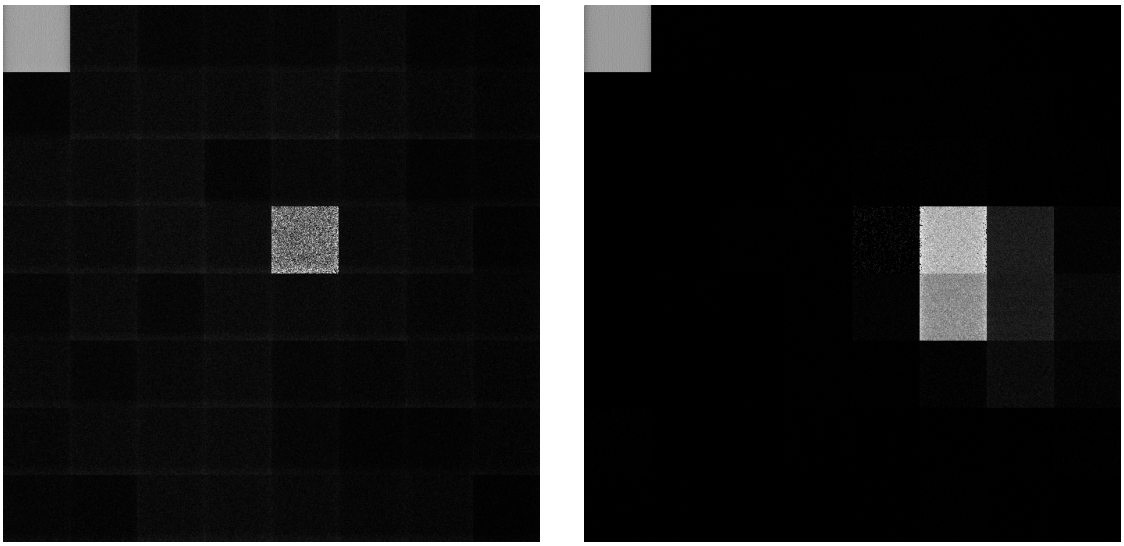

Figure 6.10.: Left: Measuring noise at the SPAD array. As reference, the first channel was driven with an internal oscillator in the FPGA. As can be seen, one of the 64 channels features a higher back-ground noise. Right: An attenuated laser is directed onto the SPAD array chip, locally triggering the active SPAD areas.

7. FPGA

Optical experiments often require components that are not accessible through standard PC interfaces. It then becomes necessary to include some kind of data acquisition/interface card that will process incoming and outgoing signals and make them usable on each end. Typically, interface cards, intended for use in microscopes, possess internal computation and synchronization resources. Common are counters that can detect and count voltage pulses from photon detectors, oscillators that can be used as a trigger source for multiple connected devices, and wave form generators used for sample scanning as described above. However, most commercial cards available today fall short of the number of physical connections or the possible scanning speed and are not necessarily compatible with standard programming languages.

In this experiment, a field programmable gate array (FPGA) is used as a powerful low-cost alternative to fulfill this role. Since it is more flexible than standard data acquisition cards, it can additionally be used for more advanced tasks. The main features implemented are fast scanning operation and image acquisition for large fields of view. The very high speed integrated circuit hardware description language (VHDL) module designed in this thesis can handle line scanning frequencies in the kHz range, while detecting the output of up to 64 single photon detectors for multi-beam scanning. It is capable of providing stable imaging speeds of up to 25 frames per second for typical scan sizes in confocal microscopy. As a result, the image acquisition speed in the experiment is foremost limited by the brightness of the fluorescent probes as well as the mechanical properties of the scanning mirrors. The VHDL module is divided into two main components, the data acquisition module and the scan controller. The data acquisition processes and stores data to provide complete images, ready for USB transfer. The scan controller receives digital wave forms via USB and is connected to the digital-to-analogue converter (DAC) that controls the four scanning mirrors. During this chapter, the reader will first be introduced to the framework of FPGA programming and its physical implementation. This is intended to build some familiarity with this rather specialized topic. Building on this introduction, all VHDL modules developed will be presented, and their structure and function will be discussed. The chapter is not simply intended to present the work that was done during this thesis, but also to act as a sort of manual for researchers considering to use FPGAs in their experiments. Especially

the last part of this chapter focuses on debugging and practical application notes.

7.1. Model specifications

The chosen FPGA is a Kintex-7(type: XC7K160T-1FFG676, Xilinx, Inc.) as part of the XEM7360 integration module (type: XEM7360-K160T, Opal Kelly Incorporated). This module features an on-board USB 3.0 micro controller, 2GB synchronous dynamic random access memory (SDRAM) and a $200\,\mathrm{MHz}$ system clock. It is the FPGA with most resources from Xilinx that still can be programmed with the free version of their development suite (Vivado Design Suite HL WebPACK). The XEM7360 adapter board provides 100 configurable digital in- and output (I/O) pins that can be soldered to connecting devices. These pins suffice to connect all devices and the necessary pins are distributed as follows. 64 for a single-photon avalanche diode (SPAD) array detector, 2 for avalanche photo detectors (APDs), 2x7 for the serial protocol to the DAC, 4 for trigger inputs and 2 for digital outputs. This leaves room for additional devices. The Kintex-7 chip itself features a higher number of I/Os (400), but the remaining 300 pins are needed for power supply, ground wires and on-board connections to the USB 3.0 controller, the SDRAM and several high speed transceivers.

7.1.1. Electrical connections

All pins on the FPGA are part of voltage banks that have to be configured for a certain voltage standard. It is important that all in- and outgoing signals match this voltage standard to prevent damage to the FPGA or the connected devices. The voltage standards that were used throughout this thesis were LVCMOS33[54] and LVCMOS18[55]. For all input signals, an oscilloscope should be used to confirm the correct values. Although for the most part electronic devices fulfill their specifications, it is important to double check that the signals do not contain voltage spikes, offsets, ringing, reflections or other unwanted effects. Since all these effects are highly frequency-dependent, the signals have to be analyzed exactly in the later used configuration.

DAC interface

One problem with standard measurement tips of oscilloscopes is that they possess a residual capacitance of about $10\,\mathrm{pF}$ through having a fairly long ground cable. This can

strongly alter the signal shape of high frequency signals from a low impedance driver, e.g. typical FPGA outputs. The FPGA was configured to provide rectangular voltage pulses with a repetition frequency of $20\,\mathrm{MHz}$ to drive the DAC. Figure 7.1 shows, how the residual capacitance of $10\,\mathrm{pF}$ completely masks the underlying voltage structure. To prevent this, instead of connecting the ground cable of the measurement tip, a small piece of flexible wire can be wound around the cable mantle and directly connected to the output. Figure 7.2 shows the configuration. It should be noted that the signal should not only be measured at the FPGA but also at the end of the cable that connects the DAC board. The measurement determined that the parameters $8\,\mathrm{mA}$ drive strength, LVCMOS33 and SLEW SLOW can be used to interface with the DAC.

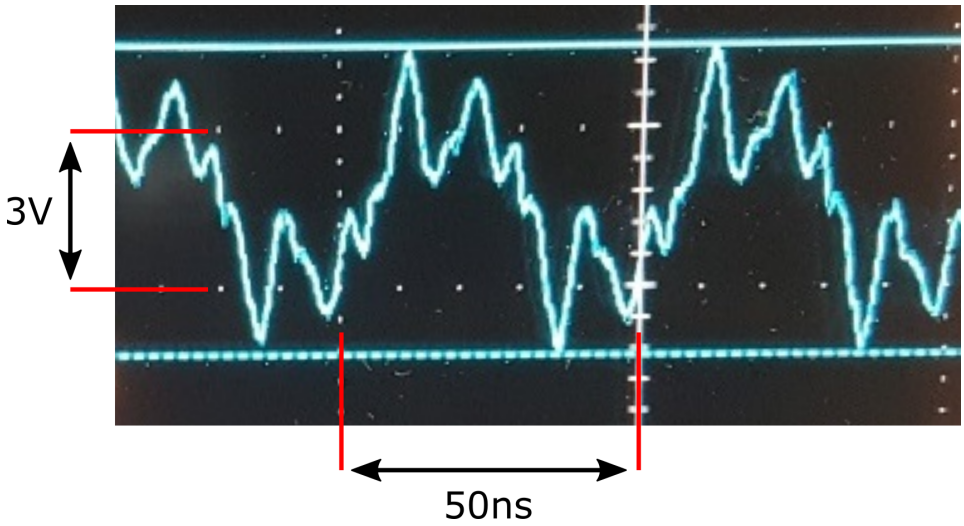

Figure 7.1.: Output of a rectangular voltage pulse series, measured on an oscilloscope with a measurement tip with residual capacitance of $10\,\mathrm{pF}$. The graph shows a voltage over time plot. It is impossible to see that the underlying signal is of a rectangular shape.

7.2. VHDL programming

In contrast to conventional programming that is structured as a series of commands that are handled by a processor, VHDL programming is comparable to designing electronic circuits on a circuit board. The FPGA contains a large amount of electronic building blocks that can be connected through a configuration file. The main building blocks are look-up tables (LUTs) and flip flops (single bit registers). However, many chips also feature more sophisticated memory elements such as block RAM. These basic building blocks can be

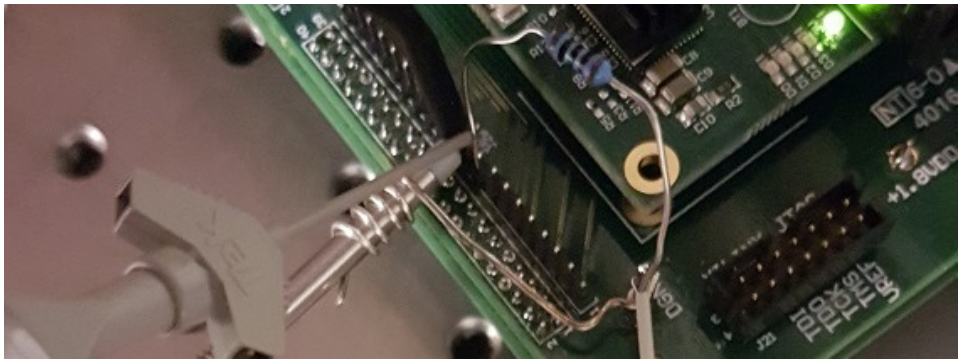

Figure 7.2.: To reduce the residual capacitance a small piece of wire is directly wound around the mantle of the measurement tip. A $100\,\Omega$ resistor is used as termination to prevent signal reflections.

used to create logic gates, binary adders or highly sophisticated programs, like an SDRAM controller. When compared to traditional programming, VHDL is the high level language, comparable to C++ or Python, while the configuration file is comparable to the compiled machine code. Since the resources can be used to create NAND or NOR gates (universal gates), it follows that the FPGA can emulate a Touring machine. Therefore, any algorithm, only limited by the available resources, can be implemented on an FPGA.

Although abstract variables types like integers can be defined in VHDL, most common variable types have a direct physical representation, e.g. the voltage states of bit registers and wires. During declaration, signals can also be instantiated with a default value. Wires should be declared with the same type as connected registers. For the std_logic type, a value of logical 0 corresponds to the signal state low, corresponding to a low voltage state in the register or wire. A value of logical 1 corresponds to the signal state high, corresponding to a high voltage state. The supply voltage levels define these states and depend on the type of FPGA and its configuration, typical values are $1.8\,\mathrm{V}$ or $3.3\,\mathrm{V}$. The signal states low and high are then defined by thresholds, e.g. any voltage below $0.5\,\mathrm{V}$ is considered low, while any voltage above $2.7\,\mathrm{V}$ is considered high. Furthermore, if a voltage state is set to low and has to be raised through another signal connection, it is called "raising a flag", while resetting to a low voltage state is then called "clearing a flag".

The Vivado development suite (Vivado Design Suite HL WebPACK) was used to write, simulate and compile VHDL code. The interested reader can refer to appendix A.1 for some examples that explain the syntax and code structure.

7.2.1. Simulations

The Vivado Suite includes a powerful simulator to examine the behavior of modules. After the design phase, a simulation is always the first step to determine correct module operation. To create a simulation, a "testbench" file has to be written. This file acts as the top module and includes the test-module instantiation as well as a timed series of simulated inputs. The simulator will check for correct syntax and signal connection restrictions. However, many critical timing restrictions are not included by default or cannot be included. It should therefore only be used to debug logic. Figure 7.3 shows the waveform output of a Vivado simulation for one of the modules used in the experiment. The test module here is a photon counter that is able to count asynchronous voltage pulses from photon detectors. The first two signals SYS_CLK and SYS_RST are universal to all modules and represent the main system clock oscillator and the system reset signal, respectively. A reset counter is used to determine when the count rate should be forwarded to the top module. Although not all timing restrictions can be included, some physical signal behavior can be approximated in the simulation. The signal connection from the photon detectors to the FPGA could lead to signal reflections in the cable and the photon detectors also have a non-negligible after-pulsing probability. Both effects would lead to a series of pulses with a small difference in arrival time. After the third pulse of SIGNAL_IN, a series of short pulses is simulating these effects, and the counter is shown to be robust against this behavior. For clarity, the internal signals of the counter have been omitted from the waveform configuration file.

7.2.2. IP cores

Vivado offers a library of predefined VHDL modules that can be integrated in a custom module for specific tasks. These modules are called semiconductor intellectual property cores (IP cores) and are subject to licensing and copyright restrictions. Their source code is non-accessible, and they have to be configured through a Vivado graphical user interface (GUI) element, the IP core generator, before integration. Each IP core has its own user manual, describing its behavior. The functions of IP cores range from simple data buffers to complex elements like SDRAM controllers. The usage of IP cores is highly recommended, since it reduces development time drastically.

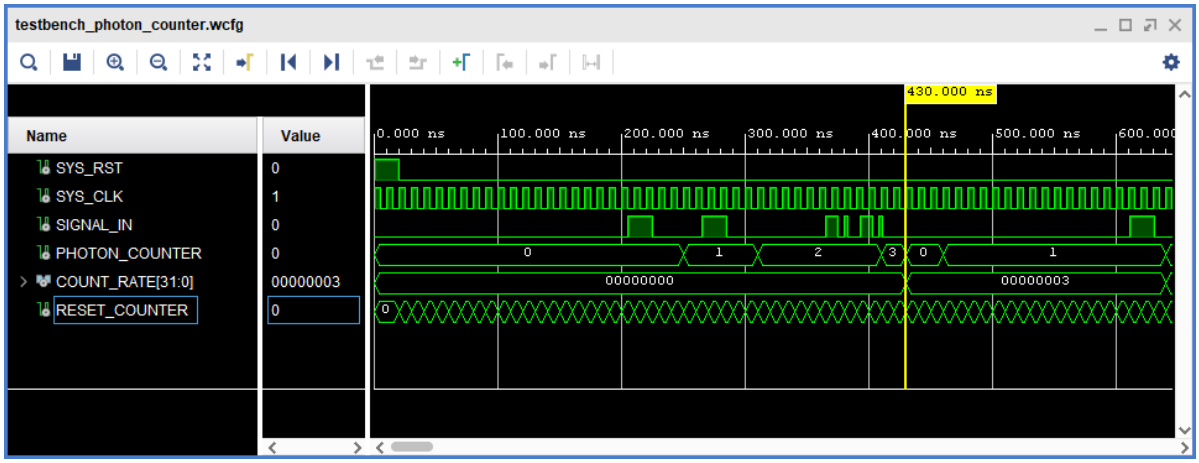

Figure 7.3.: Simulation output for a photon counter module. A series of pulses at SIGNAL_IN increments a counter, while a RESET_COUNTER determines, when the counter value should be forwarded to a top module. Physical signal imperfections are modeled by a short series of pulses following the third SIGNAL_IN pulse.

7.2.3. Floor planning - connecting to the outside world

To interface the FPGA with the outside world, Vivado needs physical constraints files. These constraint files include electrical configurations for I/O pins as well as designations that are used in the VHDL module to address these pins. The XEM7360 evaluation module (EVM) is shipped with a constraint file that specifies the connections to the on-board USB 3.0 controller. In contrast to this controller, which is a separate physical integrated circuit chip on the EVM, an SDRAM controller needs to be implemented through an IP core. A detailed instruction on https://opalkelly.com/pins/ describes how to configure this IP core for the XEM7360 and how to generate the necessary physical constraints file. To connect further devices to the FPGA, a custom circuit board was designed in our institute. It features a number of physical plugs to connect trigger lines from the piezo stage, the laser synchronization module and all photon detectors. To create a constraints file for this attachment, a Vivado floor planning project has to be created. It shows all pins of the FPGA and provides a clear way of creating VHDL designations and monitoring voltage configurations. A constraints file containing these configurations can be exported from this project.

7.2.4. Timing constraints

A synchronous FPGA operation poses timing constraints on all calculations. More precisely, a module that is triggered by an edge of SYS_CLK has to finish its calculations within the same clock cycle before the next clock edge. Awareness of this timing constraint is critical during the design phase, since it marks the difference between success and failure of any module. There are a few key points to always keep in mind. The FPGA contains a limited number of routing resources. For large designs that exhaust most of the available resources it can become increasingly difficult for the synthesis and implementation algorithms to find a routing that will still meet the timing constraints for all processes and submodules. Routing can also become a problem, when the output of one register is connected to many other registers (termed "high fan-out"). This leads to situations where the number of locally available signal lines close to the register gets exhausted and longer routes have to be used. This can be avoided by creating copies of the first register at different places on the FPGA. Furthermore, each of the basic FPGA elements has a settling time, and complex calculations containing series of elements can easily exceed a clock cycle. This can be avoided by splitting complex calculations up into multiple clock cycles. For example, a multiplication can be expressed as a series of additions.

7.2.5. USB communication

The on-board USB 3.0 controller can be used with most operating systems and common programming languages. It is the bridge between the Python microscope software and the FPGA module. The interaction between the PC and FPGA is mediated through up to 40 handshaking operations per second. Each of these handshaking operations can activate one of three different types of endpoints intended for specific purposes.

Triggers are used on the PC side to create single pulses, synchronous to the system clock, on the FPGA. Using a trigger endpoint from the FPGA side will set a flag on the PC side. This flag needs to be cleared from the PC side before it can be set again.

Wires are used to connect 32 bit registers on the FPGA to variables in Python. Here, the register can be read or altered from either the PC or FPGA side. This endpoint should not be used for larger data transfer, since the number of possible updates per second provides a narrow bottleneck.

Pipes also connect 32 bit registers. However, they allow for continuous data transfer of large data packages. On the FPGA, a buffer can be connected to a pipe and used to store an incoming data stream or provide a data package that can be read on the PC. For

example, in order to transmit an image from the FPGA to the PC, a first-in, first-out (FIFO) buffer is connected to a pipe and while the PC is reading from the buffer, the buffer itself is refilled from the SDRAM until the complete image is transferred.

7.3. Program structure

The FPGA program has a top module that includes a port list for signals defined in the physical constraint files and acts as the interface for all submodules. Figure 7.4 sketches the connections of all hardware devices that are connected to the top module as well as the structural division of the top module in scanning and imaging. Here, both parts contain a number of processes and submodules for specific tasks explained later on.

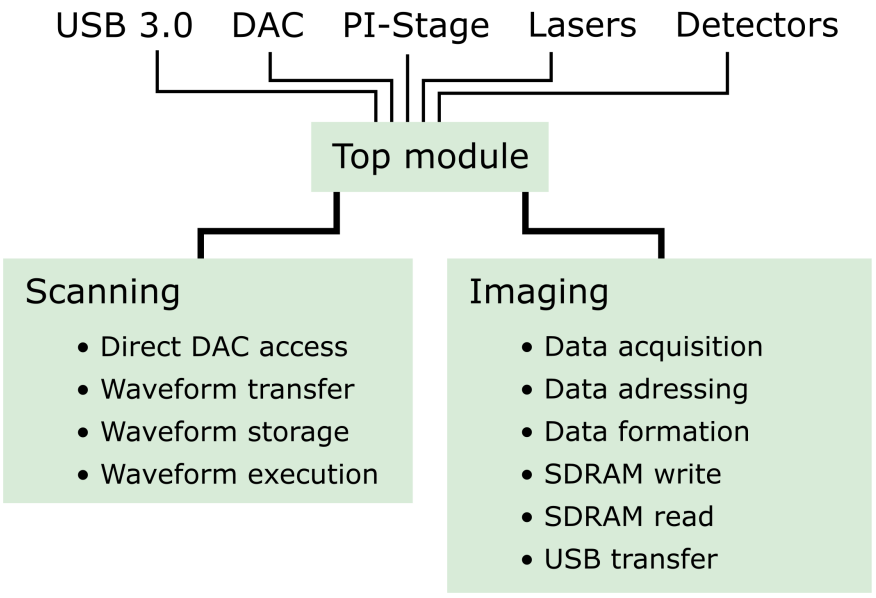

Figure 7.4.: Schematic of devices that are connected to the top module via the designations in the physical constraints files and topical division of the module into scanning and imaging.

7.4. Scanning

Mirror scanning is performed through the interaction of two modules. A scan controller reads waveform data points from a block RAM storage in the FPGA and transmits them to a DAC controller. From there, the 16-bit data points are transmitted through a 24-bit serial communication protocol to the DACs.

7.4.1. Scan controller

During the scan process, a rectangular scanning pattern is created by two scanning mirrors that repeatedly move the focal volume along a line in one spatial direction("fast axis"), while the other two mirrors are used to displace the focal volume between image lines by a small step in the other spatial direction("slow axis"). Figure 7.5 shows the structure of the waveforms for both axes. The fast axis waveform consists of two linear parts connected with a turning part, where the mirrors slow down and then accelerate in the opposite direction. The required size of this turning range depends on the scanning speed and is determined experimentally. The goal is to reach an even illumination in the image by having a constant speed of the confocal volume during pixel acquisition. During the scan, the controller repeatedly iterates over the waveform. For simplicity, the number of image lines is fixed to an even number. This way both mirrors of the fast axis will end up again at the starting point after the scan. The slow axis waveform consists of two steps, where at each step the focal volume is displaced by δs. A sigmoid function is used to create smooth transitions without overshoot and enough settling time before the linear part of the next image line. After starting into the first two lines of each image at the starting point x_0, all other lines are started at x_0'. A desired image size will not necessarily lead to integer steps in the 16-bit DAC control value for the line spacing. A constant added offset per line would need two different values for beam walking with two mirrors. Rounding these values to the nearest DAC control value introduces a rounding error. This error differs in magnitude for both mirrors and leads to an accumulation of a position and beam tilt error during the scan. Therefore, the line offset has to be defined individually for both mirrors of the slow axis by a linear ramp of rounded absolute DAC values. This linear ramp of values is attached to the slow axis waveforms (not depicted in Figure 7.5). During the linear parts of the fast axis movement, pixels are acquired. Here, the scan controller transmits two signals to the image acquisition module (LINE_EN and PIXEL_CLK). The iteration frequency over waveform points is decoupled from the pixel acquisition. This allows to define an arbitrary number of pixels per line at a higher clock frequency. Additionally, it allows to create a fine time delay $\delta\tau$ in multiples of SYS_CLK cycles ($5\,\mathrm{ns}$) after the linear part of the control signal output

starts. This is used to compensate the mechanical lag of the mirrors. In total, two DAC EVM boards are used to enable simultaneous serial communication with two scanning mirrors. This enables a higher update rate of one of the spatial directions. During the linear part of the scan, the scan controller transmits every waveform point to both fast axis mirrors. In the turning range, all 4 mirrors have to be addressed. Therefore, the waveform points are transmitted in an alternating pattern. With this scanning implementation the maximum update rate of the DACs can be used for the linear part of the fast-axis movement. This is important in order to create smooth control voltages for higher scanning speeds.

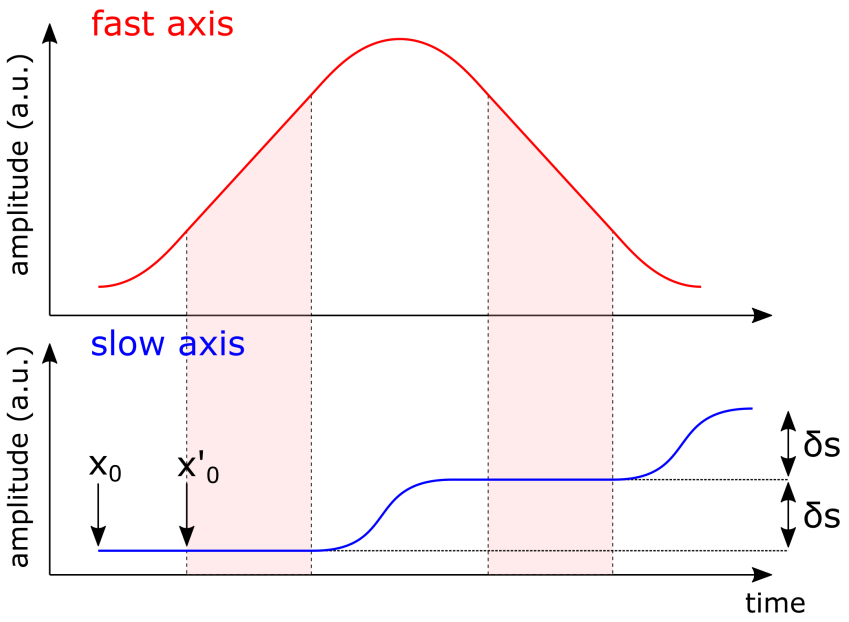

Figure 7.5.: Schematic of the waveform shape used in mirror scanning. One waveform period corresponds to two image lines. Only during the linear portion of the waveform light is collected and stored for the image. The amplitude of the turning range can be set dependent on the scanning speed. The goal is to reach evenly illuminated images. To test this behavior in the experiment, the mirror images were compared to stage scanning images until a one-to-one spatial correspondence was established.

7.4.2. DAC controller

Each DAC possesses an entry shift register, four channels with attached data registers and four corresponding active registers. This architecture allows to load new values for all chan-

nels into the DAC data registers and update the voltages through a simultaneous transfer of all values to the active registers. The communication with the DAC is facilitated through a serial protocol with 24 bits. The VHDL module is connected to a phase-locked-loop (PLL) module (IP core) providing two synchronous clocks with 20 MHz and 40 MHz. The 20 MHz clock is used as data clock, required by the DAC to operate the entry shift register during data entry. The 40 MHz clock is used as underlying clock in the communication protocol, since it is convenient to implement the timing requirements specified in the data sheet. The 24-bit data "word" is structured as follows: 2 bits channel address & 1 bit quick load & 5 bit empty & 16 bit data. The quick load bit has to be set to zero in order to transfer the contents of the shift register to the data register of a single channel. Updating the DAC value for a single channel including transmission of additional control bits takes 1.4 µs. This determines the maximum update rate of the voltage control signal.

7.4.3. Parameter Handling

The scan controller needs a number of parameters for scanning operation and to process waveform configurations. Each of these parameters has a dedicated register on the FPGA. To set these registers from the PC, two 32-bit wires of the USB host controller are used. One of the wires carries a number, indicating which parameter should be changed, while the other wire carries the parameter value. A process on the FPGA side implements a multiplexer by creating a signal connection between the parameter register and the wire carrying the new value.

7.4.4. Waveform transmission

Since the DAC has a range of 16 bits and four mirrors are connected, it is convenient to use two 32-bit pipes to transfer waveforms from the PC to the FPGA. Two 32-bit wide FIFOs are attached to these pipes. Here, each FIFO receives the waveform data points for the two mirrors with the same scan axis direction. The FIFOs can only act as intermediate storage. After the data transfer is complete, another process is used to transmit the waveform data into block random access memory (RAM).

7.5. Image acquisition

Two core design principles guided the design phase for imaging: fast image acquisition and simultaneous imaging of multiple channels. Early estimates, based on the available stimulated emission depletion (STED) beam power, suggested that imaging with up to 64 beams should lead to STED images with a resolution beating structured illumination microscopy (SIM), a popular technique in live-cell imaging with a resolution improvement of ≈ 2 compared to conventional wide field microscopy. This number was decided to still hold merit for possible imaging applications and was chosen as maximum channel number for the imaging module. A more detailed analysis for available beam power and resolution in comparison with field of view, based on later acquired experimental results, is discussed in chapter 9.2. The main bottleneck for fast image acquisition on the FPGA is the number of possible hand-shaking operations of the USB 3.0 controller (40 per second). Since for every transfer at least one hand-shaking is necessary, the image transfer speed depends on how much image data is transmitted per individual transfer initiation. The maximum specified scanning speed of the galvanometric mirrors is $f_{max} = 1$ kHz. An estimation on the number of desired pixels per image and channel (2K resolution) suggested acquisition speeds in the Hertz range. Therefore, the module was structured around the transmission of full images per individual data transfer. Images of this size would easily exhaust all register storage as well as block RAM resources on the FPGA. To circumvent this, an IP core SDRAM controller is included in the module and SDRAM is used as intermediate data storage on the EVM. In addition to the collection of image data from multiple channels, the module also includes nanosecond time gating to provide temporal separation for two color channels. This is intended to reduce cross-talk in multi-color imaging.

7.5.1. Finite State Machine

The imaging program is controlled by a finite state machine (FSM) module that handles all submodule interactions. An FSM can occupy a number of states, where every state is responsible for a separated task. Figure 7.6 shows the data flow between the imaging submodules for different states of the FSM. For visual simplicity, a few states have been omitted and only the main states have been sketched. After starting out in an idle state, the FSM transitions into a waiting state during the initiation/reset routine of the FPGA. In this state, the FSM waits for the data acquisition module to finish collecting enough data for a block of structured pixel values intended for transfer to the SDRAM. In the writing state, a communication with the SDRAM controller is established and a collected data block will be transferred to the SDRAM. The preload state is responsible for filling a FIFO buffer before

the USB transfer of the image to the PC begins. In the transfer state, this buffer is refilled with data packages from the SDRAM until a whole image has been transferred to the PC.

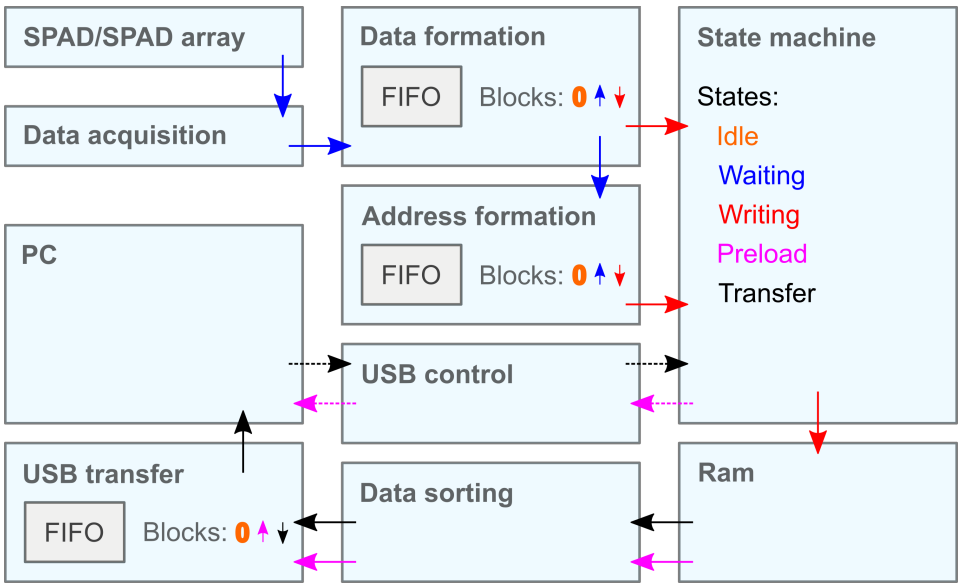

Figure 7.6.: Data flow chart for all FSM states. The color coded arrows represent data flow involved in the different FSM states. The small arrows next to the FIFO blocks represent filling and emptying the respective FIFO.

Although the general data flow in these states is, as listed, from top to bottom, the FSM can not simply cycle through the states in this order. Most tasks have multiple executions during image acquisition, and each task has a different runtime and priority. The complexity is further increased, since for maximum imaging speed the FSM also should be able to handle simultaneous image acquisition and image transfer through USB. To create the needed state transitions, the FSM relies on a set of status signals from the submodules or the PC. Figure 7.7 shows which status signals are responsible for these transitions. During an initial image acquisition the state will cycle between waiting and writing until a complete image is stored in the SDRAM. If only a single image is acquired, the state will then transition into preload and transfer. If further images are acquired during the transfer, it will start cycling through the states waiting, writing and transfer. For this, the fill level of the USB buffer is monitored. As soon as it drops below a certain threshold, a request for additional data from the SDRAM is triggered and the FSM transitions from waiting to transfer to refill the buffer. However, this transition can be canceled by a write request, since the timing restriction for the write process is more stringent. The exact interplay and constraints will become more clear in the specific module descriptions.

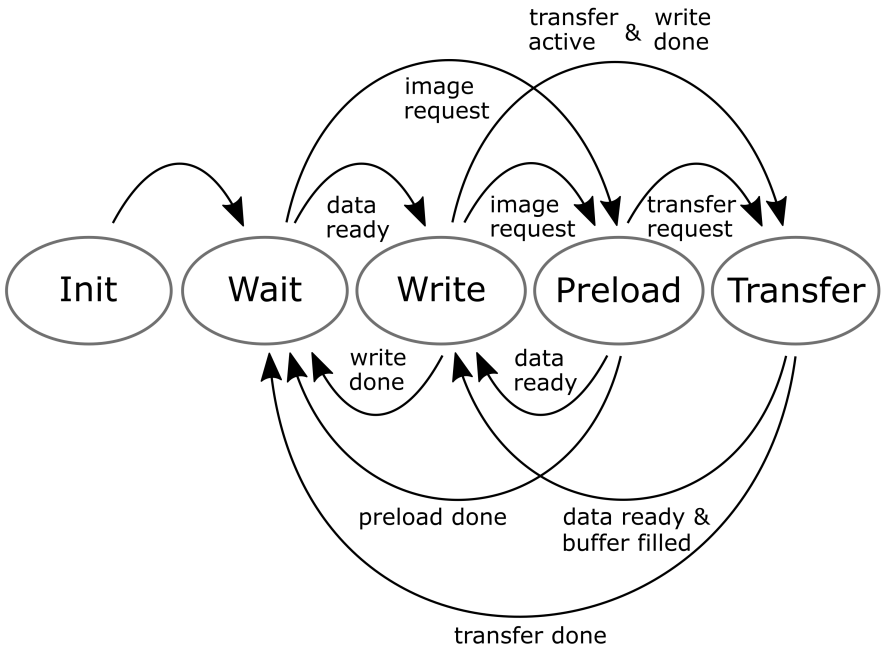

Figure 7.7.: Transition chart for all FSM states.

7.5.2. Signal acquisition

The single photon detectors used in our experiment produce voltage pulses that in turn are counted by the FPGA. At the photon detectors, each photon triggers an avalanche effect of charge carriers in a biased diode leading to a measurable current. After the current becomes measurable, the diode bias has to be reduced to zero to stop the avalanche effect and reset the diode for the next use. The time period of this reset is called "dead-time". During the dead-time, no photons can be detected, it therefore determines the maximum detection frequency. For the APDs as well as the SPAD array, this dead-time is on the order of $30\,\mathrm{ns}$. If we compare this time with the FPGA clock period at the XEM7360 of $5\,\mathrm{ns}$, this leads to a maximum requirement of six clock cycles for any synchronization circuit to keep up with the voltage pulse arriving from the detectors. For this task, the entry stage in the data acquisition on the FPGA is comprised of synchronizers, called flancter (Figure 7.8). Each flancter consists of two flip-flops, a not-gate and an XOR gate. Here, the clock entry of the first flip-flop is attached to the asynchronous signal from the photo detectors. As soon as a photon triggers a voltage pulse, the data output of this first flip-flop will go high. This flag can then be picked up and cleared by one of the following clock edges of the system clock and therefore be synchronized. The operation of the flancter requires that both flip-flop clock entries be operated mutually exclusively in time, since otherwise the

flip-flops can transition into non-defined and unresponsive states (please refer to standard literature for flip-flop operation[56]). For an ideal APD and signal connection this should be no problem, since, after a pulse is registered, the dead-time leaves enough clock cycles to reset the flancter. In a first implementation this was considered and the flancter was used as is.

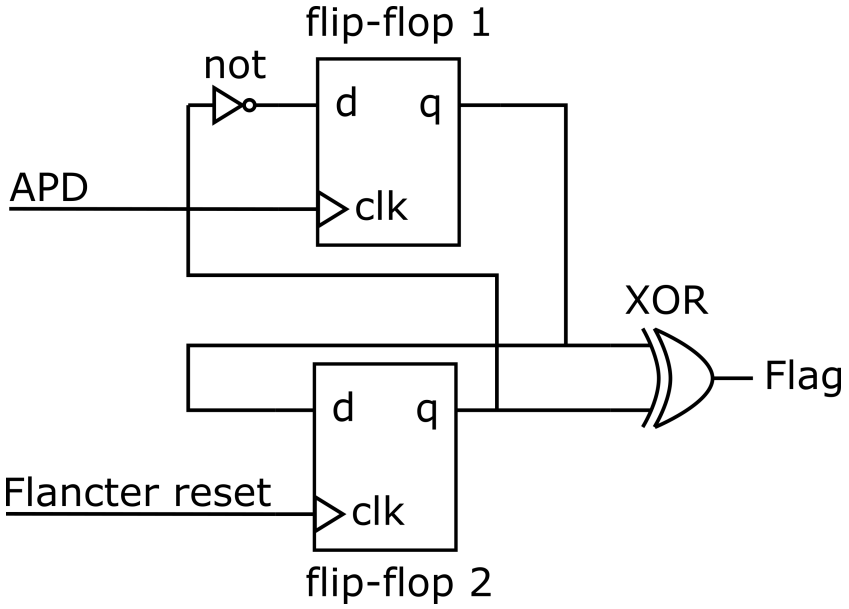

Figure 7.8.: Flancter module used with an APD. A pulse on the clock entry of the first flip-flop will set the output q to high raising the flag at the XOR gate. A pulse on the clock entry of the second flip-flop will set its output to high clearing the flag. Instability can arise, when one of the clock entries is triggered, while the other flip-flop output is still in transition.

However, this first implementation was unstable and prone to get stuck in a non-defined state. This became apparent during imaging, where the image randomly turned black after a few lines. Since the effect was observed to be power-dependent, the signal connection was investigated. We could observe smaller pulses following the main pulse, as well as what seemed like random pulses that would follow the main pulse. The signal was showing this behavior due to two physical processes. Physical signal lines can be subject to signal reflections, leading to a separation of a single pulse into multiple smaller pulses. This was know beforehand and all signal lines possess termination resistances that reduce the magnitude of these reflections below the switching threshold of the used voltage standard. Therefore, this could not explain the instability. However, another previously unknown process was involved. APDs have a small after-pulsing probability, possibly creating shorter times between consecutive pulses. This was the source of the random pulses that could

be seen on the oscilloscope and the culprit for the instability. To alleviate this problem, each flancter was followed up by two flip-flops and the entry was combined to the output flag with a NAND gate. This delays the flag of the flancter by two clock cycles and additionally blocks the flancter entry during flag reset. This introduces a total time window of $15\,\mathrm{ns}$, long enough to block any unwanted pulses. The synchronized pulses are then picked up by 16-bit counters that collected the brightness information for each image pixel. The acquisition module is controlled by two signals from the mirror scanning module or the external input of the piezo stage controller (LINE_EN and PIXEL_CLK). Here, the LINE_EN is connected with an AND gate to all signal lines and determines when photon signals should be acquired. PIXEL_CLK is used to store all counter values in an array of registers while simultaneously resetting the counters. Having another set of transfer registers gives the data formation a larger time window to process the counter values. The typical pixel acquisition time is on the order of tens to hundreds of microseconds.

Time gating

The signal acquisition module is connected to an external $15\,\mathrm{MHz}$ oscillator that synchronizes the lasers. For two-color channels, the collection of photons has to be mutually exclusive in time and synchronized to the arrival time of the excitation lasers at the sample. The repetition frequency of the excitation lasers is fixed at $15\,\mathrm{MHz}$. Each incoming pulse will trigger a small gating module that will open a gate for the collection of photons for six consecutive clock cycles in an alternating pattern for both color channels. The start of the gate can be delayed with the system clock by an integer number of $5\,\mathrm{ns}$. If this is not sufficient to get the proper temporal positioning, physical switches on the delay box can be used to displace the gate position with $10\,\mathrm{ps}$ accuracy.

7.5.3. SDRAM

The counter values have to be stored in SDRAM in larger data blocks in order to enable consecutive bulk data transfer of images to the PC. The data to and from the SDRAM is mediated through a controller module, implemented through an IP core. The detailed instructions on the IP core configuration can be found on the Opal Kelly homepage. Although the correct communication protocol is quite complex, a few key points about SDRAM and the controller are sufficient to structure the communication. The SDRAM is structured into banks, rows and columns. On the FPGA7360, there are 4 banks, each with a rectangular grid of storage cells. The width of each storage cell in this grid is 256-bit. This is also

the width of data words for communication to the controller. The controller itself is a FSM, controlling four distinct FSMs, each responsible for one bank of SDRAM. Each of the bank FSMs is responsible for the tasks of creating connections to a particular cell, reading and writing to and from the cell and refreshing the voltage state of the cell. In SDRAM each bit of storage is a capacitor that loses charge over time and has to be recharged from time to time. At the entry of the controller there are two FIFOs, one for addresses, the other for data.

Communication constraints

Naturally, multiple timing constraints arise from the structure shown above. Firstly, for a high data transfer rate, most words should be completely filled with useful information. Secondly, at refresh cycles the SDRAM is unresponsive. This behavior is mentioned in the IP core data sheet, but unfortunately this unresponsiveness is not communicated early enough by the IP core output signals, but exactly at the time it occurs. To account for this, we decided to include three 256-bit registers as a cyclic buffer at the data entry. This buffer makes it possible to stop a FIFO transfer into the data entry and not lose any data, when the SDRAM blocks its entry buffers. Lastly, the bank FSMs needs time to switch between cells. This time delay depends on the vicinity of the cells. Writing data is mainly limited by the scanning speed of the experiment, but transferring data is only limited by the USB 3.0 speed. Therefore, it makes sense to structure the data for the writing process in a way that later allows the read process to iterate over consecutive addresses.

7.5.4. Data formation module

Figure 7.9 shows how the data is structured and buffered before it gets written into SDRAM for an experiment with the maximum of 64 channels. A single SDRAM cell will store 256 bits of data and therefore 16 pixel values. To structure the data for faster readout, these pixel values should belong to neighboring pixels as opposed to originating from separate channels. Furthermore, all channels will be stored in neighboring blocks in the SDRAM, according to the same layout as their physical representations for multi-beam imaging. This allows to transfer a complete image without the need to sort the image data on the PC. To achieve this structure, the counter registers are transferred into a total of 16 pixel FIFOs. After accumulating 16 consecutive pixels from all 64 channels, a block of data is complete for transfer to the SDRAM. The address formation module will later pair each word with a corresponding address. The time to transfer all counter registers to a single

FIFO is 64 clock cycles plus overhead, approximately $0.5\,\mu s$. This is much faster than any pixel acquisition time and poses no bottleneck. The use of FIFOs as buffers also enables storing of multiple data packages, which in turn provides other SDRAM communication processes with a time window of multiple pixel acquisition times. Since it is impractical to limit image widths to multiples of 16 pixels, the module also handles the cases, where a line ends inside the SDRAM word and fills the remaining FIFOs with zeros. Further, the image scanning is bi-directional and the filling pattern has to be reversed with the scan direction. In the current implementation, this data structuring is also used for any smaller number of imaging channels. It does not matter if the image is acquired with one color channel, two color channels or any number of channels up to 64. The image acquisition always uses 64 channels, and the microscope software is used to determine which photon detector output is connected to which channel.

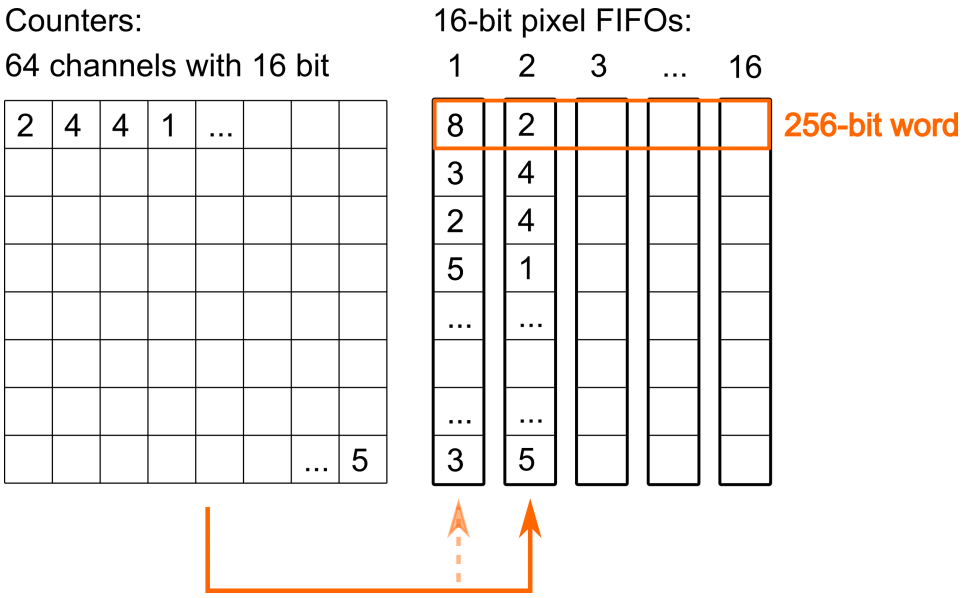

Figure 7.9.: Working principle of the data formation module. All pixel values in the counter channels are transferred into 16 FIFOs to build blocks of data intended for the transfer to SDRAM storage.

7.5.5. Address formation module

To initiate a data transfer to the SDRAM, a set of addresses is needed for each block of data. Figure 7.10 shows the address structuring for an experiment with four channels, six image rows and 32 pixels per row, leading to two 256-bit words per row and channel. The numbers correspond to the cell addresses of the SDRAM, and the blue boxes indicate

the storage space reserved for each channel. The first word of each channel is acquired simultaneously and forms a block of data, this is true for all following words. For the first transfer, the address FIFO is therefore filled with the cell addresses of the first cells in each channel. To meet the FPGA timing restrictions, it was imperative to implement the variables that keep track of the active image channel, row and column as incremental counters in order to avoid any multiplication during the address creation.

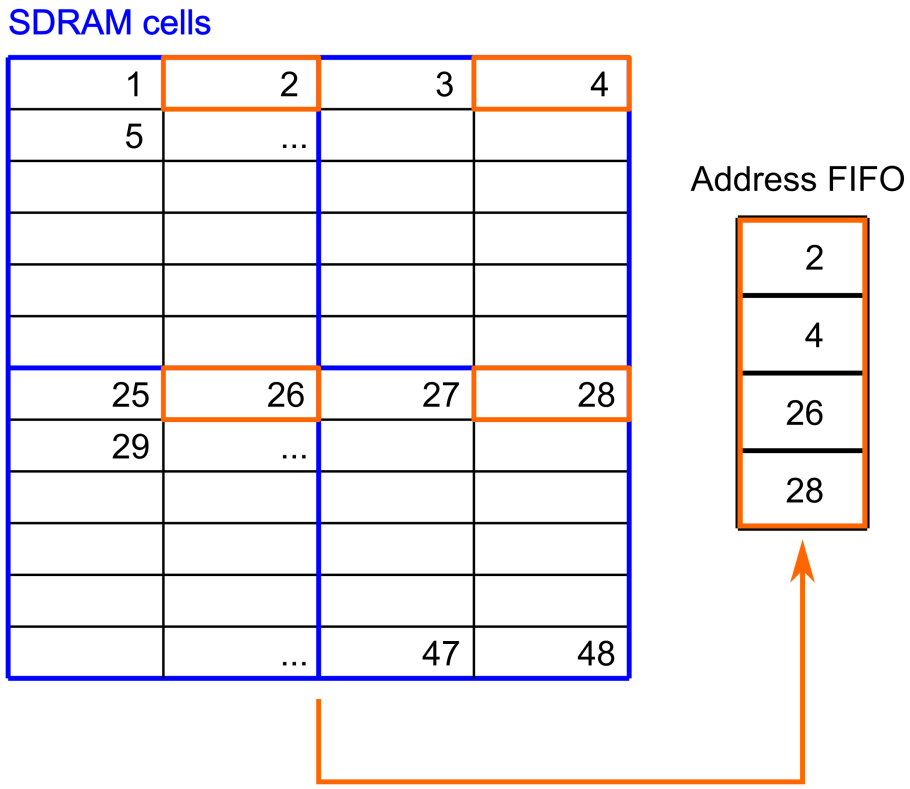

Figure 7.10.: On the left, the intended placing of 256-bit pixel words in the SDRAM cells is shown for an experiment with four neighboring channels. On the right, a FIFO is shown carrying the addresses intended for the second block of structured data.

7.5.6. Data sorting

Although the data is pre-structured in the SDRAM, the data words at the end of image lines can contain empty bits. To transfer a complete image, these empty bits have to be sorted out and the remaining data has to be stitched together into new 256-bit words for transfer.

In an earlier version of the FPGA top module, all SDRAM words contained a header with a successive numeration. This was needed for debugging, in order to track if the SDRAM communication protocol was working as intended. The data sorting module was built for these two tasks. After debugging the SDRAM communication, the header was removed from all data words and this functionality was taken out. The restructuring of the data is quite complex, since there is a major constraint originating from the communication with the SDRAM. The data stream will provide a 256-bit word each clock cycle. This does not mean that all sorting operations have to be finished within one clock cycle, but it means that there have to be multiple registers taking up the data and performing the sorting simultaneously. The module is built around multiple sets of three registers that work in an intertwined way. Figure 7.11 illustrates the working principle. The module starts by storing a word from the SDRAM in a 256-bit entry register. From there, this word gets transferred to a 512-bit shift register, while simultaneously initializing the rest of the register with zeros. Depending on the fill status of the 768-bit output register, indicated by a blue block of data, the word is shifted, so that at transfer it will align with the end of the data previously stored. The initialization of the shift register with zeros allows to perform a logical OR operation to transfer the contents of the shift register into the output registers. From there, complete 256-bit words get sent to the USB FIFO. All four steps involve only operations that each can be performed in a single clock cycle. The shift register will be ready to store another word after the transfer to the output registers, after three clock cycles. To ensure continuous operation, there are three entry and three shift registers that are operated in a cyclic fashion.

7.6. Debugging

As with any complex software, the design of an FPGA program comes with a significant time period of debugging. I want to illuminate which things should be considered to create a smooth work flow and to keep the amount of debugging time at a minimum. In general, every software manual and sample code should be used very carefully as they often contain errors. Therefore, each data communication protocol should be tested with extensive working examples. In our case this included USB transfer, transfer into and from FIFOs, transfer with block RAM, and transfer with SDRAM. Furthermore, interfacing with all physical signal lines into the FPGA has to be tested. This can be quite complex, since there is no analysis software on the FPGA and small test modules have to be written and designed in each case. In general, each module operation should be simulated, with the attempt to cover all edge cases of operation in the test-bench design. It should be stressed that good

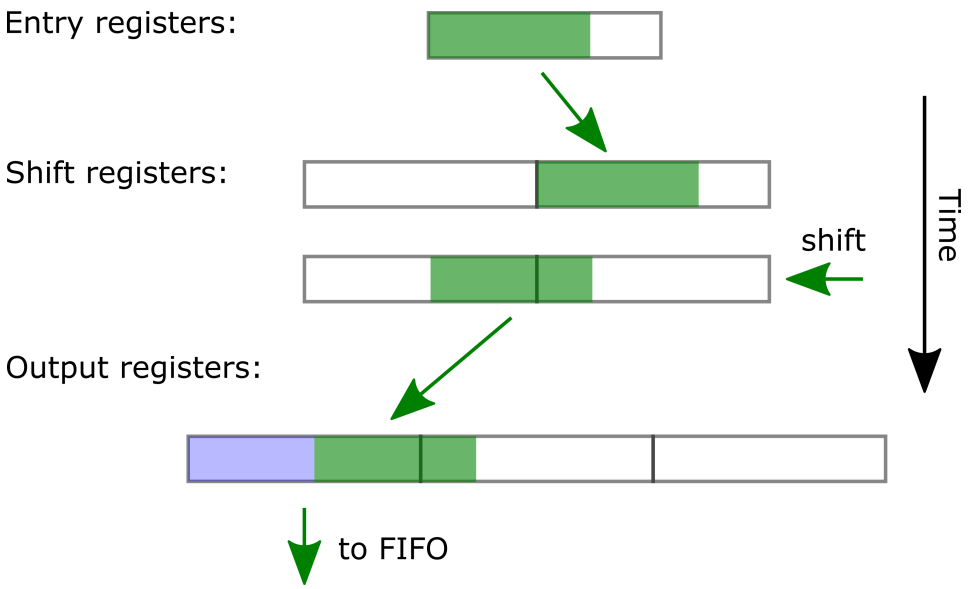

Figure 7.11.: In the sorting module complete words of data and partially filled words of data are stitched together before transfer over USB. The green arrows indicate processes that can be performed during one clock cycle, while the green shaded areas show data for the current iteration. Indicated in blue is data previously processed that was not enough to completely fill one of the output registers. At the end, one of three 256-bit registers is completely filled and transferred to the USB buffer FIFO.

simulations will save a lot of work later on. Since the interplay of all modules involves the interaction with the outside world, some of the functionality has to be tested after implementation. A single synthesis and implementation can be quite time consuming and took up to 45 minutes on our lab PC (8 cores, Intel i7 9600k, 16GB RAM). This makes it necessary to include endpoints and debug signals between the modules in the form of counters and status flags, accessible through USB. This allows to monitor module operations and debug the interplay of the modules. Here, the list of debug signals is never fixed, but adapted to the current problem in a way that tries to get a maximum of useful debug information out of a single synthesis and implementation run. For example, if image acquisition fails and shows empty blocks in the image, this list of debug signals can be used to track down the responsible submodules. If the number of data packages written from and to the SDRAM does not match, but the amount of data packages acquired by the signal acquisition module is correct, there is a good probability that the error is related to SDRAM communication or in the modules directly connected to the SDRAM. All debug signals that proved to be useful were kept in the final design to enable faster implementation of new modules and functionality in the future.

8. Software

A major part of this thesis revolved around software design on the PC. In this context, vector diffraction scripts for point spread function (PSF) and multi-beam calculations and the field programmable gate array (FPGA) program have already been introduced. This chapter will focus on the microscopy suite that is used for imaging and that controls all electronic hardware of the microscope. The chapter will first elaborate on its programming language, before explaining the program structure and the interfaces to the different hardware devices. A short note at the end of the chapter will list software that was used for data analysis/presentation.

8.1. Python

The main programming language for the microscope operating software is Python. I want to elaborate what sets it apart from other choices and the experiences I had in the lab. Two common choices for programming laboratory software at the start of the thesis were C/C++ and LabVIEW. Although Python was on the rise, many companies offered mainly C/C++ or LabVIEW application programming interfaces (APIs) for scientific equipment. While LabVIEW is a programming language with a graphical user interface (GUI) that is intended for fast implementation of laboratory software, it comes with several disadvantages. It is a commercial language and by design intended for the use with National Instruments (NI) hardware. This can restrict options when trying to expand an experiment. For example, during the acquisition of the FPGA, the NI FPGA solutions housed components that were several years old and not on par with the current standard, while being significantly more expensive. LabVIEW has the advantage that it is specifically built for scientific experiments and can be used fairly fast for signal analysis, since elements like an oscilloscope exist as precompiled building blocks. However, this advantage comes at a cost. Most precompiled elements are intellectual property with no access to source code, and therefore no modifications are possible. Also, programming with a GUI by drawing circuit diagrams can make it significantly more difficult to keep a program structured, well commented and adjustable, since code additions will frequently require restructuring of the project. In contrast, C++ is

a universal language and very comparable to Python in its usage. In fact, many Python libraries are adaptions of C++ libraries, e.g. PyQt (pronounced pie cute) is a conversion of the C++ library Qt. Although similar, some differences are relevant to the usage in stimulated emission depletion (STED) microscopy. C++ can be considered a hardware-near language, where pointers are used to point to specific memory locations, and possesses only limited type safety options. For example, writing a 64-bit integer to a 32-bit integer memory location is possible. This would spread the 64-bit integer into neighboring memory spaces and lead to undefined consequences. This demands higher attention during programming in order to avoid bugs. In contrast, type safety is no problem with Python and for the most part memory access management is happening without direct interaction of the user. Another big difference is that C++ and also LabVIEW are compiled languages, while Python is an interpreted language. A compiled language needs initial overhead, but the commands of a compiled program can be executed faster by the processor. This is ideal for programs that require complex calculations, but comes at the cost of flexibility, since the compiled program cannot be changed at run-time. Python is an interpreted language, where each line of code gets translated to machine code at run-time. This is significantly slower, but it opens up the possibility to inject additional code during run-time. This is a big advantage for prototyping, since scripts can be used to perform measurements series, overwrite function definitions and debug new functionalities before they get added to the main program. Further, the syntax in Python contributes to code readability. Instead of using semi-colons or other end-of-line characters, the code has to be structured with indentations. This leads to a more uniform code structure across different programmers and again removes another common source of bugs.

After programming with Python for several years, I would recommend this language for scientific projects with interplay of multiple hardware devices and a GUI, where critical timing precision and complex calculations on the PC side are of minor importance. At the time of writing, Python™ has found its way into scientific equipment and an increasing number of companies provide API packages. The scripting capabilities are very useful to setup flexible automated measurement series. It has one of the largest user bases in the world, recently gaining further increase through the use of Python for neural networks. This makes it easy to find existing solutions to almost every conceivable task. It has a large range of libraries that simplify interfacing with hardware. Although not unique to Python, PySerial should be mentioned in this context. It makes use of the RS232 interface, better known as COM-port. Although being an older interface, it is still widespread even among newer equipment, and half of the laboratory equipment at the STED microscope is controlled with RS232.

8.2. Microscopy suite

The current version of the microscope operating software is merging multiple control modules into a coherent software suite with an easy-to-use GUI. It controls the piezo-stage, the FPGA, the lasers, the spatial light modulator (SLM), the shutters, the piezo alignment mirrors and the camera. Besides manual alignment of the optical pathways, this software is able to control the complete experiment and is optimized to provide a range of imaging utilities, e.g. overlay of different images in multiple colors, dynamic range control and zooming. It is the end product of a long list of iterations and different approaches. The software is built on the basis of QuDi, a laboratory Python software published by Binder et al. (2017) [30]. QuDi is a modular software suite that was designed for the use of several experiments in the field of quantum optics and can be used to operate a confocal scanning microscope with data acquisition cards from NI and analog piezo scanning stages. We use QuDi due to its streamlined inclusion of new modules and a number of other features that also proved to be great quality of life improvements, e.g. the use of configuration files, automatic saving of persistent variables and the use of Jupyter notebooks (a form of scripting). However, the standard scanning modules in QuDi are not optimized for fast scanning, and an assessment of the code showed that the complete scanning module had to be re-written to accommodate the necessary changes. We therefore chose to keep only the core structure of QuDi, namely the QuDi manager that initializes and connects modules. We wrote new modules to control all hardware and improved upon the scripting capabilities of the software intended for automated measurements. The next sections describe all functionalities that were developed and added during this thesis. Special thanks should be given to Jakob Bühler, a master student who wrote or adapted several of the modules and was heavily involved in the software development for the project. More detailed information can be found in his master thesis[57].

8.2.1. Program structure

The structure of the suite can be seen in Figure 8.1. It shows the distinction into GUI, logic and hardware modules[30]. All modules can be run in a single thread, but this would interlock their functionality, e.g. making a GUI unresponsive, while some calculation is happening in an attached logic module. Also, the instantiation of objects for the module classes would lead to a one-directional flow of communication. For example, a function in a logic module could be called from a GUI module, but never accessed from a hardware module. This is where the multi-threading capability of PyQt comes in. In PyQt signals and slots can be used to communicate between different event loops belonging to different threads or

different levels of the same thread. Each event loop can be filled with a list of tasks that will be executed in succession. Signals can be used to add tasks to this event loop. Now, the flow of information can be bi-directional. For example, instead of calling a logic function from a hardware module, which is not possible, a hardware module can now emit a signal indicating the acquisition of some data. This signal is connected to a slot in the logic module. Upon emission of the signal, the slot is activated, adding some function evaluation or other task to the event loop of the logic module. PyQt offers exciting possibilities, but some pitfalls should be kept in mind when using the multi-threading functionality. The communication structure described can lead to recursive function loops when not handled with care. In a complex program it is a constant danger to lose track of all communication pathways, possibly leading to unwanted cyclic dependencies. In addition to the mentioned structure, other structural elements have to be included to prevent this eventuality. Our solution to this issue is discussed in the section about parameter handling. Furthermore, when multiple modules fill up the event loop of another module, the order in which these tasks are executed is usually important. By default, tasks are placed at the end of the event loop. However, signals can be configured, so that their task is placed next in line for execution. This functionality should, however, be used with care, since it leads to problems if multiple such requests are issued simultaneously. Also, it should be prevented that certain signals clutter the event loop of a module. This was the case with usage of certain GUI elements and is discussed in the section about timers (subsection 8.2.4).

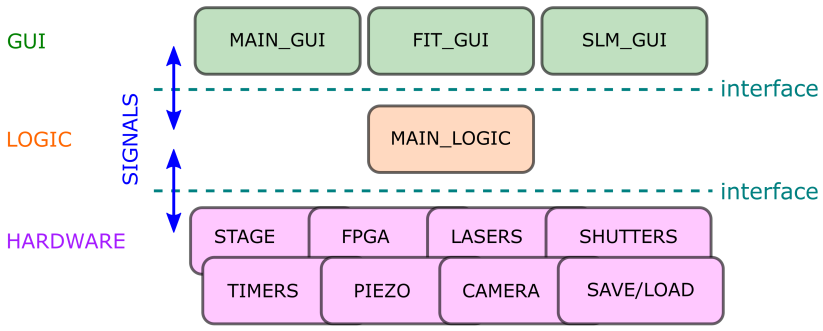

Figure 8.1.: Sketch of the underlying distinction into GUI, logic and hardware modules of the microscopy suite. Interfaces are used to connect new modules and communication across interfaces is handled with PyQt signals.

8.2.2. User interaction

To start interacting with the software, the QuDi manager needs to be started from the "start.py" script. The manager shows a list of all modules that are defined in the current configuration file. From this list, individual modules can be initiated. However all modules that have direct dependencies will automatically be started as well. All hardware modules also have dummy versions that can be defined in the configuration file. These dummy modules are used to start up the suite, if hardware is temporarily unavailable or for debugging and development purposes. The QuDi manager also has an iPython console that allows command line access to the main logic thread and all objects of the program. In this way, parameters that should not be accessible through the GUIs can be changed. After starting up the modules, the GUIs can be used to operate the microscope. As depicted in Figure 8.1, there are three GUI modules and each module is operated from a separate window.

Main GUI

Through the main window (Figure 8.2), imaging commands are executed and all necessary imaging parameters are defined. It has multiple tabs on the right that give access to scanning parameters, image saving/loading and overlay options, piezo mirror control and advanced parameters. Several sliders can be used to change the position of the piezo scanning stage or the scanning mirrors. The center piece is a customized PyQt ImageView object that is able to show acquired images and that has interactive mouse control. The mouse wheel can be used to zoom, a left mouse click can be used to move the confocal volume to a desired location in the accessible stage volume, and the right mouse button opens a menu that provides optional *.png export of the current image. The color bar on the right can be adapted to change the brightness scaling of the image. In addition to scanning, the main window also contains buttons that provide console output of FPGA debugging parameters and the buttons that are used to inject scripts during run-time.

Fit GUI

The fit GUI is used to display fitted data and a photon counter (Figure 8.3). It also is used to start manual refocusing. In refocusing, the stage can be moved in a range around its current position while collecting either reflected light or fluorescence, in order to trace the shape of an object. For example, if a gold bead is placed at the center of a Gaussian beam PSF, a movement with constant speed along one of the stage axes will produce a counter

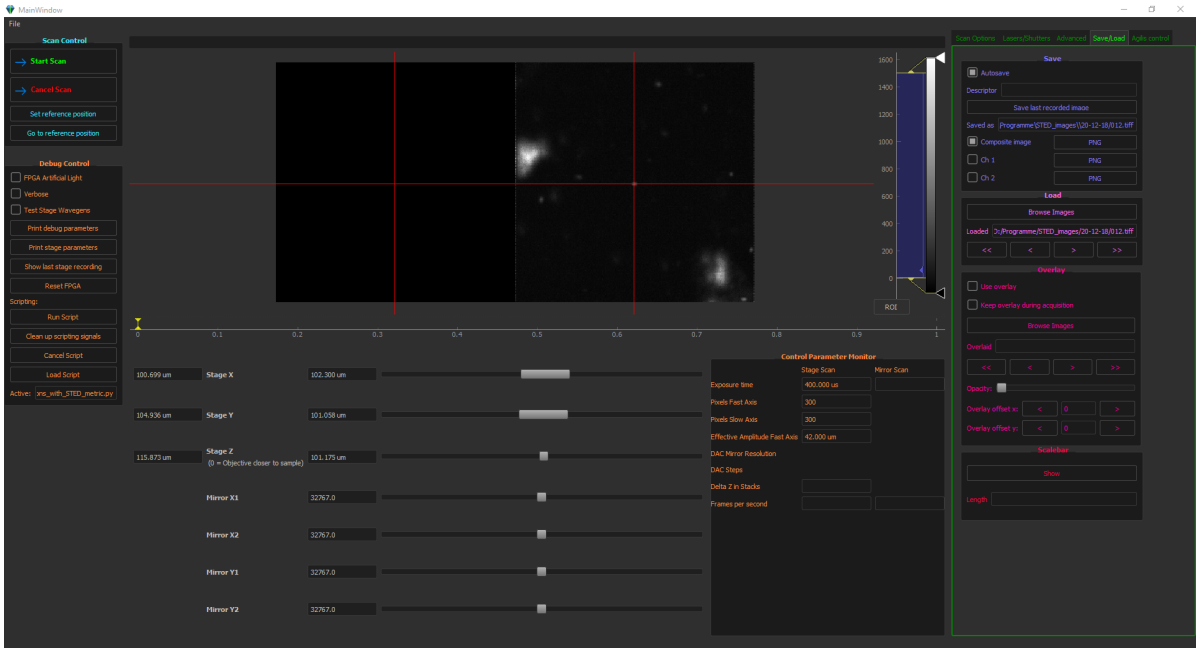

Figure 8.2.: Image of the main GUI window. From here, image acquisition is started and imaging parameters are set.

trace of Gaussian shape. This data can then be fitted, and the bead position along the axis can be calculated. This will also work if the bead is slightly off-center from the beam PSF. The procedure can therefore be used to move an object into the focus of a beam, hence the term "refocusing". This is an important procedure to counter drift in many different applications, for alignment of the laser beams in relation to each other and PSF read-outs for adaptive optics (AO) algorithms. By default, three fitting profiles can be chosen through the GUI, a Gaussian, a parabola or one that is a combination of both. These profiles can be used to refocus onto a Gaussian PSF or a STED PSF. Since the stage has some inertia, the actual position is leading the position sensor output. This can be compensated for with a lag parameter for each axis. With the help of lag compensated refocusing, the beams can be overlapped with an accuracy of $10\,\mathrm{nm}$. Since the microscope has one piezo electric mirror mount in each beam path, in the future the overlap of the beams could be automated with a script that uses refocusing.

SLM GUI

The SLM GUI consists of two windows, one window for user interactions and a second window that is sent to the SLM and displays phase profiles (Figure 8.4). In general, the

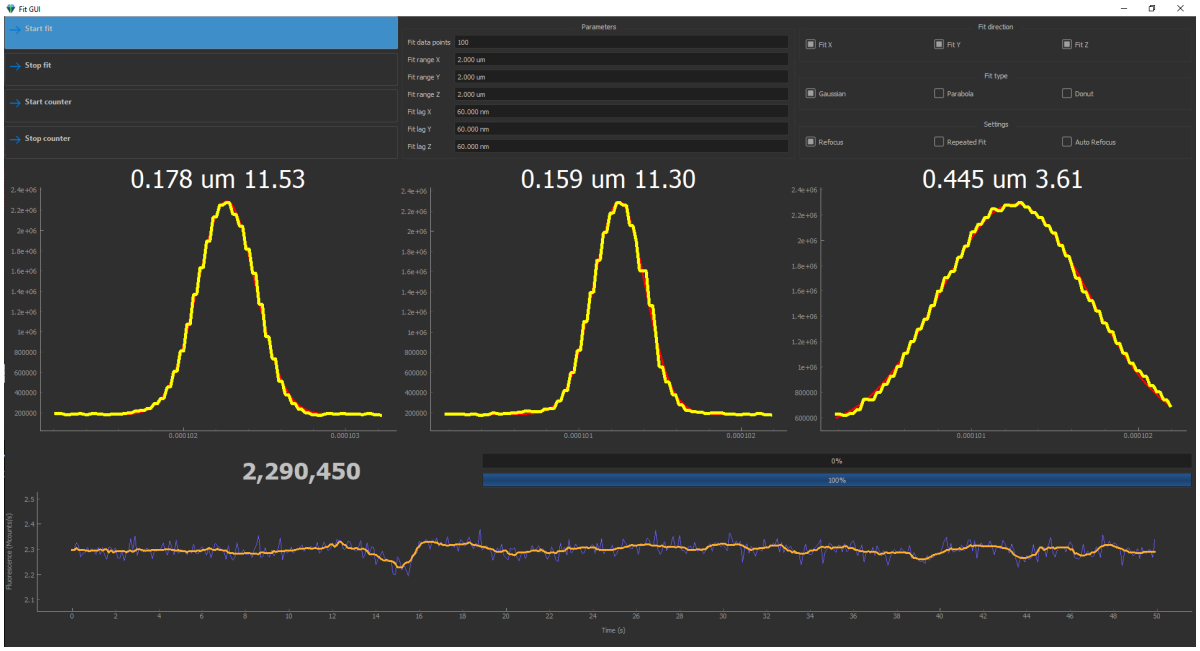

Figure 8.3.: Image of the fitting GUI window. Counter traces for all three stage dimensions can be acquired here. This is typically used to move the confocal volume onto point sources, like gold beads. The numbers in larger font above each fit represent the σ value of the Gaussian fit and the SNR. These are helpful to monitor the PSF from a position next to the optical table during detection alignment.

phase profile is a linear combination of several phase profiles or phase functions. The GUI contains a toggle button for the correction profile and a drop-down menu for all other functions. This drop-down menu contains Zernike polynomials, but also blazed gratings and a razor blade function. Behind this drop-down list is a dictionary that lists the contribution of each function to the current phase profile. It is defined as a persistent variable, so all beam manipulations will be saved automatically when the program is shut down. As discussed, the SLM is recognized by Windows 10 as a monitor. Care should be taken when adding or removing monitors from the PC, since this can change the indices of the connected monitors. In this case, the index of the SLM needs to be queried and manually changed in the GUI file before program start. The user GUI also contains two tabs for image displays. One is mirroring the phase profile of the SLM, intended to monitor correct SLM operation, while the other tab is intended for the readout of the Zyla4.2 CMOS camera.

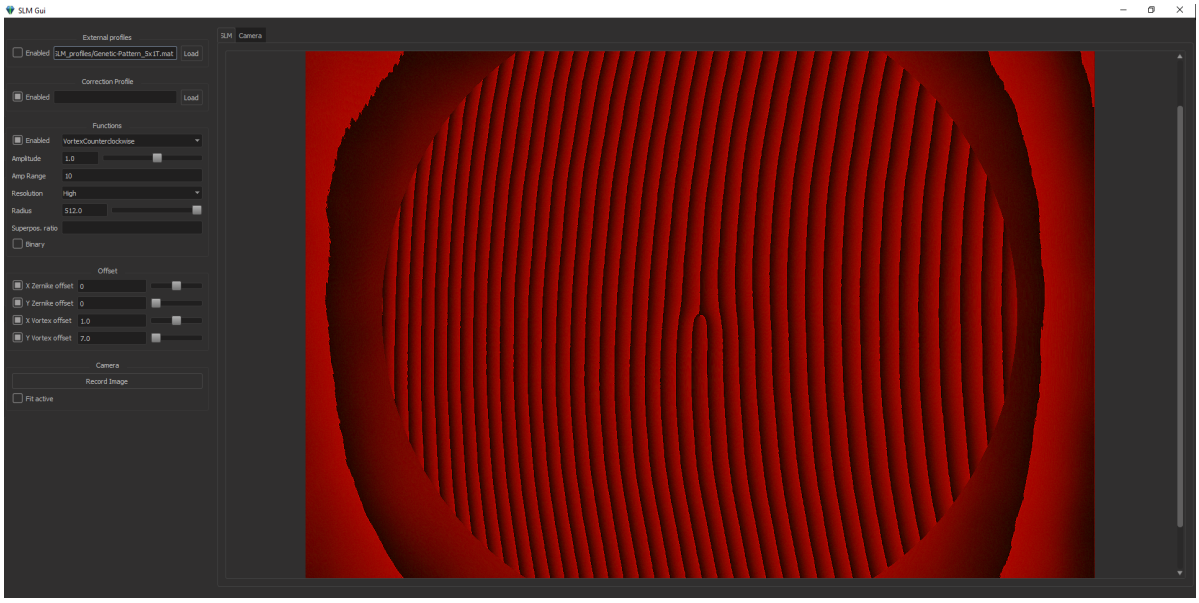

Figure 8.4.: Image of the SLM GUI window. Here, all phase profile alterations can be performed.

8.2.3. Parameter handling

The parameter update function in the main logic module is the single most important function in the software. This function and its dependencies represent the core structure of the microscope software. It was designed to create a software that is both stable and flexible. The function controls all user interactions with the program, contains a list of sanity checks, and initiates a series of responses, individual to each parameter.

The parameter update function takes the arguments parameter, value, unit, data_type and scale. The arguments parameter and value carry the name of the parameter and the desired value as strings, while the arguments unit, data_type and scale are used to interpret the value correctly. For example, one of the GUI inputs is intended to specify a scan range. The GUI element is then connected to the function with the arguments unit='um', data_type='float' and scale=1. A user can then simply enter any floating point number and it will be interpreted as a distance in micrometers. But more than that, specifying the unit as micrometers enables a regular expressions check that will search the input value string for other units related to length. After the parameter update is finished, the value in the GUI element will be updated with micrometers as unit. This enables flexible inputs for the user, but also shows the intended order of magnitude for these inputs. The parameter scale can be used, if third party modules are not using SI units and the value needs to be scaled prior to storage. After correct interpretation of the entered value, two

dictionaries that might contain the parameter are checked. The first is a dictionary of parameter boundaries the second is a dictionary of currently blocked parameters. If the parameter is outside its specified boundaries, the update is aborted and the main GUI shows an error message. The same is true when the parameter is blocked, e.g. the scan direction cannot be changed during an active scan. After confirming a valid update request, the persistent parameter is changed, and a signal is emitted to trigger a function call to a method that updates parameter dependencies. In this method, another dictionary is used to determine the programs response to the parameter update. It contains two lists of methods, one for logic responses and one for hardware responses. The logic list consist of function calls to all methods that calculate derived parameters, while the hardware list contains function calls to hardware methods. The method then iterates through both lists in succession, making sure that all responses are executed in the correct order and any hardware response is run with the new parameter values. Here, the flow of information is restricted by the order of the lists in the dictionary. The parameter update method and the dependency update method make the program very stable and make it nearly impossible for a microscope user to enter faulty values at any point. The only critical point is the correct ordering in the update lists, which has to be reviewed, every time a new parameter is added to the software.

8.2.4. Timers

The timer module contains an infinite loop with a run time of approximately $1\,\mathrm{ms}$. This time is solely determined by the time for all function executions in the loop and is measured each cycle by noting the system time. Comparing the current time to the system time will lead to a better accuracy, compared to using the Python module "time". Timers with defined time-out duration can be added to this loop and in each loop iteration the time that has passed is subtracted. As soon as the timer runs out, a signal is emitted, notifying the system of the time-out event. This signal can be connected to any desired functionality. Timers can be configured to be executed once or perpetually. For example, a perpetual timer exists that reads out photon counts per second with an update time of $100\,\mathrm{ms}$. The timer module was thought up, after realizing that GUI sliders in PyQt will constantly send update signals as fast as their function execution time permits. This clutters the event loops in an unnecessary manner and leads to program instability, for example, when using any slider while imaging. Since the number of USB interactions with the FPGA is limited, sliders and the photon counter were reduced to 10 timed updates per second to leave enough FPGA interactions for stable imaging.

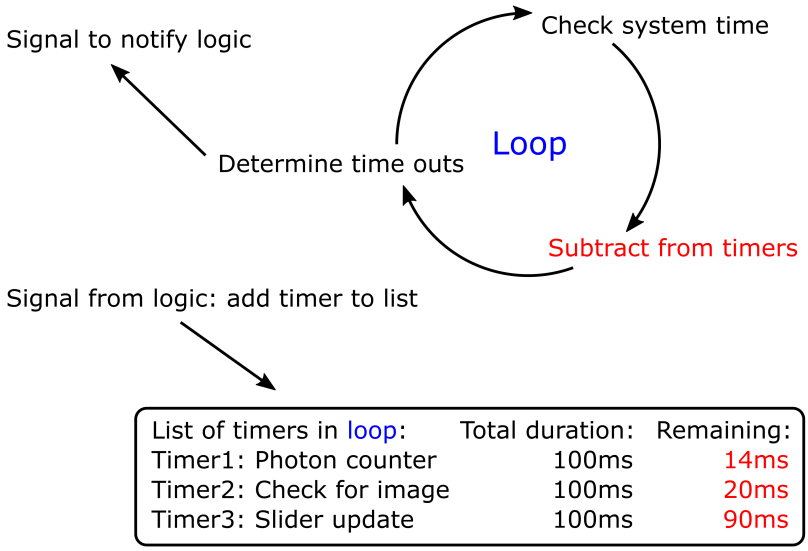

Figure 8.5.: Sketch of the timing module. The list of timers shows which logic function is connected to its timeout. Timers can be added by requests from the logic module. In a loop, the system time is measured and the difference to the last loop iteration is subtracted from the duration of the timer. As soon as the remaining time is $\leq 0\,\mathrm{s}$, a signal is emitted that notifies the logic module.

8.2.5. Image acquisition

To acquire an image, the software has to work in tandem with the FPGA. This is sketched in Figure 8.6. The FPGA does not require a specific signal to start acquisition. As described in chapter 7.5.2, it simply reacts to the trigger signals that indicate when individual pixels should be written and when light should be collected. After setting the desired scan parameters through input fields in the main GUI, a button click can initiate a scanning process with either the stage or the mirrors. Then, either the stage controller or the scan controller in the FPGA will begin to iterate through the stored waveform and emit the corresponding trigger signals. As soon as an image is available for transfer, the FPGA will notify the software. There are two communications following this notice. Firstly, the software will request a pre-load of the outgoing first-in, first-out (FIFO) buffer at the FPGA. After receiving a confirmation from the FPGA, it will activate a pipe transfer of the image. Upon completion of the transfer, the image is written into a class variable of the main logic and sent to the main GUI for display. As previously described, the FPGA can handle simultaneous acquisition and transfer. This means that the method that requests the pre-load can also initiate another scan process for further images in a timed series, stack or video.

8.2.6. Scripting

QuDi comes with a Jupyter notebook[58] interface. This is a scripting environment that is used to interact with software, while simultaneously enabling plotting of data. In principle it is very powerful. However, the interaction between QuDi and the Jupyter notebook kernel proved to be unstable. Also, it did not provide interactivity in a desired manner, since no way could be found to re-write functions and classes at run-time and use all PyQt signaling functionality.

We therefore implemented our own method of scripting. For prototyping, debugging and measurement scripts, the aim was to inject arbitrary code on run-time. To add this functionality, several methods were added to the logic and buttons were added in the main GUI. This proved to be very useful and all measurements that exceed simple image acquisition make use of this functionality. The syntax of scripts and the usage of this scripting capability is described in greater detail in appendix A.2.

8.3. Software compendium

There are many tasks related to data analysis or implementation of algorithms that are not connected to scientific instruments. For simple data fitting, Origin is a good choice. It comes with many predefined functions, and fits can be evaluated within seconds. For more complex algorithms and plotting of data, Matlab was used throughout this thesis. It was used for all PSF calulations in chapters 4/5 and was used to create most data plots for this thesis. Furthermore, Autodesk Inventor was used to create all CAD models, drawings for the mechanical workshop and a few illustrations. For image processing the free software ImageJ was used (FIJI package). It is very practical, since *.tif files can be displayed and processed. It comes with features for multi channel images and image stacks, perfect for microscopy.

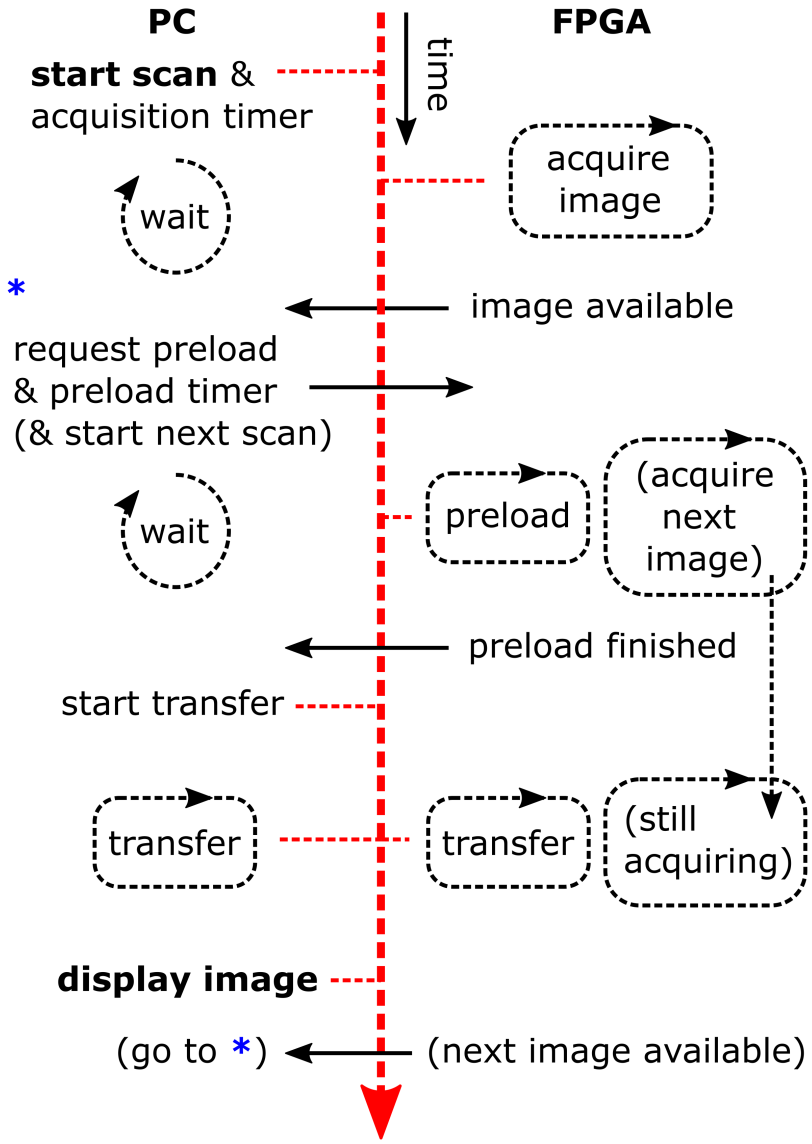

Figure 8.6.: Data flow over time for PC and FPGA during image acquisition. The start of further scans is optional, and all related tasks are depicted in brackets.

9. Measurements

In this chapter we will review the microscope performance in its current state. More general comments on our spatial light modulator (SLM) can be found in chapter 4.3 and numerical calculations for multi-beam stimulated emission depletion (STED) in chapter 5. In the first two sections, we will take a look at the diffraction efficiency of our SLM in single and multi-beam operation and review multi-beam point spread functions (PSFs) on confocal images of gold beads. In the last section we will present a comparison between confocal and STED images and give estimates on the maximum achievable STED resolution. Although both excitation beams still lack diffractive optical elements (DOEs) for multi-beam expansion and the microscope can currently only be used with dual-color single beam imaging, we can already predict its resolution for multi-beam imaging with the help of the diffraction efficiency measurements. As a preliminary experiment that showcases multi-beam STED imaging, a single beamlet of a multi-beam STED array was used in tandem with the $592\,\mathrm{nm}$ excitation beam. This will conclude the performance evaluation of the current microscope capabilities.

9.1. Spatial light modulator optimization

The first measurements with the SLM showed asymmetric diffraction behavior for the horizontal diffraction direction. Discussions with the manufacturer (Hamamatsu) and Gregor Thalhammer (Institute of Biomedical Physics, Innsbruck) revealed that this behavior is expected and due to the electrode geometry in the SLM. This leads to an asymmetry in the display of phase steps with large amplitude. To analyze this behavior, it was recommended that we look at a binary grating. At an ideal binary grating the beam will be diffracted in multiple orders, while the largest amount of transmitted intensity can be found in the first orders, left and right of the zero order with zero intensity. Through the imperfect diffraction at the SLM it is expected that the zero order contains considerable amount of intensity, with reduced intensity in the first and higher orders. We displayed a grating with pixel period of two pixels and control values that should correspond to phase values of 0 and π and measured the power of the zero-order and the first diffraction orders with a power meter.

Indeed, there was a considerable amount of power in the zero-order. To compensate for the pixel cross-talk the upper phase value of π was multiplied by an increasing scaling factor k during the measurement. For a binary grating, this multiplication with a scaling factor $k > 1$ is analog to the de-convolution for edge enhancement discussed in chapter 4.3.1 that is intended to reduce pixel cross-talk. Figure 9.1 shows the results of this measurements. We can see that only for the vertical direction (b) an increase in k leads to a significant and symmetric improvement. At a horizontal grating (a), the power in the zero-order can be reduced, but only at the cost of a similar decrease in the diffraction efficiency of the first orders. The SLM casing geometry contains mounting threads that suggest the use of a horizontal blazed grating for diffraction of the STED beam in a plane parallel to the table surface. The measurement therefore indicates that the direction of the blazed grating will have a significant influence on the diffraction efficiency and should be considered when aligning the STED beam. It also suggests that the entries in the kernel (Equation 4.23) for multi-beam profiles have to be different for the vertical and horizontal direction and that the entries in the horizontal direction have to be asymmetric.

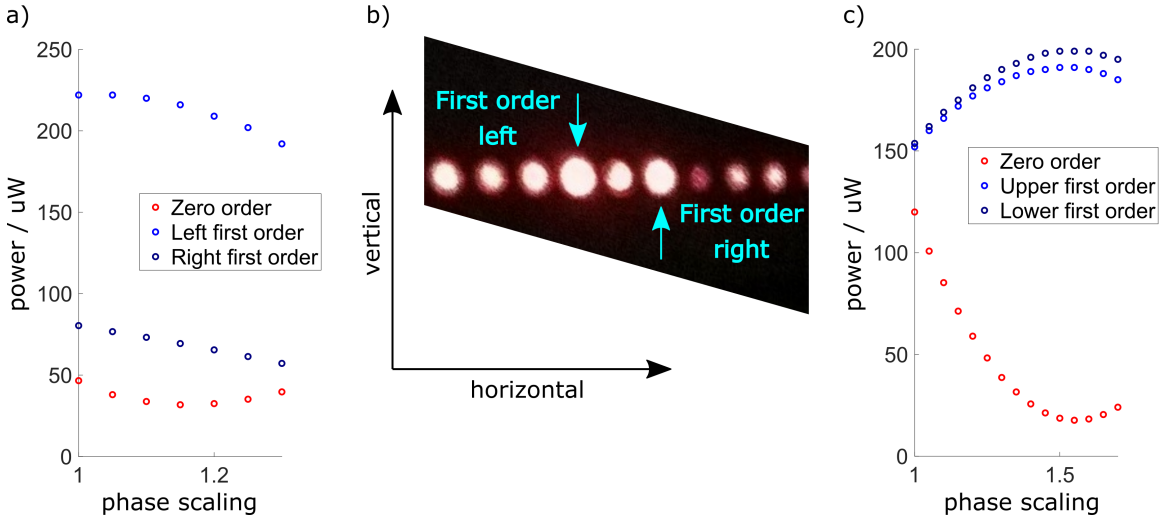

Figure 9.1.: Power measurement of the first orders and zero orders at a horizontal and vertical binary grating. Starting from control values that correspond to 0 and π in the calibration curve the SLM phase display is scaled with a factor k to compensate for the low-pass behavior of the SLM phase display. a) Horizontal binary grating. It can be seen that both first orders are strongly asymmetric. b) Photo of diffraction pattern resulting from the horizontal grating in a) on a screen. All right orders are significantly dimmer. c) In contrast, a vertical binary grating shows symmetric behavior among the first orders.

Keeping the previous measurement in mind, we now take a look at the measured values

of diffraction efficiency in the standard configuration for single beam imaging with the use of a blazed grating (Figure 9.2). Here, we set an amplitude of 20 for the Zernike mode "tilt" in the SLM GUI with a radius of 512 pixels. This corresponds to a spatial separation $\Delta x = 11\,\mu\text{m}$ of the STED beam and the zero-order in the focal plane of the objective. With the mode "tilt" the deflection angle lies in the surface plane of the optical table and keeps the beam height constant. The amplitude value of 20 was a compromise of being small enough to still have good diffraction efficiency and being large enough that the zero-order can be blocked with a razor-blade in the de-magnification telescope. Since it was known that the diffraction efficiency is asymmetric, the same tilt amplitude was investigated for a positive and negative deflection angle. This can be adjusted in the graphical user interface (GUI) by simply changing the sign of the tilt amplitude. From the results in Figure 9.1, it was expected that asymmetric kernel entries in the horizontal direction might be needed for the de-convolution. However, the best results were achieved with a symmetric kernel (Equation 4.23) with entries $A = E = B = D = 0.1$ and $C = 0.6$. For a negative tilt value without correction, the diffraction efficiency is $\eta_{-,WO} = 83.12\,\%$, while with correction the value is $\eta_{-,W} = 84.73\,\%$. This is considerably lower than the values for positive tilt $\eta_{+,WO} = 89.36\,\%$ and $\eta_{+,W} = 91.32\,\%$. In summary, using the correct diffraction direction in tandem with the de-convolution makes a difference of about $8\,\%$ in diffraction efficiency for single beam imaging.

9.2. Multi-beam characteristics

After theoretical predictions for multi-beam phase profiles for the SLM in chapter 5, we now turn towards the experimental implementation. Here, we take a closer look at the achievable diffraction efficiency and showcase the resulting field geometries with the help of confocal images on $80\,\text{nm}$ gold beads.

9.2.1. Ghost orders

It should be noted that both the weighted Gerchberg-Saxton algorithm (GSW) and the fan-out algorithm (FOA), as discussed in chapter 5, work best for an odd number of beams per spatial direction. Figure 9.3 shows the diffraction pattern of an 8 by 8 beam array created by a fan-out algorithm (FOA) phase profile and projected onto a screen. In between the desired orders, there is a pattern of so called "ghost orders". This is supposedly due to the fact that phase profiles for an even number of beams contain additional phase jumps with the magnitude π, while phase-profiles for an odd number of beams do not. Therefore, it is

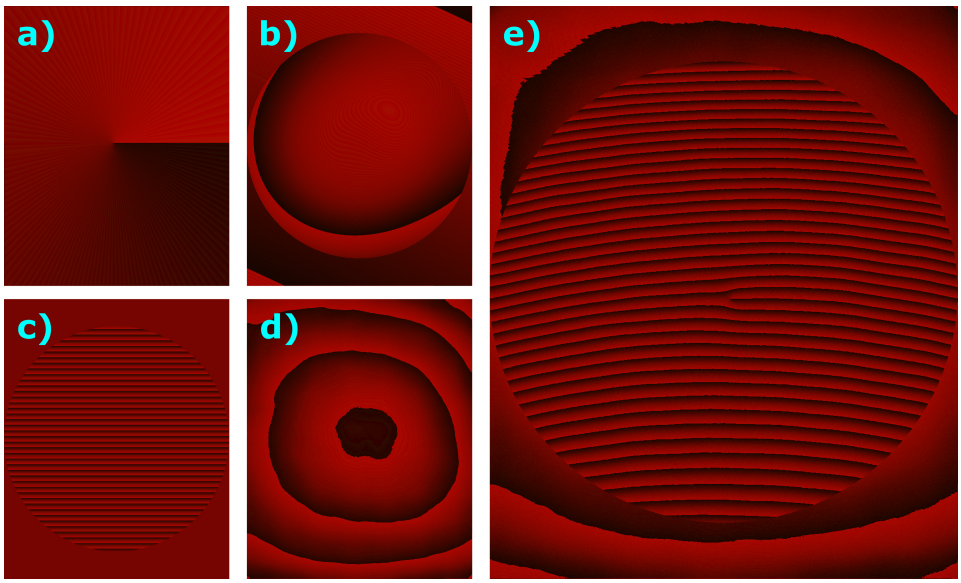

Figure 9.2.: The image shows five rotated and scaled phase profiles for the SLM. Each one has an original resolution of 1272 by 1024 pixels and horizontal orientation. The color information in these images is not post-processed and is sent through the DVI-D connector to the SLM. On a normal monitor the phase profile images look mainly red, since 12-bit control value fills the complete 8-bit range of the red color channel, while only filling the least significant 4-bits of the green color channel (chapter 4.3). a) Phase vortex used to create a STED beam. b) Zernike and tip/tilt correction. c) Zernike mode for tilt used as blazed grating. d) Correction for the inherent curvature of the SLM. e) Composite profile with all corrections. The circle radius for the Zernike polynomials corresponds to the 3σ radius of the laser beam. In this way the whole width of the SLM is used.

possible that these orders arise due to the imperfect display of phase jumps at the SLM. This effect should be considered, and for multi-beam imaging only odd numbers of beams per spatial dimension should be used.

9.2.2. Diffraction efficiency

After getting numerical estimates for the diffraction efficiency in multi-beam phase profiles in chapter 5, we now turn towards the experimental implementation. Here, we will compare the weighted Gerchberg-Saxton algorithm (GSW) as well as the FOA on the same example array that was used in the theoretical predictions. A five-by-five beam array phase profile intended for a $6\,\mu m$ spacing in the sample plane was calculated for a 1.42 NA objective

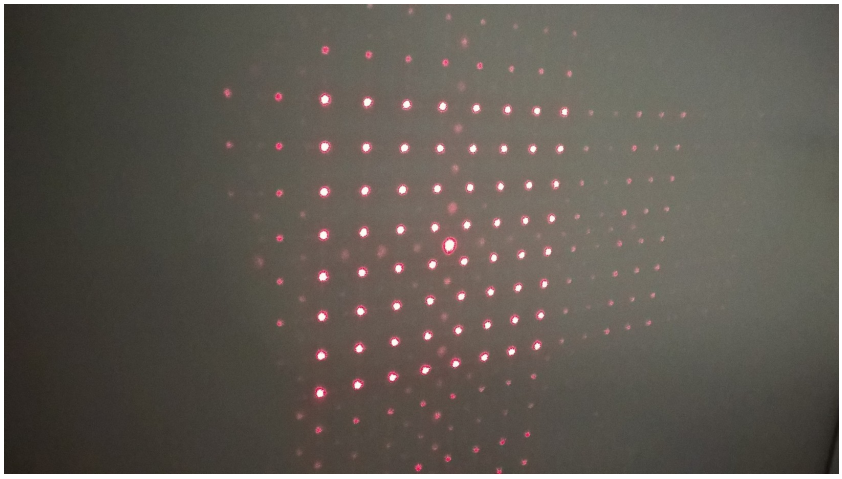

Figure 9.3.: Photo of an 8 by 8 beam array created by a FOA and projected onto a screen. For an even number of beams, the phase profiles will lead to additional "ghost orders" that are visible between the array beams. Additionally, the central zero order carries a large amount of power. Here, the diffraction angles have been amplified by an additional telescope before projection on the screen to clearly separate the orders. This is explained in more detail in the following section (subsection 9.2.2).

with focal length of $3\,\mathrm{mm}$ and a $3\,\sigma$ beam radius of $4.5\,\mathrm{mm}$ that will fill the $9\,\mathrm{mm}$ aperture of the objective. Figure 9.4 shows the respective phase profiles images of both algorithms as intended for transmission to the SLM over DVI-D. Here, the phase information is coded in the red and green color channel of a 24-bit RGB image, as described in chapter 4.3.

To analyze the diffraction efficiency, all diffracted orders have to be spatially separated. Typically, all diffraction angles in the beam bundle are small and even over a distance of several meters the beams will still overlap, prohibiting the intensity readout for a single order. To get around this, the beam can be coupled out in the middle of the telescope that de-magnifies the beam for the microscope objective. By using a second telescope lens with a much shorter focal length we can shrink the beam but increase the diffraction angles. In the standard configuration, this telescope has two lenses with focal lengths $f_1 = 30\,\mathrm{cm}$ and $f_2 = 20\,\mathrm{cm}$ to decrease the beam size by a factor of 1.5 and increase the diffraction angles by a factor of 1.5. For this measurement, the second lens was replaced by a $f_2 = 5\,\mathrm{cm}$ focal length lens.

Figure 9.5 shows the beam array on a laser viewing card with this altered lens arrangement. As can be seen by the image on the right with low ambient light, there are no ghost-orders at a grating with an odd number of beamlets per spatial direction and all higher orders with low intensity have a regular angular spacing. All orders besides the main 25 beamlets

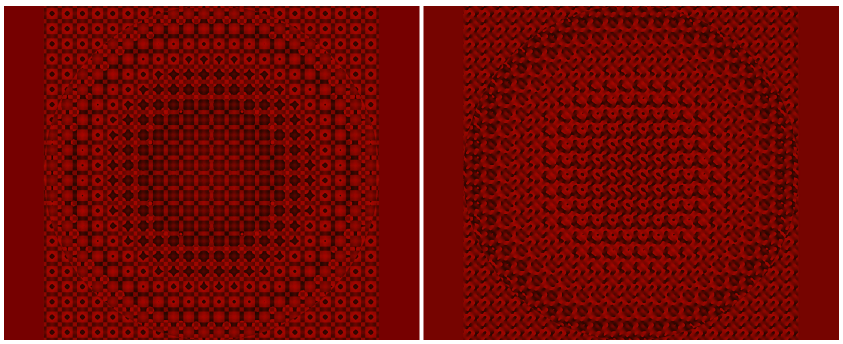

Figure 9.4.: The image shows two different 1272 by 1024 pixel phase profiles for the same target beam array of five-by-five beams with $6\,\mu\mathrm{m}$ spacing in the objective plane. On the left we can see the FOA profile, while on the right we see the GSW profile. The phase profiles contain the control values for the SLM and are coded in the red and green color channel of a 24-bit RGB image, as described in chapter 4.3 and the previous section (section 9.1). The phase profiles of the FOA can be unwrapped into smooth profiles that stretch over a range of more than 2π. This follows from the fact that the profiles are calculated from a superposition of smooth periodic functions with limited spatial frequency content. Although having a smaller diffraction efficiency than the GSW profiles, this makes them more versatile, since they can be manufactured as smooth surface reliefs on optically transparent media. In contrast, the GSW profiles can not be unwrapped.

have less than $1\,\%$ power of any main beamlet and are clearly visible in the image. This suggests that no further orders in the area of the main beam bundle carry a significant amount of power that would lead to problems for multi-beam excitation or depletion.

For an easy measurement of the diffraction efficiency, the $f_2 = 5\,\mathrm{cm}$ lens is positioned as to create a slightly convergent beam. Then, an iris can be placed at the focal point to isolate one of the orders. A mirror was used to move the beam pattern relative to the iris to iterate over all beamlets and measure their power. In principle, this measurement can also be performed with a camera. However, it would require a more difficult acquisition, one where all diffracted orders would need to focus on the chip. This is required to enable a calculation of the absolute power in each beamlet. This is in principle possible, but technically more involved, since the camera chip is small and the lens arrangement has to be fine-tuned precisely. However, a camera based read-out for only the main beamlets is feasible and should be used in the future for an automated uniformity correction procedure, as explained at the end of this section. It should be noted that the standard arrangement of the telescope was specifically designed to amplify diffraction angles in the objective back-focal plane by using the complete SLM surface. This has two advantages. Firstly, a

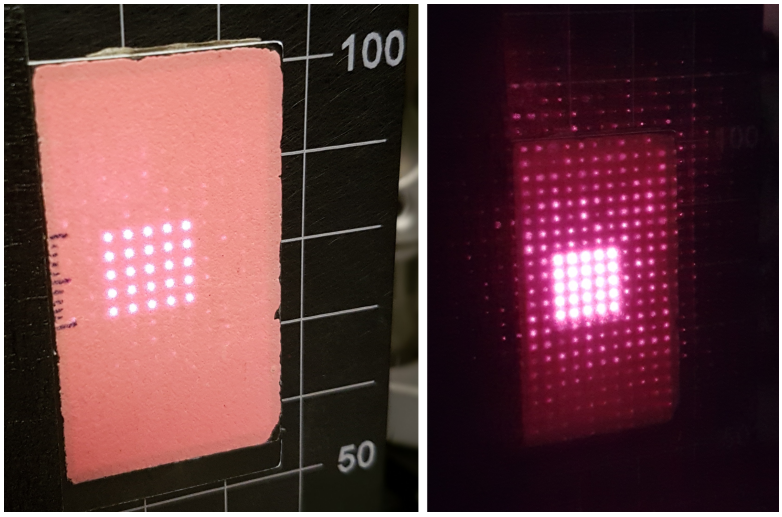

Figure 9.5.: Photos of the five-by-five beam array on a laser viewing card at ambient light and reduced ambient light. The first image is intended to provide a feeling for the spatial size. The scale bar on the card is $1\,\mathrm{cm}$. The second image better shows the higher diffraction orders that carry lower laser power ($< 1\,\%$ in relation to any main beamlet) and emphasizes that no ghost-orders can be seen. Furthermore, since the higher orders with low power are clearly visible, we can expect the pattern to not contain any undesired orders carrying significant power in the main array area.

larger beam distributed over more pixels makes use of higher resolution phase profiles. Secondly, since the diffraction efficiency degrades at larger angles, this enables a larger accessible range of diffraction angles with good diffraction efficiency.

Table 9.1 and Table 9.2 show the beam power distribution, as measured with the power meter, in all 25 beamlets for the GSW and FOA, respectively. Here, we define the diffraction efficiency as the power ratio between the sum of all beamlets and the beam before it interacts with the SLM. The measured diffraction efficiencies in the experiment were $\eta_{D,GSW,exp} = 80.63\,\%$ and $\eta_{D,FOA,exp} = 72.84\,\%$. In terms of diffraction efficiency, the GSW outperforms the FOA. This behavior is consistent with the theoretical results of chapter 5, where $\eta_{D,GSW} = 90.16\,\%$ and $\eta_{D,FOA} = 76.47\,\%$. The general drop in efficiency is also expected, based on the observations about the SLM general performance in chapter 9.1. The numerical predictions for standard deviations in power across all beamlets were $std_{A,GSW} = 3.2 \times 10^{-3}$ and $std_{A,FOA} = 2.8 \times 10^{-4}$. The measured values for the standard deviations of power across the beams are $std_{A,GSW,exp} = 2 \times 10^{-2}$ and $std_{A,FOA,exp} = 1 \times 10^{-2}$. As already expected by the theoretical values, the FOA shows better uniformity. However, since the STED resolution has a square root power depen-

Table 9.1.: Power distribution for the beam array that was created with the GSW profile. The table contains the beam power in all 25 beams in µW as measured with a power meter. The standard deviation of power across the beams is $std_{A,GSW,exp} = 2 \times 10^{-2}$, the diffraction efficiency is $\eta_{D,GSW,exp} = 80.63\,\%$. The total laser power is $9.62\,$mW.

236.4	321	305.4	308.3	313
301	301.9	351.8	310.4	301.8
297.5	324	349.4	319.2	342.4
317.7	319.3	310.7	313	327.7
272.5	290.7	322.9	355.2	285.3

Table 9.2.: Power distribution for the beam array that was created with the FOA profile. The table contains the beam power in all 25 beams in µW as measured with a power meter. The standard deviation of power across the beams is $std_{A,FOA,exp} = 1 \times 10^{-2}$, the diffraction efficiency is $\eta_{D,FOA,exp} = 72.84\,\%$. The total laser power is $9.62\,$mW.

260	280.9	251.4	288.5	275.3
268.5	290.3	276.8	301.5	268.4
254.4	296.2	358	304.4	280.9
275.8	297.4	278.2	308.3	291.2
264.4	284.7	256.5	291.7	279.5

dence, even the largest deviation in beam power will only lead to a difference in resolution of about $15\,\%$. Especially at the power values of the GSW we can see an influence of the general diffraction efficiency decrease at the outer beamlets and also the inherent asymmetry of the diffraction efficiency, due to the asymmetry of the SLM design. However, the homogeneity of the power distribution can be increased for both the FOA and the GSW. Both algorithms, discussed in chapter 5, contain terms that aim at evening out the intensity amplitudes across the beam array. More specific, for the GSW the intensity amplitudes get weighed against their mean value in each iteration and for the FOA we have the standard deviation terms for the intensity in the target function. At these points, we can artificially introduce a bias offset that is based on the experimental values. However, for this to be efficient, a camera-based read-out of the detection efficiency should be used, since this is an iterative procedure that would be too slow and impractical to implement with a manual measurement.

9.2.3. Point spread functions on gold beads

To analyze the point spread functions in an experiment, an $80\,\mathrm{nm}$ gold bead can be scanned through the focal field as discussed in 3.3.8. Since the beam array spans an area of about $24\,\mu\mathrm{m}$ by $24\,\mu\mathrm{m}$, it is important to have a sparse gold bead sample, where single gold beads can be found in an area of this size. In the detection, the channel photo multiplier (CPM) path is used in tandem with neutral density filters to attenuate the reflected light. The $400\,\mu\mathrm{m}$ pinhole in the CPM that is co-aligned with the confocal volume for single beam imaging limits the accessible area while imaging the beam bundle. Light in the focal plane will only pass through to the detection pinhole from a total area with a radius of about $20\,\mu\mathrm{m}$ about the optical axis.

In Figure 9.6, we see the resulting image when a gold bead is scanned through the main beamlets of the 5-by-5 beam array. While the center of the detection volume is at the center of the array (blue circle), the zero order of the SLM coincides with the central beam in the uppermost row (red circle). This is due to the fact that the standard alignment for single beam imaging that also was used here includes a blazed grating intended to spatially separate the confocal volume from the focal point of the zero-order. The diffraction efficiency degrades for larger diffraction angles at the SLM when going from the top row to the bottom row. As mentioned in chapter 5, the homogeneity can be adjusted by reading out the diffraction efficiency decrease and feeding it into the algorithms. However, every correction in homogeneity will be bought with a decrease in overall diffraction efficiency, since power from central orders needs to compensate the power loss at larger angles with poor diffraction efficiency.

The image allows to estimate a lower bound for the accessible range for STED with multi-beam patterns with the current SLM and microscope objective. If we move downwards from the uppermost row that contains the zero order (red circle), we can see that at a certain point (forth row of beams) the diffraction efficiency starts to decrease noticeably. A cross section over this forth row from the top (distance of $18\,\mu\mathrm{m}$ from the zero order) revealed a power decrease between $10\,\%$ to $15\,\%$. Therefore, a $30\,\mu\mathrm{m}$ by $30\,\mu\mathrm{m}$ region should be accessible without a significant reduction ($< 5\,\%$) in resolution or any further compensation for the outer beamlets. Measurements of the central minimum in the STED beams in preliminary experiments on a different SLM from the same company indicated that not just the beam power, but also its beam quality for larger diffraction angles will degrade quickly. This lead to the change in microscope design that included a telescope (T4 in Figure 3.1) for a diffraction angle increase. In general, the total diffraction efficiency could be improved further by using an SLM with a larger surface area (as long as resolution and diffraction efficiency are similar). A larger surface area then would translate to a

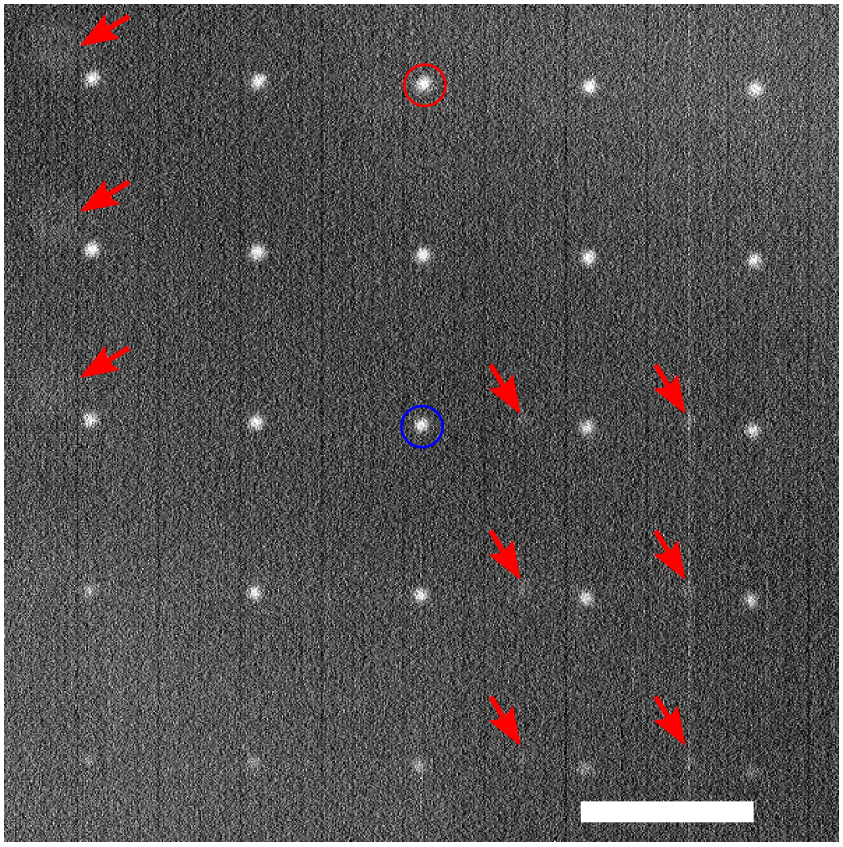

Figure 9.6.: Confocal image of the five-by-five beam array as reflected of a $80\,\mathrm{nm}$ gold bead (scalebar $6\,\mu\mathrm{m}$). Here, the central beam is co-aligned with the center of the detection pinhole (blue circle), while the zero-order is overlapping with the central beam in the uppermost row (red circle). The whole array is displaced from the zero-order with a blazed grating in the vertical direction. This is used for single beam imaging to separate the zero-order, which in this measurement coincides with the central PSF in the uppermost row. This image visualizes nicely, how the diffraction efficiency degrades for larger diffraction angles at the SLM when going from the top row to the bottom row. The red arrows indicate the partial patterns of nearby out of focus gold beads. Also, a systemic artifact can be seen in the form of vertical lines. These lines are too narrow, to be caused by scattering and could also be found in single beam images. Furthermore, mirror scanning images and images without a positional trigger of the stage did not show these lines. Since the pixel periodicity of these vertical lines does not correspond to any transfer container sizes in the FPGA, the most likely explanation is an error with the positional sensor readout of the stage.

higher factor (currently 1.5) in the de-magnification telescope in front of the microscope objective and provide larger diffraction angles at the same diffraction efficiency. In the current microscope design we can use multiplexing to divide the accessible area of $30\,\mu m$ by $30\,\mu m$ in each spatial direction by either a factor of 3, 5 or 7 to avoid ghost orders. Higher divisions can not be used in tandem with our detector array that is limited to an array of 8 by 8 single-photon avalanche diode (SPAD) detectors. Since numerical estimates (Figure 5.8) predict that, with a distance of less than $5\,\mu m$ the STED beamlets will start to overlap, a division into 7 beamlets per spatial dimension, or 49 beamlets in total, also represents a general limit for our accessible range and STED images without loss in signal-to-noise ratio (SNR).

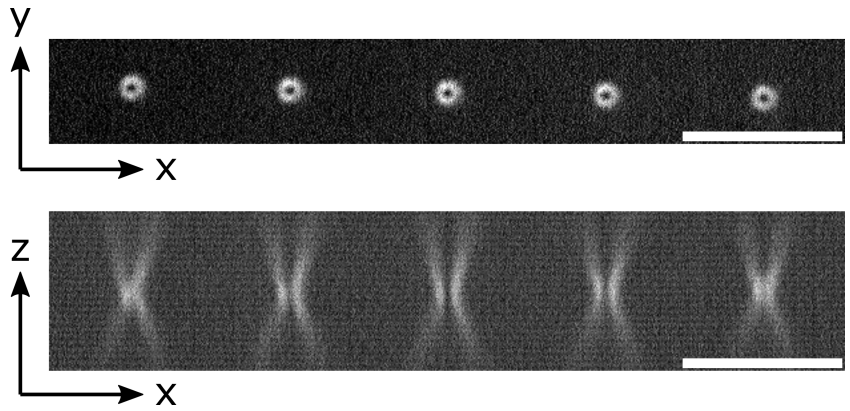

Figure 9.7.: Confocal images of a five by one STED beam array as reflected of a single $80\,nm$ gold bead (scalebar $6\,\mu m$). The upper image shows a x-y scan and the lower image shows a x-z scan. Currently the array is rotated in the x-y plane. As a result, only the central beam shows a clear minimum in the x-z scan, since the other beamlets are slightly out of plane. This is due to the current beam path configuration and can be fixed through the addition of a stable manual vertical translation and tilt stage to the SLM. This was part of the original beam path design. However, it was removed, since the acquired stage (PY005/M, Thorlabs) proofed to be unstable. Here, a better option has to be purchased in the future. Again positional or power fluctuations lead to a periodic image artifact, similar to Figure 9.6.

Figure 9.7 displays a one-dimensional array of STED beams in a scan through the focal plane (top) and a scan along the array dimension and the optical axis (bottom). The scans reveal that the current mirror configuration leads to tilt of the array in relation to the stage axis. This was known beforehand, and can be corrected through a tip/tilt or rotation stage for the SLM. For this purpose, a stage (PY005/M, Thorlabs) was acquired. However, it proofed unstable and was removed from the beam path. It should be replaced when implementing

multiplexing for the excitation lasers.

9.3. STED measurements

To get an impression of the current microscope resolution, characterization measurements were performed on two different samples. The first is a non-bleaching sample, where fluorescent nitrogen vacancy centers (NVs) in nano-diamonds are dispersed over a cover slip (subsection A.3.1). The second sample is a "STED-nanoruler" from the company GATTAquant GmbH.

9.3.1. Nitrogen-Vacancy centers in nano-diamonds

Figure 9.8 shows a single NV in confocal and STED images for comparison. The pixel dwell time for both images is $400\,\mu s$ and the pixel size is $15\,nm$. For this acquisition, the power of the $592\,nm$ excitation laser was $0.5\,mW$ at a laser repetition frequency of $15\,MHz$, while the STED laser was tuned to $300\,mW$ at a laser repetition frequency of $30\,MHz$.

We can see in the confocal image at the top of Figure 9.8 that the PSF size is not diffraction limited. This due to two reasons. Firstly, the $592\,nm$ excitation laser is still astigmatic and custom lenses have to be acquired for a correction telescope in the future. Commercially available standard focal lengths could not provide the required ratio for correction. Secondly, the fill factor of the objective aperture. Due to the Gaussian profile of the excitation laser, where the 3σ intensity radius corresponds to the objective aperture radius, the aperture was not evenly illuminated. This increases the PSF size by approximately $30\,\%$. To improve the microscope for confocal imaging, it would be an option to overfill the aperture. This would lead to a decrease in PSF size at the cost of laser power and more reflected laser light in the detection originating from reflection at the objective shoulder.

For the STED image, the Zernike polynomials astigmatism and coma were adjusted manually at the SLM until the brightness and resolution was at a maximum. This lead to a reduction of the full-width at half-maximum (FWHM) in the STED image by a factor of six. However, at the same time the maximum count-rate decreased by a factor of two, indicating that in this measurement the optimization on the SLM could be better. The SNR decreased strongly above STED powers of $300\,mW$ through loss in brightness. To acquire STED images at higher laser power, the quality of the STED PSF has to be improved further and the co-alignment of the exciation and STED beam have to be improved. Here, later measurements with the Gattaquant "STED-nanoruler" showed that fine adjustments of the

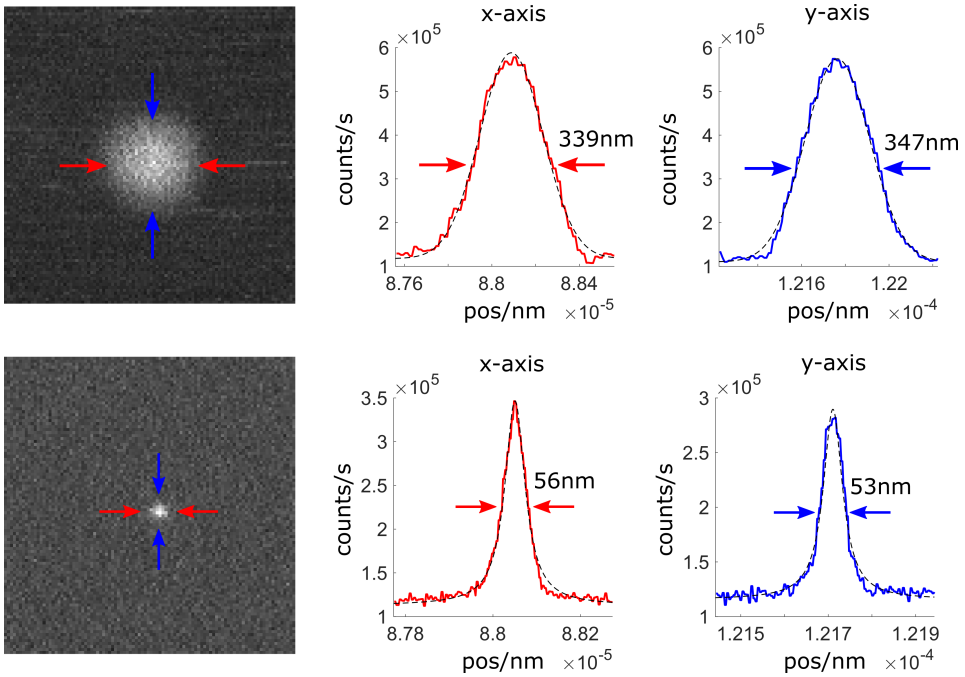

Figure 9.8.: Confocal and single-beam STED images of a NV in nanodiamond. On the right side, the PSF profiles for two stage line scans in directions perpendicular to the optical axis are plotted. The pixel dwell time for both images is $400\,\mu s$ and the pixel size is $15\,nm$. The power of the $592\,nm$ excitation laser was $0.5\,mW$ at a laser repetition frequency of $15\,MHz$, while the STED laser was tuned to $300\,mW$ at a laser repetition frequency of $300\,MHz$. Although we see a resolution improvement of ≈ 6, we should keep in mind that the $592\,nm$ laser is still astigmatic and its PSF size is not diffraction limited. As a reminder, this resolution increase is specific to NVs in nano-diamonds with their value for the saturation intensity I_{sat} (chapter 1.7).

Zernike modes tip and tilt that correspond to blazed gratings, could improve the SNR by providing a finer co-alignment of the zero-position of the STED beam and the maximum of the excitation beam. In the nanodiamond measurement only the piezo fine-adjustment mirrors had been used for relative beam positioning. The resolution in the STED image is improved by a factor of ≈ 6, but, as mentioned before, the excitation PSF size is not diffraction limited. If we calculate the resolution increase in relation to the diffraction limited excitation PSF FWHM of $208\,nm$ the factor is ≈ 4. Since this resolution increase is specific to NVs in nano-diamonds, with their value for the saturation intensity I_{sat} (chapter 1.7), the resolution improvement in other samples has to be measured separately. It should be mentioned that it was tried to increase the STED beam power. However, next to a loss in SNR, at around $500\,mW$ STED power the sample will be affected by local optical damage,

rendering the measurement impossible. It is unclear if the nano-diamond gets damaged or displaced. However, this particular NV could not be found again. Here, a high laser power is only problematic if all laser power is concentrated in a single beam. For multi-beam measurements, the laser power has to be increased, but it is distributed among multiple spatially separated beamlets. Care should be taken to not open the STED shutter before the multi-beam phase profile is loaded onto the SLM. Similarly, while a high power STED beam with larger PSF extent will not induce local optical damage, a Gaussian beam of the same total power can potentially induce optical damage. This means that also the phase vortex on the SLM has to be present before opening the STED shutter. Since the SLM update function has a run-time of about 1 second, this should be considered especially in scripted and automatic measurement series.

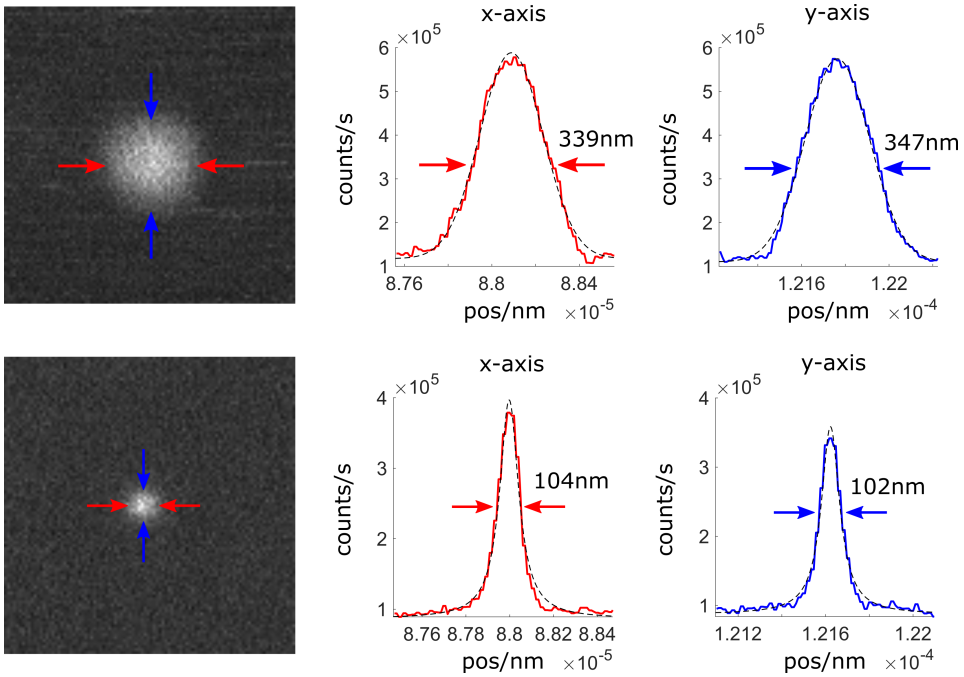

Figure 9.9.: Confocal and multi-beam STED images of a NV in nanodiamond. On the right side the PSF profiles for the two directions perpendicular to the optical axis are plotted. For this acquisition, one of the outer beamlets of a 5-by-1 beam array was overlapped with the excitation beam. Again, the pixel dwell time for both images is $400\,\mu s$ and the pixel size is $15\,nm$. The power of the $592\,nm$ excitation laser was $0.5\,mW$ at a laser repetition frequency of $15\,MHz$, while the STED laser was tuned to $300\,mW$ at a laser repetition frequency of $300\,MHz$. Since now the same STED power is distributed among five beamlets, the resolution increases by a smaller factor of ≈ 2 in relation to the diffraction limit.

As a second measurement on NVs, a 5-by-1 beam array pattern was loaded onto the

SLM to test how multi-beam profiles would behave in STED measurements. The laser power settings were kept constant, distributing the same laser power across five beamlets. The STED beam pattern was displaced to not overlap the center beam, but one of the outer orders with the excitation beam. This configuration was then used to acquire the STED image shown in Figure 9.9. As we can see, the resolution decreases by a factor of two, while the power approximately decreases by a factor of five. This corresponds to the expected behavior, since the resolution increases with the square root of the STED power. Also, the effect of maximum brightness reduction is slightly reduced, as expected for lower STED powers due to the non-linearity of the depletion effect.

Currently it is difficult to perform more precise characterizations of the resolution increase. This is due to the fact that the current microscope stage has a positional instability of about $15\,\mathrm{nm}$ perpendicular to the optical axis and $20\,\mathrm{nm}$ in the axial direction. In the future it should be replaced by a better stage. This positional instability leads to large variations in the recorded effective PSF shape. Particularly the maximum count rate could not be measured precisely. However, with the current measurements of the diffraction efficiency and resolution increase, we can give a lower limit to the resolution that will be reached in multi-beam imaging on nano-diamonds. We saw in the multi-beam characterization (especially Figure 9.6) that the diffraction efficiency is mainly dependent on the distance from the optical axis. As long as the beamlets in the array stay inside a radius of about $18\,\mu\mathrm{m}$ from the optical axis, we expect the diffraction efficiency to be comparable for 3-by-3, 5-by-5 and 7-by-7 beam arrays. After passing all optical elements in the STED beam path, including the SLM, about $80\,\%$ of the total laser power reaches the objective in single beam imaging. For multi-beam imaging, the diffraction efficiency decreases from $\eta_{single} = 91.32\,\%$ to $\eta_{multi} = 80.63\,\%$. Therefore, of the maximum available laser power of $3\,\mathrm{W}$ a residual power of about $2.1\,\mathrm{W}$ is distributed among the beamlets. This leads to $43\,\mathrm{mW}$, $84\,\mathrm{mW}$ and $233\,\mathrm{mW}$ per beamlet for 7-by-7, 5-by-5 and 3-by-3 beam arrays, respectively. We then use the powers and FWHM in the single beam NV measurement and the formula of the STED resolution with $NA = 1.42$, $\lambda = 775\,\mathrm{nm}$:

$$\Delta r \approx \frac{\lambda}{2\,NA\,\sqrt{1+\zeta}} \tag{9.1}$$

Here, Δr corresponds to the FWHM of the effective fluorescent PSF with active STED beam and we express $\zeta = \frac{P_{beamlet}}{P_{sat}}$ not by the crest intensity but by the ratio of the total power in the beamlet $P_{beamlet}$ and the saturation power P_{sat}. We then reach a value of $P_{sat} \approx 6.6\,\mathrm{mW}$. This leads to $\Delta r_{7-by-7} = 100\,\mathrm{nm}$, $\Delta r_{5-by-5} = 74\,\mathrm{nm}$ and $\Delta r_{3-by-3} = 45\,\mathrm{nm}$. It should again be emphasized that these values correspond to a lower bound specific to NVs in nano-diamonds. The current loss in brightness suggests that currently the beam is

not aberration free. With better PSF correction on the SLM, these values can be improved upon. Measurements on the STED nano-ruler, as described in the next section, showed that, with good manual alignment STED imaging without significant amplitude reduction is possible. The drawback is that the manual optimization currently leads to inconsistent results. With a better piezo stage and the replacement of a few optical mounts, the imaging and PSF readout will become more stable and the adaptive optics (AO) approaches in chapter 4.3.5 should lead to a more consistent beam correction.

9.3.2. Gattaquant STED-nanoruler

The "STED-nanoruler" consists of a linear DNA origami structure that is labeled with one Atto590 in the middle and two Atto647n on each end. The two outer fluorophores have a distance of $140\,\mathrm{nm}$. Figure 9.10 shows the comparison of the confocal and STED images and contains intensity profile plots along this "STED-nanoruler". For the acquisition, an area of $15\,\mu\mathrm{m}$ by $15\,\mu\mathrm{m}$ was scanned with $50\,\mathrm{nm}$ pixel size in the confocal image and $20\,\mathrm{nm}$ pixel size in the STED image. The pixel dwell time was $400\,\mu\mathrm{s}$ in both acquisitions. The laser powers were $P_{775\,\mathrm{nm}} = 200\,\mathrm{mW}$, $P_{592\,\mathrm{nm}} = 15\,\mu\mathrm{W}$ and $P_{634\,\mathrm{nm}} = 5.6\,\mu\mathrm{W}$. In the dual-color mode, the STED laser runs at the doubled repetition frequency for temporal color separation, leading to $100\,\mathrm{mW}$ effective STED power per color channel.

In Figure 9.10 a) the difference between the confocal and the STED image is shown. The zoom in a) highlights that all three fluorophores of the nanorulers can be resolved. For this acquisition, the manual optimization of the STED PSF on gold beads was particularly successful with a good central minimum. The measurement reflects this and shows no relevant drop in maximum fluorophore brightness. In contrast, earlier measurements on the same nanoruler sample with an older manual correction routine lead to a large loss in brightness. Therefore, it should be emphasized that any future researcher using the microscope should carefully follow the current best practice as described in chapters 3.3.8 and 4.3.4 until a reliable automated correction can be implemented. In b) and c) of Figure 9.10 we can see the brightness profiles across one of the nano-rulers in the yellow color channel and red color channel, respectively. These profiles were extracted from the original STED image with the program ImageJ, an image processing software, and plotted with Matlab. As we can see from image profiles, the STED resolution is on the order of $55\,\mathrm{nm}$. However, for this line plot a nano-ruler was chosen that looked comparatively unaffected by scan artifacts. The average over 10 different nano-rulers currently shows a mean value of $62\,\mathrm{nm}$ for Atto647n and $70\,\mathrm{nm}$ for Atto590. The reason for this becomes clear if we take a closer look at the zoom in Figure 9.10 a). Independent of the resolution, emitters in STED images are expected to show a brightness distribution that reflects the symmetry of the excitation

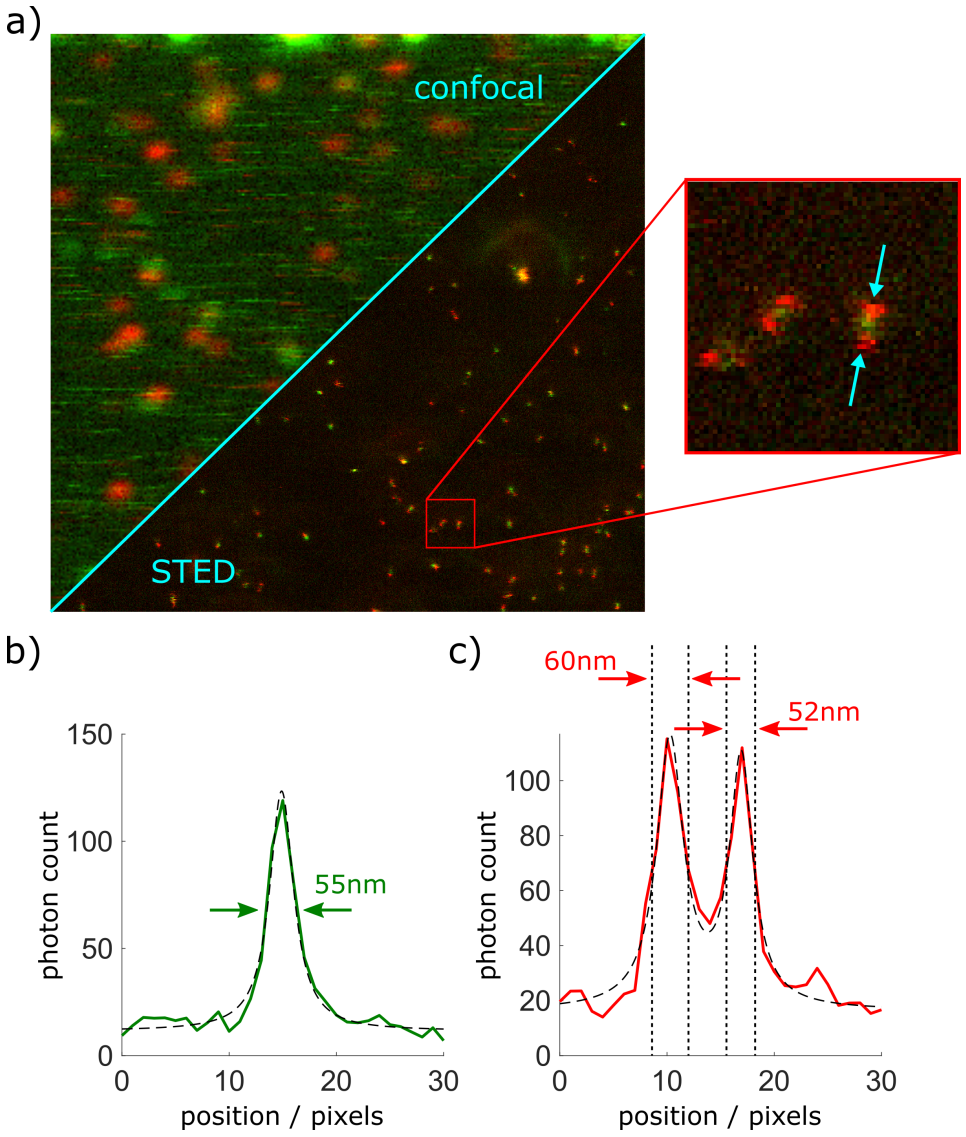

Figure 9.10.: a) Comparison of the Gattaquant "STED-nanoruler" in confocal and STED acquisition. A $15\,\mu m$ by $15\,\mu m$ area was scanned with a pixel dwell time of $400\,\mu s$ and a pixel size of $50\,nm$ (confocal) and $20\,nm$ (STED). The inset shows a close up that shows that all fluorophores can be resolved. Here, the distance between the middle label (Atto590) and the outer label (Atto647n) is $70\,nm$. b) and c) show Matlab plots of the intensity profile along the axis of the nano-ruler as extracted with ImageJ for the yellow (b) and red (c) color channel. The resolution is indicated by the values for the FWHM of each individual peak.

and more importantly the STED beam. It is save to assume that currently the brightness distribution of each emitter is mainly distorted by positional noise and does not reflect the circular symmetry of the STED beam. As a result, the value of the resolution can not be measured accurately and has to be re-examined, as soon as the microscope stability has been improved.

Similarly to the STED image, profiles across the nanorulers have been taken from the confocal image (not shown). Their PSF size is on the order of $394\,\mathrm{nm}$ for the red channel and $460\,\mathrm{nm}$ for the yellow channel. On the first glance this is counter intuitive, since the diffraction limit should lead to a narrower PSF for a lower wavelength and additionally there are two red emitters in each nanoruler. However, currently the $592\,\mathrm{nm}$ laser does not have any ellipticity and astigmatism correction. Measurements on our microscope that compared uniform aperture illumination to Gaussian illumination, where the aperture radius corresponded to the 3σ radius of the Gaussian beam intensity, showed a difference in the PSF extent of about $30\,\%$. The diffraction limit (for uniform illumination) at our objective is $210\,\mathrm{nm}$ for the $594\,\mathrm{nm}$ laser and $223\,\mathrm{nm}$ for the $634\,\mathrm{nm}$ laser. If we increase this value by about $30\,\%$ for non-uniform Gaussian illumination, the residual mismatch of the confocal PSF size with the diffraction limit is about $40\,\%$ for the yellow channel and about $30\,\%$ for the red color channel. This indicates that the laser beam correction for both excitation lasers can still be improved.

However, the deviations from the diffraction limit in the excitation PSFs sizes should lead to a negligible influence on the STED resolution according to the calculations in chapter 1.7. The measured difference in STED resolution, with $70\,\mathrm{nm}$ for the yellow color channel and $62\,\mathrm{nm}$ for the red color channel, seems to reflect the size differences of the confocal PSFs and shows a narrower PSF for the longer wavelength. However, this is due to the spectral position of the STED laser at $775\,\mathrm{nm}$ that leads to a higher probability for stimulated emission at Atto647n, which in turn leads to a higher resolution. Although the increased size of the excitation PSFs only slightly reduces the STED resolution in plane samples, it will lead to increased background and out-of-focus light for cell and tissue samples with larger axial extent. For this reason alone, it should be considered to further improve the ellipticity and astigmatism correction of the excitation lasers.

Analogous to the measurement on NVs in nanodiamonds, we can again calculate an estimate for the current resolution in multibeam imaging. A resolution value of $55\,\mathrm{nm}$ correlates to $P_{sat} \approx 4.23\,\mathrm{mW}$ in Equation 9.1. Considering the maximum available laser power at the microscope objective this would lead to $\Delta r_{7-by-7} = 82\,\mathrm{nm}$, $\Delta r_{5-by-5} = 60\,\mathrm{nm}$ and $\Delta r_{3-by-3} = 36\,\mathrm{nm}$.

10. Summary and Outlook

Although stimulated emission depletion (STED) is a super-resolution method that has now existed for two decades, it still is relevant in super-resolution live cell imaging. Other techniques show better resolution or better performance for very small fields of view in particle tracking, but in terms of acquisition speed combined with a large field of view STED is still the best candidate. Since it is ultimately a scanning-based technique, a general limitation is given by the collected fluorescence at any given time. The only way to truly improve in regard to this limitation is to increase the number of confocal volumes and detectors.

During this thesis, a two-color STED microscope was built with the necessary alterations to perform multi-beam scanning in the future. Since previous approaches with regular STED lattices showed intense bleaching, we opted for a different approach, one that will make it possible to combine the benefits of other STED implementations with a higher number of confocal volumes. We use an spatial light modulator (SLM) to create a flexible array of light beams, where up to 49 STED beamlets can be placed in a field of view of $30\,\mu\text{m}$ by $30\,\mu\text{m}$. We showed that a minimal distance of about $5\,\mu\text{m}$ should be kept to guarantee spatial separation of individual beamlets. Since the STED laser power is the main limiting factor in such an approach, we refrained from applying any spatial filter on the STED laser. The beam was instead corrected with the help of a beam profiler, cylindrical lenses and Zernike polynomials on the SLM. The diffraction efficiency on the SLM was optimized and enabled us to use about $80\,\%$ of the total laser power in a multi-beam pattern. In regard to the automatic correction with Zernike polynomials, the tested adaptive optics (AO) algorithms showed promise, but their implementation has to be improved further. Currently, their application is hampered by positional noise of the confocal volume. This needs to be addressed by acquisition of a new piezo stage and the introduction of more stable optical mounts in the beam path. Preliminary measurements suggest that with the current available laser power and STED beam quality the resolution for different rectangular grids will be on the order of $\Delta r_{7-by-7} = 82\,\text{nm}$, $\Delta r_{5-by-5} = 60\,\text{nm}$, $\Delta r_{3-by-3} = 36\,\text{nm}$ and $\Delta r_{1-by-1} = 11\,\text{nm}$. However, these estimations are based on Equation 9.1, they do not include signal-to-noise ratio (SNR) loss, the decrease of the depletion effect through vibrational relaxation rates or optical damage at high laser powers. Therefore, the value for

$\Delta r_{3-by-3} = 36$ nm will only be available with good SNR after further beam corrections and the value $\Delta r_{1-by-1} = 11$ nm is unlikely to be possible without optical damage to a sample. To complement our illumination scheme, a single-photon avalanche diode (SPAD) array detector prototype was integrated into the microscope and combined with multi-channel read-out via a field programmable gate array (FPGA). Currently the acquisition speed is still limited by the galvanometric scanning mirrors leading to a minimal STED acquisition time of 0.5 s for the complete accessible area (30 µm by 30 µm, 12.5 nm pixel size, 300 Hz scanner frequency) and a 7-by-7 beam array. However, the FPGA program will be able to work with faster scanners in the future. The complete microscope control was merged into a modular software suite that can easily be extended with new functionalities. It has an easy-to-use graphical user interface (GUI) that allows for an intuitive control of the microscope, but also features a powerful scripting routine that allows a researcher to include and test new code during runtime. Due to time limitations, the multiplexing of the excitation lasers could not yet be implemented. However, in a first iteration, inexpensive diffractive optical elements (DOEs) are available for multi-beam expansion, albeit with lower diffraction efficiency than the SLM. Since power is not a limiting factor for the excitation beams, this should be readily implemented.

Going forward, two alterations are already planned extensions for this microscope. As mentioned, the first is the multiplexing of the excitation beams, giving full access to multi-beam imaging. The second is a double pass on the SLM. This will give access to three dimensional STED as discussed in chapter 1.8. One half of the SLM will be used for the phase vortex and the second half will be used for a phase piston with variable radius. A custom-made retroreflector to facilitate this double pass has already been manufactured. This addition is foremost intended for the use in single beam imaging with emphasis on the highest possible resolution. Displaying the multi-beam phase profiles on half of the SLM area will limit the accessible diffraction angle range and negate the advantage of the beam de-magnification telescope. Considering that each pass of the SLM leads to a power loss, the best solution for three-dimensional multi-beam imaging is the addition of a piston phase mask as separate optical element. Such a phase mask can simply be placed in the beam path before the SLM. As an alternative for three dimensional multi-beam STED imaging without changes to the microscope, a STED point spread function (PSF) can be created by just replacing the phase vortex on the SLM with a phase piston. The resulting PSF will lead to a more isotropic central minimum and can be used by itself to gain axial resolution at the cost of lateral resolution.

Besides the already planned additions, other techniques (chapter 1.8) can and should be implemented as future extensions of the microscope. All of these techniques aim to lower the light dosage and increase imaging speed. However, this will include varying levels

of technical complexity and variations in implementation. Here, the first focus should be on techniques that can be added without major effort. This includes time-gated STED and power modulation. As already mentioned in chapter 1.8, time-gated STED was part of an earlier microscope design, and the necessary hardware can be connected to the existing laser delay module with minor adaptions. The power modulation method offers a resolution increase of a factor of up to two and only needs an additional computer-controlled rotation mount for the half-wave plate for power control, as well as additional computational post processing. However, since the data analysis in this regard stems from the field of fluorescence lifetime spectroscopy, there already is a large basis of existing research.

After these two additions, the focus should be on the structured illumination approach and the variable pixel dwell time approach. As proposed in York, Ingaramo, and Cooper (2017) [25], the STED PSF can be altered to have a phase step instead of a vortex. In the focal plane this leads to two elongated "lines" of intensity, leading to images with higher resolution perpendicular to the line direction. To compensate for the non isotropic resolution, the direction of resolution increase needs to be rotated on the SLM in several consecutive images. Then, a composite image has to be calculated in post processing. The implementation of this technique would either need the addition of a rotating mirror element, as proposed in York, Ingaramo, and Cooper (2017) [25] or a rework of the current scanning module in the FPGA. Although scanning in variable directions is technically possible with the current scanning mirrors, the wave tables and their interpretation on the FPGA have to be changed. However, an easy preliminary measurement is possible that will give an accurate experimental estimation of the expected benefit before implementation. Using the STED phase step, an image can be acquired and compared to the vortex image of same laser power. From these images and their Fourier transformation, an estimation can be made, as to how many images have to be acquired and how much the laser power can be reduced. It should be noted that a single image in this imaging scheme only needs a line distance corresponding to confocal images. This compensates for the larger number of images that needs to be acquired.

Although pixel-hopping as described in Vinçon et al. (2020) [28] can not easily be implemented, an interesting alteration of this method is possible that potentially even works with multi-beam imaging. Kilian et al. (2018) [2] analyzed the bleaching process in STED and showed that there is virtually no bleaching, as long as only the STED laser is active while imaging. This means it is sufficient to shut off the excitation beam for the remainder of a pixel dwell time. Although this will not lead to a speed increase, it will lead to the same reduction in bleaching. This can be implemented with an acousto-optical modulator (AOM). Already today, acousto-optical modulator (AOM) arrays are commercially available that

can not only control a single beam of light, but a linear or two dimensional array. Laser beams that get diffracted in AOMs usually suffer from degradation of their spatial profile. However, the shape of the excitation beam is far less crucial for STED imaging. For this method, two alterations to the FPGA have to be implemented. First, thresholds have to be included in the detection module that decide, whether a pixel can be considered empty or enough light was collected to correctly estimate the counts for the rest of the pixel dwell time. Second, another digital output on the FPGA would have to be implemented. The addition of thresholds is a minor adjustment, but a new parallel port will most likely exhaust the routing resources on the FPGA or the available FPGA pins. In this case, it is necessary to buy another FPGA and separate the mirror scanning module and data acquisition on two separate devices. This still should be fairly easy to implement, since both modules only communicate with two single bit signals. This approach looks very promising and I recommend it for a future implementation.

Finally, electro-optical deflectors (EODs) as scanning devices in combination with the multi-beam expansion would push STED microscopy to its speed limit, leading to the currently fastest acquisition time with a large field of view. Although this is difficult to include, it becomes especially interesting when advances in fluorophore chemistry lead to emitters that show less bleaching. Already by itself, scanning with EODs reduces photo-bleaching drastically, as shown in Schneider (2013) [1]. As a reminder, the scanning range of EODs with about $8\,\mu\mathrm{m}$ is just large enough to connect neighboring confocal volumes in multi-beam scanning. Since the acquisition speed is much higher, EODs are used to create a single STED image by multiple passes over the whole image area. Here, the speed is indeed so fast that even in each image line only a subset of pixels is imaged and each line is accumulated over multiple images. This leads to the lowest amount of bleaching for continuous scanning and is coined "interleaved imaging scheme" in Schneider (2013) [1]. It can be implemented into the current FPGA design by integrating pixel values, before transferring them to the synchronous dynamic random access memory (SDRAM).

A. Appendix

A.1. VHDL examples

Every very high speed integrated circuit hardware description language (VHDL) module or submodule can be structured in the same fashion. After a series of import statements, the module declaration, containing the inputs and outputs, is followed by the architecture declaration describing the actions of the module. In the architecture all signals are declared and all submodule types are listed. After a "begin" statement, the main body of the module code follows. Finally, a series of port maps follows to instantiate the submodules and describe the connections between module signals and the in- and outputs of submodules. The following module is a simple example of a top module connecting two submodules. Although VHDL is not case sensitive, it is best practice to capitalize all non-VHDL identifiers.

```
library IEEE;
use IEEE.STD_LOGIC_1164.ALL;
use IEEE.STD_LOGIC_UNSIGNED.ALL;

entity EXAMPLE_MODULE is
  port (
    EXAMPLE_INPUT  : in  std_logic_vector(7 downto 0);
    EXAMPLE_OUTPUT : out std_logic_vector(7 downto 0);
  );
end EXAMPLE_MODULE;

architecture BEHAVIORAL of EXAMPLE_MODULE is
  signal EXAMPLE_CONNECTION : std_logic_vector(7 downto 0);
  component SUB_MOD_A
    port (
      SUB_MOD_A_INPUT  : in  std_logic_vector(7 downto 0);
      SUB_MOD_A_OUTPUT : out std_logic_vector(7 downto 0);
    );
```

```
  end component;
  component SUB_MOD_B
    port (
      SUB_MOD_B_INPUT  : in  std_logic_vector(7 downto 0);
      SUB_MOD_B_OUTPUT : out std_logic_vector(7 downto 0);
    );
  end component;
begin
  SUB_A : SUB_MOD_A
    port map (
      SUB_MOD_A_INPUT  => EXAMPLE_INPUT,
      SUB_MOD_A_OUTPUT => EXAMPLE_CONNECTION
    );
  SUB_B : SUB_MOD_B
    port map (
      SUB_MOD_B_INPUT  => EXAMPLE_CONNECTION,
      SUB_MOD_B_OUTPUT => EXAMPLE_OUTPUT
    );
end BEHAVIORAL;
```

The following examples show how to instantiate variables. It is possible to instantiate abstract data types like integers or direct data types like wires and registers. It should be mentioned that the syntax and action of mathematical operations can differ for different data types.

```
signal EXAMPLE_INTEGER            : integer range 0 to 99 := 0;
signal EXAMPLE_ONE_BIT_REGISTER   : std_logic := '0';
signal EXAMPLE_EIGHT_BIT_REGISTER : std_logic_vector(7 downto 0) := "00000000";
signal EXAMPLE_EIGHT_BIT_WIRE     : std_logic_vector(7 downto 0) := "00000000";
```

The most important sub-structure for any sophisticated module is the process. After the begin statement processes handle most of the data processing and can be made to react to a clock signal, enabling synchronous calculations. Although asynchronous operations take part in most modules, only synchronous calculations enable the construction of large scale programs with many interacting submodules. In the following process, the rising edge of a clock signal is used to increment an 8-bit counter.

```
process(SYS_CLK, SYS_RST) is
  variable COUNTER : integer range 0 to 255;
```

```
begin
  if SYS_RST = '1' then
    COUNTER = 0;
  elsif rising_edge(SYS_CLK) then
    if COUNTER = 255 then
      COUNTER := 0;
    else
      COUNTER := COUNTER+1;
    end if;
  end if;
end process;
```

The signal names in brackets at the begin of the process are the sensitivity list, consisting of all signals that will trigger the process to execute. This list is intended for simulation and not required for compilation (for VHDL the compilation step is divided in synthesis and implementation).

A.2. Scripting in microscope suite

The basic code structure of any script that can be started from the main graphical user interface (GUI) window can be read below. It has to begin with two lists that define desired method names and signal connections that will be used by the script. Besides any user defined methods, two required methods ('run_protocol', 'finish_protocol') are necessary to be interpreted correctly by the logic. The 'run_protocol' method is simply the first method that will be executed by the program. The 'finish_protocol' method should contain a call to the scripting reset routine. The reset routine will disconnect all signal connections that were introduced at the start of the script. An important functionality for signal connections was added with the logic method 'call_method_by_name'. Since PyQt signals can only be defined on object instantiation, after any module start-up no further signals can be defined. To circumvent this restriction a general purpose signal, 'sig_continue_script', was added to the logic. If it is connected with the method 'call_method_by_name', any logic method can be triggered through a PyQt signal (self.sig_continue_script.emit('any_logic_method')). This scripting design gives full flexibility for measurements and allows to weave new functionalities in the existing signal flow.

```
try:
    # Define the methods and signals that will be used by the script
```

```
    self.list_of_methods = ['run_protocol', 'main_script_loop',
                            'finish_protocol', 'user_defined_method_1']
    self.dict_of_signals = {'sig_continue_script':
                                                    ['self', 'call_method_by_name

    def run_protocol(self):
                print("I get executed first.")
                self.sig_continue_script.emit(user_defined_method_1)

        def user_defined_method_1(self):
                print("I triggered through 'call_method_by_name'.")
                self.sig_continue_script.emit(finish_protocol)

        def finish_protocol(self):
        print("Finishing Protocol")
        self.reset_scripting()

    print("New methods have been defined!")

except Exception as e:
    print("This exception occurred: " + str(e))
```

A.3. Sample preparation

All samples have been prepared to be compatible to immersion oil (Cargille™, Type LDF).

A.3.1. Nanodiamond samples

The nitrogen vacancy center (NV) sample was prepared with the help of Richard Waltrich in the Institute of Quantum Optics, Ulm University. They provided us with NVs in nano-diamonds produced by Davydov et al. (2014) [35]. First, the microscope slide and cover slip were cleaned in a custom-built plasma cleaner. Next, the nano-diamonds, provided in an aqueous solution, were diluted in a 1:1 ratio in ultra pure ethanol. To distribute the nanodiamonds on the cover-slip, a drop of $10\,\mu L$ was dropped onto the cover slip that was spinning in a custom-built spin-coater at a rotational speed of 300 rpm. The speed was kept for one minute and afterwards the sample was left to dry for about 15 minutes. Next,

a drop of $5\,\mu$L mounting medium (2,2'-thiodiethanol 97% (TDE), refractive index 1.52) was dropped on the cover slip and the cover slip was placed on the microscope slide. Clear nail polish was used to seal the gap between microscope slide and cover slip to prevent drying out of the mounting medium.

A.3.2. Gold bead sample

Reflective gold bead maps were prepared from $80\,\mathrm{nm}$ gold colloids (ArtNo: EM.GC80, BBI solutions, Crumlin, United Kingdom). As mounting medium, a Mowiol® 4-88 solution was provided by an institute technician. Mowiol® 4-88 is a viscous fluid that, when in contact with air, drys and hardens over a couple of hours. In its dry state its refractive index matches that of immersion oil. For the sample preparation a microscope slide and cover slip were cleaned with ultra pure ethanol and lens cleaning tissues. Since the gold beads tend to aggregate, the stock solution was put in an ultrasonic bath for 5 minutes as a first step. Then a volume of $5\,\mu$L gold stock solution was mixed with $10\,\mu$L ultra pure ethanol. A $5\,\mu$L drop of this mixture was dropped onto the cover slip and dried by applying heat for about 1 second with a Bunsen burner to the underside of the cover slip. A $5\,\mu$L drop of Mowiol® solution was then sandwiched between the cover slip and the microscope slide. The sample was then dried at ambient conditions for 48 hours before first usage.

Glossary

AO adaptive optics. 51, 53, 74, 76, 79, 142, 164, 167

AOI angle of incidence. 22, 29–31, 37

AOM acousto-optical modulator. 19, 169, 170

APD avalanche photo detector. 36, 37, 48, 116, 128, 129

API application programming interface. 137, 138

CPM channel photo multiplier. 36, 37, 48, 77, 79, 157

CW continuous wave. 16, 17

DAC digital-to-analogue converter. xii, 107–109, 115–117, 123–125

DFT discrete Fourier transform. 62, 64, 69, 92

DOE diffractive optical element. 9, 26, 37, 57, 66, 83–87, 149, 168

EOD electro-optical deflector. 18–20, 170

EVM evaluation module. 24, 108, 120, 124, 126

FFC fast focus calculation. 63–65, 89, 93–96, 179, 180

FFT fast Fourier transform. 62, 64, 68, 69

FIFO first-in, first-out. 122, 125–127, 131–135, 146

FOA fan-out algorithm. 84–86, 93–95, 151–156, 180, 181, 183

FPGA field programmable gate array. ix, xi, xii, 21, 24, 26, 84, 97, 99, 101, 107, 110–113, 115–123, 125, 126, 128, 133, 134, 137, 139, 141, 145, 146, 148, 158, 168–170, 181

FSM finite state machine. 126–128, 131, 181

FWHM full-width at half-maximum. 16, 41, 160, 161, 163, 165

GA genetic algorithm. 90, 91

GFP green fluorescent protein. 4

GSA Gerchberg-Saxton algorithm. 92, 93

GSD ground state depletion. 8

GSW weighted Gerchberg-Saxton algorithm. 93–96, 151, 152, 154–156, 180, 181, 183

GUI graphical user interface. 25, 49, 80, 119, 137–147, 151, 168, 173, 181

I/O in- and output. 116, 120

IC integrated circuit. 24, 108, 110

iFFT inverse fast Fourier transform. 68

IP core semiconductor intellectual property core. 119, 120, 125, 126, 130, 131

IRF impulse response function. 3

LCOS liquid crystal on silicon. 64

LUT look-up table. 117

NA numerical aperture. 1, 2, 10, 14, 15, 42, 53, 58, 61, 63, 64

ND neutral density. 44, 45

NI National Instruments. 137, 139

NMA Nelder-Mead algorithm. 87, 89–92, 180

NV nitrogen vacancy center. xii, 51, 80, 160–163, 166, 174, 181

OD optical density. 30, 37

PBS polarizing beam splitter. 31, 49, 50

PI Physik Instrumente. 38, 97, 99

PLL phase-locked-loop. 125

PSF point spread function. 3, 6, 7, 12, 14, 15, 19, 30, 49, 53, 59, 62, 63, 72, 73, 75–81, 83, 84, 94, 100, 106, 137, 141–143, 147, 149, 158, 160–164, 166, 168, 169, 179, 180

QWP quarter wave plate. 49

RAM random access memory. 123, 125, 126, 134, 135

RMS root mean square. 109

SDRAM synchronous dynamic random access memory. 24, 116, 118–120, 122, 126, 127, 130–135, 170

SIM structured illumination microscopy. 126

SLM spatial light modulator. xi, 9, 22, 23, 26, 31, 35, 42, 49, 51, 53, 57, 58, 62, 64–70, 73–81, 84, 85, 87, 92, 93, 97, 139, 142–144, 149–160, 162–164, 167–169, 179–181

SNR signal-to-noise ratio. 7, 30, 48, 49, 53, 63, 83, 94, 143, 159–161, 167, 168

SPAD single-photon avalanche diode. ix, xi, 26, 27, 36, 37, 112, 113, 116, 128, 159, 168, 179, 180

STED stimulated emission depletion. ix–xi, 1, 8–10, 12–23, 25–31, 35–37, 40, 47–51, 53, 57, 62–65, 71–73, 75–80, 83, 84, 86, 93–95, 99, 109–111, 126, 138, 142, 149–152, 155, 157, 159–170, 179–181

STORM stochastic optical reconstruction microscopy. 8, 179

TEM transverse electromagnetic. 28, 29

TIRF total internal reflection fluorescence. 5

VHDL very high speed integrated circuit hardware description language. xi, 24, 26, 97, 115, 117–120, 125, 171, 173, 180

List of Figures

1.1. Matlab plot of Airy patterns. 2
1.2. Jablonski diagram of fluorophore energy states 5
1.3. Stokes shift at Atto590 6
1.4. Working principle of a confocal microscope 7
1.5. Stochastic optical reconstruction microscopy (STORM) reconstruction . . . 8
1.6. Deterministic super-resolution 10
1.7. Jablonski diagram of stimulated emission 11
1.8. Time evolution of state populations in stimulated emission depletion (STED) 13
1.9. Field contributions of STED point spread function (PSF) 15
1.10. Parameter dependence in pulsed STED 17

2.1. Box diagram of the STED microscope 21
2.2. Layer structure of an spatial light modulator (SLM) 23
2.3. Working principle of beam scanning 24
2.4. Schematic of the single-photon avalanche diode (SPAD) array 27
2.5. Silver mirror reflectance spectrum 32

3.1. Optical table layout 34
3.2. Fluorescence spectra in detection 37
3.3. Alignment and collimation obelisks 40
3.4. Collimation with obelisks 41
3.5. Alignment through back reflections 41
3.6. Razor blade measurement 42
3.7. Beam profiling with a camera 43
3.8. Manual stages for alignment 44
3.9. Mechanical transmission line for optically isolated components 46
3.10. Gold bead map 48

4.1. Linear optics principle 52
4.2. Sketch of an aplanatic system obeying the sine-condition 58
4.3. Fast focus calculation (FFC) for a Gaussian beam 61

4.4. FFC for a STED beam . . . 62
4.5. Polarization influence on the STED beam center . . . 63
4.6. Phase response at the SLM . . . 65
4.7. SLM calibration curve . . . 66
4.8. Graphics card comparison . . . 69
4.9. Model of optical aberration . . . 70
4.10. Sketch of spherical aberration . . . 72
4.11. Sketch of astigmatism . . . 73
4.12. Sketch of coma . . . 74
4.13. Razor blade measurement on the SLM . . . 76
4.14. Coma and spherical aberration on a Gaussian PSF . . . 77
4.15. Confocal image of a STED PSF on a gold-bead . . . 78

5.1. Working principle of the fan-out algorithm (FOA) . . . 83
5.2. FFC result of the fan-out algorithm (FOA) with the Nelder-Mead algorithm (NMA) . . . 87
5.3. Statistics of the NMA used in the FOA. . . . 88
5.4. Minimization with genetic algorithm in the FOA . . . 89
5.5. Working principle of the weighted Gerchberg-Saxton algorithm (GSW) . . . 91
5.6. FFC for a five-by-five STED beam array . . . 92
5.7. Comparison of the FOA and the weighted Gerchberg-Saxton algorithm (GSW) 93
5.8. Influence of beam spacing in an array on the STED beam quality . . . 93

6.1. Sample tower component illustration . . . 96
6.2. Wave function for stage scanning . . . 99
6.3. Ray tracing geometry . . . 100
6.4. Ray propagation through the mirror module . . . 102
6.5. Surface usage of the scanning mirrors . . . 103
6.6. Heat flow in the mirror mounting block . . . 105
6.7. Improved design of the mirror module . . . 106
6.8. Delay box connection schematic . . . 108
6.9. Photo of the electronic delay module board . . . 109
6.10. SPAD array illumination test . . . 111

7.1. Parasitic capacitance masking a rectangular voltage signal . . . 115
7.2. Low impedance measurement configuration . . . 116
7.3. Example of a very high speed integrated circuit hardware description language (VHDL) simulation in Vivado . . . 118

7.4. Top module connections and content in the field programmable gate array (FPGA) program 120
7.5. Waveform shape in mirror scanning 122
7.6. Data flow chart for the finite state machine (FSM) states 125
7.7. Transition chart for the FSM states 126
7.8. Working principle of a flancter entry point 127
7.9. Working principle of the data formation module 130
7.10. Working principle of the address formation module 131
7.11. Working principle of the data sorting module 133

8.1. Sketch of the main software structure 138
8.2. Image of the main graphical user interface (GUI) window 140
8.3. Image of the fitting GUI window 141
8.4. Image of the SLM GUI window 142
8.5. Sketch of the event loop in the timing module 144
8.6. Data flow between the PC and the FPGA during image acquisition 146

9.1. Measurement of a binary grating on SLM 148
9.2. Summary of phase profiles for the SLM 150
9.3. Photo of a beam array created by a FOA phase profile 151
9.4. Comparison between the FOA and the GSW phase profiles 152
9.5. Photos of a beam array on a laser viewing card 153
9.6. Confocal image of a beam array reflected on a gold-bead 156
9.7. Confocal image of a linear beam array reflected on a gold-bead 157
9.8. Single beam confocal and STED images of a nitrogen vacancy center (NV) 159
9.9. Single beam confocal and multi-beam STED images of a NV 160
9.10. Confocal and STED images of a Gattaquant "STED-nanoruler" 163

List of Tables

3.1. Table containing essential optical components 36

4.1. Table of primary Seidel aberrations 70
4.2. Connection between Seidel aberrations and Zernike polynomials 75

9.1. Power distribution in beamlets created with a GSW profile 154
9.2. Power distribution of beamlets created with an FOA phase profile 154

Bibliography

[1] Jale Schneider. “Entwicklung eines ultraschnellen elektro-optischen Scanners für STED-Nanoskopie”. PhD Thesis. Aachen: Publikationsserver der RWTH Aachen University, 2013. URL: http://publications.rwth-aachen.de/record/229739.

[2] Nicole Kilian et al. “Assessing photodamage in live-cell STED microscopy”. en. In: *Nature Methods* 15.10 (Oct. 2018), pp. 755–756. ISSN: 1548-7105. DOI: 10.1038/s41592-018-0145-5. URL: https://www.nature.com/articles/s41592-018-0145-5 (visited on 01/21/2020).

[3] Yong Wu et al. “Resonant Scanning with Large Field of View Reduces Photobleaching and Enhances Fluorescence Yield in STED Microscopy”. In: *Scientific Reports* 5 (Oct. 2015). ISSN: 2045-2322. DOI: 10.1038/srep14766. URL: http://www.ncbi.nlm.nih.gov/pmc/articles/PMC4589784/ (visited on 10/20/2015).

[4] Fabian Bergermann et al. “2000-fold parallelized dual-color STED fluorescence nanoscopy”. en. In: *Optics Express* 23.1 (Jan. 2015), p. 211. ISSN: 1094-4087. DOI: 10.1364/OE.23.000211. URL: https://www.osapublishing.org/oe/abstract.cfm?uri=oe-23-1-211 (visited on 10/20/2015).

[5] E. Abbe. “Beiträge zur Theorie des Mikroskops und der mikroskopischen Wahrnehmung”. de. In: *Archiv für Mikroskopische Anatomie* 9.1 (Dec. 1873), pp. 413–468. ISSN: 0176-7364. DOI: 10.1007/BF02956173. URL: https://doi.org/10.1007/BF02956173 (visited on 01/29/2020).

[6] John William Strutt Rayleigh. “Investigations in optics, with special reference to the spectroscope”. In: *The London, Edinburgh, and Dublin Philosophical Magazine and Journal of Science* 8.49 (Oct. 1879). URL: https://www.tandfonline.com/doi/abs/10.1080/14786447908639684 (visited on 02/25/2020).

[7] Bo Zhang, Josiane Zerubia, and Jean-Christophe Olivo-Marin. “Gaussian approximations of fluorescence microscope point-spread function models”. EN. In: *Applied Optics* 46.10 (Apr. 2007), pp. 1819–1829. ISSN: 2155-3165. DOI: 10.1364/AO.46.001819. URL: https://www.osapublishing.org/ao/abstract.cfm?uri=ao-46-10-1819 (visited on 02/25/2020).

[8] Adolph Baeyer. “On a new class of dyes”. In: *Reports of the German Chemical Society* 4 (1871), pp. 555–558.

[9] Larry J. Kricka and Paolo Fortina. “Analytical Ancestry: “Firsts” in Fluorescent Labeling of Nucleosides, Nucleotides, and Nucleic Acids”. en. In: *Clinical Chemistry* 55.4 (Apr. 2009), pp. 670–683. ISSN: 0009-9147. DOI: 10.1373/clinchem.2008.116152. URL: https://academic.oup.com/clinchem/article/55/4/670/5629399 (visited on 02/06/2020).

[10] Harekrushna Sahoo. “Fluorescent labeling techniques in biomolecules: a flashback”. en. In: *RSC Advances* 2.18 (2012), pp. 7017–7029. DOI: 10.1039/C2RA20389H. URL: https://pubs.rsc.org/en/content/articlelanding/2012/ra/c2ra20389h (visited on 02/06/2020).

[11] Osamu Shimomura. “Discovery of Green Fluorescent Protein (GFP) (Nobel Lecture)”. In: *Angewandte Chemie International Edition* 48.31 (2009), pp. 5590–5602. ISSN: 1521-3773. DOI: 10.1002/anie.200902240. URL: https://onlinelibrary.wiley.com/doi/abs/10.1002/anie.200902240 (visited on 02/06/2020).

[12] Gilbert N. Lewis and M. Kasha. “Phosphorescence and the Triplet State”. In: *Journal of the American Chemical Society* 66.12 (Dec. 1944). Publisher: American Chemical Society, pp. 2100–2116. ISSN: 0002-7863. DOI: 10.1021/ja01240a030. URL: https://doi.org/10.1021/ja01240a030 (visited on 11/24/2020).

[13] George Gabriel Stokes. “On the change of refrangibility of light”. In: *Philosophical Transactions of the Royal Society of London* 142 (Jan. 1852), pp. 463–562. DOI: 10.1098/rstl.1852.0022. URL: https://royalsocietypublishing.org/doi/10.1098/rstl.1852.0022 (visited on 02/12/2020).

[14] Hellen Ishikawa-Ankerhold, Richard Ankerhold, and Gregor Drummen. “Advanced fluorescence microscopy techniques—FRAP, flip, flap, FRET and flim”. In: *Molecules (Basel, Switzerland)* 17 (Dec. 2012), pp. 4047–132. DOI: 10.3390/molecules17044047.

[15] Robert H. Webb. “[1] Theoretical basis of confocal microscopy”. en. In: *Methods in Enzymology*. Vol. 307. Confocal Microscopy. Academic Press, Jan. 1999, pp. 3–20. DOI: 10.1016/S0076-6879(99)07003-2. URL: http://www.sciencedirect.com/science/article/pii/S0076687999070032 (visited on 10/09/2020).

[16] Daniel Sage et al. “Super-resolution fight club: assessment of 2D and 3D single-molecule localization microscopy software”. en. In: *Nature Methods* 16.5 (May 2019). Number: 5 Publisher: Nature Publishing Group, pp. 387–395. ISSN: 1548-7105. DOI: 10.1038/s41592-019-0364-4. URL: https://www.nature.com/articles/s41592-019-0364-4 (visited on 04/01/2020).

[17] Stefan W. Hell and Jan Wichmann. “Breaking the diffraction resolution limit by stimulated emission: stimulated-emission-depletion fluorescence microscopy”. EN. In: *Optics Letters* 19.11 (June 1994). Publisher: Optical Society of America, pp. 780–782. ISSN: 1539-4794. DOI: 10.1364/OL.19.000780. URL: https://www.osapublishing.org/ol/abstract.cfm?uri=ol-19-11-780 (visited on 03/02/2020).

[18] P. Török and P. R. T. Munro. “The use of Gauss-Laguerre vector beams in STED microscopy”. EN. In: *Optics Express* 12.15 (July 2004). Publisher: Optical Society of America, pp. 3605–3617. ISSN: 1094-4087. DOI: 10.1364/OPEX.12.003605. URL: https://www.osapublishing.org/oe/abstract.cfm?uri=oe-12-15-3605 (visited on 03/04/2020).

[19] Travis J. Gould et al. “Adaptive optics enables 3D STED microscopy in aberrating specimens”. EN. In: *Optics Express* 20.19 (Sept. 2012). Publisher: Optical Society of America, pp. 20998–21009. ISSN: 1094-4087. DOI: 10.1364/OE.20.020998. URL: https://www.osapublishing.org/oe/abstract.cfm?uri=oe-20-19-20998 (visited on 03/04/2020).

[20] Volker Westphal and Stefan W. Hell. “Nanoscale Resolution in the Focal Plane of an Optical Microscope”. In: *Physical Review Letters* 94.14 (Apr. 2005). Publisher: American Physical Society, p. 143903. DOI: 10.1103/PhysRevLett.94.143903. URL: https://link.aps.org/doi/10.1103/PhysRevLett.94.143903 (visited on 03/16/2020).

[21] Marcel Leutenegger, Christian Eggeling, and Stefan W. Hell. “Analytical description of STED microscopy performance”. EN. In: *Optics Express* 18.25 (Dec. 2010). Publisher: Optical Society of America, pp. 26417–26429. ISSN: 1094-4087. DOI: 10.1364/OE.18.026417. URL: https://www.osapublishing.org/oe/abstract.cfm?uri=oe-18-25-26417 (visited on 03/16/2020).

[22] Jeffrey R. Moffitt, Christian Osseforth, and Jens Michaelis. “Time-gating improves the spatial resolution of STED microscopy”. EN. In: *Optics Express* 19.5 (Feb. 2011). Publisher: Optical Society of America, pp. 4242–4254. ISSN: 1094-4087. DOI: 10.1364/OE.19.004242. URL: https://www.osapublishing.org/oe/abstract.cfm?uri=oe-19-5-4242 (visited on 01/06/2021).

[23] Jale Schneider et al. “Ultrafast, temporally stochastic STED nanoscopy of millisecond dynamics”. en. In: *Nature Methods* 12.9 (Sept. 2015). Number: 9 Publisher: Nature Publishing Group, pp. 827–830. ISSN: 1548-7105. DOI: 10.1038/nmeth.3481. URL: https://www.nature.com/articles/nmeth.3481/ (visited on 01/20/2021).

[24] Christian Osseforth. “Simultaneous dual-color 3D stimulated emission depletion microscopy: from design to applications”. Dissertation. Fakultät für Chemie und Pharmazie der Ludwig-Maximilians-Universität München, 2014.

[25] Andrew G. York, Maria Ingaramo, and Benjamin K. Cooper. “Line-rescanned STED microscopy is gentler and faster than point-descanned STED microscopy”. en. In: *Github.io* (Apr. 2017). URL: https://andrewgyork.github.io/rescan_line_sted/ (visited on 01/06/2021).

[26] Bi-Chang Chen et al. “Lattice light-sheet microscopy: Imaging molecules to embryos at high spatiotemporal resolution”. en. In: *Science* 346.6208 (Oct. 2014). Publisher: American Association for the Advancement of Science Section: Research Article. ISSN: 0036-8075, 1095-9203. DOI: 10.1126/science.1257998. URL: https://science.sciencemag.org/content/346/6208/1257998 (visited on 01/07/2021).

[27] Thorsten Staudt et al. “Far-field optical nanoscopy with reduced number of state transition cycles”. EN. In: *Optics Express* 19.6 (Mar. 2011). Publisher: Optical Society of America, pp. 5644–5657. ISSN: 1094-4087. DOI: 10.1364/OE.19.005644. URL: https://www.osapublishing.org/oe/abstract.cfm?uri=oe-19-6-5644 (visited on 01/20/2021).

[28] Britta Vinçon et al. “Pixel hopping enables fast STED nanoscopy at low light dose”. EN. In: *Optics Express* 28.4 (Feb. 2020). Publisher: Optical Society of America, pp. 4516–4528. ISSN: 1094-4087. DOI: 10.1364/OE.385174. URL: https://www.osapublishing.org/oe/abstract.cfm?uri=oe-28-4-4516 (visited on 01/06/2021).

[29] Maria J. Sarmento et al. “Exploiting the tunability of stimulated emission depletion microscopy for super-resolution imaging of nuclear structures”. eng. In: *Nature Communications* 9.1 (Aug. 2018), p. 3415. ISSN: 2041-1723. DOI: 10.1038/s41467-018-05963-2.

[30] Jan M. Binder et al. “Qudi: A modular python suite for experiment control and data processing”. en. In: *SoftwareX* 6 (Jan. 2017), pp. 85–90. ISSN: 2352-7110. DOI: 10.1016/j.softx.2017.02.001. URL: http://www.sciencedirect.com/science/article/pii/S2352711017300055 (visited on 03/26/2020).

[31] F. Ceccarelli et al. “Gigacount/Second Photon Detection Module Based on an Single-Photon Avalanche Diode Array”. In: *IEEE Photonics Technology Letters* 28.9 (May 2016), pp. 1002–1005. ISSN: 1041-1135. DOI: 10.1109/LPT.2016.2522974.

[32] Silvia Galiani et al. “Strategies to maximize the performance of a STED microscope”. EN. In: *Optics Express* 20.7 (Mar. 2012). Publisher: Optical Society of America, pp. 7362–7374. ISSN: 1094-4087. DOI: 10.1364/OE.20.007362. URL: https://www.osapublishing.org/oe/abstract.cfm?uri=oe-20-7-7362 (visited on 04/21/2020).

[33] Thorlabs GmbH. *Protected Silver Mirrors*. URL: https://www.thorlabs.com/newgrouppage9.cfm?objectgroup_id=903 (visited on 11/25/2020).

[34] Jonas Westberg. *Characterization of a Gaussian shapedlaser beam*. Jan. 2016. URL: https://www.umu.se/globalassets/centralwebb/studentwebben/institutioner/institutionen-for-fysik/laserfysik/186917_lab-iii.-instructions.-174901_lab-iii-measurement-of-gaussian-laser-beams-2016.pdf.

[35] V. A. Davydov et al. “Production of nano- and microdiamonds with Si-V and N-V luminescent centers at high pressures in systems based on mixtures of hydrocarbon and fluorocarbon compounds”. en. In: *JETP Letters* 99.10 (July 2014), pp. 585–589. ISSN: 1090-6487. DOI: 10.1134/S002136401410004X. URL: https://doi.org/10.1134/S002136401410004X (visited on 12/30/2020).

[36] Marcus W. Doherty et al. “The nitrogen-vacancy colour centre in diamond”. In: *Physics Reports* 528.1 (July 2013). arXiv: 1302.3288, pp. 1–45. ISSN: 03701573. DOI: 10.1016/j.physrep.2013.02.001. URL: http://arxiv.org/abs/1302.3288 (visited on 01/04/2021).

[37] Suhui Deng et al. “Effects of primary aberrations on the fluorescence depletion patterns of STED microscopy”. EN. In: *Optics Express* 18.2 (Jan. 2010). Publisher: Optical Society of America, pp. 1657–1666. ISSN: 1094-4087. DOI: 10.1364/OE.18.001657. URL: https://www.osapublishing.org/oe/abstract.cfm?uri=oe-18-2-1657 (visited on 10/19/2020).

[38] Bahaa E. A. Saleh and Marvin Carl Teich. *Fundamentals of photonics*. 2nd ed. Wiley Series in Pure and Applied Optics. Wiley, 2007. ISBN: 978-0-471-35832-9.

[39] E. Wolf and Dennis Gabor. “Electromagnetic diffraction in optical systems - I. An integral representation of the image field”. In: *Proceedings of the Royal Society of London. Series A. Mathematical and Physical Sciences* 253.1274 (Dec. 1959). Publisher: Royal Society, pp. 349–357. DOI: 10.1098/rspa.1959.0199. URL: https://royalsocietypublishing.org/doi/10.1098/rspa.1959.0199 (visited on 04/17/2020).

[40] B. Richards, E. Wolf, and Dennis Gabor. “Electromagnetic diffraction in optical systems, II. Structure of the image field in an aplanatic system”. In: *Proceedings of the Royal Society of London. Series A. Mathematical and Physical Sciences* 253.1274 (Dec. 1959). Publisher: Royal Society, pp. 358–379. DOI: 10.1098/rspa.1959.0200. URL: https://royalsocietypublishing.org/doi/10.1098/rspa.1959.0200 (visited on 04/17/2020).

[41] Marcel Leutenegger et al. “Fast focus field calculations”. EN. In: *Optics Express* 14.23 (Nov. 2006). Publisher: Optical Society of America, pp. 11277–11291. ISSN: 1094-4087. DOI: 10.1364/OE.14.011277. URL: https://www.osapublishing.org/oe/abstract.cfm?uri=oe-14-23-11277 (visited on 04/09/2020).

[42] Wolf Born. *Principles of Optics*. 4th ed. Pergamon Press, 1970.

[43] Xiang Hao et al. “Effects of polarization on the de-excitation dark focal spot in STED microscopy”. en. In: *Journal of Optics* 12.11 (Oct. 2010). Publisher: IOP Publishing, p. 115707. ISSN: 2040-8986. DOI: 10.1088/2040-8978/12/11/115707. URL: https://doi.org/10.1088%2F2040-8978%2F12%2F11%2F115707 (visited on 10/20/2020).

[44] James Wyant and Katherine Creath. “Basic Wavefront Aberration Theory for Optical Metrology”. In: *Appl Optics Optical Eng* 11 (Jan. 1992).

[45] André Klauss, Florian Conrad, and Carsten Hille. “Binary phase masks for easy system alignment and basic aberration sensing with spatial light modulators in STED microscopy”. en. In: *Scientific Reports* 7.1 (Nov. 2017). Number: 1 Publisher: Nature Publishing Group, p. 15699. ISSN: 2045-2322. DOI: 10.1038/s41598-017-15967-5. URL: https://www.nature.com/articles/s41598-017-15967-5 (visited on 09/17/2020).

[46] Mark A. A. Neil, Martin J. Booth, and Tony Wilson. “New modal wave-front sensor: a theoretical analysis”. EN. In: *JOSA A* 17.6 (June 2000). Publisher: Optical Society of America, pp. 1098–1107. ISSN: 1520-8532. DOI: 10.1364/JOSAA.17.001098. URL: https://www.osapublishing.org/josaa/abstract.cfm?uri=josaa-17-6-1098 (visited on 09/01/2020).

[47] Christian Osseforth et al. “Simultaneous dual-color 3D STED microscopy”. EN. In: *Optics Express* 22.6 (Mar. 2014). Publisher: Optical Society of America, pp. 7028–7039. ISSN: 1094-4087. DOI: 10.1364/OE.22.007028. URL: https://www.osapublishing.org/oe/abstract.cfm?uri=oe-22-6-7028 (visited on 01/07/2021).

[48] H. P. Herzig, D. Prongué, and R. Dändliker. “Design and Fabrication of Highly Efficient Fan-Out Elements”. en. In: *Japanese Journal of Applied Physics* 29.7A (July 1990). Publisher: IOP Publishing, p. L1307. ISSN: 1347-4065. DOI: 10.1143/JJAP.29.L1307. URL: https://iopscience.iop.org/article/10.1143/JJAP.29.L1307/meta (visited on 04/09/2020).

[49] D. Prongué et al. “Optimized kinoform structures for highly efficient fan-out elements”. EN. In: *Applied Optics* 31.26 (Sept. 1992). Publisher: Optical Society of America, pp. 5706–5711. ISSN: 2155-3165. DOI: 10.1364/AO.31.005706. URL: https://www.osapublishing.org/ao/abstract.cfm?uri=ao-31-26-5706 (visited on 06/15/2020).

[50] Jeffrey Lagarias et al. “Convergence Properties of the Nelder–Mead Simplex Method in Low Dimensions”. In: *SIAM Journal on Optimization* 9 (Dec. 1998), pp. 112–147. DOI: 10.1137/S1052623496303470.

[51] Roberto Di Leonardo, Francesca Ianni, and Giancarlo Ruocco. “Computer generation of optimal holograms for optical trap arrays”. en. In: *Optics Express* 15.4 (Feb. 2007), p. 1913. ISSN: 1094-4087. DOI: 10.1364/OE.15.001913. URL: https://www.osapublishing.org/oe/abstract.cfm?uri=oe-15-4-1913 (visited on 08/08/2016).

[52] Justin D. Mansell. “Integrating Wave-Optics and 5x5 Ray Matrices for More Accurate Optical System Modeling”. In: *MZA Associates Corporation, 2021 Girard Ste 150, Albuquerque, NM 87106* (2006).

[53] Michael Volk. “Unabhängige Steuerung der Freiheitsgrade eines Laserstrahls durch FPGA gesteuerte Spiegel”. Masterarbeit. Universität Ulm, Institut für Biophysik, Institut für eingebettete Systeme, 2018.

[54] *JEDEC Standard JESD8-7A - Interface Standard for 1.8V (Normal Range) Power Supply Voltage for Nonterminated Digital Integrated Circuits*. Sept. 2007. URL: https://www.jedec.org/system/files/docs/JESD8-7A.pdf.

[55] *JEDEC Standard JESD8C.01 - Interface Standard for 3.3V (Normal Range) Power Supply Voltage for Nonterminated Digital Integrated Circuits*. Sept. 2007. URL: https://www.jedec.org/system/files/docs/JESD8C-01.pdf.

[56] Brahim Haraoubia. *Non-Linear Electronics 2*. en. Elsevier, 2019. ISBN: 978-1-78548-301-1. DOI: 10.1016/C2019-0-02486-7. URL: https://linkinghub.elsevier.com/retrieve/pii/C20190024867 (visited on 12/11/2020).

[57] Jakob Bühler. “Expanding the functionalities of a STED microscope”. Master thesis. University of Ulm, Institute of Biophysics, 2020.

[58] *Project Jupyter*. URL: https://www.jupyter.org (visited on 12/11/2020).

Curriculum Vitae

Name:	Uwe Hermann Peter Jantzen
Year of birth:	1984
Place of birth:	Karlsruhe

Education

09.02.2022	Promotion, grade "magna cum laude"
2015–2021	Promotionsstudium, Universität Ulm, Institut für Biophysik
13.05.2015	Diplom, grade 1,1
2005–2015	Studium der Physik, Universität Ulm
2004–2005	Zivildienst, Kreiskrankenhaus Langenau
22.06.2004	Abitur, grade 2,4
1995–2004	Gymnasium, Robert-Bosch-Gymnasium Langenau
1993–1995	Grundschule, Ludwig-Uhland-Schule Langenau
1991–1993	Grundschule, Grundschule Völkersbach